Jordan Journal of

PHYSICS

An International Peer-Reviewed Research Journal

Volume 18, No. 3, August 2025

Jordan Journal of Physics (*JJP*): An International Peer-Reviewed Research Journal funded by the Scientific Research and Innovation Support Fund, Jordan, and published quarterly by the Deanship of Research and Graduate Studies, Yarmouk University, Irbid, Jordan.

EDITOR-IN-CHIEF: **Muhammad S. Bawa'aneh**
Department of Physics, Yarmouk University, Irbid, Jordan.
msbawaaneh@yu.edu.jo

EDITORIAL BOARD:

Prof. M-Ali H. Al-Akhras (AL-Omari)
Department of Physics, Jordan University of Science & Technology, Irbid, Jordan.
alakmoh@just.edu.jo

Prof. Riyad S. Manasrah
Department of Physics, The University of Jordan, Amman, Jordan.
r.manasrah@ju.edu.jo

Prof. Ibrahim A. Bsoul
Department of Physics, Al al-Bayt University, Mafraq, Jordan.
Ibrahimbsoul@yahoo.com

Prof. Ahmed M. Al-Khateeb
Department of Physics, Yarmouk University, Irbid, Jordan.
a.alkhateeb67@gmail.com

Prof. Khalid I. Nawafleh
Department of Physics, Mutah University, Al-Karak, Jordan.
knawaflehh@yahoo.com

ASSOCIATE EDITORIAL BOARD

Prof. Mark Hagmann
Desert Electronics Research Corporation, 762 Lacey Way, North Salt Lake 84064, Utah, U. S. A.
MHagmann@NewPathResearch.Com.

Dr. Richard G. Forbes
Dept. of Electrical and Electronic Engineering, University of Surrey, Advanced Technology Institute and Guildford, Surrey GU2 7XH, UK.
r.forbes@surrey.ac.uk

Prof. Roy Chantrell
Physics Department, The University of York, York, YO10 5DD, UK.
roy.chantrell@york.ac.uk

Prof. Susamu Taketomi
2-35-8 Higashisakamoto, Kagoshima City, 892-0861, Japan.
staketomi@hotmail.com

Editorial Secretary: Majdi Al-Shannaq.

Languages Editor: Olga Golubeva

Manuscripts should be submitted to:

Prof. Muhammad S. Bawa'aneh
Editor-in-Chief, Jordan Journal of Physics
Deanship of Research and Graduate Studies
Yarmouk University-Irbid-Jordan
Tel. 00 962 2 7211111 Ext. 2075
E-mail: *jjp@yu.edu.jo*
Website: *https://jjp.yu.edu.jo*

Jordan Journal of
PHYSICS
An International Peer-Reviewed Research Journal

Volume 18, No. 3, August 2025

INTERNATIONAL ADVISORY BOARD:

Prof. Dr. Humam B. Ghassib
Department of Physics, The University of Jordan, Amman 11942, Jordan.
humamg@ju.edu.jo

Prof. Dr. Sami H. Mahmood
Department of Physics, The University of Jordan, Amman 11942, Jordan.
s.mahmood@ju.edu.jo

Prof. Dr. Nihad A. Yusuf
Department of Physics, Yarmouk University, Irbid, Jordan.
nihadyusuf@yu.edu.jo

Prof. Dr. Hardev Singh Virk
#360, Sector 71, SAS Nagar (Mohali)-160071, India.
hardevsingh.virk@gmail.com

Dr. Mgr. Dinara Sobola
Department of Physics, Brno University of Technology, Brno, Czech Republic.
Dinara.Dallaeva@ceitec.vutbr.cz

Prof. Dr. Shawqi Al-Dallal
Department of Physics, Faculty of Science, University of Bahrain, Manamah, Kingdom of Bahrain.

Prof. Dr. Jozef Lipka
Department of Nuclear Physics and Technology, Slovak University of Technology, Bratislava, llkovicova 3, 812 19 Bratislava, Slovakia.
Lipka@elf.stuba.sk

Prof. Dr. Mohammad E. Achour
Laboratory of Telecommunications Systems and Decision Engineering (LASTID), Department of Physics, Faculty of Sciences, Ibn Tofail University, BP.133, Kenitra, Morocco (Morocco)
achour.me@univ-ibntofail.ac.ma

Prof. Dr. Ing. Alexandr Knápek
Group of e-beam lithograpy, Institute of Scientific Instruments of CAS, Královopolská 147, 612 64 Brno, Czech Republic.
knapek@isibrno.cz

Prof. Dr. Ahmad Salem
Department of Physics, Yarmouk University, Irbid, Jordan.
salema@yu.edu.jo

The Hashemite Kingdom of Jordan

Yarmouk University

Jordan Journal of
PHYSICS

An International Peer-Reviewed Research Journal
Funded by the Scientific Research and Innovation Support Fund

Volume 18, No. 3, August 2025

Instructions to Authors

Instructions to authors concerning manuscript organization and format apply to hardcopy submission by mail, and also to electronic online submission via the Journal homepage website (http://jjp.yu.edu.jo).

Manuscript Submission

Manuscripts are submitted electronically through the journal's website:

https://jjp.yu.edu.jo/

Original *Research Articles*, *Communications* and *Technical Notes* are subject to critical review by minimum of two competent referees. Authors are encouraged to suggest names of competent reviewers. *Feature Articles* in active Physics research fields, in which the author's own contribution and its relationship to other work in the field constitute the main body of the article, appear as a result of an invitation from the Editorial Board, and will be so designated. The author of a *Feature Article* will be asked to provide a clear, concise and critical status report of the field as an introduction to the article. *Review Articles* on active and rapidly changing Physics research fields will also be published. Authors of *Review Articles* are encouraged to submit two-page proposals to the Editor-in-Chief for approval. Manuscripts submitted in *Arabic* should be accompanied by an Abstract and Keywords in English.

Organization of the Manuscript

Manuscripts should be typed double spaced on one side of A4 sheets (21.6 x 27.9 cm) with 3.71 cm margins, using Microsoft Word 2000 or a later version thereof. The author should adhere to the following order of presentation: Article Title, Author(s), Full Address and E-mail, Abstract, PACS and Keywords, Main Text, Acknowledgment. Only the first letters of words in the Title, Headings and Subheadings are capitalized. Headings should be in **bold** while subheadings in *italic* fonts.

Title Page: Includes the title of the article, authors' first names, middle initials and surnames and affiliations. The affiliation should comprise the department, institution (university or company), city, zip code and state and should be typed as a footnote to the author's name. The name and complete mailing address, telephone and fax numbers, and e-mail address of the author responsible for correspondence (designated with an asterisk) should also be included for official use. The title should be carefully, concisely and clearly constructed to highlight the emphasis and content of the manuscript, which is very important for information retrieval.

Abstract: A one paragraph abstract not exceeding 200 words is required, which should be arranged to highlight the purpose, methods used, results and major findings**.**

Keywords: A list of 4-6 keywords, which expresses the precise content of the manuscript for indexing purposes, should follow the abstract.

PACS: Authors should supply one or more relevant PACS-2006 classification codes, (available at http://www.aip.org/pacs/pacs06/pacs06-toc.html)

Introduction: Should present the purpose of the submitted work and its relationship to earlier work in the field, but it should not be an extensive review of the literature (e.g., should not exceed 1 ½ typed pages).

Experimental Methods: Should be sufficiently informative to allow competent reproduction of the experimental procedures presented; yet concise enough not to be repetitive of earlier published procedures.

Results: should present the results clearly and concisely.

Discussion: Should be concise and focus on the interpretation of the results.

Conclusion: Should be a brief account of the major findings of the study not exceeding one typed page.

Acknowledgments: Including those for grant and financial support if any, should be typed in one paragraph directly preceding the References.

References: References should be typed double spaced and numbered sequentially in the order in which they are cited in the text. References should be cited in the text by the appropriate Arabic numerals, enclosed in square brackets. Titles of journals are abbreviated according to list of scientific periodicals. The style and punctuation should conform to the following examples:

1. Journal Article:

a) Heisenberg, W., Z. Phys. 49 (1928) 619.
b) Bednorz, J. G. and Müller, K. A., Z. Phys. B64 (1986) 189
c) Bardeen, J., Cooper, L.N. and Schrieffer, J. R., Phys. Rev. 106 (1957) 162.
d) Asad, J. H., Hijjawi, R. S., Sakaji, A. and Khalifeh, J. M., Int. J. Theor. Phys. 44(4) (2005), 3977.

2. Books with Authors, but no Editors:

a) Kittel, C., "Introduction to Solid State Physics", 8th Ed. (John Wiley and Sons, New York, 2005), chapter 16.
b) Chikazumi, S., C. D. Graham, JR, "Physics of Ferromagnetism", 2nd Ed. (Oxford University Press, Oxford, 1997).

3. Books with Authors and Editors:

a) Allen, P. B. "Dynamical Properties of Solids", Ed. (1), G. K. Horton and A. A. Maradudin (North-Holland, Amsterdam, 1980), p137.
b) Chantrell, R. W. and O'Grady, K., "Magnetic Properities of Fine Particles" Eds. J. L. Dormann and D. Fiorani (North-Holland, Amsterdam, 1992), p103.

4. Technical Report:

Purcell, J. "The Superconducting Magnet System for the 12-Foot Bubble Chamber", report ANL/HEP6813, Argonne Natt. Lab., Argonne, III, (1968).

5. Patent:

Bigham, C. B., Schneider, H. R., US patent 3 925 676 (1975).

6. Thesis:

Mahmood, S. H., Ph.D. Thesis, Michigan State University, (1986), USA (Unpublished).

7. Conference or Symposium Proceedings:

Blandin, A. and Lederer, P. Proc. Intern. Conf. on Magnetism, Nottingham (1964), P.71.

8. Internet Source:

Should include authors' names (if any), title, internet website, URL, and date of access.

9. Prepublication online articles (already accepted for publication):

Should include authors' names (if any), title of digital database, database website, URL, and date of access.

For other types of referenced works, provide sufficient information to enable readers to access them.

Tables: Tables should be numbered with Arabic numerals and referred to by number in the Text (e.g., Table 1). Each table should be typed on a separate page with the legend above the table, while explanatory footnotes, which are indicated by superscript lowercase letters, should be typed below the table.

Illustrations: Figures, drawings, diagrams, charts and photographs are to be numbered in a consecutive series of Arabic numerals in the order in which they are cited in the text. Computer-generated illustrations and good-quality digital photographic prints are accepted. They should be black and white originals (not photocopies) provided on separate pages and identified with their corresponding numbers. Actual size graphics should be provided, which need no further manipulation, with lettering (Arial or Helvetica) not smaller than 8 points, lines no thinner than 0.5 point, and each of uniform density. All colors should be removed from graphics except for those graphics to be considered for publication in color. If graphics are to be submitted digitally, they should conform to the following minimum resolution requirements: 1200 dpi for black and white line art, 600 dpi for grayscale art, and 300 dpi for color art. All graphic files must be saved as TIFF images, and all illustrations must be submitted in the actual size at which they should appear in the journal. Note that good quality hardcopy original illustrations are required for both online and mail submissions of manuscripts.

Text Footnotes: The use of text footnotes is to be avoided. When their use is absolutely necessary, they should be typed at the bottom of the page to which they refer, and should be cited in the text by a superscript asterisk or multiples thereof. Place a line above the footnote, so that it is set off from the text.

Supplementary Material: Authors are encouraged to provide all supplementary materials that may facilitate the review process, including any detailed mathematical derivations that may not appear in whole in the manuscript.

Revised Manuscript and Computer Disks

Following the acceptance of a manuscript for publication and the incorporation of all required revisions, authors should submit an original and one more copy of the final disk containing the complete manuscript typed double spaced in Microsoft Word for Windows 2000 or a later version thereof. All graphic files must be saved as PDF, JPG, or TIFF images.

Allen, P.B., "…………….", in: Horton, G.K., and Muradudin, A. A., (eds.), "Dynamical…….", (North……..), pp….

Reprints

Twenty (20) reprints free of charge are provided to the corresponding author. For orders of more reprints, a reprint order form and prices will be sent with the article proofs, which should be returned directly to the Editor for processing.

Copyright

Submission is an admission by the authors that the manuscript has neither been previously published nor is being considered for publication elsewhere. A statement transferring copyright from the authors to Yarmouk University is required before the manuscript can be accepted for publication. The necessary form for such transfer is supplied by the Editor-in-Chief. Reproduction of any part of the contents of a published work is forbidden without a written permission by the Editor-in-Chief.

Disclaimer

Opinions expressed in this Journal are those of the authors and neither necessarily reflects the opinions of the Editorial Board or the University, nor the policy of the Higher Scientific Research Committee or the Ministry of Higher Education and Scientific Research. The publisher shoulders no responsibility or liability whatsoever for the use or misuse of the information published by JJP.

Indexing

JJP is currently indexing in:

Scopus	**Emerging Sources Citation Index (ESCI)** Journal Impact Factor 2022 0.7
ULRICHSWEB™ GLOBAL SERIALS DIRECTORY	

Jordan Journal of
PHYSICS
An International Peer-Reviewed Research Journal

Volume 18, No. 3, August 2025

Table of Contents:

Volume 18, Number 3, 2025. pp. 251-264

Jordan Journal of Physics

ARTICLE

DFT Study of the π-π Interaction between Graphene and Liquid Crystal Molecules for the Charge Transfer Applications

Tikaram, Yogesh Kumar and **Narinder Kumar**

Department of Physics, School of Applied & Life Sciences, Uttaranchal University, Dehradun, Uttarakhand-248007, India.

Doi: **https://doi.org/10.47011/18.3.1**

Received on: 20/04/2023; Accepted on: 05/05/2024

Abstract: As the LC and GP sheets meet, the ionization potential, HOMO-LUMO gap, and cosmo area of the whole dimer (LC+GP) all drop. Every LC engages in a parallel plane (armchair) or diagonal cross-section interaction with the GP. Benzene-based liquid crystals interact strongly with graphene, whereas cyclohexane-based liquid crystals interact only weakly. Liquid crystal dimers based on benzene interact negatively with graphene. Liquid crystals composed of oxygen and nitrogen atoms exhibit interactions with graphene. Whereas nitrogen atom-based liquid crystals very faintly interact with graphene, oxygen atom-based liquid crystals do so energetically. In contrast to the nitrogen atom-based liquid crystal, the oxygen atom-based liquid crystal dimer displays a more impressive dipole moment. The strongest dipole moment is observed for the liquid crystal containing both nitrogen and oxygen atoms. The graphene sheet twisted in all the dimers, and all the liquid crystal benzene rings exhibit the π-π interaction with the graphene at a distance of ~3.5Å. The cyclohexane ring and the terminal group of the liquid crystal interact with graphene at a distance of ~2.5Å, but they do not show π-stacking.

Keywords: Graphene, Liquid crystal, Molecular interaction, π-π stacking, Density Functional Theory (DFT).

Introduction

Graphene [1] has a hexagonal arrangement of carbon atoms and acquires a 2D crystalline solid structure in a planar form [2]. The sp^2 hybridization of carbon atoms in graphene is responsible for the high charge carrier mobility, excellent mechanical flexibility, and very high thermal conductivity; hence, graphene has a wide range of applications in optical devices [3]. Owing to its large surface-to-volume ratio, graphene is particularly well suited for ultracapacitor and chemical sensor applications [4]. Its transparency and low-cost availability make it attractive for use in organic light-emitting diodes (OLEDs), touchscreen displays, and solar cells [5]. Graphene-based photodetectors operate at a very high frequency [6]. Graphene has a conical electronic bandgap structure that lies between the valence and conduction bands [7]. The valence and conduction bands overlap slightly, classifying it as a zero-bandgap semimetal. Graphene is one of the allotropes of carbon made of a single layer of carbon atoms arranged in a hexagonal lattice. Besides graphene, other allotropes of carbon are diamond, fullerene, charcoal, and carbon nanotubes. Graphene behaves as a good conductor of heat and electricity and is capable of light absorption. Graphene is about 200 times stronger than steel [9]. Graphene-based liquid crystals exhibit high-speed electro-optic switching. Their interaction with graphene is governed by л-π electron stacking. The interactions between liquid crystals and graphene through л-π electron stacking establish a planar

Corresponding Author: Narinder Kumar **Email**: knarinder7@gmail.com

arrangement of the liquid crystal in graphene-based cells. Graphene-based liquid crystals actively exhibit a nematic phase under the effect of an electric field. Basu *et al*. reported that π-π interaction of LC with GP gives rise to the physical and optical properties of dimers. The LC reduces the free ion concentration by an ion-trapping process after the communication of LC and GP; the present work also reveals an enhancement in the ionization potential of the dimer [9]. The birefringence of liquid crystals predicts a new technique to visualize domain and grain boundaries of graphene. The liquid crystal and graphene have strong epitaxial interactions, and liquid crystals have planar orientation along with graphene [10]. The anchoring forces align liquid crystals and graphene in the planar configuration. Shehzad *et al*. reported that the nematic liquid crystal on graphene usually makes six random conformations [11]. The nematic and smectic type liquid crystals impose planar alignment on the graphene surface. The decreased free ion concentration in the dimer (LC+GP) reduces the rotational viscosity that is responsible for the electro-optic switching or faster response [12]. In this work, we are using rod-like, nematic-phase LC molecules. The interaction of LC and GP affects such parameters as ionization potential, HOMO-LUMO gap, COSMO area, COSMO volume, and dipole moment of the dimer. Shen *et al*. demonstrated that doping LCs with GP enhances the physical properties of the dimer, particularly the dipole moment, because free ions in the LC are trapped by GP, thereby lowering the threshold voltage [13]. Mrukiewicz *et al*. reported that the strong π-π interaction between 5CB LC and GP makes this combination suitable for applications in LC modulators, filters, isotropic LC displays, and smart windows [14]. Fischer *et al*. reported that 5CB LC adsorbs onto GP in the armchair conformation; the present work also reveals that 5CB LCs interact with GP in the armchair conformation [15]. Basu *et al*., Kumar *et al*., and Lapanik *et al*. reported that the strong π-π interaction of LCs with GP enhances the dipole moment; the present work also reveals a dipole moment increase of H5CBP LC because it transfers the maximum charge to GP [16-17].

Computational Methodology

Graphene and liquid crystal molecules are optimized by the Gaussian 09 software package [18] with the help of DFT LC-BLYP method [19-20] and 6-31G basis set [21]. All dimers were optimized by seven DFT methods, and we have considered only the LC-BLYP minimum energy conformations of the GP and LC. All dimers were generated under free optimization (where coordinates were not fixed). Under the free optimization, all monomers (GP & LC) randomly interacted with each other and produced one minimum energy conformation. The total energy (ΔE) of the dimer (LC+GP) was calculated by the formula given below [22]

$$\Delta E = E_{el} + E_{rep} + E_{pol} + E_{disp}$$

where E_{el}, E_{rep}, $E_{pol,}$ and E_{disp} represent the attractive electrostatic, short-range repulsion, polarization, and dispersion energy, respectively.

Results and Discussion

In this work, we confirm that LCs interact with GP primarily through parallel stacking. All studied LCs are polar, which accounts for the high dipole moments observed in the dimers. The molecular weight of the dimers remains unaffected after interaction; however, the ionization potential, COSMO area, and the highest occupied molecular orbital (HOMO) and the lowest unoccupied molecular orbital (LUMO) gap decrease for all dimers upon interaction between GP and LC. The COSMO volume of the dimers either increases or decreases depending on the LC type. All LC dimers exhibit positive interaction energy, as adsorption occurs in different conformations. Among the studied LCs, H5CBP transfers the maximum charge to GP, making it most suitable for charge-transfer applications. P.P'-disubstituted diphenylacetylenes, PCH, and 7O LC also transfer appreciable charge to GP; however, H5CBP remains the most effective.

CCH5 (5-Cyclohexylcyclohexane-1,3-dione) LC & GP

Where [D-(M_1+M_2)]:- [Dimer energy {LC+GP} – (Monomer energy (M_1) {LC} + Monomer (M_2) energy {GP})]

The GP and CCH5 LC interact via parallelplane stacking. As shown in Fig. 1 and Table 1, this conformation reduces the ionization potential, HOMO–LUMO gap, dipole moment, and COSMO area, while increasing both the total energy and COSMO volume of the dimer. Because of its two cyclohexane rings, this LC exhibits modest interaction energy with the GP. Compared to the benzene ring, the cyclohexane ring shows weaker contact. Although the cyclohexane ring has a chair conformation, the benzene ring has a planar shape. A benzene ring contains carbon atoms that have undergone sp2 hybridization, whereas a cyclohexane ring has sp3 hybridization. Their respective melting and boiling points, as well as molecular masses, are different. The benzene molecule has delocalized pi-electron clouds, but the cyclohexane ring does not. Sigma bonds and pi delocalized electrons distinguish cyclohexane as an aliphatic compound and benzene as an aromatic one. Because of the electron being trapped, the CCH5 LC transfers the least amount of charge to graphene. Due to the lack of interaction in CCH5 LC, the GP sheet became somewhat distorted. At a distance of 2.85, the hydrogen atom of GP interacts with the nitrogen atom of the cyano group. At a minimum distance of 2.56, the first cyclohexane ring interacts with the general potential. At a distance of 2.54, the carbon atom of GP interacts with the second hydrogen atom of the cyclohexane ring. At a distance of 2.52, the tail of the LC contacts the GP surface.

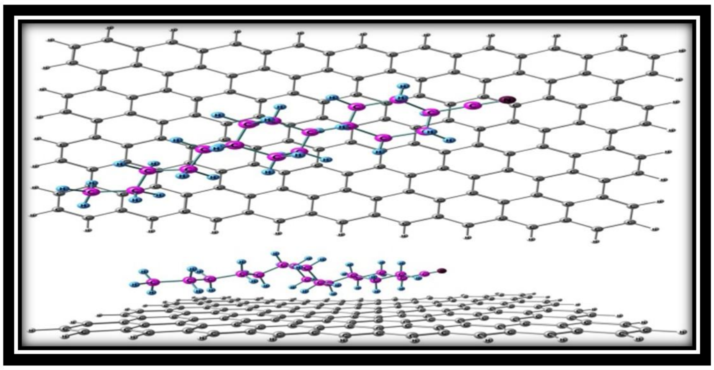

FIG. 1. Side and top views of the LC (CCH5) interacting with GP in parallel (armchair) stacking. The dielectric and optical anisotropies of all CCH molecules are much lower than those of the corresponding CB or PCH molecules. CCH-4, in particular, can serve as a liquid-crystalline solvent in spectroscopic applications. In general, CCH liquid crystals exhibit low birefringence and high negative dielectric anisotropy, making them suitable for such use.

TABLE 1. Total energy, dipole moment, ionization potential, HOMO–LUMO gap, molecular weight, COSMO area, and COSMO volume of the CCH5–GP dimer shown in Fig. 1.

CCH5_GP	Monomer (LC)	Monomer (GP)	Dimer (LC+GP)	Difference [D-(M_1+M_2)]
Total Energy (a.u.)	-756.78194	-5812.3749	-6551.2975	-17.8593
Dipole moment (Debye)	4.60	0.00	1.39	-3.21
Ionization potential (eV)	10.83	3.76	4.86	-9.73
HOMO-LUMO gap (eV)	6.59	0.16	2.15	-4.60
Molecular Weight	261.44	1859.94	2121.39	0.00
Cosmo Area $(Å)^2$	330.04	1229.95	1322.51	-237.48
Cosmo Volume $(Å)^3$	376.35	1776.96	2169.04	15.73

P.P'-disubstituted diphenylacetylenes LC & GP

The P.P'-disubstituted diphenylacetylenes LC [25] interacts diagonally with tGP in the parallel plane. The dipole moment, ionisation potential, HOMO-LUMO gap, and COSMO area in this dimer diminish when the GP and LC engage with one another in the parallel plane diagonal configuration, as illustrated in Fig. 2 and Table 2, while the total energy and COSMO volume rise. It is appropriate for solar cell applications since the P.P'-disubstituted diphenylacetylenes LC deliver roughly the same amount of charge to the graphene. The P.P'-disubstituted diphenylacetylenes LC display the interaction; however, the tail of LC does not express stacking, which causes the GP sheet to twist. At a distance of 2.63, the CH3 group bonded to the oxygen atom displays interactions with the GP. At a distance of 3.44 from GP, the oxygen atom interacts with it. At a distance of 3.41, the carbon atom of benzene interacts with the carbon atom of GP. At a distance of 3.38, the other benzene in LC interacts with the carbon atom in GP. At a distance of 2.65, the tail of the LC contacts with GP.

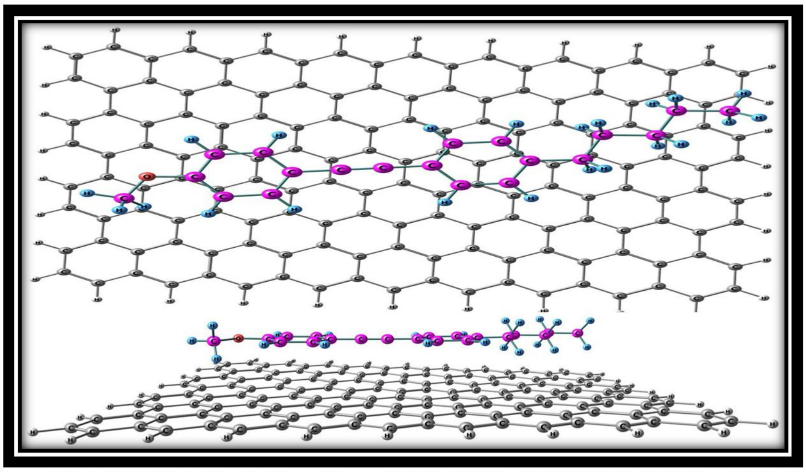

FIG. 2. Side and top view showing the interaction of LC (P.P'-disubstituted diphenylacetylenes) with GP in parallel (armchair) stacking. The electronic properties of graphene stacks depend on the stacking order and the number of layers. The interaction of molecules with graphene can be tuned by doping the graphene sheet with dopant atoms, which regulate the van der Waals forces exerted on adsorbed molecules. Functionalization of graphene typically occurs through π-π interactions between the graphene surface and other moieties. Graphene, a one-atom-thick allotrope of carbon, exhibits unique two-dimensional Dirac-like electronic excitations. The behavior of Dirac electrons in graphene can be modulated by external electric and magnetic fields, or by altering the sample's geometry and topology.

TABLE 2. Total energy, dipole moment, ionization potential, HOMO-LUMO gap, molecular weight, COSMO area, and COSMO volume of the dimer shown in Fig. 2.

P.P' D-D LC_ GP	Monomer (LC)	Dimer (LC+GP)	Difference [D-(M_1+M_2)]
Total Energy (a.u.)	-847.73885	-6642.2641	-17.8496
Dipole moment (Debye)	1.58	1.55	-0.03
Ionization potential (eV)	7.93	4.84	-6.85
HOMO-LUMO gap (eV)	6.54	2.16	-4.54
Molecular Weight	278.39	2138.33	0.00
COSMO Area (Å)^2	358.23	1307.48	-280.7
COSMO Volume (Å)^3	372.49	2152.15	2.7

5CB LC & GP

GP and the 5CB (4-Cyano-4'-pentylbiphenyl) LC [26–27] interact in the parallel plane. When GP and LC engage on the parallel plane configuration depicted in Fig. 3 and Table 3, the ionisation potential, HOMO-LUMO gap, COSMO volume, dipole moment, and COSMO area decrease, while the total energy and COSMO volume rise. According to Basu *et al.,* the physical and optical characteristics of dimers are the result of the LC and GP interacting negatively. After communicating with GP, the LC uses an ion-trapping mechanism to lower the concentration of free ions [22–23]. The contact causes the GP's zero dipole moment to grow through an ion-trapping mechanism (present work). Because 5CB LC displays the - interaction while the tail of LC does not, the GP sheet is twisted. Because of its small charge transfer to graphene, the 5CB LC is not suited for solar applications. At a distance of 3.21, the hydrogen atom of GP interacts with the nitrogen atom of the cyano group. At a distance of 2.99, the benzene from the cyano group side interacts with GP. At a distance of 3.17, the second benzene reacts with GP. At a distance of 2.61, the tail of the LC interacts with GP.

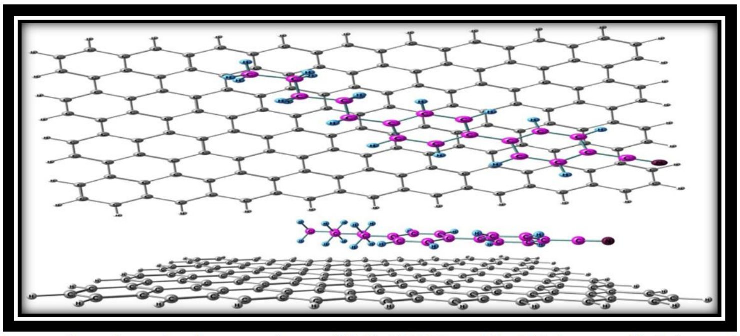

FIG. 3. Side and top views showing the interaction of LC (5CB) with GP in parallel (armchair) stacking. Density functional theory (DFT) was used to investigate the stable adsorption geometries of the liquid crystal molecule 5CB on a graphene sheet. Results indicate that the insertion reaction is likely spontaneous and irreversible, suggesting a potential pathway for tuning both liquid crystal behavior and graphene properties. The two-dimensional honeycomb structure of graphene interacts with the benzene rings of the LC through π-π electron stacking. The homeotropic alignment of the 5CB molecule on monovacancy graphene differs from its preferred planar orientation on pristine graphene.

Table 3. Total energy, dipole moment, ionization potential, HOMO-LUMO gap, molecular weight, COSMO area, and COSMO volume of the dimer shown in Fig. 3.

5CB_ GP	Monomer (LC)	Dimer (LC+GP)	Difference [D-(M_1+M_2)]
Total Energy (a.u.)	-749.588844	-6544.1145	-17.8492
Dipole moment (Debye)	5.69	2.29	-3.40
Ionization potential (eV)	9.00	4.86	-7.90
HOMO-LUMO gap (eV)	8.22	2.15	-6.23
Molecular Weight	249.35	2109.29	0.00
COSMO Area $(Å)^2$	319.15	1301.10	-248
COSMO Volume $(Å)^3$	336.56	2138.71	25.19

PCH5 (4-(trans-4-Pentylcyclohexyl)benzonitrile) LC & GP

GP and the PCH5 trans-4-pentyl-(4-cyanopheny1)-cyclohexane LC [28-29] interact on a parallel plane. When GP and LC interact with one another in A parallel plane configuration, as illustrated in Fig. 4 and Table 4, the ionisation potential, dipole moment, HOMO-LUMO gap, and COSMO area drop while the COSMO volume and total energy rise. Because it transfers more charge to graphene, the PCH5 LC is superior to the 5CB LC. Since the PCH5 LC displays the π–π interaction while the cyclohexane ring and tail of the LC do not, the GP sheet is somewhat bent. At a distance of 3.01, the cyano group's nitrogen atom interacts with GP. At a distance of 2.96, the benzene ring interacts with GP. The cyclohexane reacts with GP at a distance of 2.60. The alkyl chain contacts GP at a distance of 2.71.

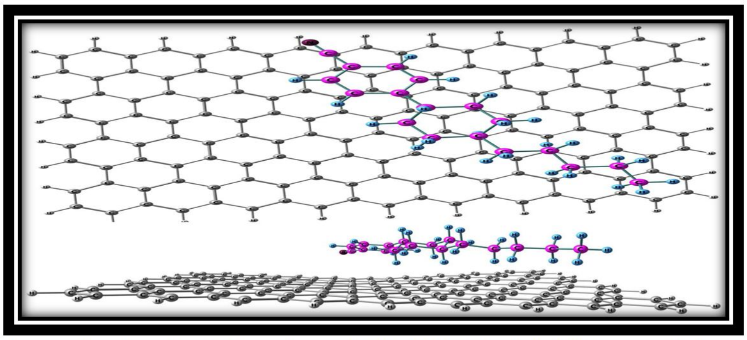

FIG. 4. Side and top views showing the interaction of LC (PCH5) with GP in parallel (armchair) stacking. The two-dimensional graphene honeycomb structure interacts with the liquid crystal's (LC) benzene rings through π–π electron stacking. The results indicate that the insertion reaction is likely spontaneous and irreversible, offering a potential pathway for controlling both liquid crystal behavior and graphene properties. PCH5 is a rod-like liquid crystal with a nematic–isotropic phase transition at 327.6 K. At a distance of 3.01, the nitrogen atom of the cyano group interacts with GP.

TABLE 4. Total energy, dipole moment, ionization potential, HOMO-LUMO gap, molecular weight, COSMO area, and COSMO volume of the dimer shown in Fig. 4.

PCH_GP	Monomer (LC)	Dimer (LC+GP)	Difference [D-(M_1+M_2)]
Total Energy (a.u.)	-753.18566	-6547.7126	-17.8479
Dipole moment (Debye)	5.42	5.06	-0.36
Ionization potential (eV)	9.74	4.93	-8.57
HOMO-LUMO gap (eV)	8.48	2.29	-6.35
Molecular Weight	255.40	2115.34	0.00
COSMO Area (Å)^2	324.82	1314.72	-240.05
COSMO Volume (Å)^3	354.51	2145.26	13.79

6O.2 or 6O.5 LC & GP

The interaction between GP and 6O.5 {4-5-Alkyl-N-(4-6-Alkyloxy-Benzylidene)-Anilines} LC [30] takes the form of a letter V. When the GP and LC interact in the form of a letter V, as illustrated in Fig. 5 and Table 5, the ionisation potential, HOMO-LUMO gap, cosmo volume, cosmo area, and dipole moment drop, while the total energy increases. Graphene does not receive charges from the 6O.5 LC at a suitable pace. Due to the π–π interaction present in 6O.5 LC, the GP sheet twisted. At a distance of 2.72, the nitrogen atom's side of the LC tail interacts with GP. At a distance of 2.78, the benzene interacts with GP on the side of the nitrogen atom. At a distance of 3.43, the nitrogen atom of the bridging group interacts with the carbon atom of GP. At a distance of 2.62, the side of benzene that interacts with GP connects with the oxygen atom. The oxygen atom of LC interacts with the carbon atom at a distance of 4.70Å. The tail of the oxygen atom side LC interacts with GP at a distance of 2.68Å.

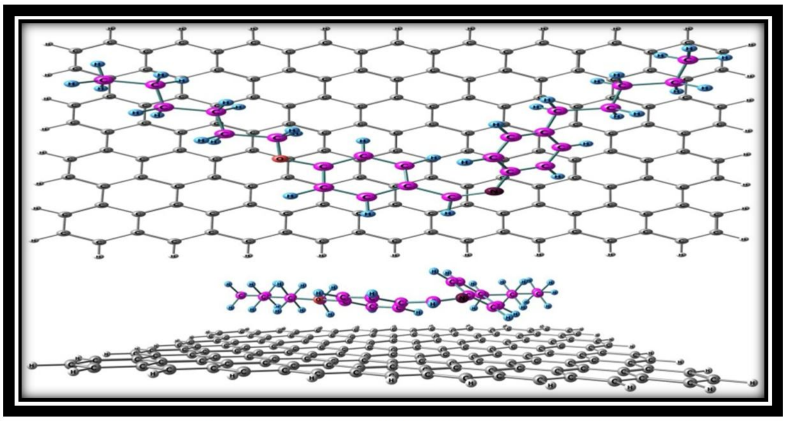

FIG. 5. Side and top views showing the interaction of LC (6O.5) with GP in a V-shaped conformation. This liquid crystal flows like a liquid but maintains molecular alignment in a crystal-like manner, producing characteristic textures observable under a microscope. 6O.5 LC has a low melting point, high boiling point, high viscosity, and low surface tension. It also exhibits high dielectric anisotropy, meaning its dielectric constant varies along different molecular axes. These properties make it useful in applications such as liquid crystal displays (LCDs), thermometers, and mood rings. Due to the π–π interaction present in 6O.5 LC, the GP sheet is twisted. At a distance of 2.72, the nitrogen atom's side of the LC tail interacts with GP.

Table 5. Total energy, dipole moment, ionization potential, HOMO-LUMO gap, molecular weight, COSMO area, and COSMO volume of the dimer shown in Fig. 5.

6O.5_ GP	Monomer (LC)	Dimer (LC+GP)	Difference [D-(M_1+M_2)]
Total Energy (a.u.)	-1060.88216	-6855.3974	-17.8596
Dipole moment (Debye)	3.78	2.19	-1.59
Ionization potential (eV)	8.16	4.85	-7.07
HOMO-LUMO gap (eV)	6.82	2.15	-4.83
Molecular Weight	351.53	2211.47	0.00
COSMO Area (Å)^2	444.56	1335.02	-339.49
COSMO Volume (Å)^3	482.40	2250.39	-8.97

7O.5 LC & GP

In parallel plane stacking, GP and 7O.5 {4-5-Alkyl-N-(4-7-Alkyloxy-Benzylidene)-Anilines} LC [31-32] interact. As GP and LC interact, as illustrated in Fig. 6 and Table 6, the ionisation potential, HOMO-LUMO gap, dipole moment, and COSMO area drop, while the total energy and COSMO volume rise. Compared to 6O.5 LC, 7O.5 has a greater charge transfer rate. Due to the π–π interaction displayed by 7O.5 LC, the GP sheet becomes twisted. At a distance of 2.62, the benzene interacts with GP from the side of the oxygen atom. At a distance of 2.55, the oxygen atom's side of the liquid crystal tail contacts with GP. At a distance of 2.90, the hydrogen atom in the bridging group interacts with GP. At a distance of 3.56, the second benzene reacts with GP. At a distance of 2.65, the tail of the LC contacts with GP.

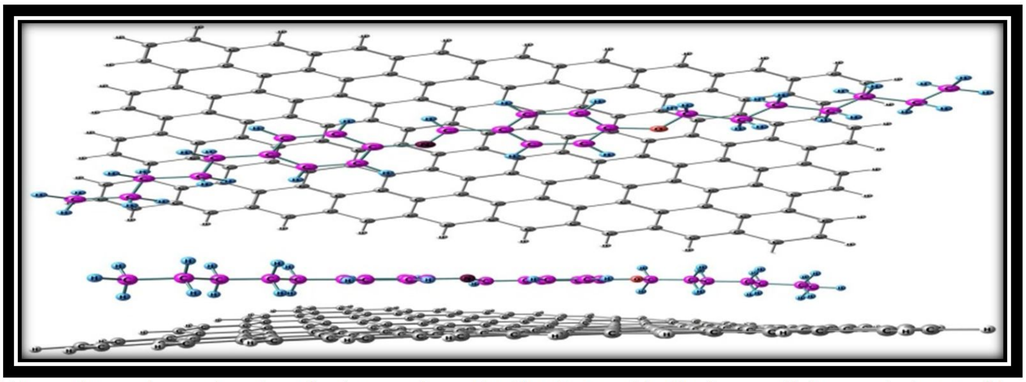

FIG. 6. Side and top views showing the interaction of LC (7O.5) with GP in parallel (armchair) stacking. The 4-5-Alkyl-N-(4-7-Alkyloxy-Benzylidene)-Anilines belong to the benzylidene aniline family, characterized by an alkyl group and an alkoxybenzylidene group attached to an aniline core. Their properties depend strongly on the length of the alkyl and alkoxy chains, which influence phase transition behavior. These compounds have also been used to design liquid crystal assemblies through hydrogen-bonding interactions. In this work, the π–π interaction of 7O.5 LC with GP causeS the graphene sheet to twist. At a distance of 2.62, the benzene interacts with GP from the side of the oxygen atom.

Table 6. Total energy, dipole moment, ionization potential, HOMO-LUMO gap, molecular weight, COSMO area, and COSMO volume of the dimer shown in Fig. 6.

7O_GP	Monomer (LC)	Dimer (LC+GP)	Difference [D-(M_1+M_2)]
Total Energy (a.u.)	-1100.06930	-6894.5935	-17.8507
Dipole moment (Debye)	3.08	2.50	-0.58
Ionization potential (eV)	8.17	4.86	-7.07
HOMO-LUMO gap (eV)	7.05	2.15	-5.06
Molecular Weight	365.55	2225.49	0.00
COSMO Area (Å)^2	477.47	1358.88	-348.54
COSMO Volume (Å)^3	502.06	2309.60	30.58

4-4' Disubstituted Biphenyls LC & GP

GP and the 4-4' disubstituted biphenyls LC [33] engage in a parallel plane stacking interaction. During the interaction seen in Fig. 7 and Table 7, the dimer's ionisation potential, dipole moment, HOMO-LUMO gap, COSMO volume, and COSMO area drop as the total energy increases. The 4-4' disubstituted biphenyls LC shows the π–π interaction, which causes the GP sheet to twist. The 4-4' disubstituted biphenyls do not transfer charges to graphene at a sufficient rate. At a distance of 3.21, the cyano group's nitrogen atom interacts with GP; at 3.26, the benzene ring adjacent to the cyano group interacts with GP; at 2.89, the second benzene ring interacts with GP; at 3.28, the oxygen atom interacts with GP; and at 2.53, the LC tail interacts with GP.

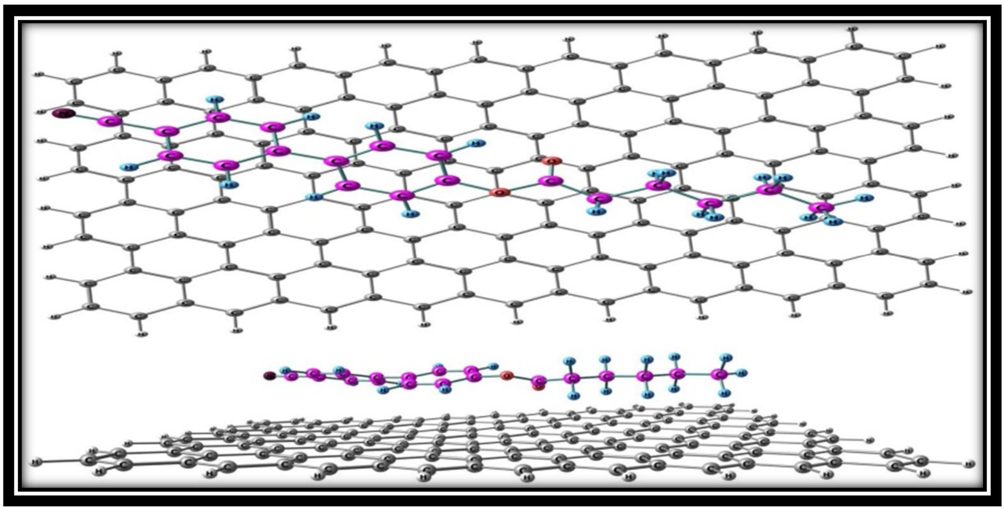

FIG. 7. Side and top showing the interaction of LC (4-4' disubstituted biphenyls) with GP in parallel (armchair) stacking. The 4-4' disubstituted biphenyls represent a homologous series of liquid crystals derived from the biphenyl moiety. One of the most widely studied members of this series is 5CB (4-cyano-4'-pentylbiphenyl), a nematic liquid crystal known for its phase transition behavior. Soluble, chemically oxidized graphene or graphene oxide sheets can form chiral liquid crystals with a twist-grain-boundary structure. Moreover, the tilt angle of nematic liquid crystals can be influenced by the number of graphene layers present. These biphenyl-based LC molecules can insert into monovacancy graphene, potentially providing a new pathway for tuning both liquid crystal alignment and graphene properties.

TABLE 7. Total energy, dipole moment, ionization potential, HOMO-LUMO gap, molecular weight, COSMO area, and COSMO volume of the dimer shown in Fig. 7.

4-4'Disubstituted Bi_ GP	Monomer (LC)	Dimer (LC+GP)	Difference [D-(M_1+M_2)]
Total Energy (a.u.)	-937.68956	-6732.2152	-17.8492
Dipole moment (Debye)	5.86	2.91	-3.67
Ionization potential (eV)	9.11	4.85	-8.02
HOMO-LUMO gap (eV)	8.47	2.14	-6.49
Molecular Weight	293.36	2153.30	0.00
COSMO Area (Å)^2	353.02	1307.96	-275.01
COSMO Volume (Å)^3	370.19	2147.09	-0.06

MBA5 or APAPA5 LC & GP

In parallel plane stacking, GP and MBA5 (p-anisylidene p-aminophenylacetate) LC [34] interact. As GP and LC interact, as demonstrated in Fig. 8 and Table 8, the ionisation potential, HOMO-LUMO gap, COSMO volume, dipole moment, and COSMO area drop, while the total energy increases. Because of the three oxygen and one nitrogen atoms in this LC, this dimer has the largest dipole moment. The MBA5 LC has a lower maximum charge transfer rate to GP. Due to the π–π interaction that MBA5 LC displays, the GP sheet becomes twisted. At a distance of 3.86, the oxygen atom with the CH3 group interacts with GP. At a distance of 2.88, the benzene from the side of a single oxygen atom interacts with GP. At a distance of 3.04, the hydrogen atom of the bridging group interacts with the carbon atom of GP. At a distance of 3.21, the other benzene in the LC interacts with GP. At a distance of 2.55 from GP, the oxygen atom interacts with it. The alkyl chain contacts GP at a 2.62 distance.

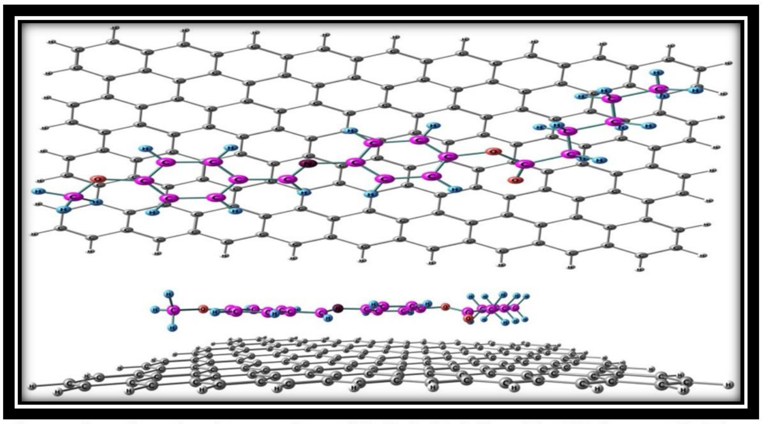

FIG. 8. Side and top views showing the interaction of LC (MBA5) with GP in parallel (armchair) stacking. This liquid crystal exhibits a characteristic texture observable under a microscope. Its optical properties depend on molecular orientation, which can be controlled by electric or magnetic fields. MBA5 has a low melting point and a high boiling point, along with high viscosity and low surface tension. It also exhibits high dielectric anisotropy, meaning its dielectric constant varies along different molecular axes.

TABLE 8. Total energy, dipole moment, ionization potential, HOMO-LUMO gap, molecular weight, COSMO area, and COSMO volume of the dimer shown in Fig. 8.

MBA5_ GP	Monomer (LC)	Dimer (LC+GP)	Difference [D-(M_1+M_2)]
Total Energy (a.u.)	-1053.10434	-6847.6278	-17.8514
Dipole moment (Debye)	2.13	1.11	-1.02
Ionization potential (eV)	8.30	4.85	-7.21
HOMO-LUMO gap (eV)	7.35	2.17	-5.34
Molecular Weight	325.40	2185.34	0.00
COSMO Area $(Å)^2$	390.57	1307.50	-313.02
COSMO Volume $(Å)^3$	406.83	2180.53	-3.26

MBC5 or PMBAB5 LC & GP

In parallel plane stacking, GP and the MBC5 {N-(p-methoxybenzylidene)-p-aminobenzonitrile} LC [35] interact. As illustrated in Fig. 9 and Table 9, when GP and LC interact with one another, the ionisation potential, dipole moment, HOMO-LUMO gap, and COSMO area drop, while the total energy and COSMO volume rise. The MBC5 LC displays the π–π interaction, which causes the GP sheet to be somewhat bent. Moreover, the MBC5 LC does not transfer charges to GP at an appropriate pace. At a distance of 3.11, the nitrogen atom of the cyano group interacts with the GP. At a distance of 3.51, the benzene ring from the cyano group interacts with GP. At a distance of 2.69, the hydrogen atom in the bridging group interacts with GP. At a distance of 2.88, the other benzene ring interacts with GP. At a distance of 3.85 from GP, the oxygen atom interacts with it. The alkyl chain contacts GP at a 2.61 distance.

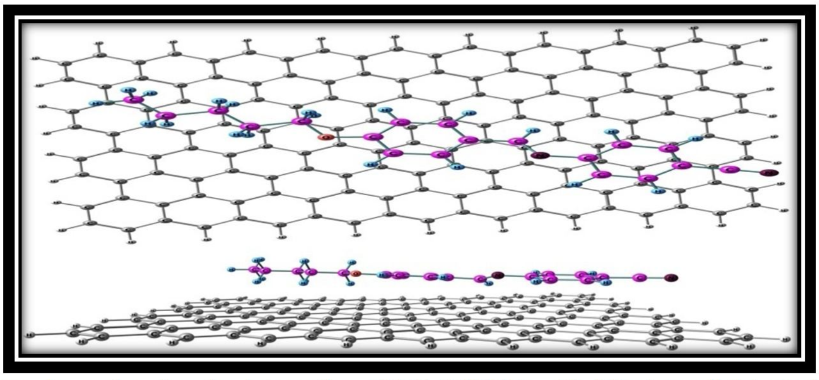

FIG. 9. Side and top views showing the interaction of LC (MBC5) with GP at parallel (armchair) stacking. The nitrogen atom of the cyano group interacts with GP at 3.11, the benzene ring adjacent to the cyano group at 3.51, the hydrogen atom in the bridging group at 2.69, and the second benzene ring at 2.88.

TABLE 9. Total energy, dipole moment, ionization potential, HOMO-LUMO gap, molecular weight, COSMO area, and COSMO volume of the dimer shown in Fig. 9.

MBC5_ GP	Monomer (LC)	Dimer (LC+GP)	Difference [D-(M_1+M_2)]
Total Energy (a.u.)	-917.79444	-6712.3187	-17.8506
Dipole moment (Debye)	7.53	3.54	-3.99
Ionization potential (eV)	8.67	4.87	-7.56
HOMO-LUMO gap (eV)	8.25	2.14	-6.27
Molecular Weight	292.37	2152.32	0.00
COSMO Area (Å)^2	364.04	1313.28	-280.71
COSMO Volume (Å)^3	373.92	2160.48	9.60

H5CBP LC & GP

GP and the H5CBP "eight 4,4′-disubstituted biphenyls" LC engage in parallel plane stacking interaction. As shown in Fig. 10 and Table 10, the interaction causes the ionization potential, HOMO-LUMO gap, and COSMO area to drop while the dipole moment, COSMO volume, and total energy rise. The H5CBP LC displays the π–π interaction; however, the tail of the LC does not express stacking, which causes the GP sheet to twist. The H5CBP LC transfers the most charge to the GP, making it ideal for applications in solar cells or electronic charge transfer. The H5CBP LC has a high concentration of free ions. At a distance of 3.19, the nitrogen atom of LC interacts with the carbon atom of GP. At a distance of 3.10, the benzene ring from the cyano group interacts with GP. At a distance of 2.98, the other benzene ring interacts with GP. At a distance of 3.61, the oxygen atom of the LC interacts with GP. At a distance of 2.49, the tail of the LC contacts GP. The oxygen atom interacts with the carbon atom at the tail's end at a distance of 3.36.

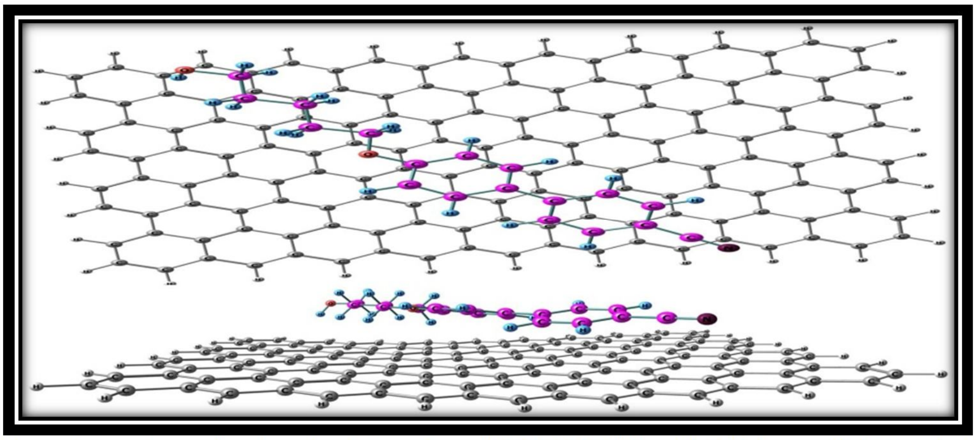

FIG. 10. Side and top views showing the interaction of LC (H5CBP) with GP in parallel (armchair) stacking. H5CBP LC transfers the most to GP, making it ideal for solar cell and electronic charge-transfer applications. The H5CBP LC has a high concentration of free ions. At a distance of 3.19, the nitrogen atom of LC interacts with the carbon atom of GP. At a distance of 3.10, the benzene ring from the cyano group interacts with GP.

TABLE 10. Total energy, dipole moment, ionization potential, HOMO-LUMO gap, molecular weight, COSMO area, and COSMO volume of the dimer shown in Fig. 10.

H5CBP_ GP	Monomer (LC)	Dimer (LC+GP)	Difference [D-(M_1+M_2)]
Total Energy (a.u.)	-899.67823	-6694.2072	-17.8459
Dipole moment (Debye)	6.52	7.55	1.03
Ionization potential (eV)	8.64	4.89	-7.51
HOMO-LUMO gap (eV)	7.80	2.14	-5.82
Molecular Weight	281.35	2141.29	0.00
COSMO Area (Å)^2	342.59	1310.54	-262.00
COSMO Volume (Å)^3	357.96	2136.21	1.29

5OCB LC & GP

GP interacts with the 5OCB (pentyloxycyanobipheny) LC [36–39] in parallel plane stacking. As shown in Fig. 11 and Table 11, the interaction causes decreases in ionisation potential, HOMO-LUMO gap, dipole moment, and COSMO area, while the COSMO volume and total energy rise. In contrast to H5CBP LC, which has two oxygen and one nitrogen atom, 5OCB LC has just one oxygen and one nitrogen atom, hence it does not have a good charge-transfer rate. Oxygen is more electronegative than nitrogen, which affects the interaction. Due to the π–π interaction displayed by 5OCB LC, the GP sheet becomes slightly bent. Key interactions include: the nitrogen atom of the cyano group with GP at a distance of 3.21; the benzene ring adjacent to the cyano group at a distance of 3.30; the second benzene ring on the oxygen side at a distance of 2.85; the LC tail at a distance of 2.52; and the oxygen atom at a distance of 3.88.

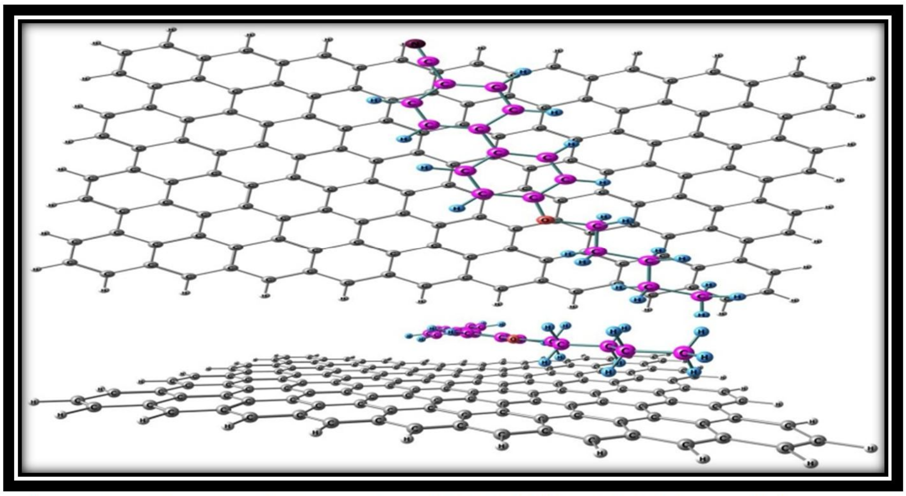

FIG. 11. Side and top views showing the interaction of LC (5OCB) with GP in parallel (armchair) stacking. Due to the - interaction exhibited by 5OCB LC, the GP sheet is slightly bent. At a distance of 3.21, the cyano group's nitrogen atom interacts with GP. At a distance of 3.30, the benzene ring from the cyano group interacts with GP. At a distance of 2.85, the second benzene ring from the side of the oxygen atom interacts with GP. At a distance of 2.52, the tail of the LC contacts with GP. At a distance of 3.88 from GP, the oxygen atom interacts with it.

TABLE 11. Total energy, dipole moment, ionization potential, HOMO-LUMO gap, molecular weight, COSMO area, and COSMO volume of the dimer shown in Fig. 11.

5OCB_ GP	Monomer (LC)	Dimer (LC+GP)	Difference [D-(M_1+M_2)]
Total Energy (a.u.)	-824.63521	-6619.1634	-17.8467
Dipole moment (Debye)	6.24	5.28	-0.96
Ionization potential (eV)	8.63	4.94	-7.45
HOMO-LUMO gap (eV)	7.78	2.30	-5.64
Molecular Weight	265.35	2125.29	0.00
COSMO Area (Å)^2	331.53	1314.41	-247.07
COSMO Volume (Å)^3	345.17	2124.85	2.72

The negative interaction energy indicates that all the LCs are adsorbed on GP. Table 12 compares the interaction energies of all dimers in decreasing order. Among them, H5CBP LC is perfectly adsorbed on GP and has the lowest (least negative) interaction energy, meaning it transfers the maximum charge to GP, making it ideal for charge-transfer applications.

6O.5 > CCH5 > MBA5 > 7O > MBC5 > P.P’-disubstituted diphenylacetylenes > 5CB > 4-4’disubstituted biphenyls > PCH5 > 5OCB > H5CBP

TABLE 12. Comparison of the interaction energy between all dimers.

Liquid crystal molecule	Conformation (LC+GP)	Interaction Energy (a.u.)
CCH5	Parallel (armchair) Stacking	-17.8593
P.P’-disubstituted diphenylacetylenes	Parallel (armchair) stacking	-17.8496
5CB	Parallel (armchair) stacking	-17.8492
PCH5	Parallel (armchair) stacking	-17.8479
6O.5	Letter V shape	-17.8596
7O.5	Parallel (armchair) stacking	-17.8507
4-4’ Disubstituted Biphenyls	Parallel (armchair) stacking	-17.8492
MBA5	Parallel (armchair) stacking	-17.8514
MBC5	Parallel (armchair) stacking	-17.8506
H5CBP	Parallel (armchair) stacking	-17.8459
5OCB	Parallel (armchair) stacking	-17.8467

It was found that the LC-BLYP approach provides more stable energies for the LC–GP conformations, as shown in Table 13, than any of the dimers optimized using the other seven DFT methods. The greater stability of a dimer (LC+GP) is expressed by the least negative energy. Given that it displays the least negative energy when compared to the other DFT techniques listed in Table 13 and has acceptable - interaction goals, the LC-BLYP approach is appropriate for the LC and GP interaction energy mechanism. Liquid crystals have many applications, including in liquid crystal displays (LCDs), liquid crystal thermometers, and mood rings. Liquid crystals can be used to create liquid crystal pixels, which are used in displays. Liquid crystals have been used in the development of new materials for energy investigations. Ongoing research focuses on the design, synthesis, characterization, and application of supramolecular and self-organizing liquid crystal systems and materials.

TABLE 13. Comparative interaction energies of dimers calculated using seven DFT methods.

Dimers\DFT Methods	M062X [40] (a.u.)	wB97XD [41] (a.u.)	Cam-B3LYP [42] (a.u.)	PBE1PBE [43] (a.u.)	M06 [44] (a.u.)	B3LYP [45] (a.u.)	LC-BLYP (a.u.) [46]
P-P'-D-D	-6660.4625	-6660.5669	-6685.9076	-6655.2269	-6658.0045	-6662.6706	-6642.2641
4-4'-D-B	-6750.5167	-6750.6121	-6748.9709	-6745.2197	-6748.0590	-6752.7458	-6732.2152
5CB	-6562.0951	-6562.1851	-6560.5496	-6556.9320	-6559.6510	-6564.2628	-6544.1145
7O	-6913.4431	-6913.6208	-6911.8510	-6908.0167	-6910.9267	-6915.7616	-6894.5935
CCH	-6569.2785	-6569.4369	-6567.7499	-6564.1317	-6566.8603	-6571.4774	-6551.2975
6O.2	-6874.1371	-6874.3065	-6872.5541	-6868.7442	-6870.3261	-6876.4409	-6855.3974
H5CBP	-6712.4075	-6712.4988	-6710.8673	-6707.1394	-6709.9619	-6714.6211	-6694.2072
MBA	-6866.1510	-6866.2695	-6864.6010	-6860.7716	-6863.6812	-6868.4251	-6847.6278
MBC	-6730.6248	-6730.7233	-6729.0740	-6725.3404	-6728.1663	-6732.8562	-6712.3187
5OCB	-6637.2445	-6637.3362	-6635.7048	-6632.0336	-6634.8025	-6639.4421	-6619.1634
PCH	-6565.6852	-6565.8099	-6564.1500	-6560.5345	-6563.2605	-6567.8732	-6547.7126

Conclusions

In this study, it was observed that the ionization potential and COSMO area decrease for all the dimers. Among the liquid crystals studied, only 6O.5 LC interacts with graphene in a V-shaped conformation, while all other LCs adopt a parallel stacking arrangement. The variations in COSMO area and COSMO volume indicate that the LCs adjust their structure in response to adsorption on graphene.

H5CBP LC transfers the most charge to graphene due to its high concentration of free ions, making it ideal for charge transfer applications. In contrast, 6O.5 LC shows maximum positive energy in an armchair conformation, resulting in less favorable adsorption on graphene. Compared to 5OCB LC, H5CBP LC interacts more effectively with graphene because of the presence of an additional oxygen atom.

When comparing CCH5 LC, which contains two cyclohexane rings, with PCH5 LC, which has one benzene ring and one cyclohexane ring, the PCH5 LC shows stronger adsorption due to the π–π interactions of the benzene ring. In all dimers, the graphene sheet twists by approximately 1.0 Å because the LC benzene rings exhibit π-π interaction at a distance of ~3.5, whereas the cyclohexane rings and terminal groups interact at a distance of ~2.5 Å without π-stacking. Finally, nitrogen atom–based LCs interact actively with graphene but do not significantly increase the dipole moment, whereas oxygen atom–based LCs enhance the dipole of the dimer through their interaction with GP. Yet, GP interacts more actively with oxygen- and nitrogen-based LCs. While both oxygen- and nitrogen-based LCs contain the necessary dipole moments, the oxygen atom-based LC dimers exhibit greater dipole moments compared to those with nitrogen atom-based LCs. Research is ongoing to design, synthesize, characterize, and apply supramolecular and self-organizing liquid crystal systems and materials.

Acknowledgments

We are very grateful to the Centre for Development of Advanced Computing (CDAC) for providing computational support for this work. We are also very thankful to Dr. Anakuthil Anoop Ayyappan (IIT KGP) for his assistance with computations. We are very thankful to Dr. Pawan Singh and Dr. Khem B. Thapa for the scientific discussion.

Funding Source: No funding was received for this work.

Conflict of Interest: The authors declare no conflicts of interest.

Data Availability Statement: Data will be made available upon reasonable request.

References

[1] Novoselov, K.S., Geim, A.K., Morozov, S.V., Jiang, D.E., Zhang, Y., Dubonos, S.V., and Firsov, A.A., Sci., 306 (2004) 666.

[2] Novoselov, K.S., Geim, A.K., Morozov, S.V., Jiang, D., Katsnelson, M.I., Grigorieva, I.V., and Firsov, A.A., Nat., 438 (2005) 197.

[3] Geim, A.K., Science, 324 (2009) 1530.

[4] Geim, A.K. and Novoselov, K.S., Nat. Mater., 6 (2007) 183.

[5] Stoller, M.D., Park, S., Zhu, Y., An, J., and Ruoff, R. S., Nano Lett., 8 (2008) 3498.

[6] Novoselov, K.S., Falko, V.I., , Colombo, L., Gellert, P.R., Schwab, M.G., and Kim, K., Nat., 490 (2012) 192.

[7] Xia, F., Mueller, T., Lin, Y.-M., Valdes-Garcia, A., and Avouris, P., Nat. Nano., (4) (2009) 839.

[8] Geim, A.K. and Novoselov, K.S., Nat. Mat., 6 (2007) 183.

[9] Mertens, R., “The Graphene Handbook”, (Lulu.com, UK, 2018).

[10] Basu, R. and Shalov, S.A., Phys. Rev. E, 96 (2017) 012702.

[11] Shehzad, M.A., Tien, D.H., Iqbal, M.W., Eom, J., Park, J.H., Hwang, C., and Seo, Y., Sci. Rep., 5 (2015) 13331.

[12] Yu, J.S., Yun, J.E., and Kim, J.H., Liq. Cryst., 40 (2013) 216.

[13] Blake, P., Brimicombe, P.D., Nair, R.R., Booth, T.J., Jiang, D., Schedin, F., Ponomarenko, L.A., Morozov, S.V., Gleeson, H.F., Hill, E.W., Geim, A.K., and Novoselov, K.S., Nano Lett., 8 (2008) 1704.

[14] Shen, Y. and Dierking, I., Appl. Sci., 9 (2019) 2512.

[15] Mrukiewicz, M., Kowiorski, K., Perkowski, P., Mazur, R., and Djas, M., Beilstein J. Nanotechnol., 10 (2019) 71.

[16] Fischer, S.A., Kołacz, J., Spillmann, C.M., and Gunlycke, D., Phy. Rev. E, 98 (2018) 052702.

[17] Kumar, A., Ganguly, P., and Biradar, A.M., Liq. Cryst., 45 (11) (2018) 1620.

[18] Frisch, M.J., Trucks, G.W., and Schlegel, H.B., “Gaussian 09”, Revision A.02, (Gaussian, Inc., Wallingford CT, 2010).

[19] Iikura, H., Tsuneda, T., Yanai, T., and Hirao, K., J. Chem. Phys., 115 (2001) 3540.

[20] Lee, C., Yang, W., and Parr, R.G., Phys. Rev. B, 37 (1988) 785.

[21] Hay, P.J. and Wadt, W.R., J. Chem. Phys., 82 (1985) 299.

[22] Gresh, N., Claverie, P., and Pullman, A., Int. J. Quantum Chem., 16 (S13) (1979) 243.

[23] Dunmur, D.A. and Tomes, A.E., Mol. Cryst. Liq. Cryst., 97 (1983) 241.

[24] Dunmur, D.A. and Toriyama, K., Liq. Cryst., 1 (1986) 169.

[25] Malthete, J., Leclercq, M., Dvolaitzky, M., Gabard, J., Billard, J., Pontikis, V., and Jacques, J., Mol. Cryst. Liq. Cryst., 23 (1973) 233.

[26] Breddels, P.A. and Mulkens, J.C.H., Mol. Cryst. Liq. Cryst., 147 (1987) 107.

[27] Coles, H.J. and Sefton, M.S., Mol. Cryst. Liq. Cryst., 3 (1986) 63.

[28] Coles, H.J. and Sefton, M.S., Mol. Cryst. Liq. Cryst., 4 (1987) 123.

[29] Siedler, L.T.S., Hyde, A.J., Pethrick, R.A., and Leslie, F.M., Mol. Cryst. Liq. Cryst., 90 (1983) 255.

[30] Bock, F.-J., Kneppeand, H., and Schneider, F., Liq. Cryst., 1 (1986) 239.

[31] Kneppe, H., Schneider, F., and Sharma, N.K., J. Chem. Phys., 77 (1982) 3203.

[32] Gray, G.W., Harrison, K.I., and Nash, J.A., Elec. Lett., 9 (6) (1973) 130.

[33] Pohl, L., Eidenschink, R., Krause, G., and Erdmann, D., Phys. Lett. A, 60 (1977) 421.

[34] Sen, S., Kali, K., Roy, S.K., and Roy, S.B., Mol. Cryst. Liq. Cryst., 126 (1985) 269.

[35] Finkenzeller, U., Geelhaar, T., Weber, G., and Pohl, L., Liq. Cryst., 5 (1989) 313.

[36] Abdoh, M.M.M., Shivaprakash, S.N.C., and Prasad, J.S., J. Chem. Phys., 77 (1982) 2570.

[37] Pestev, S. and Vill, V., “Physical Properties of Liquid Crystals”, In: “Landolt-Börnstein”, 5A, (Group VIII Advanced Materials and Technologies, Springer, 2003).

[38] Rao, P.B., Potukuchi, D.M., Murthy, J.S.R., Rao, N.V.S., and Pisipati, V.G.K.M., Cryst. Res. Technol., 27 (1992) 839.

[39] Hardouin, F. Gasparoux, H., and Delhaes, P., J. Phys. Colloquies, 36 (1975) C1.

[40] Rao, N.V.S., Pisipati, V.G.K.M., Sankar, Y.G., Potukuchi, D.M., Phase Transit., 7 (1986) 49.

[41] Dubois, J.C. and Zann, A., J. Phys. Symp., 37 (1976) C3.

[42] Leenhouts, F., de Jeu, W.H., and Dekker, A.J., J. Phys., 40 (1979) 989.

[43] Pisipati, V.G.K.M. and Rao, N.V.S.Z., Naturforsch., 39a (1984) 696.

[44] Zugenmaier, P. and Heiske, A., Liq. Cryst., 15 (6) (1993) 835.

[45] Basu, R., Kinnamon, D., and Garvey, A., Liq. Cryst., 43 (13-15) (2016) 2375.

[46] Ali, I., Sharma, S., and Bezbaruah, B., Computat. Chem., 6 (2018) 71.

Volume 18, Number 3, 2025. pp. 265-273

Jordan Journal of Physics

ARTICLE

Seasonal Variation of Heavy Metals, Uranium, and Thorium Concentration in Jordanian Dams Water

B. M. S. Amro[a], **A. Aldrabee**[a], **O. Allabadi**[a], **E. Balbeisi**[b], **O. Qudah**[a] and **K. AbuSaleem**[c]

[a] *Jordan Atomic Energy Commission (JAEC), Shafa Badran, Amman 11934, Jordan.*
[b] *Water Authority of Jordan (WAJ), Amman 11183, Jordan.*
[c] *Department of Physics, The University of Jordan, Amman 11942, Jordan.*

Doi: **https://doi.org/10.47011/18.3.2**

Received on: 31/10/2023; Accepted on: 26/06/2024

Abstract: This work investigated the seasonal variation of heavy metal concentrations in the waters of Moujib, Wala, King Talal, Kufranjeh, and Tannour dams in Jordan. Samples were collected from each dam's entrance, dam lake (reservoir), and exit. Samples were collected at the end of the rainfall season, when dams were almost full, and at the end of summer, when the water was at its lowest level. The study investigated the content of As, Cd, Cr, Hg, Mo, Ni, Pb, U, and Th elements. The results revealed that the concentrations of As, Cd, Cr, Hg, Mo, Ni, and Pb were less than the lowest detectable limit during both seasons. The Uranium average concentrations for the wet and dry seasons were 1541 and 1564 ppt, respectively, while the average concentrations of thorium for the wet and dry seasons were 7 and 119 ppt, respectively. These results are below the allowed values according to the Jordanian standard for drinking water and international guidelines. They are comparable with values reported in the literature. This work indicates that Jordanian dam water is free from heavy metals, and the content of U and Th is within accepted levels.

Keywords: Heavy metals, Uranium, Thorium, Dam water, Seasonal variation, Total dissolved solids.

PACS: Dams: 92.40Xx, Environmental Impacts-Surface water quality: *92.40.qc, Environmental Impacts -surface water: *92.40.92.40Qk, Water Quality-surface water: 92.40Qk*92.40qc

Introduction

Dams are a strategic national water resource, as they store water for domestic, industrial, agricultural, and other uses. Maintaining the quality of these resources and preventing pollution is therefore essential. Water stream sources can catch unwanted elements, such as heavy metals, and transfer them to the dam. Geochemical structure, industrial waste, mining activity, and untreated wastewater are potential sources of heavy metal pollution [1-5]. The concentration of heavy metals tends to keep building up in dam water, sediment, and aquatic organisms [6]. The concentration of unwanted elements in the dam water increases in summer due to evaporation [7], which affects water quality at the end of the season.

Consumption of contaminated dam water, or crops irrigated with such water, can transfer harmful elements into the human body. Governments define the maximum concentration limits for harmful elements found in water and

Corresponding Author: Bilal Amro **Email**: belal.amro@jaec.gov.jo

continuously monitor them. Table 1 summarizes the limits of some elements in drinking water as set by the Jordan Standards and Metrology Organization (JSMO) [8], and by the World Health Organization (WHO) [9]. It could be noticed that limit values set by JSMO are generally comparable to those of WHO. Nevertheless, the WHO didn't set limits for some elements as they were not considered a health hazard, as described in Table 1.

Heavy metals are a particularly harmful group of elements that may originate naturally or from industrial activities [10]. For instance, aluminum salts are widely used in water treatment, which could lead to increased concentrations of aluminum in drinking water [9]. Having a low concentration of natural Al in the dam water is essential to get low levels of Al in treated water. Arsenic is found widely in the Earth's crust, and it can enter surface waters through weathering of exposed rocks. It could also come from coolants used in industry. Lead and cadmium are widely used in car batteries, fertilizers, and pesticides; they could reach the dam through running water [9]. Therefore, monitoring the quality of water in dams is essential to control the probable contamination.

TABLE 1. Upper limit concentrations (mg/L) of selected elements in drinking water as set by JSMO and WHO.

Element	Upper Limit JSMO[5] (mg/L)	Upper Limit WHO [6] (mg/L)	Notes
As	0.01	0.01	
Cd	0.003	0.003	
Cr	0.05	0.05	
Hg	0.006	0.006	
Mo	0.09	NA	Concentrations of Mo, found in drinking water, are generally below health concerns (WHO).
Ni	0.07	0.07	
Pb	0.01	0.01	
U	< 0.5 Bq/l	0.03**	Total Alpha emitters < 0.5 Bq/l (JSMO)
Th	0.5 Bq/l	<1 Bq/l	Total Alpha emitters < 0.5 Bq/l (JSMO) ^{232}Th guidance level <1 Bq/l (WHO)
TDS*	1000	1000	

* TDS: Total Dissolved Solids

** Only hazardous elements were considered

Jordan is one of the most water-scarce regions in the world. Management of water resources is important to meet the increasing demand for water in the country [11, 12]. Protecting water sources and reservoirs against contamination is essential to sustain water resources. Salamah *et al.* [4] identified various threats to Jordan's dams, with industrial wastewater carrying high concentrations of heavy metals being one of the most significant. Drinking water in Jordan is affected by seasonal variations [13]. Therefore, this work aims to highlight the impact of seasonal variation on heavy metal concentrations in dam water across Jordan. Dams store rainwater during the winter season, which is subsequently used for drinking and irrigation during the summer. For this study, major dams were selected. The location, capacity, water resources, and purpose of use for these dams are listed in Table 2 [14].

King Talal Dam catchment lies within the Zarqa River basin, with the Zarqa River and Wadi Rmemeen feeding the dam with water. The Zarqa basin has an arid climate in the southeastern and eastern regions and rainy, humid conditions in the west. Significant industrial activities are located near the Zarqa River, and their wastewater is frequently discharged into the river. In addition, wastewater from Khirbet As-Samra is discharged into the dam through the Zarqa River, and from the Baqa'a treatment plant through Wadi Rmemeen [15].

TABLE 2. Some properties of major dams in Jordan considered in this work (capacity in MCM: Million Cubic Meters).

Dam	Governorate	Total Capacity (MCM)	River/ Wadi	Purpose
Mujib	Al-Karak	31.2	Wadi Mujib	Irrigation, Municipal, and Industrial
Wala	Madaba	9.3[*]	Wadi Wala	Irrigation, Municipal, and Industrial
King Talal	Jerash	86	Zarqa river	Irrigation and Electricity
Kufranjeh	Ajloun	8	Wadi Kufranjeh	Irrigation and Municipal
Tannour	Tafilah	16.8	Wadi Al-Hassa	Irrigation and Industrial

[*] Wala Dam is getting an upgrade to increase its capacity up to ~29 MCM.

Mujib Dam catchment has a high slope with Wadi Saeda and Wadi Nukhaila feeding it with water. The dam suffers from frequent flood events, suggesting a significant sediment accumulation [16]. The catchment area includes Wala Dam as well [17]. The catchment has moderate agricultural activity and almost no industry, suggesting minimum or low pollution [18].

Kufranjeh Dam is newly established in Ajloun to solve the water scarcity in the city. The catchment area has a Mediterranean-type climate. Its topography is hilly with slopes toward the west, and the main water resources are from precipitation and spring waters. The dam receives effluents from the Kufranja wastewater treatment plant as well [19]. Al-Tannur Dam is located in Wadi Hasa. Wadi Hasa has a Mediterranean-type climate, characterized by hot, dry summers and cold, wet winters. Most of the catchment area is semi-arid, and the temperature exhibits large seasonal and diurnal variations [20].

Materials and Methodology

This section describes the sample collection, preparation, and measurement.

Sample Collection

The dams for this work were selected according to two criteria: first, they have a large capacity, and second, they are geographically distributed around the country to represent all regions in Jordan. A map showing the locations of the studied dams, marked in red, is provided in Fig. 1.

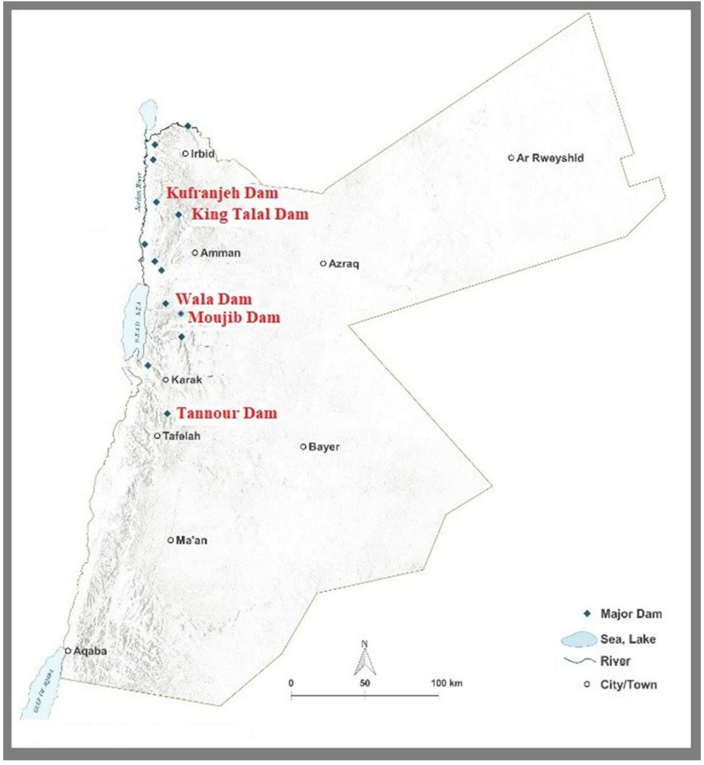

FIG. 1. Map of the dams investigated in this study.

For each dam, three sampling locations were considered: the dam lake, the exit, and close to the entrance of the dam. Samples were collected twice a year during the wet and dry seasons. The entrance samples demonstrate the quality of the water feeding into the dam. The dam lake samples represent the stored content of the dam and were collected at a depth of 1 m below the surface. The sample collection tool is shown in Fig. 2. This tool is equipped with a depth indicator to ensure accurate collection at 1 m below the surface.

FIG. 2. The sample collection tool used to collect samples from the dam lake.

Exit samples were collected directly from the exit pipe in the case of King Talal Dam and Mujib Dam. For all other dams, exit samples were taken from running water right after the exit, collected just below the surface. The geographic coordinates of all sampling points can be found in Table 3. The bottle used for sample collection was first rinsed with some water from the sample location, and then it was filled with the sample. TDS was measured in situ from the bottle directly after sample collection.

TABLE 3. Coordinates of samples collected from dams in this work. Points that were not available are marked as NA.

Dam	Entrance Coordinates		Dam-lake Coordinates		Exit Coordinates	
	N	E	N	E	N	E
Mujib	31°26'36"	35°49'42"	31°26'34"	35°48'58"	31°26'44"	35°49'07"
Wala	NA	NA	31°34'08"	35°48'15"	NA	NA
King Talal	32°11'33"	35°50'16"	32°11'18"	35°48'13"	32°11'25"	35°47'53"
Kufranjeh	32°16'06"	35°38'52"	32°16'07"	35°38'37"	32°16'02"	35°38'26"
Tannour	30°58'05"	35°43'29"	30°58'19"	35°42'47"	30°58'30"	35°42'43"

The first round of sampling took place in 2019, with two collections from the same locations to investigate seasonal variations in heavy metals, U, and Th concentrations due to evaporation during the summer. The last rainfall occurred at the beginning of May 2019. The first set of samples was collected during June and July 2019, representing the wet season, and the second set was collected in November 2019, representing the dry season. Fig. 3 demonstrates the sample collection point from the dam-lake of Mujib Dam for both the wet and dry seasons. During the wet season, the dam was full and the plant in the left corner appeared green and hydrated, whereas in the dry season, the water level had decreased significantly, and the plant was dry.

Another sampling round was conducted in 2021, which was drier than the previous year, with rainfall below the average seasonal precipitation. Many dams were completely empty towards the end of 2021. Samples were collected in October 2021 from the bodies of Mujib, Kufranjeh, and King Talal Dams, as these were the only dams that still contained water. The scarcity of water during this period suggests a corresponding increase in the concentration of the elements of interest.

FIG. 3. These pictures were taken from the same sample location at Mujib dam-lake, showing the difference between the wet and dry seasons. These pictures were captured during sample collection in 2019. The collection point is marked by an X.

Sample Preparation and Measurement

Once a sample was collected, the pH, temperature, and TDS were measured in the field. Samples were filtered to remove solid particles before the measurement was performed. Then HNO_3 acid was added until the pH of the water was less than two. The samples were analyzed at JAEC using an Agilent 7500 Inductively Coupled Plasma Mass Spectrometer ICP-MS with an in-house method accredited to ISO 17025. 10.0 ml of each sample was placed in Teflon vials, and 3.0 ml of HNO_3 and 2.0 ml of H_2O_2 were added. Samples were transferred to the advanced microwave digestion station (Milestone, model Ethos). During digestion, samples were heated in the microwave for 40 minutes to reach 230ºC, which was maintained for 30 minutes, and then the sample was cooled down to room temperature. After this process, samples were transferred to a 50.0 ml polypropylene centrifuge tube and topped up with distilled water until the total volume was 50.0 ml, and then centrifuged at 2000 - 3000 rpm for 10 minutes. The ICP-MS device was calibrated using MISA-06-1, MISA-05-1, U, Th, and As standards. An internal standard of Rh and Bi was used for quality control, with the accepted recovery of 85-115%. The total measurement uncertainty was estimated to be 10% for all the measurements. For comparison purposes, some of the samples were sent to the Water Authority of Jordan (WAJ).

At WAJ, different analytical techniques were applied according to the element: arsenic (As) was measured using atomic absorption hydride generation with an electrically heated cell, while mercury (Hg) was measured using an atomic absorption spectrometer (GTA model AA800, Perkin Elmer) calibrated with As and Hg standard solutions. Samples for this method are measured as is with no extra additives. Uranium (U) and thorium (Th) were analyzed using an ICP-MS (Nexion 300X, Perkin Elmer) equipped with a preconcentration column, which allows achieving detection limits of 0.58 ppt for U and 0.85 ppt for Th. Calibration was performed with U and Th standards, using Re as an internal standard. All other elemental measurements at

WAJ were completed using ICP-OES. Both JAEC and WAJ laboratories have ISO 17025 accreditation and participate in national and international intercomparison tests. The lower limits of detection for both laboratories are shown in Table 4.

Results and Discussion

The results of the TDS measurements for the 2019 wet and dry seasons are shown in Fig. 4. The TDS of the samples during the dry season increased due to evaporation. The TDS for samples collected in the 2021 season rose significantly as evaporation occurred over an extended period. The TDS of the samples collected from King Talal, Kufranjeh, and Mujib dams in the 2021 dry season were 1280, 601, and 2143 mg/L, respectively. Comparing these values with those from 2019, a clear increase in all three dams can be noticed, as shown in Fig. 4. The smallest increase was observed at King Talal Dam, which is continuously fed by the Zarqa River throughout the year. Kufranjeh Dam showed an increase in TDS. Mujib Dam experienced a substantial increase in TDS, likely due to significantly lower precipitation in southern Jordan during 2021, resulting in a very low water level at the time of sampling.

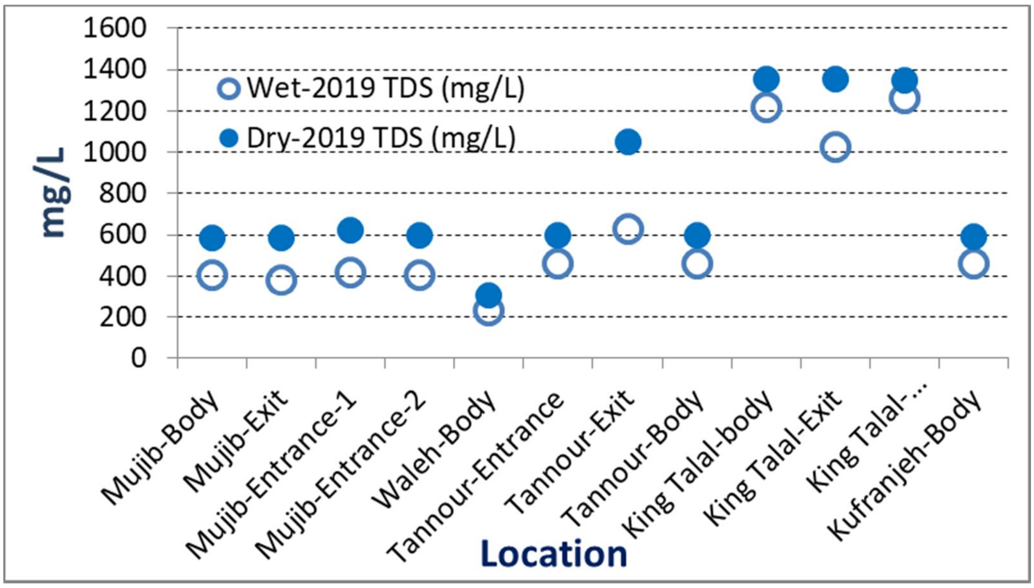

FIG. 4. Comparison between the wet and dry seasons TDS content at each point of the studied dams.

The lower limits of detection for all elements measured at both JAEC and WAJ laboratories are presented in Table 4. For all samples collected, across all points and seasons, including the extremely dry 2021 season, the concentrations of the investigated heavy metals were below these detection limits. Notably, the lower detection limits at both laboratories are equal to or lower than the maximum allowable levels set by JSMO and WHO, as listed in Table 1.

These results indicate that the water in Jordanian dams remains within national and international quality standards, even under dry-season conditions. Therefore, the dam water is safe for various uses, including domestic consumption, irrigation, and industrial applications.

TABLE 4. Lowest limit of detection (mg/L) for the elements investigated in this work at both JAEC and WAJ.

Element	JAEC (mg/L)	WAJ (mg/L)
As	< 0.005	< 0.005
Cd	< 0.005	< 0.003
Cr	< 0.005	< 0.005
Hg	< 0.001	< 0.00015
Mo	< 0.005	< 0.010
Ni	< 0.001	< 0.010
Pb	< 0.001	< 0.005

These results are consistent with the results found in the literature. For example, the Mujib dam water has previously been reported to contain Cd, Cr, Pb, and Ni at concentrations of <0.02, <0.02, <0.01, and <0.02 µg/l, respectively [18]. Another study highlighted the concentration of heavy metals in the Kufranjeh Dam and reported heavy metal concentrations as follows: Cd <0.0025 mg/L, Mo <0.01 mg/L, and Hg <0.001 mg/L [19]. A Small concentration of heavy metals in King Talal Dam were reported in the literature. The reported values were: 0.00557 mg/l of Cd, 0.02701 mg/l of Cr, 0.018205 mg/l of Pb, and 0.040955 mg/l of Ni. These findings align with the results of this study. It is worth noting that the 2019 sampling period coincided with multiple floods in Jordan, including at least four controlled flooding events at King Talal Dam [21]. This indicates that the large amount of freshwater that fed the dam in 2019 diluted the concentrations of these heavy metals, so they were not detected in this work.

Table 5 summarizes the concentrations of heavy metals in dam water from this study, other studies in Jordan, and selected international cases. The results of this work showed that all the element concentrations were below the detection limits. The results in Table 5 showed the absence of Cd and Ni in the water of Al-Wehdah Dam, which is consistent with the results of this work. The work described in [7] shows the presence of traces of Cr and Pb, but this is consistent with the results of this work, as this dam was out of the scope of this work. The next column in Table 5 shows the concentration of heavy metals in the lake of Atatürk Dam in Turkey. These results are consistent with the results of this work, as the heavy metals were below detection limits except for some traces of Ni [22]. For Nairobi Dam in Kenya, the average heavy metal concentrations during the wet and dry seasons showed higher values than those observed in this work, but still within the permissible values of the WHO [1, 9]. Generally, the wet season concentrations are lower than dry season values, mirroring the TDS trend observed in this study [1]. Mercury was reported in Sarawak, Malaysia, in the Dam water with a concentration of 0.000039 mg/l [2].

TABLE 5. Concentration of heavy elements in dam water reported around the world, locally, and in this study.

Element	Concentration (mg/L)				
	This Study	Al-Taani, 2013 [7] (Wehda Dam)	Karadede and Unlu, 2000 (Turkey) [22]	Ndeda and Manohar, 2014 (Kenya) [1]	
				Wet	Dry
As	<LLD	-	-	-	-
Cd	<LLD	<LLD	<LLD	3.76 ± 0.15	5.12 ± 0.18
Cr	<LLD	0.09	-	-	-
Hg	<LLD	-	<LLD	-	-
Mo	<LLD	-	<LLD	-	-
Ni	<LLD	<LLD	0.0132	1.20 ± 0.13	2.11 ± 0.12
Pb	<LLD	0.012	<LLD	11.67 ± 0.21	16.78 ± 0.21

Table 6 presents the uranium concentrations measured in the dams during the wet and dry seasons of 2019. For the wet season, uranium levels ranged from 776 to 2216 ppt, with an average of 1541 ppt, while in the dry season, concentrations ranged from 605 to 2490 ppt, averaging 1564 ppt. Both averages are well below the WHO guideline limit of 30,000 ppt. These results are consistent with literature values; for instance, the average ^{238}U concentration reported for five dams in Morocco was 928 ppt [23], and typical surface water concentrations generally remain below 4000 ppt [24].

Uranium concentrations in Jordanian dam water are particularly important due to the presence of phosphate deposits in southern Jordan. Jiries *et al.* [25] reported high uranium levels in effluent water from phosphate ore processing. From Table 6, it is evident that dams in northern Jordan, such as King Talal and Kufranjeh, have approximately half the uranium concentrations of dams in southern Jordan, including Tannour and Mujib. Tannour Dam exhibits the highest uranium levels, likely due to inflow from the Al-Hisa and Al-Abyad phosphate mining effluents. Establishing these baseline values is essential for future monitoring and management of uranium in Jordanian water resources.

TABLE 6. Uranium concentrations (ppt) in water samples.

Dam	U(ppt) – Wet	U(ppt) – Dry
King Talal	1461	1446
Kufranjeh	1197	1535
Wala	776	605
Mujib	2056	1744
Tannour	2216	2490
Average	1541	1564

The results of thorium concentrations for the wet and dry seasons of 2019 are presented in Table 7. During the wet season, the concentration ranged between 3 and 17 ppt, with an average of 7 ppt. In the dry season, concentrations ranged between 49 and 190 ppt, with an average of 119. The increase in concentration during the dry season is consistent with the increase in TDS values between the two seasons. These average values of thorium are much less than the 1206 ppt value reported in dam water in Morocco [23].

TABLE 7. Thorium concentrations (ppt) in water samples.

Dam	Th (ppt) – Wet	Th (ppt) – Dry
King Talal	3	190
Kufranjeh	8	49
Wala	17	105
Mujib	2	117
Tannour	5	133
Average	7	119

Conclusion

Water samples from large dams in Jordan have been collected during wet and dry seasons. The selected dams cover most regions in the northern and southern parts of Jordan, including Moujib, Wala, King Talal, Kufranjeh, and Tannour. The TDS of the samples was measured on-site, and the results showed that the TDS increased significantly during the dry season due to evaporation. Concentrations of As, Cd, Cr, Hg, Mo, Ni, and Pb were measured in water samples at JAEC and WAJ laboratories. The results showed that their concentration is less than the lower limits of detection for all seasons. U and Th concentrations were measured using ICP-MS at WAJ laboratories. The concentrations of uranium varied from 2 to 17 ppt during the wet season and from 605 to 2490 ppt during the dry season, while the concentrations of thorium varied between 2 and 17 ppt during the wet season and 49 and 190 ppt during the dry season. The results for TDS and the heavy metals in the studied dams did not exceed the allowed national JSMO limits and international WHO limits, even after the end of the dry season. These findings indicate that the dam water in Jordan is of good quality and safe for drinking purposes.

Acknowledgment

We extend our sincere gratitude to the Jordan Atomic Energy Commission (JAEC) for their invaluable support throughout this research. Their assistance in sample analysis and transportation was instrumental in the success of our study. We would like to express our appreciation to Mr. Thamer Alhajjaj and Mr. Karam Alkhalaileh for their dedicated efforts during sample collection.

Additionally, we acknowledge the Water Authority of Jordan (WAJ) for providing the sampling tools, field TDS measurements, and sample analysis, which significantly enriched the to the findings reported in this study.

References

[1] Ndeda, L.A. and Manohar, S., J. of Environ. Sci. Toxicol. Food Technol., 8 (5) (2014) 68.

[2] Sim, S.F., Ling, T.Y., Nyanti, L., Gerunsin, N., Wong, Y.E., and Kho, L.P., J. Chem., 2016 (2016) 1.

[3] Manasrah, W., Hilat, I., and El-Hasan, T., Environ. Earth Sci., 60 (3) (2010) 613.

[4] Salamah, E., El-Hasan, T., and Abu-Jamah, M., Eng., 15 (9) (2023) 514.

[5] Al-Hamaiedeh, H., Al-Rfo'u, F., Al-Hamaideh, K.D., El-Hasan, T., and Alakayleh, Z., Jordan Iraqi Geo. J., 56 (2) (2023) 48.

[6] Linnik, P.M. and Zubenko, I.B., Res. Manag., 5 (2000) 11.

[7] Al-Taani, A.A., Arab. J. Geosci., 6 (4) (2013) 1131.

[8] Jordan Standard and Measurement Organization (JSMO), "Water – Drinking Water Standard JS 286:2015" (JSMO, 2015).

[9] World Health Organization (WHO), "Guidelines for Drinking-water Quality", 4th Ed. (WHO, 2011), ISBN: 9789241548151.

[10] El-Hasan, T. and Al-Tarawneh, A., Jordan J. Earth Environ. Sci. (JJEES), 11 (3) (2020) 202.

[11] Hadadin, N., Qaqish, M., Akawwi, E., and Bdour, A., Desalination, 250 (1) (2010) 197.

[12] Mustafa, D., Altz-Stamm, A., and Scott, L.M., World Dev., 79 (2016) 164.

[13] Al-Harahsheh, A., Al-Tarawneh, A., Al-Ma'abreh, A., Ramadeen, S., El-Hasan, T., and Al-Alawi, M.M., Heliyon, 9 (1) (2023) 18862.

[14] Hadadin, N., Can. J. of Pure Appl. Sci., 9 (1) (2015) 3279.

[15] El-Radaideh, N., Al-Taani, A.A., and Al Khateeb, W.M., Environ. Earth Sci., 76 (132) (2017).

[16] El-Radaideh, N., Al-Taani, A.A., and Al Khateeb, W.M., Environ. Monit. Assess., 189 (143) (2017).

[17] El-Radaideh, N.M., Geosci. J., 20 (2016) 77.

[18] Al-Harahsheh, S.T. and Al-Amoush, H.R., J. Earth Environ. Sci., 3 (2) (2010) 111.

[19] Abualhaija, M.M. and Mohammad, A.H., J. Ecol. Eng., 22 (9) (2021) 159.

[20] Ijam, A. and Al-Bdoor, A., Civ. Environ. Res., 8 (6) (2016) 79.

[21] Rida, M., "King Talal Dam flood for the fourth time in 40 years", youm7.com, (2019), accessed: June 2024.

[22] Karadede, H. and Unlu, E., Chemosphere, 41 (9) (2000) 1371.

[23] Amrane M. and Oufni L., J. Radiat. Res. Appl. Sci., 10 (3) (2017) 246.

[24] Smedley, P.L. and Kinniburgh, D.G., Appl. Geochem., 148 (2023) 105534.

[25] Jiries, A., El-Hasan, T., Al-Hiwati, M., and Seiler, K.P., Mine Water Environ., 23 (3) (2004) 133.

Volume 18, Number 3, 2025. pp. 275-300

Jordan Journal of Physics

ARTICLE

Analysis of the Relativistic and Non-relativistic Non-commutative Quantum Systems Subject to Improved Inversely Quadratic Hellmann Potential Model in 3D-(R and NR)-NCQS Symmetries

A. Maireche

Laboratory of Physics and Material Chemistry, Faculty of Sciences, Department of Physics, University of M'sila, University Pole, Road Bourdj Bou Arreiridj,M'sila 28000, Algeria.

Doi: **https://doi.org/10.47011/18.3.3**

Received on: 19/11/2023; Accepted on: 25/04/2024

Abstract: Although the principles of non-commutative quantum mechanics date back as far as quantum mechanics known in the literature, that is, over a century ago, recent years have seen a resurgence of interest in the outcomes of this ancient theory to lead the scene of specialized research in this field. We present an improved inversely quadratic Hellman model (I-IQHPM) and determine its new eigenvalue solutions within the framework of three-dimensional relativistic/non-relativistic non-commutative quantum space (3D-(R and NR)-NCQS). The parametric Bopp's shifts approach and standard perturbation theory are used within the frameworks of the 3D-(R and NR)-NCQS to examine the novel high- and low-energy spectra under the deformed Dira, Klein-Gordon, and Schrödinger regimes for the I-IQHPM. We obtained new eigen solutions for the bosonic particles (spin-0, 1,...) and fermionic particles with spin and p-spin symmetries, with spin/p-spin = 1/2 accounting for the atomic quantum numbers (j, l, s, m), mixed potential depths (A and B), the screening parameter α, and discrete deformation parameters (Φ, χ, ζ). We recovered many potentials in the deformed Dirac equation (DE), deformed Klein-Gordon equation (KGE), and deformed Schrödinger equation (SE), including the newly modified Coulomb potential and the modified IQYP. The non-relativistic eigenvalue solutions of the I-IQHPM are then applied to obtain the spin-averaged mass spectra of heavy mesons such as $c\bar{c}$ and $b\bar{b}$. To complete this study, we explore the new partition function (PF) $Z_{nc}^{qh}(n, A, B, \beta, l, \Phi, \chi, \zeta)$ for the I-IQHPM, expressed as a function of the corresponding PF $Z_{qh}^{nl}(n, A, B, \beta, \lambda, l)$ for the IQHP potentials and the non-commutativity parameters (Φ, χ, ζ). Other thermodynamic properties (TPs), such as new mean energy $U_{nc}^{qh}(\beta, l, \Phi, \chi, \zeta)$, new mean free energy $F_{nc}^{qh}(n, A, B, \beta, l, \Phi, \chi, \zeta)$, new entropy $S_{nc}^{qh}(n, A, B, \beta, l, \Phi, \chi, \zeta)$, and new heat capacity $C_{nc}^{qh}(n, A, B, \beta, l, \Phi, \chi, \zeta)$, are determined for the I-IQHPM in the context of the deformed Schrödinger equation (SE). We highlight that our results are consistent with the previous works presented in the literature $(\Phi, \chi, \zeta) \rightarrow (0,0,0)$, corresponding to the absence of space deformation. The general solutions of the non-commutative KGE, DE, and SE, along with the expressions for the new energy levels and thermodynamic properties, are explicitly obtained under the I-IQHPM within the 3D-(R and NR)-NCQS framework.

Keywords: Inversely quadratic Hellman; Non-commutative space.

PACs: 32.60.+i, 02.30. Gp.; 12.39.Jh ; 65.40.Gr ; 31.15.Md.

Corresponding Author: A. Maireche **Email**: abdelmadjid.maireche@univ-msila.dz

1. Introduction

The search for solutions of non-relativistic and relativistic wave equations of quantum mechanics and, in its extension, known to researchers with non-commutative quantum mechanics (NCQM), has been of interest to many researchers recently, for the SE (describes the behavior of particles on the atomic and subatomic scale at low energy), KGE (describes the behavior of scalar particles, such as mesons at high energy), DE (describes the behavior of fermions particles that have half-integer spins like electrons, protons, and neutrons at high energy), and Duffin-Kemmer-Petiau equation (describes particles with higher spin-1,2,.. at high energies). Expanding the range of applications requires the interaction of two or more potential models. The idea of non-reciprocity is not new; it has been around for about a century. It was proposed in the 1930s by Heisenberg and Snyder in 1947 [1]. Recently, many researchers have investigated the effect of deformation in phase-space on some properties of quantum systems. For instance, we refer to recent works related to our topic [2-8]. This paper aims to study the 3D (KGE, DE, and SE) with the inversely quadratic Hellmann (IQH) potential model in the context of deformed space-space, which combines the Colombian potential $(-\frac{A}{r})$ and inversely quadratic Yukawa potential $\frac{B\,exp(-\alpha r)}{r^2}$ as described in the literature. Within the Schrödinger equation (SE) framework, Turkoglu *et al.* investigated the intraband nonlinear optical properties of a GaAs quantum well with IQH potential [9]. Recently, Njoku *et al.* [10] applied the Nikiforov-Uvarov method (NUM) to obtain DE solutions under spin and pseudo-spin symmetry limits and used the energy and wave function to examine the Shannon information entropy of the system [11]. Onyenegecha *et al.* [12] provided approximate analytical solutions for the SE with an IQH-Kratzer potential, deriving the energy eigenvalues and corresponding wave functions. Ghanbari [13] reported calculations of third-harmonic generation in a GaAs spherical quantum dot under the IQH potential, while Chang *et al.* [14] examined second-harmonic generation under hydrostatic pressure and temperature, determining energy levels and wave functions. Additional studies on the IQH potential are cited in [15-20]. NCQM, like all quantum mechanics known in the literature, relies on additional postulates. The first concerns the non-commutation of position-position and momentum-momentum operators $(Q_\mu^{(s,h,i)} * Q_\nu^{(s,h,i)}$ and $\pi_\mu^{(s,h,i)} * \pi_\nu^{(s,h,i)})$ are different from $(Q_\nu^{(s,h,i)} * Q_\mu^{(s,h,i)}$ and $\pi_\nu^{(s,h,i)} * \pi_\mu^{(s,h,i)})$, (the notion $(*)$ stands for the Weyl-Moyal star product, as defined below) [21-26]. This alternative theory is known as NC-phase space (NCPS) if the two hypotheses are established simultaneously. At the same time, it is called NC-space-space (NCSS) in the case of adopting only the first hypothesis (read the previous references for more investigation). It is important to notice that the works of Connes [27-29] and Seiberg-Witten [30] helped develop NCQM concepts of NCQM that are of scientific value and applicable to physical systems, especially in quantum field theory. We have studied modified IQH potential plus inversely quadratic potential in the deformed Schrödinger equation (DSE) framework and obtained new exact non-relativistic energy eigenvalues [31]. Researchers have achieved great success based on the foundations of relativistic and non-relativistic quantum mechanics. Still, unfortunately, many physical problems of great importance remain without solutions, including gravity remaining outside the framework of the standard model, as well as the well-known problem of renormalizability. All of this was an excuse to search for appropriate solutions. The most vital alternative is currently a candidate for solving these 3D-(R and NR)-NCQS regimes. It should be noted that we had some previous studies that were indirectly related to the Hellmann potential, which takes the form $(-\frac{A}{r}+\frac{B\,exp(-\alpha r)}{r})$ in the literature in the context of DES [32-34])] and the deformed KGE [35]. In this work, we are motivated to investigate the solutions to the deformed (KGE, DE, and SE) with the improved inversely quadratic Hellmann potential model (I-IQHPM) in the context of (3D-(R and NR)-NCQS) regimes. In addition to demonstrating the NC influence on the TPs of the deformed space-space's I-IQHPM. We believe that no researcher has yet addressed this study in the literature. The I-IQHPM ($V_{qh}(Q)$ and $S_{qh}(Q)$) will be the focus of our current research. This will be expressed using the analytical formulas below.

$$\begin{cases} V_{qh}(Q) = V_{qh}(r) - \frac{\partial V_{qh}(r)}{\partial r}\frac{L.\Phi}{2r} + O(\Phi^2) \\ S_{qh}(Q) = S_{qh}(r) - \frac{\partial S_{qh}(r)}{\partial r}\frac{L.\Phi}{2r} + O(\Phi^2) \end{cases} \quad (1)$$

The well-known expressions of the inversely quadratic Hellmann potential model, $(V_{qh}(r), S_{qh}(r),$ in the context of 3D-R(QM) and 3D-NR(QM) symmetries are given by [10-13, 20]:

$$\begin{pmatrix} V_{qh}(r) \\ S_{qh}(r) \end{pmatrix} = \begin{pmatrix} -\frac{A}{r} + \frac{B\,exp(-\alpha r)}{r^2} \\ -\frac{A_S}{r} + \frac{B_S\,exp(-\alpha r)}{r^2} \end{pmatrix} \cong \begin{pmatrix} -\frac{A+\alpha B}{r} + \frac{B}{r^2} + \frac{\alpha^2 B}{2} \\ -\frac{A_S+\alpha B_S}{r} + \frac{B_S}{r^2} + \frac{\alpha^2 B_S}{2} \end{pmatrix} \quad (2)$$

where A/A_S, B/B_S, and α are the strengths of the Coulomb potential $\left(-\frac{A/A_S}{r}\right)$, the inversely quadratic Yukawa potential $\frac{B/B_S\,exp(-\alpha r)}{r^2}$, and the screening parameter, respectively. Higher-order terms beyond r^2 in the Taylor expansion are neglected. Positions in the 3D-NCQS and 3D-QM regimes are denoted by $(Q \text{ and } r)$, respectively. The symbol $\mathbf{L}.\mathbf{\Phi}$ represents the scalar product between $\mathbf{L}(L_x, L_y, L_z)$ and $\mathbf{\Phi}(\theta_{12}, \theta_{23}, \theta_{13})/2$, presented physically as the angular momentum operator and infinitesimal non-commutativity vector, respectively. The self-adjoint differential operators $Q_\mu^{(s,h,i)}$and $\pi_\nu^{(s,h,i)}$ may arise in several significant variations in the context of the deformed quantum group. Canonical structure, Lie structure, and quantum plane (CS, LS, and QP, respectively) are well-known representations of the Schrödinger, Heisenberg, and interaction images. Those operators that perform the new algebra natural units $\hbar = c = 1$ are applied in this work [34, 36-42]:

$$\left[x_\mu^{(s)}, p_\nu^{(s)}\right] = \left[x_\mu^{(h)}, p_\nu^{(h)}\right] = \left[x_\mu^{(i)}, p_\nu^{(i)}\right] = i\delta_{\mu\nu} \Rightarrow \left[Q_\mu^{(s)}, \pi_\nu^{(s)}\right]_* = \left[Q_\mu^{(h)}, \pi_\nu^{(h)}\right]_* = \left[Q_\mu^{(i)}, \pi_\nu^{(i)}\right]_* = i\hbar_{eff}\delta_{\mu\nu} \quad (3.1)$$

The above equations are combined into a single formula, which is presented in the following format:

$$\left[x_\mu^{(s,h,i)}, p_\nu^{(s,h,i)}\right] = i\delta_{\mu\nu} \Rightarrow \left[Q_\mu^{(s,h,i)}, \pi_\nu^{(s,h,i)}\right]_* = i\hbar_{eff}\delta_{\mu\nu} \quad (3.2)$$

and

$$\left[x_\mu^{(s)}, x_\nu^{(s)}\right] = \left[x_\mu^{(h)}, x_\nu^{(h)}\right] = \left[x_\mu^{(i)}, x_\nu^{(i)}\right] = 0 \Rightarrow \left[Q_\mu^{(s)}, Q_\nu^{(s)}\right]_* = \left[Q_\mu^{(h)}, Q_\nu^{(h)}\right]_* = \left[Q_\mu^{(i)}, Q_\nu^{(i)}\right]_* = \begin{cases} i\varepsilon_{\mu\nu}\theta\text{: CS variety,} \\ ih_{\mu\nu}^{\alpha}Q_\alpha^{(s,h,i)}\text{: LS variety,} \\ iG_{\mu\nu}^{\alpha\beta}Q_\alpha^{(s,h,i)}Q_\beta^{(s,h,i)}\text{: QP variety.} \end{cases} \quad (4.1)$$

The above equations (4.1) are combined into a single formula, which is presented in the following format:

$$\left[x_\mu^{(s,h,i)}, x_\nu^{(s,h,i)}\right] = 0 \Rightarrow \left[Q_\mu^{(s,h,i)}, Q_\nu^{(s,h,i)}\right]_* = \begin{cases} i\varepsilon_{\mu\nu}\theta\text{: CS variety,} \\ ih_{\mu\nu}^{\alpha}Q_\alpha^{(s,h,i)}\text{: LS variety,} \\ iG_{\mu\nu}^{\alpha\beta}Q_\alpha^{(s,h,i)}Q_\beta^{(s,h,i)}\text{: QP variety.} \end{cases} \quad (4.2)$$

The new symbol $[D, M]_*$ plays the role of the commutator with the star product:

$$[D, M]_* = D * M - M * D$$

Here, X and Y can be equal to $Q_\mu^{(s,h,i)}$ or $\pi_\nu^{(s,h,i)}$. In 3D-(R and NR)-NCQS symmetries, the deformed generalized coordinates (GC) $Q_\mu^{(s,h,i)}(x_\mu^s/x_\mu^h/x_\mu^i)$ and $\pi_\mu^{(s,h,i)}(p_\mu^s/p_\mu^h/p_\mu^i)$, while the corresponding deformed generalizing momenta (GM) in 3D-RQM and 3D-NRQSM symmetries are $x_\mu^{(s,h,i)}(x_\mu^s, x_\mu^h, x_\mu^i)$ and $p_\mu^{(s,h,i)}(p_\mu^s, p_\mu^h, p_\mu^i)$, respectively. In 3D-(R and NR)-NCQS regimes, the new uncertainty relation corresponds to the LHS of Eqs. (3.1) and (3.2) can be expressed as follows:

$$\left|\Delta x_\mu^{(s)}\Delta p_\nu^{(s)}\right| = \left|\Delta x_\mu^{(h)}\Delta p_\nu^{(h)}\right| = \left|\Delta x_\mu^{(i)}\Delta p_\nu^{(i)}\right| \geq \hbar\delta_{\mu\nu}/2 \Rightarrow \left|\Delta Q_\mu^{(s)}\Delta \pi_\nu^{(s)}\right| = \left|\Delta Q_\mu^{(h)}\Delta \pi_\nu^{(h)}\right| = \left|\Delta Q_\mu^{(i)}\Delta \pi_\nu^{(i)}\right| \geq \hbar_{eff}\delta_{\mu\nu}/2 \quad (5.1)$$

Which is combined into a single formula and presented in the following format:

$$\left|\Delta x_\mu^{(s,h,i)}\Delta p_\nu^{(s,h,i)}\right| \geq \hbar\delta_{\mu\nu}/2 \Rightarrow \left|\Delta Q_\mu^{(s,h,i)}\Delta \pi_\nu^{(s,h,i)}\right| \geq \hbar_{eff}\delta_{\mu\nu}/2 \quad (5.2)$$

The RHS of Eqs. (4.1) and (4.2) permitted us to construct a new uncertainty relation as follows:

$$\left|\Delta Q_{\mu}^{(s)}\Delta Q_{\nu}^{(s,)}\right| = \left|\Delta Q_{\mu}^{(h)}\Delta Q_{\nu}^{(h)}\right| = \left|\Delta Q_{\mu}^{(i)}\Delta Q_{\nu}^{(i)}\right| \geq \begin{cases} \frac{\theta|\varepsilon_{\mu\nu}|}{2} \text{ In the context of CS vision,} \\ \frac{\beta_{\mu\nu}}{2} \text{ In the context of LS vision,} \\ \frac{L_{\mu\nu}}{2} \text{ In the context of QP vision.} \end{cases} \quad (6.1)$$

The above equations (6.1) are combined into a single formula, which is presented in the following format:

$$\left|\Delta Q_{\mu}^{(s,h,i)}\Delta Q_{\nu}^{(s,h,i)}\right| \geq \begin{cases} \frac{\theta|\varepsilon_{\mu\nu}|}{2} \text{ In the context of CS vision,} \\ \frac{\beta_{\mu\nu}}{2} \text{ In the context of LS vision,} \\ \frac{L_{\mu\nu}}{2} \text{ In the context of QP vision} \end{cases} \quad (6.2)$$

with $\beta_{\mu\nu}$ and $L_{\mu\nu}$ are equal to the average values:

$$\begin{cases} \beta_{\mu\nu} = \left|\left\langle \sum_{\alpha}^{3} \left(f_{\mu\nu}^{\alpha} Q_{\alpha}^{(s,h,i)}\right)\right\rangle\right| \\ L_{\mu\nu} = \left\langle \sum_{\alpha,\beta}^{3} \left(G_{\mu\nu}^{\alpha\beta} Q_{\alpha}^{(s,h,i)} Q_{\beta}^{(s,h,i)}\right)\right\rangle \end{cases} \quad (7)$$

The novel subdivision that appears in Eq. (6), which includes three uncertainty relations, has no precedent in the existing literature. We have extended the modified equal-time non-commutative canonical commutation relations to include Heisenberg and interaction pictures in addition to the ordinary Schrödinger picture. The symbol $\delta_{\mu\nu}$ is just the Kronecker notation, $\theta_{\mu\nu} = \theta\varepsilon_{\mu\nu}$ is an antisymmetric constant matrix with the dimensionality (length)^2, parameterizing the deformation of space-space, $\varepsilon_{\mu\nu}$ is an antisymmetric tensor operator describing the NC of space-time ($\varepsilon_{\mu\nu} = -\varepsilon_{\nu\mu} = 1$ for $\mu \neq \nu$ and $\varepsilon_{\varepsilon\varepsilon} = 0$), $\theta \in R$ is the parameter of the non-commutativity, $\hbar_{eff} \cong \hbar$ is the effective Planck constant, while μ and ν are equal to (1,2,3). The new deformed scalar product $(f * g)(x)$ is defined by the Weyl-Moyal $(*)$ product for the canonical variety expressed as [43-50]:

$$(f * g)(x) \approx (fg)(x) - \frac{i\varepsilon^{\mu\nu}\theta}{2}\partial_{\mu}^{x} f \partial_{\nu}^{x} g\Big]_{x^{\mu}=x^{\nu}} + O(\theta^2) \quad (8)$$

The first term, $(fg)(x)$, is the usual product in the 3D-RQM and 3D-NRQSM regimes, while the additive part $\left(-\frac{i\varepsilon^{\mu\nu}\theta}{2}\partial_{\mu}^{x} f \partial_{\nu}^{x} g\Big]_{x^{\mu}=x^{\nu}}\right)$ presents the effect of deformed space. Following this critical introduction, the remainder of this work is organized as follows:

Section 2 provides an overview of the IQHPM in the context of 3D-KGE, 3D-SE, and 3D-DE. Section 3 analyzes the 3D-DKGE, 3D-DDE, and 3D-DSE using the Bopp shift approach to derive the effective potential of the I-IQHPM. The corrected global energies for bosonic particles with spin (0,1,…) and fermionic particles under spin and pseudo-spin symmetry (spin/p-spin)-1/2 are obtained by applying standard time-independent perturbation theory to evaluate the expectation values of the radial terms ($\frac{1}{r^4}$ and $\frac{1}{r^3}$). Section 4 discusses significant examples in both relativistic and non-relativistic regimes, offering insights valuable to both readers and experts. Section 5 examines the effect of deformed space under the new inversely quadratic Hellmann model within 3D-NR(NCQS) symmetries, focusing on the spin-averaged mass spectra of heavy meson systems. Section 6 explores how deformation influences thermal properties, including the I-IQHPM's partition function, mean energy, free energy, specific heat, and entropy. Section 7 concludes with a concise summary of the main findings of this investigation.

2. A Brief Review of Relativistic and Non-relativistic Quantum Systems Subject to the IQHPM in 3D-RQM and 3D-NRQM Regimes

In order to make a valid physical comparison between a quantum system subject to the inversely quadratic Helmann potential model (IQHPM) in the framework of the quantum mechanical symmetries known in the literature and its extension, it is helpful to review this in the framework of the symmetries examined so far in the literature. This system satisfies the following two radial KGE and SE:

$$\left(\frac{d^2}{dr^2} + E_{nl}^{eh2} - M^2 - \frac{l(l+1)}{r^2} - \left(-\frac{A+\alpha B}{2r} + \frac{B}{2r^2} + \frac{\alpha^2 B}{4}\right)^2 + \left(-\frac{A_s+\alpha B_s}{2r} + \frac{B_s}{2r^2} + \frac{\alpha^2 B_s}{4}\right)^2 - \left(E_{nl}^{qh}\left(-\frac{A+\alpha B}{r} + \frac{B}{r^2} + \frac{\alpha^2 B}{2}\right) + M\left(-\frac{A_s+\alpha B_s}{r} + \frac{B_s}{r^2} + \frac{\alpha^2 B_s}{2}\right)\right)\right) R_{nl}(r) = 0 \quad (9)$$

and

$$\left(\frac{d^2}{dr^2}+2\mu\left(E_{nl}^{qh}+\frac{A}{r}-\frac{B\,exp(-\alpha r)}{r^2}-\frac{l(l+1)}{2\mu r^2}\right)\right)U_{nl}(r)=0 \qquad (10)$$

Here, M/μ are the masses of the boson particles (spin-0,1,...), and non-relativistic particles, respectively, while E_{nl}^{qh}/E_{nl}^{qh} are the relativistic/non-relativistic eigenvalues, and (n,l) represent the principal and spin-orbit coupling terms. Since the IQHPM has spherical symmetry, the wavefunction can be expressed as $\Psi(r,\Omega_3)$ of the known forms $\frac{R_{nl}(r)/U_{nl}(r)}{r}Y_m^l(\theta,\phi)$, where $Y_m^l(\theta,\phi)$ is spherical harmonics and m is the projections on the Oz-axis. For equal scalar and vector potential, the radial component $R_{nl}(r)$ satisfies the following simplified differential equation:

$$(\frac{d^2}{dr^2}+E_{nl}^{eh2}-M^2-\frac{l(l+1)}{r^2}-\left(-\frac{A+\alpha B}{r}+\frac{B}{r^2}+\frac{\alpha^2 B}{2}\right)\left(E_{nl}^{qh}+M\right))R_{nl}(r)=0 \qquad (11)$$

Njoku *et al.* and Alhaidari *et al.* [51] applied a scheme to write the radial part of the KGE in Eq. (11) by restyling the vector and scalar potentials $\left(V_{qh}(r),S_{qh}(r)\right)$ by $\left(-\frac{A+\alpha B}{2r}+\frac{B}{2r^2}+\frac{\alpha^2 B}{4},-\frac{A_s+\alpha B_s}{2r}+\frac{B_s}{2r^2}+\frac{\alpha^2 B_s}{4}\right)$ under the non-relativistic limit. Using $V_{qh}(r)$ from Eq. (3) with $(V_{qh}(r)=S_{qh}(r)\Leftrightarrow\ A=A_s\ and\ B=B_s)$ in Eq. (11), we obtain:

$$\left(\frac{d^2}{dr^2}+E_{nl}^{qh2}-\mu^2-Z_{nl}^{qh}(r)-\frac{l(l+1)}{r^2}\right)R_{nl}(r)=0 \qquad (12)$$

with

$$Z_{nl}^{qh}(r)=\left(E_{nl}^{qh}+M\right)\left(-\frac{A+\alpha B}{r}+\frac{B}{r^2}+\frac{\alpha^2 B}{2}\right) \qquad (13)$$

The three-dimensional radial Schrödinger wave equation is given as:

$$\left(\frac{d^2}{dr^2}+2\mu\left(E_{nl}^{qh}+\frac{A+\alpha B}{r}-\frac{B}{r^2}-\frac{\alpha^2 B}{2}-\frac{l(l+1)}{2\mu r^2}\right)\right)U_{nl}(r)=0 \qquad (14)$$

Njoku *et al.* [10, 11] applied the NUM to obtain the expression of the wave function $\Psi(r,\Omega_3)$ as a function of the associated Laguerre polynomial $L_n^{(2\sqrt{\Omega_{nl}})}\left(-2\sqrt{\chi_{nl}}r\right)$ in usual relativistic quantum symmetries:

$$\Psi(r,\Omega_3)=N_{nl}^{g}\frac{r^{\frac{1}{2}+\sqrt{\Omega_{nl}}}}{r}\times exp\left(-\sqrt{\chi_{nl}}r\right)L_n^{2\sqrt{\Omega_{nl}}}\left(2\sqrt{\chi_{nl}}r\right)Y_l^m(\Omega_3) \qquad (15)$$

with

$$\begin{cases}\Omega_{nl}=-\left(E_{nl}^{qh2}-\mu^2\right)+\frac{\alpha^2 B}{2}\\ \chi_{nl}=\left(E_{nl}^{qh}+M\right)B+l(l+1)+\frac{1}{4}\\ N_{nl}^{g}=\frac{\left(2\sqrt{\chi_{nl}}\right)^{1+\sqrt{\Omega_{nl}}}}{\sum_{i+0}^{n}\left(\frac{1}{n-i}\right)\frac{\Gamma\left(2\sqrt{\Omega_{nl}}+2+i\right)}{i!}}\end{cases} \qquad (16)$$

Here, the radial part for relativistic KGE is:

$$U_{nl}(r)=N_{nl}^{g}r^{\frac{1}{2}+\sqrt{\Omega_{nl}}}\,exp\left(-\sqrt{\chi_{nl}}r\right)L_n^{2\sqrt{\Omega_{nl}}}\left(2\sqrt{\chi_{nl}}r\right).$$

The corresponding relativistic energy E_{nl}^{qh} of the IQH potential is given by

$$1+2n+\sqrt{\left(E_{nl}^{qh}+\mu\right)B+l(l+1)+\frac{1}{4}}\ \sqrt{\left(E_{nl}^{qh}+\mu\right)\frac{\alpha^2 B}{2}-\left(E_{nl}^{qh2}-\mu^2\right)}-\left(E_{nl}^{qh}+\mu\right)(A+\alpha B)=0. \qquad (17)$$

For the non-relativistic limit, the energy eigenvalues are given by [13,20]:

$$E_{nl}^{qh}=\frac{\alpha^2 B}{2}-2\mu\left[\frac{A+\alpha B}{1+2n+\sqrt{(2l+1)^2+8\mu B}}\right]^2\equiv\delta-\frac{1}{2\mu}\left[\frac{\varphi}{(n+\Xi)}\right]^2 \qquad (18)$$

The corresponding non-relativistic wave function $\Psi^{nr}(r,\Omega_3)$ obtained by applying a transformation of the form ($E_{nl}^{qh}+\mu\rightarrow2\mu$ and $E_{nl}^{qh}-\mu\rightarrow E_{nl}^{qh}$) and substituting it into Eq. (15), we obtain:

$$\Psi^{nr}(r,\Omega_3)=N_{nl}^{nr}\frac{r^{\frac{1}{2}+\sqrt{\Omega_{nl}^{0}}}}{r}\times exp\left(-\sqrt{\chi_{nl}^{0}}r\right)L_n^{2\sqrt{\Omega_{nl}^{0}}}\left(2\sqrt{\chi_{nl}^{0}}r\right)Y_l^m(\Omega_3) \qquad (19)$$

with

$$\begin{cases} \Omega_{nl}^{0} = -2\mu E_{nr}^{qh} + \frac{\alpha^2 B}{2} \\ \chi_{nl}^{0} = 2\mu B + l(l+1) + \frac{1}{4} \\ N_{nl}^{nr} = \frac{\left(2\sqrt{\chi_{nl}^{0}}\right)^{1+\sqrt{\Omega_{nl}^{0}}}}{\sum_{i=0}^{n} \binom{1}{n-i} \frac{\Gamma\left(2\sqrt{\Omega_{nl}^{0}}+2+i\right)}{i!}} \\ \delta = \frac{\alpha^2 B}{2} \\ \Xi = \frac{1}{2} + \sqrt{\left(l+\frac{1}{2}\right)^2 + 2\mu B} \\ \varphi = \mu(A + \alpha B) \end{cases} \tag{20}$$

Here, $\sum_{i=0}^{n} \binom{a}{n-i}$ is a generalized binomial coefficient, which is computed by the multiplicative formula:

$$\sum_{i=0}^{n} \binom{a}{n-i} = \frac{a!}{(n-1)!(a-n-1!)} \tag{21}$$

The corresponding radial $R_{nl}(r)$ part for the non-relativistic Schrödinger equation is:

$$R_{nl}(r) = N_{nl}^{nr} r^{\frac{1}{2}+\sqrt{\Omega_{nl}^{0}}} exp\left(-\sqrt{\chi_{nl}^{0}} r\right) L_{n}^{2\sqrt{\Omega_{nl}^{0}}}\left(2\sqrt{\chi_{nl}^{0}} r\right)$$

In the DE, the spinor $\Psi_{nk}(r,\theta,\phi)$ can be presented in column (2×1) $\begin{pmatrix} \frac{F_{nk}(r)}{r} Y_{jm}^{l}(\theta,\phi) \\ i\frac{G_{nk}(r)}{r} Y_{jm^p}^{l^p}(\theta,\phi) \end{pmatrix}$, where $F_{nk}(r)$ and $G_{nk}(r)$ are the upper and lower components of the Dirac spinor $\Psi_{nk}(r,\theta,\phi)$, while $Y_{jm}^{l}(\theta,\phi)$ and $Y_{jm^p}^{l^p}(\theta,\phi)$ are the spin and pseudo-spin spherical harmonics. Here, (m, m^p) are the projections on the *Oz*-axis. In the condition:

$$\begin{cases} \Sigma_{qh}(r) = \frac{A+\alpha B}{r} + \frac{B}{r^2} + \frac{\alpha^2 B}{2} \text{ and } \frac{d\Delta_{qh}(r)}{dr} = 0 \\ \Rightarrow \Delta_{qh} = C_s = 0\text{: for spin symmetry} \\ \Delta_{qh}(r) = \frac{A+\alpha B}{r} + \frac{B}{r^2} + \frac{\alpha^2 B}{2} \text{ and } \frac{d\Sigma_{qh}(r)}{dr} = 0 \\ \Rightarrow \Sigma_{qh} = C_p = 0\text{: for p-spin symmetry} \end{cases} \tag{22}$$

While $F_{nk}^{s}(r)$ and $G_{nk}^{ps}(r)$ for spin symmetry and pseudo-spin symmetry obtained from:

$$\begin{aligned}&(\frac{d^2}{dr^2} - k(k+1)r^{-2} - (M + E_{nk}^{s} - C_s) \\ &\left(M - E_{nk}^{s} + \Sigma_{qh}(r)\right) F_{nk}^{s}(r) = 0\end{aligned} \tag{23}$$

and

$$\begin{aligned}&(\frac{d^2}{dr^2} - k(k-1)r^{-2} - \left(M - E_{nk}^{ps} + C_p\right) \\ &\left(M + E_{nk}^{p} - \Delta_{qh}(r)\right)) G_{nk}^{p}(r) = 0\end{aligned} \tag{24}$$

where $k(k-1)$ and $k(k+1)$ are equal $l^p(l^p-1)$ and $l(l+1)$, respectively. Turkoglu *et al.* and Njoku *et al.* [9, 10] applied the NU method to obtain the expressions for the upper component $F_{nk}^{s}(r)$ and lower component $G_{nk}^{ps}(r)$ as associated Laguerre polynomials $L_{n}^{2\sqrt{\Omega_{nk}^{r}}}(2\sqrt{\chi_{nk}^{r}} r)$ and $L_{n}^{2\sqrt{\Omega_{nk}^{r}}}\left(2\sqrt{\chi_{nk}^{p}} r\right)$ in 3D-RQM symmetry as

$$F_{nk}^{s}(r) = N_{nl}^{rs} \frac{r^{\frac{1}{2}+\sqrt{\Omega_{nk}^{s}}}}{r} exp\left(-\sqrt{\chi_{nk}^{r}} r\right) L_{n}^{2\sqrt{\Omega_{nk}^{s}}}\left(2\sqrt{\chi_{nk}^{s}} r\right) \tag{25}$$

and

$$G_{nk}^{ps}(r) = N_{nl}^{rp} \frac{r^{\frac{1}{2}+\sqrt{\Omega_{nk}^{p}}}}{r} exp\left(-\sqrt{\chi_{nk}^{p}} r\right) L_{n}^{2\sqrt{\Omega_{nk}^{p}}}\left(2\sqrt{\chi_{nk}^{p}} r\right) \tag{26}$$

Here, $\Omega_{nk}^{s}/\Omega_{nk}^{p}$, $\chi_{nk}^{s}/\chi_{nk}^{p}$, and N_{nk}^{sd}/N_{nk}^{pd} are equal to:

$$\begin{cases} \Omega_{nk}^{s} = (M + E_{nk}^{s} - C_s)B + k(k+1) + \frac{1}{4} \\ \chi_{nk}^{s} = -(M + E_{nk}^{s} + C_s)(M - E_{nk}^{s}) \\ \quad +(M + E_{nk}^{s} - C_s)\frac{\alpha^2 B}{2} \\ N_{nk}^{rs} = \frac{\left(2\sqrt{\chi_{nk}^{s}}\right)^{1+\sqrt{\Omega_{nk}^{s}}}}{\sum_{i=0}^{n} \binom{1}{n-i} \frac{\Gamma\left(2\sqrt{\Omega_{nk}^{s}}+2+i\right)}{i!}} \end{cases} \tag{27}$$

and

$$\begin{cases} \Omega_{nk}^{p} = \left(M - E_{nk}^{p} + C_p\right)B + k(k-1) + \frac{1}{4} \\ \chi_{nk}^{p} = -\left(M - E_{nk}^{p} + C_p\right)\left(M + E_{nk}^{p}\right) \\ \quad +\left(M - E_{nk}^{p} + C_p\right)\frac{\alpha^2 B}{2} \\ N_{nk}^{rp} = \frac{\left(2\sqrt{\chi_{nk}^{p}}\right)^{1+\sqrt{\Omega_{nk}^{p}}}}{\sum_{i=0}^{n} \binom{1}{n-i} \frac{\Gamma\left(2\sqrt{\Omega_{nk}^{p}}+2+i\right)}{i!}} \end{cases} \tag{28}$$

The energy equations for spin symmetry and p-spin symmetry are determined from [10]:

$$\begin{aligned}&\sqrt{(M + E_{nk}^{s} - C_s)\left(M - E_{nk}^{s} + \frac{\alpha^2 B}{2}\right)}\Big(1 + 2n + \\ &\sqrt{(2k+1)^2 - 4B(M + E_{nk}^{s} - C_s)}\Big) - \\ &(M + E_{nk}^{s} - C_s)(A + \alpha B) = 0\end{aligned} \tag{29}$$

and

$$\sqrt{\left(M-E_{nk}^{p}+C_{p}\right)\left(M+E_{nk}^{p}-\frac{\alpha^{2}B}{2}\right)}\left(1+2n+\sqrt{(2k-1)^{2}-4B\left(M-E_{nk}^{p}+C_{ps}\right)}\right)+\left(M-E_{nk}^{p}+C_{p}\right)(A+\alpha B)=0 \qquad (30)$$

The lower and upper components, $G_{nk}^{s}(s)$ and $F_{nk}^{p}(s)$ of spin symmetry and pseudo-spin symmetry are obtained by applying the following expressions:

$$G_{nk}^{s}(r)=\frac{1}{M+E_{nk}^{s}}\left(\frac{d}{dr}+\frac{k}{r}\right)F_{nk}^{s}(s)$$

and

$$F_{nk}^{p}(r)=\frac{1}{M-E_{nk}^{p}}\left(\frac{d}{dr}-\frac{k}{r}\right)G_{nk}^{p}(s)$$

In the following section, we will introduce the I-IQHPM, as well as investigate the new deformed relativistic and non-relativistic quantum theory for boson particles (spin-0, 1,...), and fermionic particles with spin and pseudo-spin symmetry (spin/p-spin)-1/2 in deformed space-space symmetries.

3. New Investigation of the Deformed Relativistic and Non-relativistic Wave Functions Subject to the I-IQHPM in Deformed Space-Space:

3.1Application of Bopp's Shift Method within the I-IQHPM

Under the I-IQHPM in deformed space-space symmetries, we examine the impact of relativistic and non-relativistic non-commutative space on quantum systems with KGE, DE, and SE, using the main approaches presented in the introduction. Our goal is accomplished by utilizing the new ideas presented in the introduction and Eqs. (4), (5), and (8), which are summed through new connections that are defined by the concept of the Weyl-Moyal star product and new non-commutative canonical commutation relations (NNCCCRs). The standard radial KG and SE equations in Eqs. (12), (14), (23), and (24) in the context of spac-space deformations or 3D-(R and NR)-NCQS can be rewritten as follows using these data:

$$\left(\frac{d^{2}}{dr^{2}}+E_{nl}^{2}-\mu^{2}-X_{nl}^{qh}(r)-\frac{l(l+1)}{r^{2}}\right)*R_{nl}(r)=0 \qquad (31)$$

$$\left(\frac{d^{2}}{dr^{2}}-k(k+1)r^{-2}-\left(M+E_{nk}^{s}-C_{s}\right)\left(M-E_{nk}^{s}+\Sigma_{qh}(r)\right)\right)*F_{nk}^{s}(r)=0 \qquad (32)$$

$$\left(\frac{d^{2}}{dr^{2}}-k(k-1)r^{-2}-\left(M-E_{nk}^{ps}+C_{p}\right)\left(M+E_{nk}^{p}-\Delta_{qh}(r)\right)\right)*G_{nk}^{p}(r)=0 \qquad (33)$$

and

$$\left(\frac{d^{2}}{dr^{2}}+2\mu\left(E_{nl}^{qh}-V_{qh}(r)-\frac{l(l+1)}{2\mu r^{2}}\right)\right)*U_{nl}(r)=0 \qquad (34)$$

Quantum field theory may involve non-commutativity in two ways. The first approach is to re-express the different non-commutative physical fields, e.g., $\left(\boldsymbol{\Psi}_{\mathbf{nl}},\boldsymbol{\Phi}_{\mathbf{nl}},\mathbf{e}_{\boldsymbol{\mu}}^{\mathbf{a}},\mathbf{F}_{\boldsymbol{\alpha\beta}}\right)$ as a function of their fields $\left(\Psi_{nl},\Phi_{nl},e_{\mu}^{a},F_{\alpha\beta}\right)$ in the well-known ordinary quantum mechanics, and the non-commutative parameters $\Phi(\eta_{12},\eta_{23},\eta_{13})/2$. This procedure is analogous to a Taylor expansion [28, 29, 52-57]. The second approach reformulates the modified operators $(Q\ and\ \pi)$ in terms of the standard quantum operators (x and p) known in the QM symmetry and the properties of space associated with the non-commutative parameters $\boldsymbol{\Phi}(\theta_{12},\theta_{23},\theta_{13})/2$. Both methods yield equivalent physical results. As is well known among specialists, F. Bopp proposed a new quantization rule where (x and p) → ($Q=x-\frac{i}{2}\partial_{p}$ and $\pi=p+\frac{i}{2}\partial_{x}$) instead of the usual correspondence $(x\ and\ p)\rightarrow(Q=x\ and\ Q=p+\frac{i}{2}\partial_{x})$. This procedure is known as Bopp's shift method [58-62], or Bopp quantization [61]. The Weyl-Moyal star product, $G(x,p)*F(x,p)$, induces Bopp's shift method in the sense that it is replaced by $G(x-\frac{i}{2}\partial_{p},p+\frac{i}{2}\partial_{x})*F(x,p)$ [62]. Applying these concepts enables us to transform the equations presented in Section 2 into new formulations within the framework of extended quantum mechanics, both in its relativistic and non-relativistic regimes, as shown below.

$$\begin{cases} X_{nl}^{qh}(r)*R_{nl}(r)=X_{nl}^{qh}(Q)R_{nl}(r) \\ \frac{l(l+1)}{r^{2}}*R_{nl}(r)=\frac{l(l+1)}{Q^{2}}R_{nl}(r) \\ \left(E_{nl}^{2}-\mu^{2}\right)*R_{nl}(r)=\left(E_{nl}^{2}-\mu^{2}\right)R_{nl}(r) \end{cases} \qquad (35)$$

$$\begin{cases} -k(k+1)r^{-2} * F_{nk}^{s}(r) = -k(k+1)Q^{-2}F_{nk}^{s}(r) \\ (M+E_{nk}^{s}-C_{s})\left(M-E_{nk}^{s}+\Sigma_{qh}(r)\right) * F_{nk}^{s}(r) = \\ \quad (M+E_{nk}^{s}-C_{s})\left(M-E_{nk}^{s}+\Sigma_{qh}(Q)\right)F_{nk}^{s}(r) \\ k(k-1)r^{-2} * G_{nk}^{p}(r) = k(k-1)Q^{-2} * G_{nk}^{p}(r) \\ \left(M-E_{nk}^{ps}+C_{p}\right)\left(M+E_{nk}^{p}-\Delta_{qh}(r)\right) * G_{nk}^{p}(r) = \\ \quad \left(M-E_{nk}^{ps}+C_{p}\right)\left(M+E_{nk}^{p}-\Delta_{qh}(Q)\right)G_{nk}^{p}(r) \end{cases} \tag{36}$$

and

$$\begin{cases} V_{qh}(r) * U_{nl}(r) = V_{qh}(Q)U_{nl}(r) \\ \frac{l(l+1)}{2\mu r^{2}} * U_{nl}(r) = \frac{l(l+1)}{2\mu Q^{2}}U_{nl}(r) \end{cases} \tag{37}$$

It should be mentioned that many specialist researchers have been attracted to Bopp's shift approach since its application provides a key to solving fundamental equations in the context of phase-space and deformed spaces. In the non-relativistic framework corresponding to the Schrödinger equation, many physical problems are treated within phase-space and deformed space symmetries [63-69]. As for the study of relativistic systems within the framework of the deformed KGE, this method has been adopted over the last decade to solve multiple problems ([70-77]. In addition, Bopp's shift approach has been applied to the study of deformed Dirac and the deformed Duffin-Kemmer-Petiau equations [78-85]. It is worth noting that Bopp's shift method allows us to reduce Eqs. (31), (32), (33), and (34) to the simplest form:

$$\left(\frac{d^{2}}{dr^{2}}+E_{nl}^{2}-M^{2}-X_{nl}^{qh}(Q)-\frac{l(l+1)}{Q^{2}}\right)R_{nl}(r) = 0 \tag{38}$$

$$\left(\frac{d^{2}}{dr^{2}}-\frac{k(k+1)}{Q^{2}}-(M+E_{nk}^{s}-C_{s})\left(M-E_{nk}^{s}+\Sigma_{qh}(Q)\right)-\Sigma_{qh}^{pert}(r)\right)F_{nk}(r) = 0 \tag{39}$$

$$\left(\frac{d^{2}}{dr^{2}}-\frac{k(k-1)}{Q^{2}}-\left(M-E_{nk}^{ps}+C_{p}\right)\left(M+E_{nk}^{p}-\Delta_{qh}(Q)\right)-\Delta_{qh}^{pert}(r)\right)G_{nk}(r) = 0 \tag{40}$$

and for the non-relativistic case,

$$\left(\frac{d^{2}}{dr^{2}}+2\mu\left(E_{nl}^{qh}-V_{qh}(Q)-\frac{l(l+1)}{2\mu Q^{2}}\right)\right)R_{nl}(r) = 0 \tag{41}$$

Here, $V_{qh}(Q)$ and $\frac{l(l+1)}{2\mu Q^{2}}$ are obtained from $V_{qh}(r)$ and $\frac{l(l+1)}{2\mu r^{2}}$ by replacing r with the non-commutative parameter Q as follows:

$$\begin{cases} V_{qh}(r) \rightarrow V_{qh}(Q) = -\frac{A+\alpha B}{Q}+\frac{B}{Q^{2}}+\frac{\alpha^{2}B}{2} \\ \qquad \frac{l(l+1)}{2\mu r^{2}} \rightarrow \frac{l(l+1)}{2\mu Q^{2}} \end{cases}$$

By applying Bopp's shift method, or the canonical quantization method, Eqs. (4) and (8), which introduces the Weyl-Moyal star concept, these equations reduce to simplified algebraic forms. This is possible because the method relies on the fundamental principles of quantization and operator algebra widely used in the literature [58-62]:

$$\begin{cases} \left[Q_{\mu}^{(s)},\pi_{\nu}^{(s)}\right] = \left[Q_{\mu}^{(h)},\pi_{\nu}^{(h)}\right] = \left[Q_{\mu}^{(i)},\pi_{\nu}^{(i)}\right] = i\hbar_{eff}\delta_{\mu\nu} \\ \left[Q_{\mu}^{(s)},Q_{\nu}^{(i)}\right] = \left[Q_{\mu}^{(h)},Q_{\nu}^{(h)}\right] = \left[Q_{\mu}^{(i)},Q_{\nu}^{(i)}\right] = i\theta_{\mu\nu} \end{cases} \tag{42.1}$$

These can be combined into a single formula, which is presented in the following format:

$$\begin{cases} \left[Q_{\mu}^{(s,h,i)},\pi_{\nu}^{(s,h,i)}\right] = i\hbar_{eff}\delta_{\mu\nu} \\ \left[Q_{\mu}^{(s,h,i)},Q_{\nu}^{(s,h,i)}\right] = i\theta_{\mu\nu} \end{cases} \tag{42.2}$$

In 3D-(R and NR)-NCQS regimes, the Nc set of variables ($Q_{\mu}^{(s,h,i)}$and $\pi_{\nu}^{(s,h,i)}$) of Eq. (42) can be expressed in terms of their commutative counterparts ($x_{\mu}^{(s,h,i)}$and $p_{\nu}^{(s,h,i)}$) using the Seiberg-Witten map:

$$\begin{pmatrix} Q_{\mu}^{(s)} \\ \pi_{\mu}^{(s)} \end{pmatrix} = \begin{pmatrix} x_{\mu}^{(s)}-\left(\sum_{\nu=1}^{3}\frac{i\theta_{\mu\nu}}{2}p_{\nu}^{(s)}\right) \\ +O(\Phi^{2}) \\ p_{\mu}^{(s)}+O(\eta^{2}) \end{pmatrix} \tag{43.1}$$

$$\begin{pmatrix} Q_{\mu}^{(h)} \\ \pi_{\mu}^{(h)} \end{pmatrix} = \begin{pmatrix} x_{\mu}^{(h)}-\left(\sum_{\nu=1}^{3}\frac{i\theta_{\mu\nu}}{2}p_{\nu}^{(h)}\right) \\ +O(\Phi^{2}) \\ p_{\mu}^{(h)}+O(\eta^{2}) \end{pmatrix} \tag{43.2}$$

and

$$\begin{pmatrix} Q_{\mu}^{(i)} \\ \pi_{\mu}^{(i)} \end{pmatrix} = \begin{pmatrix} x_{\mu}^{(i)}-\left(\sum_{\nu=1}^{3}\frac{i\theta_{\mu\nu}}{2}p_{\nu}^{(i)}\right) \\ +O(\Phi^{2}) \\ p_{\mu}^{(i)}+O(\eta^{2}) \end{pmatrix} \tag{43.3}$$

Equations (43.1), (43.2), and (43.3) can be combined into a single formula:

$$\begin{pmatrix} Q_\mu^{(s,h,i)} \\ \pi_\mu^{(s,h,i)} \end{pmatrix} = \begin{pmatrix} x_\mu^{(s,h,i)} - \left(\sum_{\nu=1}^{3} \frac{i\theta_{\mu\nu}}{2} p_\nu^{(s,h,i)}\right) \\ +O(\Phi^2) \\ p_\mu^{(s,h,i)} + O(\eta^2) \end{pmatrix} \tag{43.4}$$

This allows us to determine the operators (Q^2, $\frac{1}{Q^2}\frac{k(k+1)}{Q^2}$, $\frac{k(k-1)}{Q^2}$, and $\frac{l(l+1)}{2\mu Q^2}$) in the 3D-(R and NR)-NCQS symmetries as follows:

$$\begin{cases} Q^2 = r^2 - \mathbf{L.\Phi} + O(\Phi^2) \text{ For 3D-DKGE} \\ Q^2 = r^2 - \begin{cases} \mathbf{L.\Phi} \text{ for spin symmetry} \\ \mathbf{L^p.\Phi} \text{ for p-spin symmetry} \end{cases} \\ \qquad +O(\Phi^2) \\ \frac{k(k+1)}{Q^2} = \frac{k(k+1)}{r^2} + \frac{k(k+1)}{r^4}\mathbf{L.\Phi} + O(\Phi^2) \\ \frac{k(k-1)}{Q^2} = \frac{k(k-1)}{r^2} + \frac{k(k-1)}{r^4}\mathbf{L^p.\Phi} + O(\Phi^2) \\ \frac{l(l+1)}{2\mu Q^2} = \frac{l(l+1)}{2\mu r^2} + \frac{l(l+1)}{2\mu r^4}\mathbf{L.\Phi} + O(\Phi^2) \end{cases} \tag{44}$$

Furthermore, the Taylor expansions of $X_{nl}^{qh}(Q)$, $\Sigma_{qh}(Q)$, $\Delta_{qh}(Q)$, and $V_{qh}(Q)$ may be stated in 3D-(R and NR)- (NCQS) symmetries as:

$$\begin{cases} Z_{nl}^{qh}(Q) = Z_{nl}^{qh}(r) - \frac{1}{2r}\frac{\partial Z_{nl}^{qh}(r)}{\partial r}\mathbf{L.\Phi} + O(\Phi^2) \\ \Sigma_{qh}(Q) = \Sigma_{qh}(r) - \frac{1}{2r}\frac{\partial \Sigma_{qh}(r)}{\partial r}\mathbf{L.\Phi} + O(\Phi^2) \\ \Delta_{qh}(Q) = \Delta_{qh}(r) - \frac{1}{2r}\frac{\partial \Delta_{qh}}{\partial r}\mathbf{L^p.\Phi} + O(\Phi^2) \\ V_{qh}(Q) = V_{qh}(r) - \frac{1}{2r}\frac{\partial V_{qh}}{\partial r}\mathbf{L.\Phi} + O(\Phi^2) \end{cases} \tag{45}$$

Equations (43) and (44) can be substituted into Eqs. (31), (32), (33), and (34), to provide the following like-Schrödinger equations.

$$\left(\frac{d^2}{dr^2} + E_{nl}^2 - M^2 - Z_{qh}^{qh}(r) - Z_{r-qh}^{pert}(r)\right)R_{nl}(r) = 0 \tag{46}$$

$$\left(\frac{d^2}{dr^2} - \frac{k(k+1)}{r^2} - (M + E_{nk}^s - C_s)\left(M - E_{nk}^s + \Sigma_{qh}(r)\right) - \Sigma_{qh}^{pert}(r)\right)F_{nk}(r) = 0 \tag{47}$$

and

$$\left(\frac{d^2}{dr^2} - \frac{k(k-1)}{r^2} - \left(M - E_{nk}^p + C_p\right)\left(M + E_{nk}^{ps} - \Delta_{qh}(r)\right) - \Delta_{qh}^{pert}(r)\right)G_{nk}(r) = 0 \tag{48}$$

and

$$\left(\frac{d^2}{dr^2} + 2\mu\left(E_{nl}^{qh} - V_{qh}(r) - \frac{l(l+1)}{2\mu r^2}\right) + 2\mu Z_{nr-qh}^{pert}(r)\right)U_{nl}(r) = 0 \tag{49}$$

with

$$Z_{r-qh}^{pert}(r) = \left(\frac{l(l+1)}{r^4} - \frac{1}{2r}\frac{\partial Z_{nl}^{qh}(r)}{\partial r}\right)\mathbf{L.\Phi} + O(\Phi^2) \tag{50}$$

$$\Sigma_{qh}^{pert}(r) = \frac{k(k+1)}{r^4}\mathbf{L.\Phi} - (M + E_{nk}^s)\frac{\partial \Sigma_{qh}(r)}{\partial r}\frac{\mathbf{L.\Phi}}{2r} + O(\Phi^2) \tag{51}$$

$$\Delta_{qh}^{pert}(r) = \frac{k(k-1)}{r^4}\mathbf{L^p.\Phi} - \left(M - E_{nk}^{ps}\right)\frac{\partial \Delta_{qh}(r)}{\partial r}\frac{\mathbf{L^p.\Phi}}{2r} + O(\Phi^2) \tag{52}$$

and

$$Z_{nr-qh}^{pert}(r) = \left(\frac{1}{2r}\frac{\partial V_{qh}}{\partial r} - \frac{l(l+1)}{2\mu r^4}\right)\mathbf{L.\Phi} + O(\Phi^2) \tag{53}$$

These equations express the interaction of the topological properties of the deformed space (resulting from space deformation $\mathbf{\Phi}$) with the I-IQHPM in this space through the direct coupling between $\left(-\frac{1}{2r}\frac{\partial Z_{nl}^{qh}(r)}{\partial r}\right)$, $\left(\frac{1}{2r}\frac{\partial V_{qh}}{\partial r}\right)$, $\frac{\partial \Sigma_{qh}(r)}{\partial r}\frac{\mathbf{L.\Phi}}{2r}$, $\frac{\partial \Delta_{qh}(r)}{\partial r}\frac{\mathbf{L^p.\Phi}}{2r}$, $\frac{k(k+1)}{r^4}$, $\frac{k(k-1)}{r^4}$, and $\frac{l(l+1)}{r^4}$, together with the angular momentum operators $\mathbf{L}(L_x, L_y, L_z)$ and $\mathbf{L^p}(L_x^p, L_y^p, L_z^p)$. After a profound calculation, one gets:

$$-\frac{1}{2r}\frac{\partial Z_{nl}^{qh}(r)}{\partial r} = \left(E_{nl}^{qh} + M\right)\left(\frac{A+\alpha B}{2r^3} + \frac{B}{r^4}\right) \tag{54}$$

$$-(M + E_{nk}^s)\frac{1}{2r}\frac{\partial \Sigma_{qh}(r)}{\partial r} = (M + E_{nk}^s)\left(-\frac{A+\alpha B}{2r^3} + \frac{B}{r^4}\right) \tag{55}$$

$$-\left(M - E_{nk}^{ps}\right)\frac{1}{2r}\frac{\partial \Delta_{qh}(r)}{\partial r} = \left(M - E_{nk}^{ps}\right)\left(-\frac{A+\alpha B}{2r^3} + \frac{B}{r^4}\right) \tag{56}$$

and

$$\frac{1}{2r}\frac{\partial V_{qh}}{\partial r} = \frac{A+\alpha B}{2r^2} - \frac{B}{r^4} \tag{57}$$

I am substituting Eqs. (54), (55), (56), and (57) into Eqs. (50), (51), (52), and (53). The spontaneously generated terms $Z_{qh}^{pert}(r)$, $\Sigma_{qh}^{pert}(r)$, $\Delta_{qh}^{pert}(r)$, and $Z_{nr-qh}^{pert}(r)$ for the I-

IQHPM can be described as a result of the topological characteristics of space deformation:

$$Z_{r-qh}^{pert}(r)=\left(\frac{l(l+1)+\left(E_{nl}^{qh}+M\right)B}{r^4}-\frac{\left(E_{nl}^{qh}+M\right)(A+\alpha B)}{2r^3}\right)\mathbf{L}.\boldsymbol{\Phi}+O(\Phi^2) \quad (58)$$

$$\Sigma_{qh}^{pert}(r)=\left(\frac{k(k+1)+\left(M+E_{nk}^{s}\right)B}{r^4}-\frac{\left(M+E_{nk}^{s}\right)(A+\alpha B)}{2r^3}\right)\mathbf{L}.\boldsymbol{\Phi}+O(\Phi^2) \quad (59)$$

$$\Delta_{qh}^{pert}(r)=\left(\frac{k(k-1)+\left(M-E_{nk}^{ps}\right)B}{r^4}-\frac{\left(M-E_{nk}^{ps}\right)(A+\alpha B)}{2r^3}\right)\mathbf{L^p}.\boldsymbol{\Phi}+O(\Phi^2) \quad (60)$$

and

$$Z_{nr-qh}^{pert}(r)=\left(\frac{B-l(l+1)}{2\mu r^4}+\frac{A+\alpha B}{2r^3}\right)\mathbf{L}.\boldsymbol{\Phi}+O(\Phi^2) \quad (61)$$

In 3D-(R/NR)NCQS symmetries, the global effective potentials $Z_{qh}^{nc-eff}(r)$, $\Sigma_{qh}^{nc-eff}(r)$, $\Delta_{qh}^{nc-eff}(r)$, and $V_{nr-qh}^{nc-eff}(r)$ can be expressed as a function of corresponding effective potentials $Z_{qh}^{eff}(r)$, $\Sigma_{qh}^{eff}(r)$, $\Delta_{qh}^{eff}(r)$, and $V_{nr-qh}^{eff}(r)$ in 3D-(Ra and NR)QM symmetries as follows:

$$\begin{cases} Z_{qh}^{nc-eff}(r)=Z_{qh}^{eff}(r)+\left(\frac{l(l+1)}{r^4}-\frac{1}{2r}\frac{\partial Z_{nl}^{qh}(r)}{\partial r}\right)\mathbf{L}.\boldsymbol{\Phi}+O(\Phi^2) \\ \Sigma_{qh}^{nc-eff}(r)=\Sigma_{qh}^{eff}(r)+\left(\frac{k(k+1)}{r^4}+\left(M+E_{nk}^{s}\right)\left(\frac{A+\alpha B}{2r^3}+\frac{B}{r^4}\right)\right)\mathbf{L}.\boldsymbol{\Phi}+O(\Phi^2) \\ \Delta_{qh}^{nc-eff}(r)=\Delta_{qh}^{eff}(r)+\left(\frac{k(k-1)}{r^4}+\left(M-E_{nk}^{p}\right)\left(\frac{A+\alpha B}{2r^3}+\frac{B}{r^4}\right)\right)\mathbf{L^p}.\boldsymbol{\Phi}+O(\Phi^2) \\ V_{nr-qh}^{nc-eff}(r)=V_{qh}^{eff}(r)-\left(\frac{l(l+1)}{2\mu r^4}-\frac{1}{2r}\frac{\partial V_{qh}(r)}{\partial r}\right)\mathbf{L}.\boldsymbol{\Phi}+O(\Phi^2) \end{cases} \quad (62)$$

with

$$\begin{cases} Z_{qh}^{eff}(r)=Z_{nl}^{qh}(r)+\frac{l(l+1)}{r^2} \\ \Sigma_{qh}^{eff}(r)=\Sigma_{qh}(r)+\frac{k(k+1)}{r^2} \\ \Delta_{qh}^{eff}(r)=\Delta_{qh}(r)+\frac{k(k-1)}{r^2} \\ V_{qh}^{eff}(r)=V_{qh}(r)+\frac{l(l+1)}{2\mu r^2} \end{cases} \quad (63)$$

In 3D-(R and NR)-NCQS symmetries, the new potential under study (improved inversely quadratic Hellmann potential) is expanded to include additional terms (terms $\frac{1}{r^4}$ and $\frac{1}{r^3}$) that express its interaction with the topological properties of deformed space and the corresponding expression (inversely quadratic Hellmann potential) in the framework of QM known in the literature. The new additive parts $Z_{qh}^{pert}(r)$, $\Sigma_{qh}^{pert}(r)$, $\Delta_{qh}^{pert}(r)$, and $Z_{nr-qh}^{pert}(r)$ are proportional to the infinitesimal couplings $\mathbf{L}.\boldsymbol{\Phi}$ and $\mathbf{L^p}.\boldsymbol{\Phi}$. From the perspective of physics, this is logical, as it explains the interaction between the physical properties of the investigated potential ($\mathbf{L}$ and $\mathbf{L^p}$) and the topological characteristics arising from the deformation of space-space given by $\boldsymbol{\Phi}$. Based on this reasoning, we consider the additive effective potential as a very infinitesimal part compared with the central effective potentials $Z_{qh}^{eff}(r)$, $\Sigma_{qh}^{eff}(r)$, $\Delta_{qh}^{eff}(r)$, and $V_{qh}^{eff}(r)$ (parent/main potentials) in the symmetries of 3D(R and NR)-NCQS symmetries. That is, the inequalities $Z_{qh}^{pert}(r)\ll Z_{qh}^{eff}(r)$, $\Sigma_{qh}^{pert}(r)\ll\Sigma_{qh}^{eff}(r)$, $\Delta_{qh}^{pert}(r)(r)\ll\Delta_{qh}^{eff}(r)$, and $Z_{nr-qh}^{pert}(r)\ll V_{qh}^{eff}(r)$ are satisfied.

Consequently, the application of time-independent perturbation theory (TIPT) becomes a practical and rigorous method for solving this physical problem, as it is supported by strong justification. This approach enables us to provide a comprehensive prescription for calculating the energy levels of generalized excited states $(n,l,m,m^p)^{th}$.

3.2 Relativistic Expectation Values for Deformed KGE under the I-IQHPM

The main goal of this section is to apply TIPT in 3D-(R and NR)-NCQS symmetries to evaluate the expectation values of the relativistic KGE ($\left\langle\frac{1}{r^4}\right\rangle_{(nlm)}^{rk-qh}$ and $\left\langle\frac{1}{r^3}\right\rangle_{(nlm)}^{rk-qh}$) for boson particles, taking into account the unperturbed wave functions $\Psi(r,\Omega_3)$, which we have seen previously in Eq. (15). After calculations, one gets the expectations values ($\left\langle\frac{1}{r^4}\right\rangle_{(nlm)}^{rk-qh}$ and $\left\langle\frac{1}{r^3}\right\rangle_{(nlm)}^{rk-qh}$) using the TIPT in the first order as follows:

$$\left\langle\frac{1}{r^4}\right\rangle_{(nlm)}^{rk-qh}=\frac{N_{nl}^{g2}}{\left(2\sqrt{\chi_{nl}}\right)^{2\sqrt{\Omega_{nl}}-4}}\int_0^{+\infty} z^{2\sqrt{\Omega_{nl}}-3}\,exp(-z)\left[L_n^{2\sqrt{\Omega_{nl}}}(z)\right]^2 dz \quad (64)$$

and

$$\left\langle\frac{1}{r^3}\right\rangle_{(nlm)}^{rk-qh}= \frac{N_{nl}^{g2}}{\left(2\sqrt{\chi_{nl}}\right)^{2\sqrt{\Omega_{nl}}-3}}\int_0^{+\infty} z^{2\sqrt{\Omega_{nl}}-2}\,exp(-z)\left[L_n^{2\sqrt{\Omega_{nl}}}(z)\right]^2 dz \tag{65}$$

We have introduced a new variable $z=2\sqrt{\chi_{nl}}r$ and used abbreviations $\langle\mathcal{M}\rangle_{(nlm)}^{rk-qh}=\langle n,l,m|\mathcal{M}|n,l,m\rangle$ to avoid the extra burden of writing, with $\mathcal{M}$ equal to $\frac{1}{r^4}$ and $\frac{1}{r^3}$. We calculate the integrals in Eqs. (64) and (65) by applying the following special integral formula [86]:

$$\int_0^{+1} z^{a+b}\,exp(-z)\,[L_n^a(z)]^2 dz= \sum_{i=0}^{n}\binom{b}{n-i}\frac{\Gamma(a+b+1+i)}{i!} \tag{66}$$

where $\Gamma(a+b+1+i)$ is the Gamma function. By comparing Eqs. (64) and (65) with the integrals in Eq. (66), we obtain:

$$\left\langle\frac{1}{r^4}\right\rangle_{(nlm)}^{rk-qh}=X_{nl}^{k1}\sum_{i=0}^{n}\binom{-3}{n-i}\frac{\Gamma(2\sqrt{\Omega_{nl}}-2+i)}{i!} \tag{67}$$

and

$$\left\langle\frac{1}{r^3}\right\rangle_{(nlm)}^{rk-qh}=X_{nl}^{k2}\sum_{i=0}^{n}\binom{-2}{n-i}\frac{\Gamma(2\sqrt{\Omega_{nl}}-1+i)}{i!}, \tag{68}$$

where X_{nl}^{k1} and X_{nl}^{k2} are equal to $\frac{N_{nl}^{g2}}{\left(2\sqrt{\chi_{nl}}\right)^{2\sqrt{\Omega_{nl}}-4}}$ and $\frac{N_{nl}^{g2}}{\left(2\sqrt{\chi_{nl}}\right)^{2\sqrt{\Omega_{nl}}-3}}$, respectively. By examining the unperturbed relativistic wave function in Eq. (15) and another wave function $\Psi^{nr}(r,\Omega_3)$ in Eq. (19), in addition to the upper $F_{nk}^{s}(r)$ and lower $G_{nk}^{ps}(r)$ components in Eqs. (25) and (26) of the spinor of the DE, we note that there is a possibility to move from the unperturbed relativistic wave function $\Psi(r,\Omega_3)$ to the other non-relativistic wave function $\Psi^{nr}(r,\Omega_3)$ and the upper $F_{nk}^{s}(r)$ and lower $G_{nk}^{ps}(r)$ components by making the following substitutions:

$$N_{nl}^{g}\Leftrightarrow\left(N_{nl}^{nr},N_{nl}^{rs},N_{nl}^{rp}\right)\ \Omega_{nl}\Leftrightarrow \left(\Omega_{nl}^{0},\Omega_{nk}^{s},\Omega_{nk}^{p}\right)\text{ and }\chi_{nl}\Leftrightarrow\left(\chi_{nl}^{0},\chi_{nk}^{s},\chi_{nk}^{p}\right) \tag{69}$$

This makes it possible for us to determine the non-relativistic expectation values ($\left\langle\frac{1}{r^4}\right\rangle_{(nlm)}^{nr-qh}$, $\left\langle\frac{1}{r^3}\right\rangle_{(nlm)}^{nr-qh}$) [see Eqs. (70) and (71) below], the relativistic Dirac expectation values ($\left\langle\frac{1}{r^4}\right\rangle_{(nlm)}^{rs-qh}$, $\left\langle\frac{1}{r^3}\right\rangle_{(nlm)}^{rs-qh}$) for spin-symmetry [see Eqs. (72) and (73) below], and ($\left\langle\frac{1}{r^4}\right\rangle_{(nlm)}^{rp-qh}$, $\left\langle\frac{1}{r^3}\right\rangle_{(nlm)}^{rp-qh}$) for pseudo-spin symmetry [see Eqs. (74) and (75) below] directly from Eqs. (67) and (68), without re-calculation:

$$\left\langle\frac{1}{r^4}\right\rangle_{(nlm)}^{nr-qh}=X_{nl}^{nr1}\sum_{i=0}^{n}\binom{-3}{n-i}\frac{\Gamma\left(2\sqrt{\Omega_{nl}^{0}}-2+i\right)}{i!} \tag{70}$$

$$\left\langle\frac{1}{r^3}\right\rangle_{(nlm)}^{nr-qh}=X_{nl}^{nr2}\sum_{i=0}^{n}\binom{-2}{n-i}\frac{\Gamma\left(2\sqrt{\Omega_{nl}^{0}}-1+i\right)}{i!} \tag{71}$$

$$\left\langle\frac{1}{r^4}\right\rangle_{(nlm)}^{rs-qh}=X_{nl}^{rs1}\sum_{i=0}^{n}\binom{-3}{n-i}\frac{\Gamma\left(2\sqrt{\Omega_{nl}^{s}}-2+i\right)}{i!} \tag{72}$$

$$\left\langle\frac{1}{r^3}\right\rangle_{(nlm)}^{rs-qh}=X_{nl}^{rs2}\sum_{i=0}^{n}\binom{-2}{n-i}\frac{\Gamma\left(2\sqrt{\Omega_{nl}^{s}}-1+i\right)}{i!} \tag{73}$$

$$\left\langle\frac{1}{r^4}\right\rangle_{(nlm)}^{rp-qh}=X_{nl}^{rp1}\sum_{i=0}^{n}\binom{-3}{n-i}\frac{\Gamma\left(2\sqrt{\Omega_{nl}^{p}}-2+i\right)}{i!} \tag{74}$$

and

$$\left\langle\frac{1}{r^3}\right\rangle_{(nlm)}^{rp-qh}=X_{nl}^{rp1}\sum_{i=0}^{n}\binom{-2}{n-i}\frac{\Gamma\left(2\sqrt{\Omega_{nl}^{p}}-1+i\right)}{i!} \tag{75}$$

with X_{nl}^{nr1}, X_{nl}^{nr2}, X_{nl}^{rs1}, X_{nl}^{rs2}, X_{nl}^{rp1}, and X_{nl}^{rp1} equal to $\frac{N_{nl}^{nr2}}{\left(2\sqrt{\chi_{nl}^{0}}\right)^{2\sqrt{\Omega_{nl}^{0}}-4}}$, $\frac{N_{nl}^{nr2}}{\left(2\sqrt{\chi_{nl}^{0}}\right)^{2\sqrt{\Omega_{nl}^{0}}-3}}$, $\frac{N_{nl}^{rs2}}{\left(2\sqrt{\chi_{nl}^{s}}\right)^{2\sqrt{\Omega_{nl}^{s}}-4}}$, $\frac{N_{nl}^{rs2}}{\left(2\sqrt{\chi_{nl}^{s}}\right)^{2\sqrt{\Omega_{nl}^{s}}-3}}$, $\frac{N_{nl}^{rp2}}{\left(2\sqrt{\chi_{nl}^{p}}\right)^{2\sqrt{\Omega_{nl}^{p}}-4}}$, and $\frac{N_{nl}^{rp2}}{\left(2\sqrt{\chi_{nl}^{p}}\right)^{2\sqrt{\Omega_{nl}^{p}}-3}}$, respectively.

3.3 Impact of Space Deformation on Relativistic and Non-relativistic Energies with Interaction under the I-IQHPM in 3D-(R/NR) NCQS Symmetries

This subsection focuses on applying our physical approach, based on the superposition principle, to calculate the total energy values in 3D-(R/NR) NCQS symmetries. The global effective potentials $Z_{qh}^{nc-eff}(r)$ and $V_{nr-qh}^{nc-eff}(r)$ are the sum of three potentials: $Z_{nl}^{qh}(r)+\frac{l(l+1)}{r^2}+Z_{qh}^{pert}(r)$, $\varSigma_{qh}(r)+\frac{k(k+1)}{r^2}+\varSigma_{qh}^{pert}(r)$, $\varDelta_{qh}(r)+\frac{k(k-1)}{r^2}+\varDelta_{qh}^{pert}(r)$, $V_{qh}(r)+\frac{l(l+1)}{2\mu r^2}+V_{nr-qh}^{pert}(r)$. These effective potentials are responsible for generating the total relativistic and non-relativistic energy spectra within the framework of deformed space-space and in the presence of a topological defect. Logically, the effective potentials $Z_{nl}^{qh}(r)+\frac{l(l+1)}{r^2}$, $\varSigma_{qh}(r)+\frac{k(k+1)}{r^2}$, $\varDelta_{qh}(r)+\frac{k(k-1)}{r^2}$, and $V_{qh}(r)+\frac{l(l+1)}{2\mu r^2}$ are responsible for the relativistic energies of the KGE and DE (E_{nl}^{qh}, E_{nk}^{s}, E_{nk}^{p}) and the non-relativistic energy E_{nl}^{qh}, as reported in the literature and shown in Eqs. (17), (29), (30), and (18). These potentials dominate in the absence of deformed space. In contrast, the spontaneously generated potentials $Z_{qh}^{pert}(r)$, $\varSigma_{qh}^{pert}(r)$, $\varDelta_{qh}^{pert}(r)$, and $V_{nr-qh}^{pert}(r)$ arise from deformed space and play the role of the self-sources of corrected relativistic and no-relativistic energies in 3D-(R/NR)NCQS symmetries. Considering that the NC parameter $\varPhi(\eta_{12},\eta_{23},\eta_{13})/2$ is arbitrary, it can be dealt with physically. Firstly, the influence of the perturbed spin-orbit can be generated from perturbed potentials $Z_{qh}^{pert}(r)$, $\varSigma_{qh}^{pert}(r)$, $\varDelta_{qh}^{pert}(r)$, and $V_{nr-qh}^{pert}(r)$, corresponding to the boson particles and antiparticles with spin-s (e.g., spin-0,1,...), fermions particles with spin symmetry (spin-1/2) and fermion particles with spin or pseudo-spin symmetry (spin-1/2) The perturbed spin-orbit effective potentials are obtained by replacing the coupling of the angular momentum operators $\mathbf{L}$ and $\mathbf{L^p}$ operators with the non-commutative vector $\mathbf{\Phi}(\theta_{12},\theta_{23},\theta_{13})/2$ using the following physical couplings:

$$\begin{cases} \mathbf{L}.\mathbf{\Phi}\rightarrow\varPhi\,\mathbf{L}.\mathbf{S} \\ \text{For DKGE, DDE and DSE} \\ \mathbf{L^p}.\mathbf{\Phi}\rightarrow\varPhi\,\mathbf{L^p}.\mathbf{S^p} \\ \text{For DDE only} \end{cases}, \tag{76}$$

where $\varPhi=\sqrt{\theta_{12}^2+\theta_{23}^2+\theta_{13}^2}$. The spins of the boson particles (spin-0,1,…), fermion particles with spin symmetry (spin-1/2), and fermion particles with pseudo-spin symmetry (spin-1/2) are oriented parallel to the vector $\mathbf{\Phi}(\theta_{12},\theta_{23},\theta_{13})/2$, which interacts with the I-IQHPM. Moreover, we apply the well-known transformation in relativistic and non-relativistic QM:

$$\begin{cases} \varPhi\mathbf{L}.\mathbf{S}\rightarrow\frac{\varPhi}{2}\left(\mathbf{J}^2-\mathbf{L}^2-\mathbf{S}^2\right) \\ \text{For DKGE, DDE and DSE} \\ \varPhi\mathbf{L^p}.\mathbf{S^p}\rightarrow\frac{\varPhi}{2}\left(\mathbf{J}^2-\mathbf{L^{p2}}-\mathbf{S^{p2}}\right) \\ \text{For DDE only} \end{cases} \tag{77}$$

It is well-known in the literature that $[j(j+1)-l(l+1)-s(s+1)]/2$ represents the eigenvalues of the operator G^2 for boson particles and antiparticles (negative energy) with spin $(s=1,2..)$. Additionally, the values $\{|l-s|,|l-s|+1,\dots,|l+s|\}$ are just the possible values of $\{j\}$. Furthermore, the operators ($\mathbf{H_{nc}^{qh}}$, $\mathbf{J^2}$, $\mathbf{L^2}$, $\mathbf{L^{p2}}$, $\mathbf{S^2}$, $\mathbf{S^{p2}}$ and $\mathbf{J_z}$) form a complete set of conserved quantities in the context of deformed space-space symmetry. The eigenvalues of G^2 are equal to the values g_b, g_f^s, g_f^p for boson particles (spin-0,1,...), fermion particles under spin, and pseudo-spin symmetry (spin/p-spin)-1/2, respectively, and $g_{f,b}^{nr}$ is for DSE with spin-1/2,0,1,....

$$g_b=\frac{1}{2}[j(j+1)-l(l+1)-s(s+1)] \tag{78}$$

For spin-0,1,...

$$g_f^s=\frac{1}{2}\begin{cases} j(j+1)-l(l+1)-3/4\equiv g_f^{up-s} \\ \text{For } j=l+\frac{1}{2} \\ j(j+1)-l(l+1)-3/4\equiv g_f^{dp-s} \\ \text{For } j=l-\frac{1}{2} \end{cases} \tag{79}$$

$$g_f^p=\frac{1}{2}\begin{cases} j(j+1)-l(l+1)-3/4\equiv g_f^{up-p} \\ \text{For } j=l^p+\frac{1}{2} \\ j(j+1)-l(l-1)-3/4\equiv g_f^{dp-p} \\ \text{For } j=l^p-\frac{1}{2} \end{cases} \tag{80}$$

and

$$g_{f,b}^{nr}=\frac{1}{2}[j(j+1)-l(l+1)-s(s+1)] \tag{81}$$

For DSE with spin-1/2,0,1,...

with $|l-s|\le j\le|l+s|$ for the boson particles, $\left|l-\frac{1}{2}\right|\le j\le\left|l+\frac{1}{2}\right|$ for spin symmetry with spin-1/2, and $\left|l^p-\frac{1}{2}\right|\le j\le\left|l^p+\frac{1}{2}\right|$ for pseudo-spin symmetry with spin-1/2. As a direct preliminary result, the energy correction values$\varDelta E_{qh}^{r-so2}(n,A,B,\alpha,\varPhi,j,l,s)$, $\varDelta E_{qh}^{s-so}(n,A,B,\alpha,\varPhi,j,l,s)$,

$\varDelta E_{qh}^{p-so}(n,A,B,\alpha,\varPhi,j,l^p,s^p)$, and $\varDelta E_{qh}^{nr-so}(n,A,B,\alpha,j,l,s)$ arise from the perturbed effective potentials: $Z_{qh}^{pert}(r)$, $\varSigma_{qh}^{pert}(r)$, $\varDelta_{qh}^{pert}(r)$, and $V_{nr-qh}^{pert}(r)$ for the $(n,l,m)^{th}$ excited state in the context of deformed space-space symmetry:

$$\varDelta E_{qh}^{so2}(n,A,B,\alpha,\varPhi,j,l,s) = \varPhi g_b \left\langle Z_{qh}^{pert}(r)\right\rangle_{(nlm)}^{r}(n,A,B,\alpha) \tag{82}$$

$$\varDelta E_{qh}^{s-so}(n,A,B,\alpha,\varPhi,j,l,s) = \left\langle \varSigma_{qh}^{pert}(r)\right\rangle_{(nlm)}^{r}\begin{cases} g_f^{up-s} & \text{For } j = l+\frac{1}{2} \\ g_f^{dp-s} & \text{For } j = l-\frac{1}{2}\end{cases} \tag{83}$$

$$\varDelta E_{qh}^{p-so}(n,A,B,\alpha,\varPhi,j,l^p,s^p) = \left\langle \varDelta_{qh}^{pert}(r)\right\rangle_{(nlm)}^{r}\begin{cases} g_f^{up-p} & \text{For } j = l^p+\frac{1}{2} \\ g_f^{dp-p} & \text{For } j = l^p-\frac{1}{2}\end{cases} \tag{84}$$

and

$$\varDelta E_{qh}^{nr-so}(n,A,B,\alpha,j,l,s) = \varPhi g_{f,b}^{nr}\left\langle Z_{qh}^{pert}(r)\right\rangle_{(nlm)}^{nr}(n,A,B,\alpha) \tag{85}$$

The global relativistic and NR-relativistic expectation values $\left\langle Z_{qh}^{pert}\right\rangle_{(nlm)}^{r}(n,A,B,\alpha)$, $\left\langle \varSigma_{qh}^{pert}(r)\right\rangle_{(nlm)}^{r}(n,A,B,\alpha)$, $\left\langle \varDelta_{qh}^{pert}(r)\right\rangle_{(nlm)}^{r}$, and $\left\langle Z_{qh}^{nr-p}\right\rangle_{(nlm)}^{nr}(n,A,B,\alpha)$ for boson particles (spin-0,1,...) and fermion particles under spin and pseudo-spin symmetry (spin/p-spin)-1/2, generated by the effect of the I-IQHPM, are given by:

$$\left\langle Z_{qh}^{pert}(r)\right\rangle_{(nlm)}^{r} = \left(l(l+1) + \left(E_{nl}^{qh} + M\right)\right)B\left\langle\frac{1}{r^4}\right\rangle_{(nlm)}^{rk-qh} - \left(E_{nl}^{qh} + M\right)(A+\alpha B)/2\left\langle\frac{1}{r^3}\right\rangle_{(nlm)}^{rk-qh} \tag{86}$$

$$\left\langle \varSigma_{qh}^{pert}(r)\right\rangle_{(nlm)}^{r} = (k(k+1) + (M + E_{nk}^{s})B)\left\langle\frac{1}{r^4}\right\rangle_{(nlm)}^{rs-qh} - (M + E_{nk}^{s})(A+\alpha B)/2\left\langle\frac{1}{r^3}\right\rangle_{(nlm)}^{rs-qh} \tag{87}$$

$$\left\langle \varDelta_{qh}^{pert}(r)\right\rangle_{(nl^pm^p)}^{r} = \left(k(k-1) + \left(M - E_{nk}^{p}\right)B\right)\left\langle\frac{1}{r^4}\right\rangle_{(nlm)}^{rp-qh} - \left(M - E_{nk}^{p}\right)(A+\alpha B)/2\left\langle\frac{1}{r^3}\right\rangle_{(nlm)}^{rp-qh} \tag{88}$$

and

$$\left\langle Z_{qh}^{p}(r)\right\rangle_{(nlm)}^{nr} = \left(\frac{B-l(l+1)}{2\mu}\left\langle\frac{1}{r^4}\right\rangle_{(nlm)}^{nr-qh} + \frac{A+\alpha B}{2}\left\langle\frac{1}{r^3}\right\rangle_{(nlm)}^{nr-qh}\right) \tag{89}$$

The influence of the magnetic perturbative effective potentials, which produce the perturbed potentials $Z_{qh}^{pert}(r)$, $\varSigma_{qh}^{pert}(r)$, $\varDelta_{qh}^{pert}(r)$, and $Z_{qh}^{nr-p}(r)$ under the I-IQHPM in 3D-(R/NR)NCQS symmetries, represents a second significant physical contribution. This new effect is achieved through the following replacement procedure without repeating the previous calculations:

$$\mathbf{L}.\mathbf{\Phi} \rightarrow \chi\mathbf{L}.\aleph \text{ with } \aleph = \aleph e_z \tag{90}$$

This transformation accounts for the physical condition related to matching physical units $[\varPhi] = [\chi][\aleph] \equiv (\text{length })^2$. The new physical quantity $\aleph$ is the intensity of the magnetic field created by the effect of the deformed space, while χ is a new infinitesimal non-commutativity parameter. For simplicity, the induced magnetic field $\aleph$ is aligned along the (Oz) axis, consistent with the arbitrary orientation of the vector $\mathbf{\Phi}(\theta_{12},\theta_{23},\theta_{13})/2$. In addition, we apply the well-known quantum mechanical identity:

$$\langle n',l',m'|L_z|n,l,m\rangle = m\delta_{m'm}\delta_{l'l}\delta_{n'n} \tag{91}$$

The magnetic quantum number m is restricted to $(-|l| \leq m \leq +|l|)$. All of these factors enable the identification of the new squared energy shift $\varDelta E_{qh}^{mg2}(n,A,B,\alpha,\chi,m)$, $\varDelta E_{qh}^{s-mg}(n,A,B,\alpha,\chi,m)$, $\varDelta E_{qh}^{p-mg}(n,A,B,\alpha,\chi,m^p)$ and $\varDelta E_{qh}^{nr-mg}(n,A,B,\alpha,\chi,m)$ for boson particles, fermion particles with spin symmetry, and fermion particles with pseudo-spin symmetry. This is a result of the perturbed Zeeman effect, which was induced automatically under the influence of the IQHPM for the $(n,l,m)^{th}$ excited state in 3D-(R and NR)-NCQS symmetries as follows:

$$\varDelta E_{qh}^{mg2}(n,A,B,\alpha,\chi,m) = \chi\aleph\left\langle Z_{qh}^{pert}(r)\right\rangle_{(nlm)}^{r}(n,A,B,\alpha)m \tag{92}$$

$$\varDelta E_{qh}^{s-mg}(n,A,B,\alpha,\chi,m) = \chi\aleph\left\langle \varSigma_{qh}^{pert}(r)\right\rangle_{(nlm)}^{r}(n,A,B,\alpha)m \tag{93}$$

$$\Delta E_{qh}^{p-mg}(n,A,B,\alpha,\Phi,\chi,m^p) = \chi\aleph\langle\Delta_{qh}^{pert}(r)\rangle_{(nlm)}^{r}(n,A,B,\alpha)m^p \tag{94}$$

and

$$\Delta E_{qh}^{nr-mg}(n,A,B,\alpha,\chi,m) = \chi\aleph\langle Z_{qh}^{nr-p}(r)\rangle_{(nlm)}^{nr}(n,A,B,\alpha)m \tag{95}$$

After this achievement, we examine a new energy correction that is no less important than what we saw previously under the I-IQHPM in 3D-(R and NR)-NCQS symmetries. This new addition to energy values comes from the effective potentials $Z_{r-qh}^{pe-ro}(r)$, $\Sigma_{qh}^{pe-rot}(r)$, $\Delta_{qh}^{pe-rot}(r)$, and $Z_{qh}^{nr-r}(r)$. We consider the boson particles (or antiparticles) undergoing rotation with angular velocity Ω. The features of this subjective phenomenon are determined by replacing the arbitrary vector $\mathbf{\Phi}(\theta_{12},\theta_{23},\theta_{13})/2$ with $\zeta\mathbf{\Omega}$, which allows us to replace the previous coupling $\mathbf{L}.\mathbf{\Phi}$ with the new coupling $\zeta\mathbf{L}.\mathbf{\Omega}$, as follows:

$$Z_{r-qh}^{pert}(r) \to Z_{qh}^{pe-ro}(r) = \zeta\left(\frac{l(l+1)+\left(E_{nl}^{qh}+M\right)B}{r^4} - \frac{\left(E_{nl}^{qh}+M\right)(A+\alpha B)}{2r^3}\right)\mathbf{L}.\mathbf{\Omega} + O(\Omega^2) \tag{96}$$

$$\Sigma_{qh}^{pert}(r) \to \Sigma_{qh}^{pe-rot}(r) = \zeta\left(\frac{k(k+1)+(M+E_{nk}^{s})B}{r^4} - \frac{(M+E_{nk}^{s})(A+\alpha B)}{2r^3}\right)\mathbf{L}.\mathbf{\Omega} + O(\Omega^2) \tag{97}$$

$$\Delta_{qh}^{pert}(r) \to \Delta_{qh}^{pe-rot}(r) = \zeta\left(\frac{k(k-1)+(M-E_{nk}^{ps})B}{r^4} - \frac{(M-E_{nk}^{ps})(A+\alpha B)}{2r^3}\right)\mathbf{L}^{\mathbf{p}}.\mathbf{\Omega} + O(\Omega^2) \tag{98}$$

and

$$Z_{qh}^{nr-p}(r) \to Z_{qh}^{nr-r}(r) = \zeta\left(\frac{B-l(l+1)}{2\mu r^4} + \frac{A+\alpha B}{2r^3}\right)\mathbf{L}.\mathbf{\Omega} + O(\Omega^2) \tag{99}$$

This takes into account the physical condition related to the matching of physical units: $[\Phi] = [\zeta][\mathbf{\Omega}\aleph] \equiv (\text{length})^2$. We consider ζ as an infinitesimal real proportional constant. As it is mentioned before, the rotational velocity Ω is chosen parallel to the (Oz) axis $(\Omega = \Omega e_z)$ to simplify the calculations. This does not affect the physical content of the physical issue under study. The purpose is only to obtain results simply and straightforwardly. The perturbed induced spin-orbit coupling is then changed to become a new form as follows:

$$Z_{qh}^{pe-ro}(r) \to \zeta\Omega\left(\frac{l(l+1)+\left(E_{nl}^{qh}+M\right)B}{r^4} - \frac{\left(E_{nl}^{qh}+M\right)(A+\alpha B)}{2r^3}\right)\mathbf{L}_z + O(\Omega^2) \tag{100}$$

$$\Sigma_{qh}^{pe-rot}(r) \to \zeta\Omega\left(\frac{k(k+1)+(M+E_{nk}^{s})B}{r^4} - \frac{(M+E_{nk}^{s})(A+\alpha B)}{2r^3}\right)\mathbf{L}_z + O(\Omega^2) \tag{101}$$

$$\Delta_{qh}^{pe-rot}(r) \to \zeta\Omega\left(\frac{k(k-1)+(M-E_{nk}^{ps})B}{r^4} - \frac{(M-E_{nk}^{ps})(A+\alpha B)}{2r^3}\right)\mathbf{L}_{\mathbf{z}}^{\mathbf{p}} + O(\Omega^2) \tag{102}$$

and

$$Z_{qh}^{nr-r}(r) \to \zeta\Omega\left(\frac{B-l(l+1)}{2\mu r^4} + \frac{A+\alpha B}{2r^3}\right)\mathbf{L}_{\mathbf{z}} + O(\Omega^2) \tag{103}$$

The new corresponding corrected square energies $E_{qh}^{rot2}(n,A,B,\alpha,\zeta,m)$, $\Delta E_{qh}^{s-rot}(n,A,B,\alpha,\zeta,m)$, $\Delta E_{qh}^{p-rot}(n,A,B,\alpha,\zeta,m^p)$, and $\Delta E_{qh}^{nr-rot}(n,A,B,\alpha,\zeta,m)$ of the boson particles (spin-0,1,...), fermion particles under spin and pseudo-spin symmetry (spin/p-spin)-1/2 due to the perturbed effective potentials $Z_{qh}^{pert}(r)$, $\Sigma_{qh}^{pert}(r)$, $\Delta_{qh}^{pert}(r)$, and $V_{qh}^{pert}(r)$ which are induced automatically by the influence of the improved inversely quadratic Hellmann potential model for the $(n,l,m)^{th}$ excited state in the context of deformation space-space symmetry as follows:

$$\Delta E_{qh}^{rot2}(n,A,B,\alpha,\zeta,m) = \zeta\Omega\langle Z_{qh}^{pert}(r)\rangle_{(nlm)}^{r}(n,A,B,\alpha)m \tag{104}$$

$$\Delta E_{qh}^{s-rot}(n,A,B,\alpha,\zeta,m) = \zeta\Omega\langle \Sigma_{qh}^{pert}(r)\rangle_{(nlm)}^{r}(n,A,B,\alpha)m \tag{105}$$

$$\Delta E_{qh}^{p-rot}(n,A,B,\alpha,\Phi,\zeta,m^p) = \zeta\Omega\langle \Delta_{qh}^{pert}(r)\rangle_{(nl^pm^p)}^{r}(n,A,B,\alpha)m^p \tag{106}$$

and

$$\Delta E_{qh}^{nr-rot}(n,A,B,\alpha,\zeta,m) = \zeta\Omega\langle Z_{qh}^{p}(r)\rangle_{(nlm)}^{nr}(n,A,B,\alpha)m \tag{107}$$

Notably, this physical phenomenon was previously studied by the authors in [87], who investigated rotating isotropic and anisotropic harmonically confined ultra-cold Fermi gases at zero temperature in two and three dimensions. In their work, the rotational term was manually introduced into the Hamiltonian. In contrast, the results obtained here arise automatically through self-correction: the effect emerges internally via the interaction with space deformation, without any external influence. This is a direct consequence of the rotation operators $Z_{r-qh}^{pe-ro}(r)$, $\Sigma_{qh}^{pe-rot}(r)$, $\Delta_{qh}^{pe-rot}(r)$, and $Z_{nr-qh}^{pe-rot}(r)$ induced automatically by the improved inversely quadratic Hellmann potential model. So far, we have accomplished the most important physical corrections related to energy. Now, we apply the principle of physical superposition, which allows us to combine the different corrections. Thus, in the symmetries of the 3D-(R/NR)NCQS regimes, the total relativistic and non-relativistic new energies $E_{nc}^{r-qh}(n,A,B,\alpha,\Phi,\chi,\zeta,j,l,s,m)$, $E_{nc}^{s-qh}(n,A,B,\alpha,\Phi,\chi,\zeta,j,l,s,m)$, $E_{nc}^{p-qh}(n,A,B,\alpha,\Phi,\chi,\zeta,j,l,s,m^p)$, and $E_{nc-nl}^{nr-qh}(n,A,B,\alpha,\Phi,\chi,\zeta,j,l,s,m)$ for the boson particles (spin-0,1,...) and fermion particles under spin and pseudo-spin symmetry (spin/p-spin)-1/2 with I-IQHPM, corresponding to the generalized $(n,l,m)^{th}$ excited states, are expressed as:

$$E_{nc}^{qh}(n,A,B,\alpha,\Phi,\chi,\zeta,j,l,s,m)=E_{nl}^{qh}+ [\langle Z_{qh}^{pert}(r)\rangle_{(nlm)}^{r}((\chi\aleph+\zeta\Omega)m+\Phi g_b)]^{1/2} \tag{108}$$

$$E_{nc}^{s-qh}=E_{nk}^{s}+\langle\Sigma_{qh}^{pert}(r)\rangle_{(nlm)}^{r}\left((\chi\aleph+\zeta\Omega)m+\begin{cases} g_f^{up-s} & \text{For } j=l+\frac{1}{2}\\ g_f^{dp-s} & \text{For } j=l-\frac{1}{2}\end{cases}\right) \tag{109}$$

$$E_{nc}^{p-qh}=E_{nk}^{p}+\langle\Delta_{qh}^{pert}(r)\rangle_{(nl^pm^p)}^{r}\left((\chi\aleph+\zeta\Omega)m+\begin{cases} g_f^{up-p} & \text{For } j=l^p+\frac{1}{2}\\ g_f^{dp-p} & \text{For } j=l^p-\frac{1}{2}\end{cases}\right) \tag{110}$$

and

$$E_{nc-nl}^{nr-qh}=\frac{\alpha^2B}{2}-2\mu\left[\frac{A+\alpha B}{1+2n+\sqrt{(2l+1)^2+8\mu B}}\right]^2+ \langle Z_{qh}^{p}(r)\rangle_{(nlm)}^{nr}\left[(\chi\aleph+\zeta\Omega)m+\Phi g_{f,b}^{nr}\right] \tag{111}$$

where E_{nl}^{qh}, E_{nk}^{s}, and E_{nk}^{p} are the relativistic energies under the improved inversely quadratic Hellmann potential model obtained from Eqs. (18), (29), and (30). It is important to note that the corrected energy values in Eq. (108) can be generalized to include negative energy (boson antiparticles, e.g., as π^+) and positive relativistic energy (boson particles, e.g., π^-) as:

$$E_{t-nc}^{qh}= \pm|E_{nl}^{qh}|\pm[\langle X_{qh}^{pert}(r)\rangle_{(nlm)}^{r}((\chi\aleph+\zeta\Omega)m+\Phi g_b)]^{1/2} \tag{112}$$

The latter can be reformulated using the so-called step $\theta(|E_{nc}^{qh}|)$ function as follows:

$$E_{t-nc}^{qh}=|E_{nc}^{qh}|\theta(|E_{nc}^{qh}|)-|E_{nc}^{qh-s}|\theta(-|E_{nc}^{qh}|) \tag{113}$$

This generalization extends naturally to fermion and antifermion particles, where fermions carry positive energy and antifermions carry negative energy. It should be noted that these energy corrections are consistent with the first order of infinitesimal NC-parameters (Φ,χ,ζ). Higher-order corrections proportional to higher powers of these parameters are beyond the scope of this work.

4. Special Cases Resulting Directly from the I-IQHPM in 3D-(R and NR)-NCQS Symmetries

This section investigates several special cases that emerge directly from the improved inversely quadratic Hellmann potential model in 3D-(R and NR)-NCQS symmetries. These cases follow naturally from Eqs. (108)–(111). By appropriately adjusting the potential parameters of the I-IQHPM, we obtain the following:

- Setting $B=\alpha=0$ allows us to get a new modified Coulomb potential. In this situation, the total relativistic and non-relativistic new energies $E_{nc}^{r-c}(n,A,\Phi,\chi,\zeta,j,l,s,m)$, $E_{nc}^{s-c}(n,A,\Phi,\chi,\zeta,j,l,s,m)$, $E_{nc}^{p-c}(n,A,\Phi,\chi,\zeta,j,l,s,m^p)$, and $E_{nc-nl}^{nr-c}(n,A,\Phi,\chi,\zeta,j,l,s,m)$ are obtained for boson particles (spin-0, 1, …) and fermion particles under spin and pseudo-spin symmetry (spin/p-spin)-1/2 in the modified Coulomb potential model, corresponding to the generalized $(n,l,m,m^p)^{th}$ excited states in 3D-(R and NR)-NCQS symmetries:

$$E_{nc}^{c}(n,A,\Phi,\chi,\zeta,j,l,s,m)=E_{nl}^{c}+ [\langle Z_{c}^{pert}(r)\rangle_{(nlm)}^{r}((\chi\aleph+\zeta\Omega)m+\Phi g_b)]^{1/2} \tag{114}$$

$$E_{nc}^{s-c}n,A,\Phi,\chi,\zeta,j,l,s,m = E_{nk}^{cs} + \left\langle \Sigma_c^{pert}(r)\right\rangle_{(nlm)}^{r}\left((\chi\aleph+\zeta\Omega)m + \begin{cases} g_f^{up-s} \text{ For } j = l+\frac{1}{2} \\ g_f^{dp-s} \text{ For } j = l-\frac{1}{2}\end{cases}\right) \quad (115)$$

$$E_{nc}^{p-c}(n,A,\Phi,\chi,\zeta,j,l,s,m^p) = E_{nk}^{cp} + \left\langle \Delta_c^{pert}(r)\right\rangle_{(nl^p m^p)}^{r}\left((\chi\aleph+\zeta\Omega)m + \begin{cases} g_f^{up-p} \text{ For } j = l^p+\frac{1}{2} \\ g_f^{dp-p} \text{ For } j = l^p-\frac{1}{2}\end{cases}\right) \quad (116)$$

and

$$E_{nc-nl}^{nr-c}(n,A,\Phi,\chi,\zeta,j,l,s,m) = -\frac{\mu A^2}{(n+l+1)} + \left\langle Z_c^{p}(r)\right\rangle_{(nlm)}^{nr}\left[(\chi\aleph+\zeta\Omega)m + \Phi g_{f,b}^{nr}\right] \quad (117)$$

The energy relation in Eq. (114) agrees completely with the results reported in Refs. [71, 88]. The new relativistic Dirac energies in Eqs. (115) and (116) are consistent with the results of Ref. [36]. The first term in Eqs. (115) and (116) are the relativistic eigenvalues E_{nk}^{cs} and E_{nk}^{cp} in 3D-RQM symmetries, which can be determined from Refs. [89, 90] [see Eqs. (46) and (47)]. We note that the new non-relativistic energy in Eq. (117) agrees with previously established results as a particular case in Refs. [6, 91, 92]. The corresponding new relativistic and non-relativistic expectation values $\left\langle Z_c^{pert}(r)\right\rangle_{(nlm)}^{r}$, $\left\langle \Sigma_c^{pert}(r)\right\rangle_{(nlm)}^{r}$, $\left\langle \Delta_c^{pert}(r)\right\rangle_{(nl^p m^p)}^{r}$, and $\left\langle Z_c^{p}(r)\right\rangle_{(nlm)}^{nr}$ of the modified Coulomb potential models are obtained from the limits:

$$\begin{cases} \left\langle Z_c^{pert}(r)\right\rangle_{(nlm)}^{r} = \lim\limits_{(B,\alpha)\to(0,0)}\left\langle Z_{qh}^{pert}(r)\right\rangle_{(nlm)}^{r} \\ \quad = (E_{nl}^{c}+M)A/2\lim\limits_{(B,\alpha)\to(0,0)}\left\langle\frac{1}{r^3}\right\rangle_{(nlm)}^{rk-qh} \\ \left\langle \Sigma_c^{pert}(r)\right\rangle_{(nlm)}^{r} = \lim\limits_{(B,\alpha)\to(0,0)}\left\langle \Sigma_{qh}^{pert}(r)\right\rangle_{(nlm)}^{r} \\ \quad = (M+E_{nk}^{cs})A/2\lim\limits_{(B,\alpha)\to(0,0)}\left\langle\frac{1}{r^3}\right\rangle_{(nlm)}^{rs-qh} \\ \left\langle \Delta_c^{pert}(r)\right\rangle_{(nl^p m^p)}^{r} = \lim\limits_{(B,\alpha)\to(0,0)}\left\langle \Delta_{qh}^{pert}(r)\right\rangle_{(nl^p m^p)}^{r} \\ \quad = \left(M-E_{nk}^{cp}\right)A/2\lim\limits_{(B,\alpha)\to(0,0)}\left\langle\frac{1}{r^3}\right\rangle_{(nlm)}^{rp-qh} \\ \left\langle Z_c^{p}(r)\right\rangle_{(nlm)}^{nr} = \lim\limits_{(B,\alpha)\to(0,0)}\left\langle Z_{qh}^{nr-p}(r)\right\rangle_{(nlm)}^{nr} \\ \quad = -\frac{A}{2}\lim\limits_{(B,\alpha)\to(0,0)}\left\langle\frac{1}{r^3}\right\rangle_{(nlm)}^{nr-qh} \end{cases} \quad (118)$$

➢ If we choose $A = 0$, we obtain the modified inversely quadratic Yukawa potential (IIQYP). From Eqs. (108)-(111), the total relativistic and non-relativistic energies $E_{nc}^{r-q}(n,B,\alpha,\Phi,\chi,\zeta,j,l,s,m)$, $E_{nc}^{s-q}(n,B,\alpha,\Phi,\chi,\zeta,j,l,s,m)$, $E_{nc}^{p-q}(n,B,\alpha,\Phi,\chi,\zeta,j,l,s,m^p)\ B,\alpha,\Phi,\chi,\zeta,j,l,s,m^p)$ and $E_{nc-nl}^{nr-q}(n,B,\alpha,\Phi,\chi,\zeta,j,l,s,m)$

are obtained for bosons (spin 0,1,…) and fermions under spin and pseudo-spin symmetries (spin/p-spin)-1/2 within the IIQYP model, corresponding to the generalized $(n,l,m,m^p)^{th}$ excited states in 3D-(R and NR)-NCQS symmetries:

$$E_{nc}^{q}(n,B,\alpha,\Phi,\chi,\zeta,j,l,s,m) = E_{nl}^{q} + \left[\left\langle Z_{qc}^{pert}(r)\right\rangle_{(nlm)}^{r}((\chi\aleph+\zeta\Omega)m + \Phi g_b)\right]^{1/2} \quad (119)$$

$$E_{nc}^{s-q} = E_{nk}^{qs} + \left\langle \Sigma_q^{pert}(r)\right\rangle_{(nlm)}^{r}\left((\chi\aleph+\zeta\Omega)m + \begin{cases} g_f^{up-s} \text{ For } j = l+\frac{1}{2} \\ g_f^{dp-s} \text{ For } j = l-\frac{1}{2}\end{cases}\right) \quad (120)$$

$$E_{nc}^{p-q}(n,B,\alpha,\Phi,\chi,\zeta,j,l,s,m^p) = E_{nk}^{qp} + \left\langle \Delta_q^{pert}(r)\right\rangle_{(nl^p m^p)}^{r}\left((\chi\aleph+\zeta\Omega)m + \begin{cases} g_f^{up-p} \text{ For } j = l^p+\frac{1}{2} \\ g_f^{dp-p} \text{ For } j = l^p-\frac{1}{2}\end{cases}\right) \quad (121)$$

and

$$E_{nc-nl}^{nr-q} = \frac{\alpha^2 B}{2} - \frac{2\mu\alpha^2 B^2}{\left(1+2n+\sqrt{(2l+1)^2+8\mu B}\right)^2} + \left\langle Z_q^{pert}(r)\right\rangle_{(nlm)}^{nr}\left[(\chi\aleph+\zeta\Omega)m+\Phi g_{f,b}^{nr}\right] \tag{122}$$

The energy relation in Eq. (119) is in full agreement with previously reported results. The relativistic Dirac energies in Eqs. (120) and (121) are consistent with Ref. [93]. The first terms in Eqs. (120) and (121) are the relativistic eigenvalues of E_{nk}^{qs} and E_{nk}^{qp} in 3D-RQM symmetries, which can be determined from Ref. [94, 95]. The non-relativistic case given in Eq. (122) agrees as a special case with Ref. [96]. Its first two terms represent the non-relativistic energy in 3D-NRQM symmetry [97]. The corresponding expectation values $\left\langle Z_c^{pert}(r)\right\rangle_{(nlm)}^{r}$, $\left\langle \Sigma_q^{pert}(r)\right\rangle_{(nlm)}^{r}$, $\left\langle \Delta_q^{pert}(r)\right\rangle_{(nl^p m^p)}^{r}$, and $\left\langle Z_q^{p}(r)\right\rangle_{(nlm)}^{nr}$ for the IIQYP model are obtained from the following limits:

$$\begin{cases} \left\langle Z_q^{pert}(r)\right\rangle_{(nlm)}^{r} = \lim\limits_{A\to 0}\left\langle Z_{qh}^{pert}(r)\right\rangle_{(nlm)}^{r} \\ \left\langle \Sigma_q^{pert}(r)\right\rangle_{(nlm)}^{r} = \lim\limits_{A\to 0}\left\langle \Sigma_{qh}^{pert}(r)\right\rangle_{(nlm)}^{r} \\ \left\langle \Delta_q^{pert}(r)\right\rangle_{(nl^p m^p)}^{r} = \lim\limits_{A\to 0}\left\langle \Delta_{qh}^{pert}(r)\right\rangle_{(nl^p m^p)}^{r} \\ \left\langle Z_q^{p}(r)\right\rangle_{(nlm)}^{nr} = \lim\limits_{A\to 0}\left\langle Z_{qh}^{nr-p}(r)\right\rangle_{(nlm)}^{nr} \end{cases} \tag{123}$$

5. Study of Spin-Averaged Mass Spectra of Heavy Mesons under the IQH in 3D-NRQM and 3D-NR(NCQS) Regimes

The potential considered in this study (the IQH model) has two basic properties: attraction (confinement) at long distances and repulsion at small distances, appropriate to the dimensions studied. These properties qualify it to be a reaction potential for quarkonium systems such as charmonium $c\bar{c}$ and bottomonium $b\bar{b}$. As a result, we devote this section to calculating the mass spectra of heavy meson systems, which have the quark and antiquark flavor under the IQH model in 3D-NRQM and 3D-NR(NCQS) regimes. Additionally, we divide the IQH model, which appears in Eq. (2), into two main parts $V_1(r)$ and $V_2(r)$ that play different roles in 3D-NRQM symmetries. The first part is defined as

$$V_1(r) = \frac{B}{r^2} + \frac{\alpha^2 B}{2} \tag{124}$$

which combines an inverse quadratic potential $\frac{B}{r^2}$ with a constant potential $\frac{\alpha^2 B}{2}$. This part satisfies the limit:

$$\underset{\alpha\to 0}{Lim}\left(\frac{B}{r^2} + \frac{\alpha^2 B}{2}\right) = \frac{B}{r^2} \tag{125}$$

and, as a positive value, reproduces the terms $(\frac{d}{r^2} + e)$ of the generalized Cornell potential (GCP) [99]. Thus, $(\frac{B}{r^2}$ and $\frac{\alpha^2 B}{2})$ can be compared with $(\frac{d}{r^2}$ and $e)$, respectively, which are responsible for confinement at large distances. The second part, $V_2(r)$, similar to the Coulomb potential, which appears in the generalized Cornell potential, has the form:

$$V_2(r) = -\frac{A+\alpha B}{r} \tag{126}$$

The above result, as a negative value, completely simulates the Colombian potential $(-c/r)$ in the GCP [98] because this part potential satisfies the following limit:

$$\underset{\alpha\to 0}{Lim}\left(-\frac{A+\alpha B}{r}\right) = -\frac{A}{r} \tag{127}$$

The second term plays a role similar to the Colombian potential. The result of this analysis is that the potential under study is considered a means of interaction between the quarkonium system. We calculate the new mass of quarkonium M_{nc-nl}^{qh-hm} in three-dimensional non-relativistic non-commutative QM symmetries, using our formula, which has the following form:

$$M_{nc-nl}^{qh-hm} = 2m_q + \begin{cases} \frac{1}{3}\begin{pmatrix} \left(E_{nc-nl}^{nr-qh}\right)^U + \left(E_{nc-nl}^{nr-qh}\right)^M \\ +\left(E_{nc-nl}^{nr-qh}\right)^L \end{pmatrix} & \text{for spin-1} \\ E_{nc-nl}^{nr-qh} \text{ for spin-0} \end{cases} \tag{128}$$

Here, m_q is the quark mass, while $\left(E_{nc-nl}^{nr-qh}\right)^U$, $\left(E_{nc-nl}^{nr-qh}\right)^M$, $\left(E_{nc-nl}^{nr-qh}\right)^L$ and $\left(E_{nc-nl}^{nr-qh}\right)^U$ are the new energy eigenvalues that correspond to $(j = l+1$ and spin $-1)$, $(j = l$ and spin-*one*), $(j = l-1$ and spin/one), and $(j = l$ and spin-0) under the improved inversely quadratic Hellmann potential model in 3D-NR-NCQS regimes. It results from the generalization of the original relationship known in the literature [98-100]:

$$M_{nl}^{qh-hm} = 2m_q + E_{nl}^{nr} \tag{129}$$

where E_{nl}^{nr} is the non-relativistic energy under the inversely quadratic Hellmann potential model, which is determined by Eq. (18). We have replaced the energy eigenvalues E_{nl}^{nr} with average values $\frac{1}{3}$ $(\left(E_{nc-nl}^{nr-qh}\right)^{U}$ + $\left(E_{nc-nl}^{nr-qh}\right)^{M}$+ $\left(E_{nc-nl}^{nr-qh}\right)^{L}$) that have spin-1 with three different values of j, while for spin-0, the values E_{nl}^{nr} are replaced with E_{nc-nl}^{nr-qh} because it represents a single value. We need to replace the factor $g_{f,b}^{nr}$ with new generalized values as follows:

$$g_{f,b}^{nr} = \begin{cases} l/2 \text{ For } j = l+1 \text{and } s = 1 \\ -1 \text{ For } j = l \text{ and } s = 1 \\ (-2l-2)/2 \text{ For } j = l-1 \text{ and } s = 1 \\ 0 \text{ For } j = l \text{ and } s = 0, \end{cases} \tag{130}$$

which allows us to obtain (E_{nc-nl}^{my-u}, E_{nc-nl}^{my-m}, and E_{nc-nl}^{my-l}) and E_{nc-nl}^{nr-my} for heavy meson systems such as ($c\bar{c}$ and $b\bar{b}$):

1- For the case of $j = l+1$ and spin/one, the improved IQH model induces the energy values $\left(E_{nc-nl}^{nr-qh}\right)^{U}$ that are expressed by the following formula:

$$\left(E_{nc-nl}^{nr-qh}\right)^{U} = \frac{\alpha^2 B}{2} - 2\mu\left[\frac{A+\alpha B}{1+2n+\sqrt{(2l+1)^2+8\mu B}}\right]^2 + \left\langle Z_{qh}^{p}\right\rangle_{(nlm)}^{nr}\left[(\chi\aleph+\zeta\Omega)m + \Phi g_{f,b}^{nr}\right] \tag{131}$$

2- For the case of $j = l$ and spin/one, the improved IQH model induces the energy values $\left(E_{nc-nl}^{nr-qh}\right)^{M}$ that are expressed by the following formula:

$$\left(E_{nc-nl}^{nr-qh}\right)^{M} = \frac{\alpha^2 B}{2} - 2\mu\left[\frac{A+\alpha B}{1+2n+\sqrt{(2l+1)^2+8\mu B}}\right]^2 + \left\langle Z_{qh}^{p}\right\rangle_{(nlm)}^{nr}\left((\beta\aleph+\zeta\Omega)m - \Phi\right) \tag{132}$$

3- For the case of $j = l-1$ and spin/one, the improved IQH model induces the energy values $\left(E_{nc-nl}^{nr-qh}\right)^{L}$ that are expressed by the following formula:

$$\left(E_{nc-nl}^{nr-qh}\right)^{L} = \frac{\alpha^2 B}{2} - 2\mu\left[\frac{A+\alpha B}{1+2n+\sqrt{(2l+1)^2+8\mu B}}\right]^2 + \left\langle Z_{qh}^{p}\right\rangle_{(nlm)}^{nr}\left((\beta\aleph+\zeta\Omega)m - \Phi(l+1)\right), \tag{133}$$

while for the case of $\left(j = l \text{ and spin-0}\right)$, the energy values E_{nl}^{nc} produced by the improved inversely quadratic Hellmann potential model can be expressed as follows:

$$E_{nl}^{nc} = \frac{\alpha^2 B}{2} - 2\mu\left[\frac{A+\alpha B}{1+2n+\sqrt{(2l+1)^2+8\mu B}}\right]^2 + \left\langle Z_{qh}^{p}\right\rangle_{(nlm)}^{nr}(\beta\aleph+\zeta\Omega)m) \tag{134}$$

By substituting Eqs. (127)-(130) into Eq. (124), the expression of the mass spectrum $M_{nc-nl}^{qh-hm}(A,B,\alpha,\Phi,\beta,\zeta)$ of heavy mesons systems such as ($c\bar{c}$ and $b\bar{b}$) in the context of deformed space-space symmetry under the influence of the improved inversely quadratic Hellmann potential model as a function of corresponding mass spectra M_{nl}^{qh-hm} in the ordinary non-relativistic quantum mechanics regime and non-commutativity parameters (Φ,β,ζ) can be expressed as

$$M_{nc-nl}^{qh-hm}(A,B,\alpha,\Phi,\beta,\zeta) = M_{nl}^{my-hm} + \begin{cases} \left\langle Z_{qh}^{p}\right\rangle_{(nlm)}^{nr}\left((\tau\aleph+\chi\Omega)m - \frac{(l+4)}{6}\Phi\right) \text{ for spin-1} \\ \left\langle Z_{qh}^{p}\right\rangle_{(nlm)}^{nr}(\beta\aleph+\zeta\Omega)m) \text{ for spin-0} \end{cases} \tag{135}$$

The first term on the RHS of Eq. (135) is the ordinary spin-averaged mass spectrum $M_{nl}^{qh-hm} \equiv M_{nl}^{qh-hm}(A,B,\alpha)$ of heavy meson systems, e.g., ($c\bar{c}$ and $b\bar{b}$), under the Schrödinger equation with the inversely quadratic Hellmann model in the ordinary three-dimensional non-relativistic quantum mechanics regime:

$$M_{nl}^{qh-hm}(A,B,\alpha) = 2m_q + \frac{\alpha^2}{2\mu}l(l+1) + \frac{\alpha^2 B}{2} - 2\mu\left[\frac{A+\alpha B}{1+2n+\sqrt{(2l+1)^2+8\mu B}}\right]^2 \tag{136}$$

It is extended to include δM_{nc-nl}^{qh-hm} in 3D-NR(NCQS) symmetries:

$$\delta M_{nc-nl}^{qh-hm} = \begin{cases} \left\langle Z_{qh}^{p}\right\rangle_{(nlm)}^{nr}\left((\tau\aleph+\chi\Omega)m - \frac{(l+4)}{6}\Phi\right) \\ \text{For spin-1} \\ \left\langle Z_{qh}^{p}\right\rangle_{(nlm)}^{nr}(\beta\aleph+\zeta\Omega)m) \\ \text{For spin-0} \end{cases} \tag{137}$$

The above result depends on the atomic quantum numbers (n,j,l,s,m), the potential parameters (A,B,α), and the non-commutativity parameters (Φ,β,ζ). To verify the validity of our results, we apply the following physical limit:

$$\lim_{(\Phi,\beta,\zeta)\to(0,0,0)} M_{nc-nl}^{qh-hm}(A,B,\alpha,\Phi,\beta,\zeta) = M_{nl}^{qh-hm}(A,B,\alpha) \quad (138)$$

6. Thermodynamic Quantities at the Non-relativistic Limit: Mesons under the IQHPM and I-IQHPM in 3D-NRQM and its Extended Symmetries

In 3D-NR(NCQS) symmetries, TPs of the improved inversely quadratic Hellmann potential model are studied in this section at the non-relativistic limit. The PF must be determined to deduce the other thermal properties, such as internal energy, entropy, free energy, and specific heat capacity. These are all necessary steps toward accomplishing this goal. Direct summing over all potential energy levels at a particular temperature T can be used to derive the PF [101-103]:

$$Z_{qh}^{nl}(n,A,B,\beta,\lambda,l) = \sum_{n=0}^{\lambda} exp\left(-\beta E_{nl}^{nr}\right) \Rightarrow Z_{qh}^{nc}(n,A,B,\beta,l,\alpha_{max},\Phi,\beta,\zeta) = \sum_{n=0}^{\alpha_{max}} exp\left(-\beta E_{nc}^{nr}\right) \quad (139)$$

Here, $Z_{qh}^{nl}(n,A,B,\beta,\lambda,l)$ and $Z_{qh}^{nc}(n,A,B,\beta,l,\alpha_{max},\Phi,\beta,\zeta)$ are the partition functions of the IQHPM and I-IQHPM, respectively. At the same time, λ and λ are the upper bound vibration quantum numbers (the maximum quantum numbers) in the context of both deformation space and usual 3D-non-relativistic quantum mechanics. Furthermore, $\beta = \frac{1}{KT}$, where K is the Boltzmann constant. From the beginning, we accept as a given that the new PF $(Z_{qh}^{nc}(n,A,B,\beta,l,\alpha_{max}))$ is dependent on non-commutativity parameters $(\Phi$,β,$\zeta)$. This dependence is expected, since the results themselves are explicitly tied to these parameters. The maximum quantum number α_{max} in deformation space, as a function of the corresponding value λ in three-dimensional non-relativistic quantum mechanics, is given by:

$$\left.\frac{dE_{nl}^{nr}}{dn}\right]_{n=\lambda} = 0 \Rightarrow \left.\frac{dE_{nc}^{qh}}{dn}\right]_{n=\alpha_{max}} \Rightarrow \alpha_{max} = \lambda + \lambda_{per}^{qh} \quad (140)$$

with

$$\lambda_{per}^{qh} = \frac{d}{dn}\left(\left\langle Z_{qh}^{p}\right\rangle_{(nlm)}^{nr}(\chi\aleph + \zeta\Omega)m + \Phi g_{f,b}^{nr}\right)\Bigg]_{n=\alpha_{max}} \quad (141)$$

Further, we can rewrite the non-relativistic energy E_{nc-nl}^{nr-qh} in the context of deformation space-space symmetries E_{nc-nl}^{nr-qh} in Eq. (111) for the case $l \neq 0$ as follows:

$$E_{nc-nl}^{nr-qh} = E_{nl}^{nr} + \Delta E(n,A,B,\alpha,\chi,\zeta,\Phi) \quad (142)$$

with

$$\begin{cases} E_{nl}^{qh} = \frac{\alpha^2 B}{2} - 2\mu\left(\frac{A+\alpha B}{1+2n+\sqrt{(2l+1)^2+8\mu B}}\right)^2 \\ \qquad \equiv \delta - \frac{1}{2\mu}\left(\frac{\varphi}{n+\Xi_{qh}^{nl}}\right)^2 \\ \Delta E(n,A,B,\alpha,\chi,\zeta,\Phi) = \\ \left\langle Z_{qh}^{p}(r)\right\rangle_{(nlm)}^{nr}\left[(\chi\aleph + \zeta\Omega)m + \Phi g_{f,b}^{nr}\right] \end{cases} \quad (143)$$

and

$$\begin{cases} \delta = \frac{\alpha^2 B}{2} \\ \Xi_{hp}^{nl} = \frac{1}{2} + \sqrt{\left(l+\frac{1}{2}\right)^2 + 2\mu B} \\ \varphi = \mu(A+\alpha B) \end{cases} \quad (144)$$

In the context of deformation space-space symmetries, at high temperatures in the classical limit, the new modified PF $Z_{qh}^{nc}(n,A,B,\beta,l,\alpha_{max})$ can be expressed as an integral:

$$Z_{qh}^{nc}(n,A,B,\beta,l,\alpha_{max},\Phi,\beta,\zeta) = \int_0^{\alpha_{max}} exp\left(-\beta E_{nc}^{nr-qh}(\rho)\right)(\rho)d\rho \quad (145)$$

Here, ρ is equal to $\left(n + \Xi_{qh}^{nr}\right)$ in the classical limit. We saw earlier that the corrected energy $\Delta E(A,B,\alpha,\chi,\zeta,\Phi)$ is small compared to the principal/parent expression E_{nl}^{qh}, therefore, logically, we find the following:

$$exp\left(-\beta E_{nc-nl}^{nr-qh}\right) = exp\left(-\beta E_{nr}^{qh}\right) - \beta\Delta E(n,A,B,\alpha,\chi,\zeta,\Phi)\, exp\left(-\beta E_{nr}^{qh}\right), \quad (146)$$

which gives:

$$Z_{qh}^{nc}(n,A,B,\beta,l,\alpha_{max},\Phi,\beta,\zeta) = \int_0^{\alpha_{max}} exp\left(-\beta E_{nl}^{nr-qh}\right)\left(1 - \beta\Delta E(n,A,B,\alpha,\chi,\zeta,\Phi)\right) d\rho\ , \quad (147)$$

considering these approximations, especially Eq. (146). Therefore, it can be rewritten to a modified PF $Z_{qh}^{nc}(\beta, l, \alpha_{max})$ in Eq. (147), in the framework of deformation space-space as follows:

$$Z_{qh}^{nc}(n, A, B, \beta, l, \alpha_{max}, \Phi, \beta, \zeta) = Z_{qh}^{nr}(n, A, B, \beta, \lambda, l) - \langle Z_{qh}^{p} \rangle_{(nlm)}^{nr} \left[(\chi \aleph + \zeta \Omega) m + \Phi g_{f,b}^{nr} \right] Z_{qh}^{nr}(n, A, B, \beta, \lambda, l) \qquad (148)$$

If we set $l = 0$, the expectation values vanish, $\langle X_{qh}^{p}(r) \rangle_{(n0m)}^{nr} = 0$. Thus, the non-relativistic energy $E_{qh}^{nr-nc}(l = 0)$ in 3D-NR-NCQS symmetries will be identified with corresponding values E_{n0}^{nr} in the three-dimensional non-relativistic quantum mechanics that can be obtained from Eq. (143) as:

$$E_{qh}^{nr-nc}(l = 0) \equiv E_{n0}^{nr} = \delta - \frac{1}{2\mu} \left(\frac{\varphi}{n + \Xi_{hp}^{n0}} \right)^2 \qquad (149)$$

Here, Ξ_{hp}^{n0} is obtained from Eq. (144) as follows:

$$\Xi_{hp}^{n0} = \frac{1}{2} + \sqrt{\frac{1}{4} + 2\mu B} \qquad (150)$$

By comparing Eq. (149) with Eq. (17) of Ref. [12], which has the form $(\gamma - q \left(\frac{\Omega}{n+\sigma} \right)^2)$, we clearly discover the possibility of moving between the two equations through the following compatible transitions:

$$\begin{cases} \gamma \leftrightarrow \delta \\ \sigma \leftrightarrow \Xi_{hp}^{n0} \\ q \leftrightarrow \frac{1}{2\mu} \\ D_e \to 0 \end{cases} \qquad (151)$$

Thus, the partition functions $Z_{qh}^{nl}(\beta, \lambda, l = 0)$ of the IQHPM with $l = 0$ can be deduced directly from Eq. (21) in Ref. [12],

$$Z_{qh}^{nl}(n, A, B, \beta, \lambda, l = 0) = \sqrt{-\beta M_{qh}} \sqrt{\pi}\, erf \left(\frac{\sqrt{-\beta M_{qh}}}{\Xi_{hp}^{n0} + \alpha_{max}} \right) - \sqrt{-\beta M_{qh}} \sqrt{\pi}\, erf \left(\frac{\sqrt{-\beta M_{qh}}}{\Xi_{hp}^{n0}} \right) + \left(\Xi_{hp}^{n0} + \alpha_{max} \right) \times exp \left(\frac{-\beta M_{qh}}{\left(\Xi_{hp}^{n0} + \alpha_{max}{}^2 \right)} \right) - \Xi_{hp}^{n0}\, exp \left(\frac{-\beta M_{qh}}{\Xi_{hp}^{n02}} \right) \qquad (152)$$

with

$$M_{qh} = \frac{\varphi^2}{2\mu} = \frac{\mu}{2} (A + \alpha B)^2 \qquad (153)$$

Here, $erf \left(i \frac{\sqrt{\beta M_{qh}}}{\Xi_{hp}^{n0} + \alpha_{max}} \right)$ presents the imaginary error function. If we compare Eqs. (143) and (149), it is possible to find mutual mobility between them through $\Xi_{hp}^{n0} \leftrightarrow \Xi_{hp}^{nl}$. Thus, it is possible to obtain the PF $Z_{qh}^{nl}(\beta, \lambda, l)$ of the IQHPM with $l \neq 0$ from the expression $Z_{qh}^{nl}(\beta, \lambda, l = 0)$ in Eq. (152) without new calculations, in the framework of usual 3D-NRQM symmetry:

$$Z_{qh}^{nl}(n, A, B, \beta, \lambda, l) = \sqrt{-\beta M_{qh}} \sqrt{\pi}\, erf \left(\frac{\sqrt{-\beta M_{qh}}}{\Xi_{hp}^{nl} + \alpha_{max}} \right) - \sqrt{-\beta M_{qh}} \sqrt{\pi}\, erf \left(\frac{\sqrt{-\beta M_{qh}}}{\Xi_{hp}^{nl}} \right) + \left(\Xi_{hp}^{n} + \alpha_{max} \right) \times exp \left(\frac{-\beta M_{qh}}{\left(\Xi_{hp}^{nl} + \alpha_{max}{}^2 \right)} \right) + \left(\Xi_{hp}^{n} + \alpha_{max} \right) exp \left(\frac{-\beta M_{qh}}{\Xi_{hp}^{nl2}} \right) \qquad (154)$$

The impact of space deformation on thermodynamic values of the I-IQHPM, such as new mean energy $U_{nc}^{qh}(n, A, B, \beta, l, \Phi, \chi, \zeta)$, new free energy $F_{nc}^{qh}(n, A, B, \beta, l, \Phi, \chi, \zeta)$, and new entropy $S_{nc}^{qh}(n, A, B, \beta, l, \Phi, \chi, \zeta)$, can be obtained from the modified PF $Z_{qh}^{nc}(n, A, B, \beta, \alpha_{max})$ in Eq. (149). We begin with the influence of the space deformation on the new mean energy $U_{nc}^{qh}(n, A, B, \beta, l, \Phi, \chi, \zeta)$, which is the energy required to prepare or improve the system's internal condition. The impact of deformed space on mean energy $U(n, A, B, \beta, \lambda, l)$ for an I-IQHPM is obtained by applying the following formula:

$$\Delta U(n, A, B, \beta, l, \Phi, \chi, \zeta) \equiv U_{nc}^{qh}(n, A, B, \beta, l, \Phi, \chi, \zeta) - U_{qh}^{nl}(n, A, B, \beta, \lambda, l) = -\frac{\partial}{\partial \beta} \left(ln\, Z_{qh}^{nc}(n, A, B, \beta, l, \alpha_{max}) - ln\, Z_{qh}^{nl}(n, A, B, \beta, \lambda, l) \right) \qquad (155)$$

Thus, the effect of deformed space on mean energy under the I-IQHPM can be found through a straightforward calculation:

$$\Delta U_{nc}^{qh}(n, A, B, \beta, l, \Phi, \chi, \zeta) = \frac{\langle V_{nr-hp}^{pert} \rangle_{(nlm)}^{nr} \left[(\chi \aleph + \zeta \Omega) m + \Phi g_{f,b}^{nr} \right]}{1 - \beta \langle Z_{qh}^{p} \rangle_{(nlm)}^{nr} \left[(\chi \aleph + \zeta \Omega) m + \Phi g_{f,b}^{nr} \right]} \qquad (156)$$

Thus, in the context of deformed space symmetry, the new mean energy $U_{nc}^{qh}(n, A, B, \beta, l, \Phi, \chi, \zeta)$ for the I-IQHPM is equal to the corresponding values in the framework of the usual three-dimensional non-relativistic quantum mechanics symmetry $U_{qh}^{nl}(n,A,B,\beta,\lambda,l)$, plus the impact of deformed space on it, as follows:

$$U_{nc}^{qh}(n,A,B,\beta,l,\Phi,\chi,\zeta) = U_{qh}^{nl}(n,A,B,\beta,\lambda,l) + \frac{\left\langle V_{nr-hp}^{pert}\right\rangle_{(nlm)}^{nr}\left[(\chi\aleph+\zeta\Omega)m+\Phi g_{f,b}^{nr}\right]}{1-\beta\left\langle Z_{qh}^{p}\right\rangle_{(nlm)}^{nr}\left[(\chi\aleph+\zeta\Omega)m+\Phi g_{f,b}^{nr}\right]} \tag{157}$$

After a straightforward calculation, the mean energy $U_{qh}^{nl}(\beta,\lambda,l)$ for the inversely quadratic Hellmann potential model in 3D-NRQM symmetries can be obtained as:

$$U_{qh}^{nl}(n,A,B,\beta,\lambda,l) = -\frac{\partial\, lnZ_{qh}^{nr}(n,A,B,\beta,\lambda,l)}{\partial\beta} = \frac{-M_{qh}X}{W} \tag{158}$$

with

$$X = \frac{\sqrt{\pi}}{2\sqrt{y}}erf\Big(\frac{\sqrt{y}}{\varXi_{hp}^{nl}+\alpha_{max}}\Big)\frac{exp\left(\frac{-y}{\varXi_{hp}^{nl}+\alpha_{max}}\right)}{\varXi_{hp}^{nl}+\alpha_{max}} - \frac{\sqrt{\pi}}{2\sqrt{y}}erf\left(\frac{\sqrt{y}}{\varXi_{hp}^{nl}}\right) + \frac{exp\left(\frac{y}{\left(\varXi_{hp}^{nl}+\alpha_{max}{}^{2}\right)}\right)}{\left(\varXi_{hp}^{nl}+\alpha_{max}\right)} \tag{159}$$

and

$$W = \Big(\sqrt{y}\sqrt{\pi}\,erf\left(\frac{\sqrt{y}}{\varXi_{hp}^{nl}+\alpha_{max}}\right) - \sqrt{y}\sqrt{\pi}\,erf\left(\frac{\sqrt{y}}{\varXi_{hp}^{nl}}\right) + \big(\varXi_{hp}^{n} + \alpha_{max}\big)\,exp\left(\frac{y}{\left(\varXi_{hp}^{nl}+\alpha_{max}\right)}\right) - \varXi_{hp}^{n}\,exp\left(\frac{-y}{\varXi_{hp}^{nl2}}\right) \tag{160}$$

with $y = \sqrt{-\beta M_{qh}}$. The impact of deformed space on the free energy $F_{nc}^{qh}(n,A,B,\beta,\lambda,l)$ of the inversely quadratic Hellmann potential model is obtained by applying:

$$\begin{aligned}\Delta F_{nl}^{qh}(n,A,B,\beta,l,\lambda,\Phi,\chi,\zeta) &\equiv F_{nc}^{qh}(n,A,B,\beta,l,\Phi,\chi,\zeta) - \mathrm{F}_{nl}^{qh}(n,A,B,\beta,\lambda,l) \\ &= -\frac{1}{\beta}ln\,Z_{qh}^{nc}(n,A,B,\beta,l,\Phi,\chi,\zeta) - \left(-\frac{1}{\beta}\partial\, ln\,Z_{qh}^{nr}(n,A,B,\beta,\lambda,l)\right)\end{aligned} \tag{161}$$

A profound calculation gives the impact of deformed space on the free energy $\Delta F_{nc}^{qh}(n,A,B,\beta,l,\Phi,\chi,\zeta)$ of the I-IQHPM as:

$$\Delta F_{nl}^{qh}(\beta,l,\Phi,\chi,\zeta) \equiv -\frac{1}{\beta}ln\left[1-\beta\left\langle Z_{qh}^{p}\right\rangle_{(nlm)}^{nr}\left[(\chi\aleph+\zeta\Omega)m+\Phi g_{f,b}^{nr}\right]\right] \tag{162}$$

Thus, in the context of deformed space symmetry, the new free energy $F_{nc}^{qh}(n,A,B,\beta,l,\Phi,\chi,\zeta)$ of the I-IQHPM is equal to the corresponding values in the usual 3D-NRQM symmetry $F_{qh}^{nl}(n,A,B,\beta,\lambda,l)$, plus the impact of deformed space on it:

$$F_{nc}^{qh}(n,A,B,\beta,l,\Phi,\chi,\zeta) = F_{qh}^{nl}(n,A,B,\beta,\lambda,l) - -\frac{1}{\beta}ln\left[1-\beta\left\langle Z_{qh}^{p}\right\rangle_{(nlm)}^{nr}\left[(\chi\aleph+\zeta\Omega)m+\Phi g_{f,b}^{nr}\right]\right] \tag{163}$$

with

$$F_{qh}^{nl}(n,A,B,\beta,\lambda,l) = -\frac{1}{\beta}ln\Big(\sum_{\alpha=1}^{4}A_{\alpha}\Big) \tag{164}$$

and

$$A_1 = \sqrt{-\beta M_{qh}}\sqrt{\pi}\,erf\left(\frac{\sqrt{-\beta M_{qh}}}{\varXi_{hp}^{nl}+\alpha_{max}}\right)$$

$$A_2 = -\sqrt{-\beta M_{qh}}\sqrt{\pi}\,erf\left(\frac{\sqrt{-\beta M_{qh}}}{\varXi_{hp}^{nl}}\right)$$

$$A_3 = \left(\varXi_{hp}^{n} + \alpha_{max}\,exp\left(\frac{-\beta M_{qh}}{\left(\varXi_{hp}^{nl}+\alpha_{max}{}^{2}\right)}\right)\right)$$

$$A_4 = -\varXi_{hp}^{nl}\,exp\left(\frac{-\beta M_{qh}}{\varXi_{hp}^{nl2}}\right)$$

The impact of deformed space on the specific heat capacity $C_{nc}^{qh}(n,A,B,\beta,l,\Phi,\chi,\zeta)$ of the I-IQHPM is determined by using the following expression:

$$\begin{aligned}\Delta C_{nl}^{qh}(n,A,B,\beta,l,\Phi,\chi,\zeta) &\equiv C_{nc}^{qh}(n,A,B,\beta,l,\Phi,\chi,\zeta) - C_{nl}^{qh}(n,A,B,\beta,\lambda,l) \\ &= -k\beta^{2}\frac{\partial}{\partial\beta}\left(\Delta U_{nc}^{qh}(n,A,B,\beta,l,\Phi,\chi,\zeta)\right)\end{aligned} \tag{165}$$

After a straightforward calculation, it gives the impact of deformed space on the free energy

$\Delta C^{qh}_{nl}(n,A,B,\beta,l,\Phi,\chi,\zeta)$ under the impact of I-IQHPM as:

$$\Delta C^{qh}_{nl}(n,A,B,\beta,l,\Phi,\chi,\zeta)= -k\beta^2\frac{\left\langle Z^p_{qh}\right\rangle^{nr}_{(nlm)}\left[(\chi\aleph+\zeta\Omega)m+\Phi g^{nr}_{f,b}\right]^2}{exp\left(2\beta\left\langle Z^p_{qh}\right\rangle^{nr}_{(nlm)}\left[(\chi\aleph+\zeta\Omega)m+\Phi g^{nr}_{f,b}\right]\right)} \quad (166.1)$$

Thus, in the context of deformed space symmetry, the new mean energy $C^{qh}_{nc}(n,A,B,\beta,l,\Phi,\chi,\zeta)$ of the I-IQHPM is equal to the corresponding values in the usual 3D-NRQM symmetry $C^{nl}_{qh}(n,A,B,\beta,\lambda,l)$, plus the impact of deformed space on it:

$$C^{qh}_{nc}(n,A,B,\beta,l,\Phi,\chi,\zeta)=C^{nl}_{qh}(n,A,B,\beta,\lambda,l)- -k\beta^2\frac{\left\langle Z^p_{qh}\right\rangle^{nr}_{(nlm)}\left[(\chi\aleph+\zeta\Omega)m+\Phi g^{nr}_{f,b}\right]^2}{exp\left(2\beta\left\langle Z^p_{qh}\right\rangle^{nr}_{(nlm)}\left[(\chi\aleph+\zeta\Omega)m+\Phi g^{nr}_{f,b}\right]\right)} \quad (166.2)$$

The impact of deformed space $\Delta S^{qh}_{nc}(n,A,B,\beta,l,\Phi,\chi,\zeta)$ on the entropy $S^{qh}_{nc}(n,A,B,\beta,\lambda,l)$ is determined by applying the following formula:

$$\Delta S^{qh}_{nc}(n,A,B,\beta,l,\Phi,\chi,\zeta)\equiv S^{qh}_{nc}(n,A,B,\beta,l,\Phi,\chi,\zeta)- S^{qh}_{nl}(n,A,B,\beta,\lambda,l)= k\beta^2\frac{\partial}{\partial\beta}\left(\Delta F^{qh}_{nc}(n,A,B,\beta,l,\Phi,\chi,\zeta)\right) \quad (167)$$

After a straightforward calculation, the impact of deformed space on the entropy $\Delta S^{qh}_{nc}(n,A,B,\beta,l,\Phi,\chi,\zeta)$ of the I-IQHPM can be expressed as follows:

$$\Delta S^{qh}_{nc}(n,A,B,\beta,l,\Phi,\chi,\zeta)\equiv k\beta\frac{\left\langle Z^p_{qh}\right\rangle^{nr}_{(nlm)}\left[(\chi\aleph+\zeta\Omega)m+\Phi g^{nr}_{f,b}\right]}{1-\beta\left\langle Z^p_{qh}\right\rangle^{nr}_{(nlm)}\left[(\chi\aleph+\zeta\Omega)m+\Phi g^{nr}_{f,b}\right]} \quad (168)$$

Thus, in 3D-NR(NCQS) symmetries, the new entropy $S^{qh}_{nc}(n,A,B,\beta,l,\Phi,\chi,\zeta)$ of the I-IQHPM is equal to the values $S^{nl}_{qh}(n,A,B,\beta,\lambda,l)$ in the context of 3D-NRQM symmetry, plus the impact of deformed space on the I-IQHPM in Eq. (168), as follows:

$$S^{qh}_{nc}(n,A,B,\beta,l,\Phi,\chi,\zeta)=S^{nl}_{qh}(n,A,B,\beta,\lambda,l)+ k\beta\frac{\left\langle V^p_{hp}\right\rangle^{nr}_{(nlm)}\left[(\chi\aleph+\zeta\Omega)m+\Phi g^{nr}_{f,b}\right]}{1-\beta\left\langle Z^p_{qh}\right\rangle^{nr}_{(nlm)}\left[(\chi\aleph+\zeta\Omega)m+\Phi g^{nr}_{f,b}\right]} \quad (169)$$

with

$$S^{nl}_{qh}(n,A,B,\beta,\lambda,l)=k\ln Z^{nr}_{qh}(n,A,B,\beta,\lambda,l)- k\beta\frac{\partial\ln Z^{nr}_{qh}(n,A,B,\beta,\lambda,l)}{\beta} \quad (170)$$

If the space deformation effect vanishes when the simultaneous limits $(\Phi,\chi,\zeta)\to(0,0,0)$ are satisfied, the additive thermodynamic parts $\Delta Z^{qh}_{nl}(n,A,B,\beta,l,\Phi,\chi,\zeta)$, $\Delta U^{qh}_{nl}(n,A,B,\beta,l,\Phi,\chi,\zeta)$, $\Delta F^{qh}_{nl}(n,A,B,\beta,l,\Phi,\chi,\zeta)$, $\Delta S^{qh}_{nl}(n,A,B,\beta,l,\Phi,\chi,\zeta)$ and $\Delta C^{qh}_{nl}(n,A,B,\beta,l,\Phi,\chi,\zeta)$ also vanish, and the following results are achieved:

$$\lim_{(\Phi,\chi,\zeta)\to(0,0,0)}\Delta Z^{qh}_{nl}(n,A,B,\beta,l,\Phi,\chi,\zeta)=0\Leftrightarrow \lim_{(\Phi,\chi,\zeta)\to(0,0,0)}Z^{qh}_{nc}(n,A,B,\beta,l,\Phi,\chi,\zeta)= Z^{qh}_{nl}(n,A,B,\beta,\lambda,l), \quad (171)$$

$$\lim_{(\Phi,\chi,\zeta)\to(0,0,0)}\Delta U^{qh}_{nl}(n,A,B,\beta,l,\Phi,\chi,\zeta)=0\Leftrightarrow \lim_{(\Phi,\chi,\zeta)\to(0,0,0)}U^{qh}_{nc}(n,A,B,\beta,l,\Phi,\chi,\zeta)= U^{qh}_{nl}(n,A,B,\beta,\lambda,l), \quad (172)$$

$$\lim_{(\Phi,\chi,\zeta)\to(0,0,0)}\Delta F^{qh}_{nl}(n,A,B,\beta,l,\Phi,\chi,\zeta)=0\Leftrightarrow \lim_{(\Phi,\chi,\zeta)\to(0,0,0)}F^{qh}_{nc}(n,A,B,\beta,l,\Phi,\chi,\zeta)= F^{qh}_{nl}(n,A,B,\beta,\lambda,l), \quad (173)$$

$$\lim_{(\Phi,\chi,\zeta)\to(0,0,0)}\Delta S^{qh}_{nl}(n,A,B,\beta,l,\Phi,\chi,\zeta)=0\Leftrightarrow \lim_{(\Phi,\chi,\zeta)\to(0,0,0)}S^{qh}_{nc}(n,A,B,\beta,l,\Phi,\chi,\zeta)= S^{qh}_{nl}(n,A,B,\beta,\lambda,l), \quad (174)$$

and

$$\lim_{(\Phi,\chi,\zeta)\to(0,0,0)}\Delta C^{qh}_{nl}(n,A,B,\beta,l,\Phi,\chi,\zeta)=0\Leftrightarrow \lim_{(\Phi,\chi,\zeta)\to(0,0,0)}C^{qh}_{nc}(n,A,B,\beta,l,\Phi,\chi,\zeta)= C^{qh}_{nl}(n,A,B,\beta,\lambda,l). \quad (175)$$

We end this section by searching for special cases of importance by applying the same data that we included in the fourth paragraph of our current research.

- In the case of $B=\alpha=0$, one obtains the new PF $Z^{cp}_{nc}(n,A,\beta,l,\Phi,\chi,\zeta)$, mean energy $U^{cp}_{nc}(n,A,\beta,l,\Phi,\chi,\zeta)$, free new energy $F^{cp}_{nc}(n,A,\beta,l,\Phi,\chi,\zeta)$, the new entropy $S^{cp}_{nc}(n,A,\beta,l,\Phi,\chi,\zeta)$, and specific new heat capacity $C^{cp}_{nc}(n,A,\beta,l,\Phi,\chi,\zeta)$. Equations (148), (157), (163), (166.1), and (167) under the new modified Coulomb potential in 3D-(R and NR)-

NCQS symmetries are expressed as:

$$Z_{nc}^{cp}(n,A,\beta,l,\Phi,\chi,\zeta)=\lim_{(B,\alpha)\to(0,0)} Z_{nc}^{qh}(n,A,B,\beta,l,\Phi,\chi,\zeta), \quad (176)$$

$$U_{nc}^{cp}(n,A,\beta,l,\Phi,\chi,\zeta)=\lim_{(B,\alpha)\to(0,0)} U_{nc}^{qh}(n,A,B,\beta,l,\Phi,\chi,\zeta), \quad (177)$$

$$F_{nc}^{cp}(n,A,\beta,l,\Phi,\chi,\zeta)=\lim_{(B,\alpha)\to(0,0)} F_{nc}^{qh}(n,A,B,\beta,l,\Phi,\chi,\zeta), \quad (178)$$

$$S_{nc}^{cp}(n,A,\beta,l,\Phi,\chi,\zeta)=\lim_{(B,\alpha)\to(0,0)} S_{nc}^{qh}(n,A,B,\beta,l,\Phi,\chi,\zeta), \quad (179)$$

and

$$C_{nc}^{cp}(n,A,\beta,l,\Phi,\chi,\zeta)=\lim_{(B,\alpha)\to(0,0)} C(n,A,B,\beta,l,\Phi,\chi,\zeta). \quad (180)$$

- In the case of $A=0$, we can get the new PF $Z_{nc}^{iqy}(n,B,\beta,l,\Phi,\chi,\zeta)$, mean energy $U_{nc}^{iqy}(n,B,\beta,l,\Phi,\chi,\zeta)$, free new energy $F_{nc}^{iqy}(n,B,\beta,l,\Phi,\chi,\zeta)$, the new entropy $S_{nc}^{iqy}(n,B,\beta,l,\Phi,\chi,\zeta)$, and specific new heat capacity $C_{nc}^{iqy}(n,\mathrm{B},\beta,l,\Phi,\chi,\zeta)$. These quantities follow from Eqs. (148), (157), (163), (166.1), and (167) under the modified IQYP, in 3D-(R and NR)-NCQS symmetries as:

$$Z_{nc}^{iqy}(n,B,\beta,l,\Phi,\chi,\zeta)=\lim_{A\to 0} Z_{nc}^{qh}(n,A,B,\beta,l,\Phi,\chi,\zeta), \quad (181)$$

$$U_{nc}^{iqy}(n,A,\beta,l,\Phi,\chi,\zeta)=\lim_{A\to 0} U_{nc}^{qh}(n,A,B,\beta,l,\Phi,\chi,\zeta), \quad (182)$$

$$F_{nc}^{iqy}(n,A,\beta,l,\Phi,\chi,\zeta)=\lim_{A\to 0} F_{nc}^{qh}(n,A,B,\beta,l,\Phi,\chi,\zeta), \quad (183)$$

$$S_{nc}^{iqy}(n,A,\beta,l,\Phi,\chi,\zeta)=\lim_{A\to 0} S_{nc}^{qh}(n,A,B,\beta,l,\Phi,\chi,\zeta), \quad (184)$$

and

$$C_{nc}^{iqy}(n,A,\beta,l,\Phi,\chi,\zeta)=\lim_{A\to 0} C(n,A,B,\beta,l,\Phi,\chi,\zeta). \quad (185)$$

Physically, this means that we obtain the values of the TPs in the three-dimensional non-relativistic quantum mechanics symmetry when the three limits $(\Phi,\chi,\zeta)\to(0,0,0)$ are applied simultaneously.

7. Conclusion

In the present work, we have considered the 3D-RQM and 3D-NRQM mechanical implications of a non-commutative geometric model in which the parameters of the non-commutativity are constants. We solved the deformed relativistic wave equations (both 3D-DKGE and 3D-DDE) and 3D-DSE for the I-IQHPM. We obtained new analytical expressions for its energy eigen solutions in the framework of deformation space-space symmetry using the well-known Bopp's shift method and independent time standard perturbation theory. The new relativistic energy eigenvalues appear to be sensitive to quantum numbers $(n,j,l,s\ and\ m)$, mixed potential depths (A and B), the screening parameter α, and non-commutativity parameters (Φ, β and ζ). Furthermore, different special cases of the improved inversely quadratic Hellmann potential model have been obtained by changing the potential's parameters, including a new modified Coulomb potential and a new inversely quadratic Yukawa potential. We investigated the spin-averaged mass spectra of heavy mesons under the I-IQHPM in 3D-NRQM and 3D-NR(NCQS) symmetries, the spin-averaged mass spectra M_{nl}^{qh-hm} in 3D-NR(NCQS), equal to the spin-averaged mass spectra M_{nl}^{qh-hm} of heavy mesons ($c\bar{c}$ and $b\bar{b}$) in 3D-NRQM symmetries, plus the effect of deformation space-space δM_{nc-nl}^{my-hm}, as given in Eq. (137). We also analyzed the effect of space deformation on thermodynamic quantities, including the induced PF $\Delta Z_{nl}^{qh}(n,A,B,\beta,l,\Phi,\chi,\zeta)$, the generated mean energy $\Delta U_{nl}^{qh}(n,A,B,\beta,l,\Phi,\chi,\zeta)$, the induced free energy $\Delta F_{nl}^{qh}(n,A,B,\beta,l,\Phi,\chi,\zeta)$, the generated entropy $\Delta S_{nl}^{qh}(n,A,B,\beta,l,\Phi,\chi,\zeta)$, and the induced specific heat capacity $\Delta C_{nl}^{qh}(n,A,B,\beta,l,\Phi,\chi,\zeta)$. We have shown that the corresponding new thermodynamic quantities in 3D-NR-NCQS symmetries (the new PF $Z_{nc}^{qh}(n,A,B,\beta,l,\Phi,\chi,\zeta)$, mean energy $U_{nc}^{qh}(n,A,B,\beta,l,\Phi,\chi,\zeta)$, free energy $F_{nc}^{qh}(n,A,B,\beta,l,\Phi,\chi,\zeta)$, entropy $S_{nc}^{qh}(\beta,l,\Phi,\chi,\zeta)$, and specific heat capacity $C_{nc}^{qh}(n,A,B,\beta,l,\Phi,\chi,\zeta)$), for the I-IQHPM are equal to their values in the literature (the new PF$Z_{qh}^{nl}(n,A,B,\beta,\lambda,l)$, the mean energy

$U_{qh}^{nl}(n,A,B,\beta,\lambda,l)$, the free energy $F_{qh}^{nl}(n,A,B,\beta,\lambda,l)$, the entropy $S_{qh}^{nl}(\beta,\lambda,l)$, and specific heat capacity $C_{qh}^{nl}(\beta,\lambda,l)$) plus the effect of the deformation of space-space($\Delta Z_{nl}^{qh}(n,A,B,\beta,l,\Phi,\chi,\zeta)$, $\Delta U_{nl}^{qh}(n,A,B,\beta,l,\Phi,\chi,\zeta)$, $\Delta F_{nl}^{qh}(n,A,B,\beta,l,\Phi,\chi,\zeta)$, $\Delta S_{nl}^{qh}(n,A,B,\beta,l,\Phi,\chi,\zeta)$, and $\Delta C_{nl}^{qh}(n,A,B,\beta,l,\Phi,\chi,\zeta)$, respectively). It is worth noting that we recovered the energy equations for the KGE, DE, and SE in the framework of three-dimensional relativistic quantum mechanics and three-dimensional non-relativistic quantum mechanics symmetries for the three simultaneous limits $(\Phi,\chi,\zeta)\rightarrow(0,0,0)$. Physically, this means that we obtained the values of the relativistic and non-relativistic energy of bosonic and fermionic particles with high and low energies, or the TPs observed in previous studies [10-13, 20], within the framework of relativistic and non-relativistic quantum mechanics known in the literature. This new formulation provides a fresh look at relativistic and non-relativistic quantum mechanics based on 3D-KGE, 3D-DE, and 3D-SE under I-IQHPM in non-commutative space and inspires some innovative mathematical structures.

This research was supported by the Research Fund of the LPCM at the University of M'sila and by the Algerian DGRSDT. We are grateful to the anonymous reviewers for their insightful comments and recommendations, which helped us significantly improve this work.

Reference

[1] Snyder, H.S., Phys. Rev., 71 (1947) 38.

[2] Zeng, X.X., Aslam, M.I., and Saleem, R., Phys. J. C, 83 (2023) 129.

[3] Rayimbaev, J., Bokhari, A.H., and Ahmedov, B., Class. Quantum Grav., 39 (2022) 075021.

[4] Baruah, A., Goswami, P., and Deshamukhya, A., New Astron., 99 (2023) 101956.

[5] Maireche, A., Mol. Phys., 121 (16) (2023) e2225649.

[6] Maireche, A., Mol. Phys., 121 (13) (2023) e2205968.

[7] Maireche, A., Indian J. Phys., 97 (2023) 519.

[8] Maireche, A., Rev. Mex. Fís., 69 (2023) 030801.

[9] Turkoglu, A., Dakhlaoui, H., Durmuslar, A.S., Mora-Ramos, M.E., and Ungan, F.A.T.İ.H., Eur. Phys. J. B, 94 (2021) 111.

[10] Njoku, I.J., Onyenegecha, and Okereke, C.J., Chin. J. Phys., 79 (2022) 436.

[11] Njoku, I.J., Onyenegecha, C.P., Okereke, C.J., Nwaokafor, P., and Abara, C.C., Phys. Open, 15 (2023) 100152.

[12] Onyenegecha, C.P., El Anouz, K., Opara, A.I., Njoku, I.J., Okereke, C.J., and El Allati, A., Heliyon J., 7 (2021) e08617.

[13] Ghanbari, A., Opt. Quantum Electron., 55 (2023) 222.

[14] Chang, C., Li, X., Duan, Y., and Zhao, Z., Indian J. Phys., 97 (2023) 1465.

[15] Ituen, A.D.A.E.E., and Ntekim, E.B.U.V.N., Adv. Phys. Theor. Appl., 61 (2017) 1.

[16] Hitler, L., Ita, B.I., Isa, P.A., Nelson, N.I., Oseph, I.J., Ivan, O., and Magu, T.O., World J. Appl. Phys., 2017 (2017) 109.

[17] Ita, I., Int. J. Recent Adv. Phys., 2 (2013) 25.

[18] Ita, B.I. and Ikeuba, A.I., J. At. Mol. Phys., 2013 (2013) 582610.

[19] Chang, C., Li, X., and Zhuang, J., Fundam. Appl., 51 (2022) 101029.

[20] Máthé, L., Onyenegecha, C., Farcaş, A., Pioraş-Ţimbolmaş, L., Solaimani, M., and Hassanabadi, H., Phys. Lett. A, 397 (2021) 127262.

[21] Connes, A., J. High Energ. Phys., 02 (1998) 003.

[22] Hassanabadi, H., Hosseini, S.S., and Zarrinkamar, S., Int. J. Theor. Phys., 54 (2015) 251.

[23] Giri, S., Eur. Phys. J. Plus, 137 (2022) 181.

[24] Zeng, X.X., Eur. Phys. J. C, 83 (2023) 129.

[25] Trampetić, J. and You, Phys. J. Rev. D, 105 (7) (2022) 075016.

[26] Kan, N., Aoyama, T., and Shiraishi, K., Class. Quantum Grav., 40 (1) (2022) 015010.

[27] Connes, A., Nucl. Phys. Proc. Suppl., 18B (1991) 29.

[28] Connes, A., "Non-commutative Geometry", P. Academic, (Springer, 1994).

[29] Connes, A., J. Math. Phys., 36 (11) (1995) 6194.

[30] Seiberg, N. and Witten, E., J. High Energ. Phys., 1999 (09) (1999) 32.

[31] Maireche, A., J. Nanosci. Curr. Res., 2 (3) (2017) 115.

[32] Maireche, A., Ukr. J. Phys., 65 (11) (2020) 987.

[33] Maireche, A., To Phys. J., 5 (2020) 51.

[34] Maireche, A., Rev. Mex. Fís., 68 (2) (2022) 020801-1.

[35] Maireche, A., Mod. Phys. Lett. A, 36 (33) (2021) 2150232.

[36] Maireche, A., Ukr. J. Phys., 67 (7) (2022) 485.

[37] Kurkov, M. and Vitale, P., J. High Energ. Phys., 2022 (2022) 32.

[38] Gnatenko, K.P. and Tkachuk, V.M., Mod. Phys. Lett. A, 31 (5) (2016) 1650026.

[39] Maireche, A., Jordan J. Phys., 16 (1) (2023) 31.

[40] Terashima, S., Phys. Lett. B, 482 (1-3) (2000) 276.

[41] Maireche, A., Ukr. J. Phys., 67 (3) (2022) 183.

[42] Darroodi, M., Mehraban, H., and Hassanabadi, H., Mod. Phys. Lett. A, 33 (35) (2018) 1850203.

[43] N'Dolo, E.E., Samary, D.O., Ezinvi, B., and Ounkonnou, M.N., Int. J. Geom. Methods Mod. Phys., 17 (05) (2020) 2050078.

[44] Maireche, A., Int. J. Geom. Methods Mod. Phys., 19 (06) (2022) 2250085.

[45] Gnatenko, K.P. and Tkachuk, V.M., Int. J. Mod. Phys. A, 33 (07) (2018) 1850037.

[46] Maireche, A., Few-Body Syst., 63 (2022) 63.

[47] Aghababaei, S. and Rezaei, G., Commun. Theor. Phys., 72 (2020) 125101.

[48] Maireche, A., Rev. Mex. Fís. 68 (5) (2022) 050702-1.

[49] Maireche, A., Rev. Mex. Fís., 69 (3) (2023) 030801.

[50] Gouba, L., Int. J. Mod. Phys. A, 31 (19) (2016) 1630025.

[51] Alhaidari, D., Bahlouli, H., and Al-Hasan, A., Phys. Lett. A, 349 (1-4) (2006) 87.

[52] Aschieri, P. and Castellani, L., Eur. Phys. J. Spec. Top., 232 (2023) 3733.

[53] Connes, A., Cuntz, J., Rieffel, M.A., and Yu, G., Oberwolfach Rep., 10 (3) (2013) 2553.

[54] Ho, P.M., Kao, H.C., Phys. Rev. Lett., 88 (15) (2002) 151602.

[55] Dalabeeh, M.A., J. Phys. A: Math. Gen., 38 (7) (2005) 1553.

[56] Motavalli, H. and Akbarieh, A.R., Mod. Phys. Lett. A, 25 (29) (2010) 2523.

[57] Mirza, B. and Mohadesi, M., Commun. Theor. Phys. (Beijing, China), 42 (2004) 664.

[58] Bopp, F., Ann. Inst. Henri Poincaré, 15 (2) (1956) 81.

[59] Mezincescu, L., "Star Operation in Quantum Mechanics", (https://arxiv.org/abs/hep-th/0007046) (2000)

[60] Gamboa, J., Loewe, M., and Rojas, J.C., Phys. Rev. D, 64 (2001) 067901.

[61] Curtright, T., Fairlie, D., and Zachos, C., Phys. Rev. D, 58 (1998) 025002.

[62] Santos, J.F.G., J. Mater. Phys., 61 (12) (2020) 122101.

[63] Harko, T. and Liang, S.D., Eur. Phys. J. C, 79 (2019) 300.

[64] Solimanian, M., Naji, J., and Ghasemian, K., Eur. Phys. J. Plus, 137 (2022) 331.

[65] Luo, Y.Q., Cui, Y., Long, Z.W., *et al.*, Int. J. Theor. Phys., 50 (2011) 2992.

[66] Bernardini, A.E. and Bertolami, O., Phys. Lett. B, 835 (2022) 137549.

[67] Mustafa, G., Hassan, Z., and Sahoo, P., Ann. Phys., 437 (1) (2022) 68751.

[68] Gnatenko, K.P. and Shyiko, O.V., Mod. Phys. Lett. A, 33 (16) (2018) 1850091.

[69] Wang, J. and Li, K., J. Phys. A Math. Theor., 40 (9) (2007) 2197.

[70] Maireche, A., Few-Body Syst., 63 (2022) 54.

[71] Maireche, A., Few-Body Syst., 62 (2021) 66.

[72] Maireche, A., J. Phys. Stud., 25 (4) (2021) 4301.

[73] Maireche, A., East Eur. J. Phys., 2022 (4) (2022) 200.

[74] Maireche, A., Bulg. J. Phys., 50 (1) (2023) 054.

[75] Maireche, A., Int. J. Geom. Meth. Mod. Phys., 18 (13) (2021) 2150214.

[76] Maireche, A., Indian J. Phys., 97 (2023) 3567.

[77] Maireche, A., YJES, 19 (2) (2022) 78.

[78] Abyaneh, M.Z. and Farhoudi, M., Eur. Phys. J. Plus, 136 (2021) 863.

[79] Dąbrowski, L. and D'Andrea, F., Lett. Math. Phys., 108 (2018) 1323.

[80] Derakhshani, Z. and Ghominejad, M., Chin. J. Phys., 54 (5) (2016) 761.

[81] Maireche, A., Int. J. Geom. Meth. Mod. Phys., 20 (10) (2023) 2350162.

[82] Cuzinatto, R.R., De Montigny, M., and Pompeia, P.J., Class. Quantum Grav., 39 (2022) 075007.

[83] Aounallah, H. and Boumali, A., Phys. Part. Nucl. Lett., 16 (2019) 195.

[84] Saidi, A. and Sedra, M.B., Mod. Phys. Lett. A, 35 (5) (2020) 2050014.

[85] Chargui, Y. and Dhahbi, A., Eur. Phys. J. Plus, 138 (2023) 26.

[86] Gradshteyn, I.S., Ryzhik, I.M., Jeffrey, A., and Zwillinger, D., "Table of Integrals, Series and Products", (Elsevier Academic Press, 2007).

[87] Medjedel, S. and Bencheikh, K., Phys. Lett. A, 383 (2019) 1915.

[88] Maireche, A., Few-Body Syst., 62 (2021) 12.

[89] Dong, S.H., J. Phys. A: Math. Gen., 36 (2003) 4977.

[90] Gu, X.Y., Ma, Z.Q., and Dong, S.H., Int. J. Mod. Phys. E, 11 (2002) 335.

[91] Maireche, A., J. Nano-Electron. Phys., 10 (2018) 06015.

[92] Maireche, A., Int. Lett. Chem. Phys. Astron., 73 (2017) 31.

[93] Maireche, A., Spin J., 11 (4) (2021) 2150029.

[94] Hamzavi, M., Ikhdair, S.M., and Ita, B.I., Phys. Scr., 85 (2012) 045009.

[95] Ikot, A.N., Maghsoodi, E., Zarrinkamar, S., and Hassanabadi, H., Few-Body Syst., 54 (2013) 2027.

[96] Maireche, A., J. Nano-Electron. Phys., 9 (2017) 02017.

[97] Inyang, E.P., Iwuji, P.C., Ntibi, J.E., Omugbe, E., Ibanga, E.A., and William, E.S., East Eur. J. Phys., 2022 (2) (2022) 43.

[98] Kumar, V. and Singh, R.M., Mod. Phys. Lett. A, 37 (2022) 2250010.

[99] Abu-Shady, M., Abdel-Karim, T.A., and Ezz-Alarab, S.Y., J. Egypt. Math. Soc., 27 (2019) 14.

[100] Rani, R. and Bhardwaj, S.B., Chand. Commun. Theor. Phys., 70 (2018) 179.

[101] Jia, S., Wang, C.W., Zhang, L.H., Peng, X.L., Zeng, R., and You, X.T., Chem. Phys. Lett., 676 (2017) 150.

[102] Song, X.Q., Wang, C.W., and Jia, C.S., Chem. Phys. Lett., 673 (2017) 50.

[103] Onyenegecha, P., Oguzie, E.E., Njoku, I.J., Omame, A., Okereke, C.J., and Ukewuihe, U.M., Eur. Phys. J. Plus, 136 (2021) 1153.

Volume 18, Number 3, 2025. pp. 301-308

Jordan Journal of Physics

ARTICLE

Exploring the Density, Viscosity and Physico-chemical Characteristics of Dextran in Aqueous Glycine: An Ultrasonic Analysis

Niharika Das[a,b] and **Subhraraj Panda**[b]

[a] *Research Scholar, Department of Physics.*

[b] *Centurion University of Technology and Management, Odisha, India.*

Doi: **https://doi.org/10.47011/18.3.4**

Received on: 30/11/2023; *Accepted on: 17/04/2024*

Abstract: The density (ρ), viscosity (η), and ultrasonic speed (U) of the systems of dextran with glycine in the aqueous medium were measured at 30, 35, 40, 45, and 50 ^{0}C. Ultrasonic interferometers were used to measure the ultrasonic speed at four distinct frequencies: 1, 5, 9, and 12 MHz. The acoustic parameters, namely, free volume, internal pressure, absorption coefficient, Rao's constant, and Wada's constant, were calculated using the measured density (ρ), viscosity (η), and ultrasonic speed (U). The variations of these parameters with temperature and frequency provided insights into molecular mobility, distinct types of intermolecular interactions, and the strength of solute–solvent interactions between dextran (0.5%) and glycine (2M). The findings regarding a structural reorganisation in the aqueous dextran solution were explained. The solute-solvent interactions were more significant across all temperatures used for the investigation. Changes in acoustic properties were minimal with frequency variation, suggesting that rapid molecular motion limits intermolecular interactions. This analysis provides detailed information regarding liquid solutions' physical and chemical behavior.

Keywords: Dextran, Glycine, Ultrasonic speed, Density, Viscosity, Acoustic parameters.

1. Introduction

Liquids can be studied using ultrasound to understand their physicochemical characteristics better. Ultrasonic measurements are frequently used to examine the molecular interactions in pure liquids, liquid mixtures, and ionic interactions in solutions containing single or mixed solutes [1-4]. Industrial and technological processes use the research of the solution properties of liquid mixtures that have polar and non-polar components. The thermodynamic characteristics and intermolecular interactions of binary mixtures are widely estimated via ultrasonic research. One of the physical characteristics that aids in comprehending the nature of the liquid state is the sound velocity. The thermodynamic characteristics such as free volume (V_f), internal pressure (P_i), absorption coefficient or attenuation coefficient (α), Rao's constant (R), and Wada's constant (W) can be calculated using the measured values of sound velocity (u), density (ρ), and viscosity(η) [5-7].

These deduced characteristics provide an easy way to examine liquid mixtures' thermodynamic properties, which is impossible with other approaches. When paired with other water resources, ultrasonic research is widely employed to study molecular interactions. Extensive research has focused on molecular interactions in various product forms and mixtures [8-10]. It is crucial to the advancement of molecular research. Due to its capacity to highlight the physicochemical behavior of the medium, ultrasonic technology has recently proven to be an invaluable tool for investigating the behavior of liquids and solids [11-13]. Nondestructive testing (NDT) typically utilizes

Corresponding Author: Subhraraj Panda **Email**: subhraraj4u@gmail.com

it. NDT allows the assessment of material properties without causing any damage. This method uses a variety of business and scientific analyses to look into qualities without doing any harm. Common NDT methods include eddy current testing, low coherence interferometry, magnetic particle testing, radiography, and ultrasonic testing. Information on the structural and molecular alterations in liquid mixtures can be significantly increased using ultrasound techniques [14-18]. These techniques also offer helpful details regarding the mixing solution and its temperature dependency within the context of the theory of physical acoustics [19-22]. The ultrasonic speed technique is a fascinating and valuable method for examining the physicochemical characteristics of liquids, electrolytic solutions, and polymeric solutions [23-25].

The medical, pharmaceutical, leather, textile, chemical, and solvent solutions sectors all use these solutions extensively. For their applications in these industries, the study, comprehension, and analysis of the thermodynamic properties of mixtures and liquid solutions are crucial [26-27]. A critical test to determine a substance's qualities is how well ultrasonic waves penetrate it. Variations in temperature and concentration help understand the structure and the numerous connections of bound molecular complexes and other relevant molecular processes. Using the velocity and associated acoustic parameters, we can characterize the thermodynamic, physical, and chemical properties of liquid mixtures, such as molecule association and dissociation [28-30]. In the present study, an effort has been made to examine how dextran (0.5%) interacts with a 2M glycine solution. At five different temperatures between 303 and 323 K and frequencies between 1 and 12 MHz, we have calculated acoustic characteristics such as V_f, P_i, α, R, and W. The only polysaccharide that is water-soluble is dextran. Many businesses, particularly the pharmaceutical industry, use dextran and its derivatives [31-35].

The organic molecule glycine has the chemical formula HO2CCH2NH2. Glycine is commonly used in our body's biological processes and is used by the body to produce proteins. Given the significance of dextran and glycine, a thorough investigation of dextran and glycine has been conducted in this study.

Continuing from our earlier research, we now combine glycine and dextran at room temperature. We have taken further efforts to effectively consider the physicochemical behavior of dextran at varying temperatures in glycine. Understanding thermal behavior, phase transitions, rheological properties, reaction kinetics, and processing aspects of polymer solutions under different thermal conditions is critical for various industrial and scientific applications involving polymers.

2. Materials and Methods

Materials

Dextran with a molecular weight of 70,000 Da (Hi-Media) was used at a concentration of 0.5% in freshly distilled water. Glycine (2M, Fisher Scientific) was used as the solvent. Both materials were of analytical reagent (AR) grade and were used without further purification [36–37].

Measurements

(a) *Ultrasonic velocity (U)*: Ultrasonic velocity measurements were conducted using an ultrasonic interferometer (Model M-84, M/SMittal Enterprises, New Delhi) at temperatures ranging from 30 to 50°C. Measurements were performed at four frequencies (1, 5, 9, and 12 MHz) with an accuracy of ±0.056% m.s-1.

The ultrasonic velocity in the medium was calculated based on the wavelength (λ) using the interferometer [20-21]. Measurements were made with a temperature accuracy of 0.1 K. The ultrasonic velocity was calculated as:

$$\lambda = \frac{2d}{n} \quad \text{or} \quad U = f.\lambda = \frac{2fd}{n}$$

where n is the number of anode current maxima (or minima) over a distance d, which is the total movement of the micrometer screw for a maximum or minimum deflection. f is the ultrasonic frequency.

(b) *Density (ρ)*: The density of the solution was measured using a 10 mL pycnometer [36–37] with a precision of 0.0001 kg m^{-3}. Measurements were averaged over three trials. The density was calculated as:

$$\rho_2 = \frac{w_2}{w_1}\rho_1$$

where w_1 and w_2 denote the weights of distilled water and the solution, respectively, and ρ_1 and

ρ_2 denote the densities of distilled water and the solution.

(c) *Viscosity measurement*: An Ostwald viscometer [36-37], standardized with distilled water, was used. The viscosity measurement is precise to 0.001 mN s m^{-2}. The viscosities of the solution were calculated.

The η was calculated using the standard equation:

$$\eta_2 = \eta_1 \left(\frac{t_2}{t_1}\right)\left(\frac{\rho_2}{\rho_1}\right)$$

where η_1 and η_2 are the distilled water and solution viscosities, and t_1 and t_2 are the respective flow times of water and the solution.

3. Theoretical Aspect

The acoustic and thermodynamic characteristics listed below were calculated as follows [38-39]:

Free volume: $V_f = \left(\frac{M_{eff}U}{K\eta}\right)^{\frac{3}{2}}$

Internal pressure: $P_i = bRT\left(\frac{k\eta}{U}\right)^{3/2}\left(\frac{\rho^{2/3}}{M_{eff}^{7/6}}\right)$

Attenuation coefficient: $\propto = \frac{8\pi^2\eta f^2}{3\rho U^3}$

Rao’s constant: $R = \frac{M_{eff}}{\rho} U^{1/3}$

Wada’s constant: $W = \frac{M_{eff}}{\rho} \beta^{-1/7}$

where M_{eff} is the effective molecular weight of the solution ($M_{eff} = \Sigma miXi$, where mi and Xi are the molecular weight and mole fraction of solute and solvent), b = 2 for all liquids, $k = 4.281 \times 10^9$, f is the frequency of the medium's ultrasonic wave, and β is the adiabatic compressibility.

4. Results and Discussion

The ρ and η of dextran in glycine at temperatures 303, 308, 313, 318, and 323 K are presented in Table 1.

TABLE 1. ρ and η.

T in kelvin	(ρ) Kg.m^{-3}	(η) 10^{-3} N.s.m^{-2}
303	1055.482	1.129
308	1054.261	1.023
313	1052.431	0.955
318	1050.006	0.902
323	1045.998	0.831

TABLE 2. U and V_f.

T in kelvin	U m.s^{-1}				V_f (10^{-3}m^3·mol^{-1})			
	Frequency in MHz				Frequency in MHz			
	1	5	9	12	1	5	9	12
303	1613.000	1605.750	1602.450	1600.000	6.098	6.057	6.039	6.025
308	1622.000	1615.500	1612.350	1610.000	7.131	7.089	7.068	7.052
313	1628.000	1621.250	1620.000	1616.000	7.951	7.902	7.893	7.863
318	1632.267	1627.250	1624.950	1622.400	8.696	8.656	8.638	8.617
323	1635.000	1630.750	1629.000	1627.200	9.856	9.817	9.801	9.785

TABLE 3. P_i and α.

T in kelvin	P_i (10^3 N·m^{-2})				α (10^6(np·m^{-1})			
	Frequency in MHz				Frequency in MHz			
	1	5	9	12	1	5	9	12
303	132.70	133.00	133.14	133.24	6.371	159.474	525.297	929.054
308	127.93	128.19	128.32	128.41	5.469	137.043	450.199	792.583
313	125.24	125.50	125.54	125.70	5.019	126.729	413.838	733.980
318	123.30	123.49	123.58	123.68	4.593	116.440	381.718	673.582
323	119.82	119.98	120.04	120.11	4.173	105.410	343.526	609.527

TABLE 4. R and W.

T in kelvin	R (m^{3}mole^{-1})(m s^{-1})$^{1/3}$(10^{-3})				W (m^{3}mole^{-1})(N m^{-2})$^{1/7}$(10^{-3})			
	Frequency in MHz				Frequency in MHz			
	1	5	9	12	1	5	9	12
303	1.111	1.109	1.109	1.108	2.113	2.110	2.109	2.108
308	1.114	1.113	1.112	1.112	2.119	2.116	2.115	2.114
313	1.118	1.116	1.116	1.115	2.124	2.122	2.121	2.120
318	1.121	1.120	1.120	1.119	2.130	2.128	2.127	2.126
323	1.126	1.125	1.125	1.124	2.138	2.136	2.136	2.135

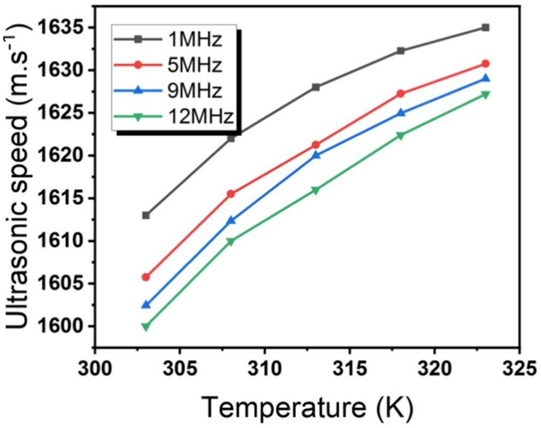

FIG. 1. Ultrasonic speed vs temperature.

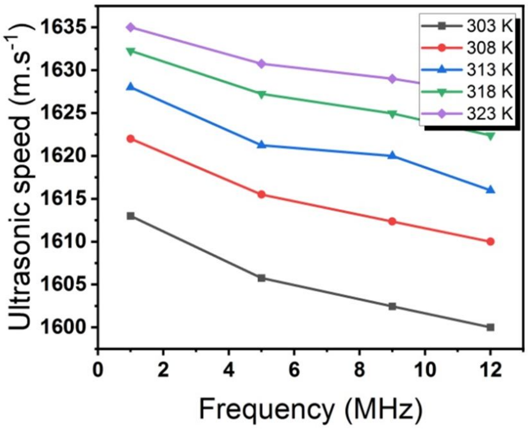

FIG. 2. Velocity vs frequency.

It has been found that when the temperature rises, ultrasonic velocity increases (Fig. 1). Ultrasonic velocity is found to increase with temperature at a specific frequency and to progressively decrease at frequencies between 5 and 9 MHz. This is because the polymer solution's structural alterations cause the intermolecular tensions to diminish. A drop in velocity like this suggests that there is a weak molecular interaction happening between the solvent and the liquid. When the frequency is low (1 MHz), however, the situation is the opposite. It shows structural readjustment, adding glycine to the polymer solution, which causes association in the component [40]. The association results from persistent dipoles in the water molecules, which induce dipoles. For temperature, ultrasonic velocity falls with increasing frequency due to increased agitation between molecules, which decreases speed at a higher frequency [41]; such a decrease in speed is a sign of a frail molecular connection between the molecules making up the solute and solvent. (Fig. 2).

The speed changes more with temperature for glycine compared to water. This suggests that there are more parts in a certain area, making the medium more packed and strengthening the interactions between dextran and glycine compared to water. The viscosity changes with temperature and the amount of solute in both water and glycine. Molecular forces, like hydrogen bonds and charge transfer complexes, play a role in this. Intermolecular forces, which are weak forces between charged particles, are present in water and glycine.

At a constant concentration of liquid components, free volume ($V_f \alpha U^{3/2}$) increases with temperature because molecular velocity increases. It is observed that free volume increases (Fig. 3) and internal pressure decreases (Fig. 5) with an increase in the temperature of the solution. As expected, the solute and solvent molecules' constituent parts display the opposite trend from the internal pressure [42-44], pointing to a tenuous chemical link. That indicates that free volume is increasing because the molecules arrange themselves so that void space is more accessible. With increased temperature, internal pressure drops as the molecules' attraction forces weaken. As the molecules' intermolecular attraction wanes, internal pressure drops. Figs. 4 and 6 demonstrate that the free volume and internal pressure frequency exhibit minimal variation as the frequency increases, aligning with the frequency axis. This indicates that the free volume and internal pressure remain relatively constant with increasing frequency. At lower frequencies, these characteristics enable the waves to interact with a greater number of molecules by penetrating deeper into the solutions.

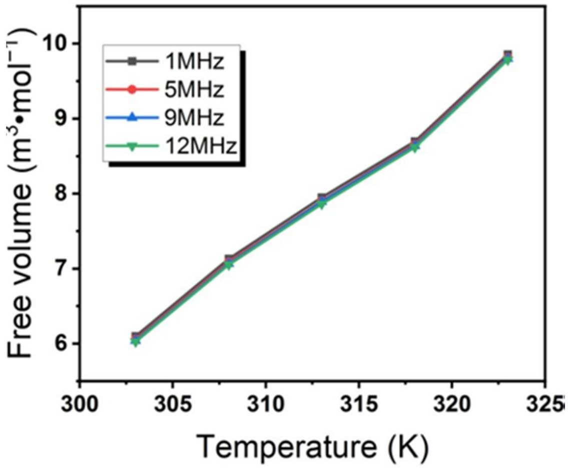

FIG. 3. Free volume vs temperature.

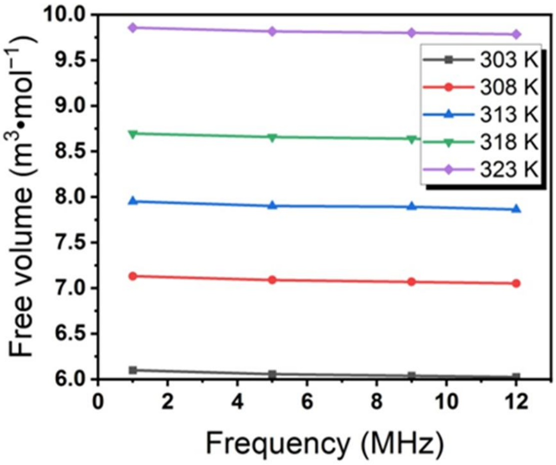

FIG. 4. Free volume vs frequency.

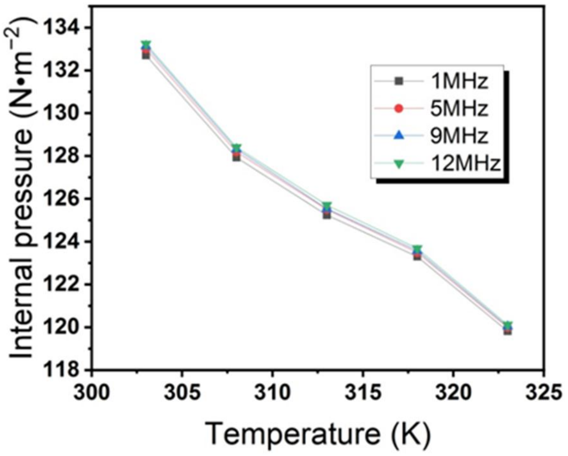

FIG. 5. Internal pressure vs temperature

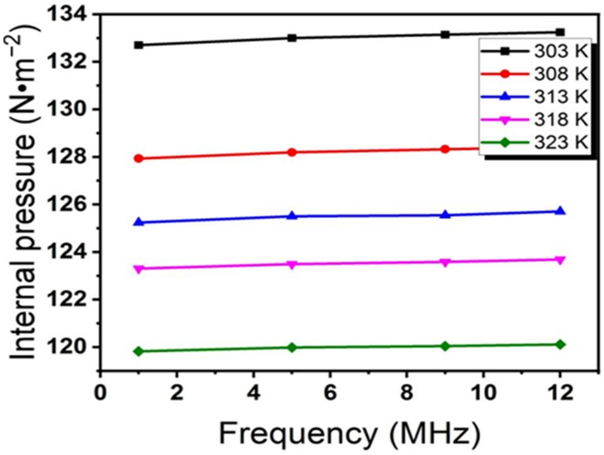

FIG. 6. Internal pressure vs frequency

Low-frequency ultrasound induces molecular rearrangements, increasing the free volume of the solutions. Conversely, it constrains the number of molecules that the waves may engage with at high frequencies by restricting their ability to penetrate deeply into the solutions. Thus, in comparison to low frequencies, high-frequency ultrasonic waves may exert a lesser impact on the available space for movement. Utilizing low-frequency ultrasound can induce cavitation in a material, wherein the oscillating pressure of the waves leads to the formation of tiny cavities or bubbles filled with vapor. The localized pressure waves generated upon the bursting of these bubbles might lead to an increase in the internal pressure of the material. The influence of cavitation is most evident in liquids and polymer solutions, where it can enhance the process of mixing, promote chemical reactions, or facilitate the dispersion of particles. At higher frequencies, ultrasonic waves have shorter wavelengths, which leads to less joint cavitation. This, in turn, causes localized pressure fluctuations owing to the fluid motion induced by the waves. Despite being less in magnitude compared to cavitation-induced pressure changes at low frequencies [45-49], these pressure fluctuations can still occur.

The absorption coefficient at lower frequencies (1 and 5 MHz) is parallel to the temperature axis, showing no effect from temperature, and it steadily declines at higher temperatures, suggesting that the molecules are arranged so that more void space is available, indicating an increase in free volume. The absorption coefficient proliferates as frequency rises since it is inversely related to the square of frequency [50-53].

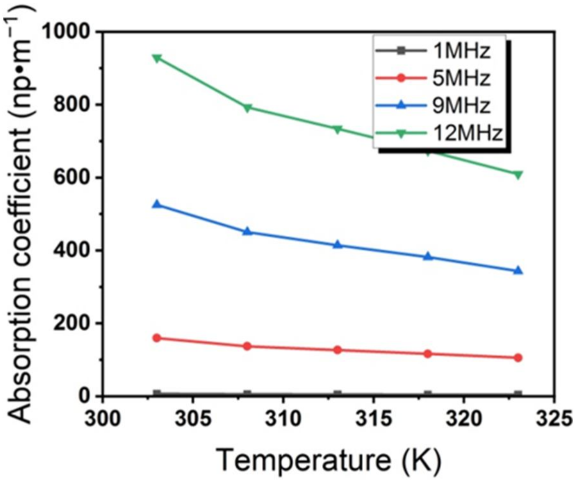

FIG. 7. Absorption coefficient vs temperature.

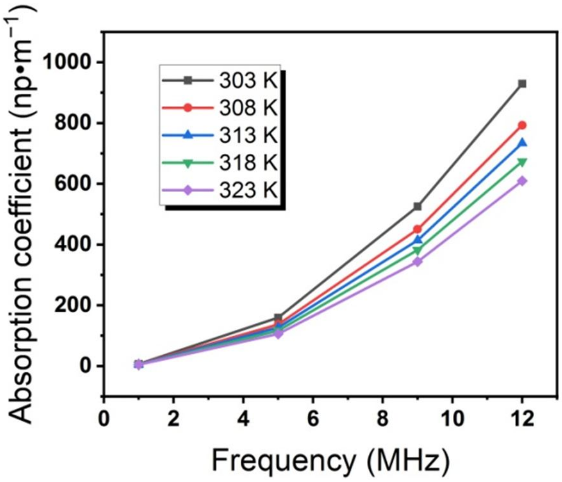

FIG. 8. Absorption coefficient vs frequency.

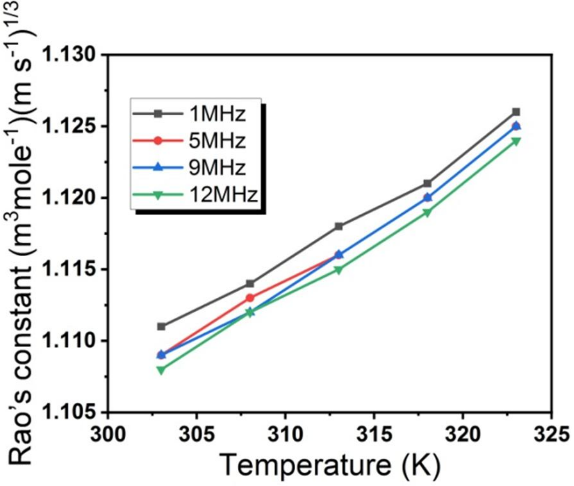

FIG. 9. Rao's constant vs temperature.

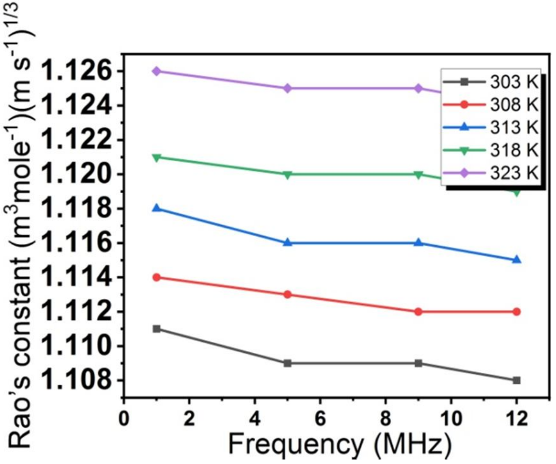

FIG. 10. Rao's constant vs frequency.

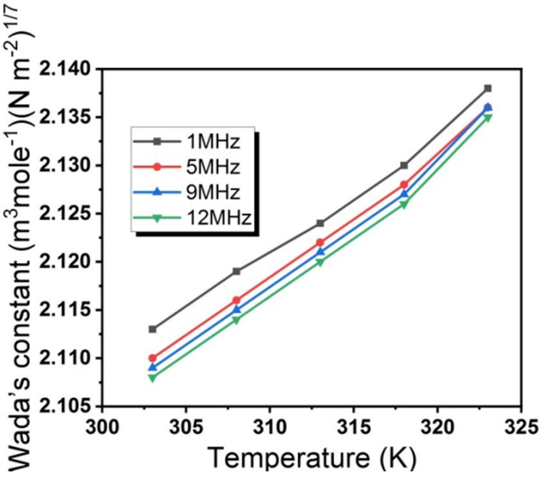

FIG. 11. Wada's constant vs temperature.

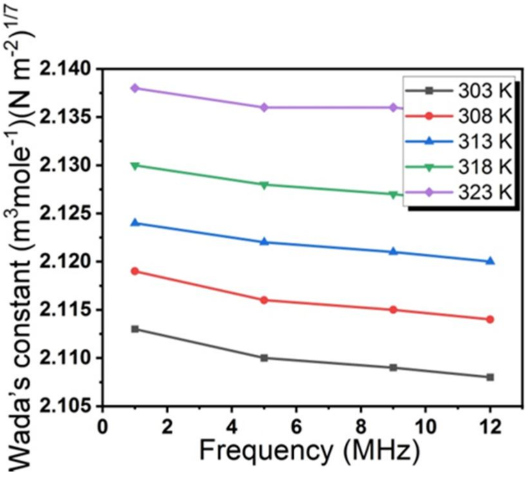

FIG. 12. Wada's constant vs frequency.

Rao's constant (R) and Wada's constant (W) increase with increasing temperature (Figs. 9 and 11), demonstrating the interaction between the molecules of the solvent and the solute. Figures 10 and 12 show that the variation of "R" and "W" with frequency is practically parallel to the frequency axis, showing a relatively tiny change in "R" and "W" with increasing frequency [54-62].

5. Conclusion

The acoustic properties of dextran in 2M glycine solution were examined at varying temperatures and frequencies. The molecules travel quickly and have little time to communicate as the frequency rises, so there is little change in the auditory characteristics. The findings demonstrate that the particular solute-solvent interactions are crucial in explaining how acoustic characteristics change with temperature.

Acknowledgment

The authors gratefully acknowledge the support of the staff of the Department of Physics, ABIT, Cuttack, for their assistance.

References

[1] Alisha, S.B., Subha, M.C.S., and Rao, K.C., J. Pure Appl. Ultrason., 23 (1/2) (2001) 26.

[2] Prabakar, S. and Rajagopal, K., J. Pure Appl. Ultrason., 27 (2/3) (2005) 41.

[3] Panda, S., Curr. Mater. Sci., 16 (2) (2023) 217.

[4] Ali, A., Nain, A.K., and Kamil, M., Thermochim. Acta, 274 (1996) 209.

[5] Srilalitha, S., Subha, M.C.S., and Chowdoji Rao, K., J. Pure Appl. Ultrason., 18 (1996) 59.

[6] Wankhade, S. and Kene, S., Sci. Rev. Chem. Commun., 2 (3) (2012) 355.

[7] Panda, S., Asia-Pac. J. Sci. Technol., 27 (6) (2022) 1.

[8] Jyothirmai, G., Nayeem, S.M., Khan, I., and Anjaneyulu, C., J. Therm. Anal. Calorim., 132 (1) (2018) 693

[9] Aswale, S., Aswale, S., and Ramteke, B., Int. J. Chem. Environ. Pharm. Res., 3 (1) (2012) 58.

[10] Panda, S., Songklanakarin J. Sci. Technol., 44 (4) (2022) 1125.

[11] Saxena, I., Kumar, V., and Gupta, A., J. Solution Chem., 2023 (2023) 1.

[12] Nikam, P.S., Hasan, M., and Pathak, R.B., J. Pure Appl. Ultrason, 18 (1996) 19.

[13] Panda, S., Curr. Microwave Chem., 9 (1) (2022) 30.

[14] Shrivastava, B., Mishra, A., and Phadke, S., Trans. Tech. Publications Ltd, 312 (2011) 358.

[15] Smirnova, A., Konoplev, G., Mukhin, N., Stepanova, O., and Steinmann, U., J. Compos. Sci., 4 (4) (2020) 151.

[16] George, T., Paul, J., and Pukkunnen, E.B., Ann. Rom. Soc. Cell Biol., 2021 (2021) 8912.

[17] Kalimulla, T., Babu, S., Das, D., Gowrisankar, M., and Rao, K.G., J. Pharm. Sci. Res., 11 (7) (2019) 2645.

[18] Panda, S. Curr. Microwave Chem., 10 (2) (2023) 237.

[19] Idoux, J.P., McCurry, C.K., and Aminabhavi, T.M., J. Chem. Eng. Data, 39 (1994) 261.

[20] Lagemann, R.T. and Dunbar, W.S., J. Phys. Chem., 49 (5) (1945) 428.

[21] Suryanarayana, C.V. and Pugazhendhi, P., Indian J. Pure Appl. Phys., 24 (1986) 406.

[22] Panda, S., Bulg. J. Phys., 49 (2) (2022) 136.

[23] Tabhane, P.V., Chimankar, O.P., and Tabhane, V.A., J. Chem. Pharm. Res., 4 (6) (2012) 3051.

[24] Rajulu, A.V., Sreenivasulu, G., and Raghuraman, K.S., Indian J. Chem. Technol., 1 (1994) 302.

[25] Panda, S., Recent Innov. Chem. Eng., 15 (2) (2022) 138.

[26] Patnaik, P., Chakraborty, N., Kaur, P., Juglan, K.C., and Kumar, H., Int. Adv. Funct. Smart Mater., 2022 (2022) 403.

[27] Kaur, K. and Juglan, K.C., Der Pharma Chem., 7 (2) (2015) 160.

[28] Tiwari, S., Kusmariya, B.S., Tiwari, A., Pathak, V., and Mishra, A.P., J. Taibah Univ. Sci., 11 (1) (2017) 101.

[29] Sharma, A.K., Sharma, R., and Gangwal, A., Curr. Phys. Chem., 8 (3) (2018) 222.

[30] Panda, S., Indian J. Pharma. Educ. Res., 54 (3) (2020) 630.

[31] Gil, E.C., Colarte, A.I., El Ghzaoui, A., Durand, D., Delarbre, J.L., and Bataille, B., Eur. J. Pharm. Biopharm., 68 (2008) 319.

[32] Jeanes, A., Haynes, W.C., Wilham, C.A., Rankin, J.C., Melvin, E.H., Austin, M.J., Cluskey, J.E., Fisher, B.E., Tsuchiya, H.M., and Rist, C.E., J. Am. Chem. Soc., 76 (20) (1954) 5041.

[33] Arond, L.H. and Frank, H.P., J. Phys. Chem., 58 (11) (1954) 953.

[34] Barshtein, G., Tamir, I., and Yedgar, S., Eur. Biophys. J., 27 (1998) 177.

[35] Pribush, A., Zilberman-Kravits, D., and Meyerstein, N., Eur. Biophys. J., 36 (2007) 85.

[36] Panda, S. and Mahapatra, A.P., J. Pure Appl. Ultrason., 39 (2017) 83.

[37] Panda, S., Indian J. Nat. Sci., 10 (59) (2020) 18436.

[38] Panda, S. and Mahapatra, A.P., Clay Res., 38 (1) (2019) 35.

[39] Panda, S. and Mahapatra, A.P., Int. J. Innov. Technol. Explor. Eng., 8 (11) (2019) 742.

[40] Alisha, S.B., Banu, S.N., Rao, K.K., Subha, M.C.S., and Rao, K.C., Indian J. Adv. Chem. Sci., 5 (3) (2017) 148.

[41] Pal, A., Kumar, H., Kumar, B., and Gaba, R., J. Mol. Liq., 187 (2013) 278.

[42] Singla, M., Jindal, R., and Kumar, H., Thermochim. Acta, 591 (2014) 140.

[43] Panda, S. and Mahapatra, A.P., World J. Pharm. Life Sci., 4 (12) (2018) 76.

[44] Panda, S. and Mahapatra, A.P., J. Pure Appl. Ultrason., 40 (2018) 100.

[45] Magotra, U., Sandarve, G.V., and Sharma, M., J. Chem. Pharm. Res., 6 (6) (2014) 809.

[46] Shankarwar, A.G., Shelke, V.A., and Shankarwar, S.G., Adv. Appl. Sci. Res., 2 (2011) 426.

[47] Panda, S. and Mahapatra, A.P., Int. J. Pure Appl. Phys., 12 (1) (2016) 71.

[48] Khanuja, P., Chourey, V.R., and Ansari, A.A., J. Chem. Pharm. Res., 4 (6) (2012) 3047.

[49] Parmar, M.L. and Thakur, R.C., J. Mol. Liq., 128 (1-3) (2006).

[50] Panda, S. and Mahapatra, A.P., Int. J. Chem. Phys. Sci., 5 (5) (2016) 15.

[51] Sinha, B., Roy, P.K., and Roy, M.N., Acta Chim. Slov., 57 (2010) 651.

[52] Khanuja, P., Chem. Sci. Trans., 2 (4) (2013) 1268.

[53] Pal, A. and Kumar, A., Indian J. Chem., 62 (2023) 735.

[54] Panda, S. and Mahapatra, A.P., Int. J. Sci. Res., 22 (2015) 503.

[55] Singh, G., Patyar, P., Kaur, T., and Kaur, G., J. Mol. Liq., 222 (2016) 804.

[56] Ramasami, P. and Kakkar, R., J. Chem. Thermodyn., 38 (11) (2006) 1385.

[57] Ali, K.F. and Hummadi, H.H., Al-Nahrain J. Sci., 10 (1) (2007) 13.

[58] Kant, S.H.A.S.H.I. and Sharma, K.A.M.I.N.I., Chem. Sci. Trans., 2 (2013) 911.

[59] Panda, S. and Mahapatra, A.P., Library Arch. Phys. Res., 6 (1) (2015) 6.

[60] Sarkar, A. and Sinha, B., J. Serb. Chem. Soc., 78 (8) (2013) 1225.

[61] Tiwari, V. and Pande, R., Thermochim. Acta, 443 (2) (2006) 206.

[62] Panda, S., Rom. J. Biophys., 33 (3) (2023) 105.

Volume 18, Number 3, 2025. pp. 309-317

Jordan Journal of Physics

ARTICLE

Optimization of the Third Electrode Design in Electrostatic Einzel Lenses

Alaa A. H. Ahmad[a], **Abdullah I. M. Alabdullah**[a] and
Mohammed A. Hussein[b]

[a] *Department of physics, College of Sciences, University of Mosul, Mosul, Iraq.*
[b] *College of Education for Women, University of Kirkuk, Kirkuk, Iraq.*

Doi: **https://doi.org/10.47011/18.3.5**
Received on: 10/01/2024; Accepted on: 22/07/2024

Abstract: In this study, we designed an electrostatic Einzel lens with three electrodes. The two electrodes at each end were set to the ground potential, while a positive potential was applied to the central electrode. We explored the impact of changing the geometry of the third electrode on the trajectory of paraxial electron beams and the two-dimensional emittance. Notably, altering the outer diameter of the third electrode while keeping other parameters constant had a clear effect on the equipotential surface. This modification improved the electric potential and electric field distribution within the lens, resulting in enhancements in beam emittance of approximately 73% and a reduction in the cross-over radius of the paraxial trajectory by 27%. Moreover, we introduced a cylindrical shape for the third electrode, acting as a cover for the first and second electrodes. Investigating its length revealed further enhancements in the path of the paraxial beam of electrons by 37% and reduced beam emittance by 76%. These findings highlight the importance of optimizing the third electrode's design to achieve superior performance in charged particle optics applications. The study demonstrates the potential of employing novel geometries and configurations to enhance the overall efficiency of electrostatic Einzel lenses.

Keywords: Electrostatic lenses, Einzel lens, Ion beam focusing, Particle optics, Third electrode, Outer radius, Length.

1. Introduction

Electrostatic lenses are used for various purposes, as acceleration of both electron and ion rays. The theoretical framework for electrostatic lenses was developed between 1930 and 1955. In many instances, the ion optics featuring electrostatic lenses is commonly referred to as electron optics. These electrostatic lenses have a substantial impact on the design of low-energy electrostatic accelerators, such as the Cockcroft–Walton and Van de Graaff accelerators, which are widely used for preparing low-energy electron and ion beams for experiments involving the scattering of particles. Some storage rings have been created with exclusive use of electrostatic deflection and focusing devices [1]. Another significant application of the electrostatic lens is in the design of a hemispherical energy analyzer, a device intended to examine the kinetic energy of electrons across different energy levels. Energy analyzers are one of the most important and most used electrostatic analyzers at the present time [2]. The geometry of the electrodes is critical to the performance of electrostatic lenses, as it directly affects the electron beam diameter at the image plane and enables precise control of beam

Corresponding Author: Alaa A. H. Ahmad **Email**: alaahakeim@uomosul.edu.iq

acceleration and deceleration. The electrostatic lens is essential to the development of cutting-edge technologies in various fields, including electron and ion beam systems, particle accelerators, and advanced microscopy [3]. Electrostatic lenses are also employed in compound lenses (magnetic-electric), which enhance optical performance and increase the resolving power of objective lenses in scanning transmission electron microscopes (STEM) [4].

An Einzel lens, also known as a unipotential lens, is an electrostatic lens for charged particles, designed to focus the particles while preserving their initial energy. It comprises a series of three or more cylindrical or rectangular apertures, or tubes, arranged in line with a central axis. In ion optics, the purpose of the Einzel lens is to focus ions in flight by manipulating the electric field along their path [5]. The symmetry of the electrostatic potential inside the lens ensures that the particles (electrons and ions) maintain their initial energy upon exiting the lens. However, the velocity of outer particles is adjusted in a manner that leads them to converge toward the axis, resulting in a slight delay in their arrival at the focal point compared to particles traveling along a straight path [6]. This phenomenon can be observed in Fig. 1.

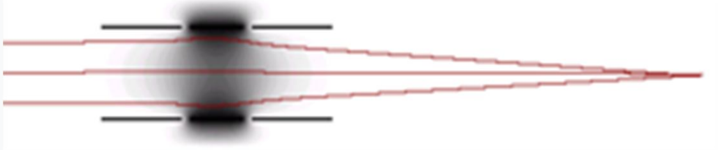

FIG. 1. A perspective view of an Einzel lens.

The formula describing the alteration in radial velocity for a particle as it transitions between any two cylinders within the lens is as follows:

$$\Delta v_r = \int \frac{G E_r(r,z)}{M v_z} dz \tag{1}$$

Here, the z-axis runs through the center of the lens, and (r) represents the direction perpendicular to the z-axis. In the case when the lens is constructed using cylindrical electrodes, the electric field is uniform and symmetrical with respect to the z-axis. E_r (r, z) represents the radial component of the electric field, M denotes the mass of the particle traveling through the field, v_r is the particle's velocity, and G is its charge. The integral is computed over the region between the polepieces, which is where the focusing effects of the lens occur. The dual poles (or plates) function as an electrostatic immersion lens, and as a result, an Einzel lens can be described as two or more such electrostatic immersion lenses combined. To select the focal length of the lens, one can apply Eq. (1) twice for each set of poles (plates) [7].

The concept of the beam emittance parameter has been introduced as a key parameter for evaluating beam quality. Emittance, similar to brightness, represents a characteristic of electron beams that offers important information about their propagation characteristics [8]:

$$r'' = \frac{\varepsilon^2}{r^3} = \frac{\varepsilon_n^2}{\gamma^2 \beta^2 r^3} \tag{2}$$

where $\mathcal{E}$ is the emittance, β is the beam brightness, and γ is the transport parameter.

Beams exhibiting random variations in their transverse velocities display a divergence in angle concerning the propagation axis. This angular spread places constraints on the ability to effectively focus such beams. So, emittance is a gauge of a beam's parallelism and the evaluation of beam quality for various applications. [9].

The current research seeks to discover the optimal genesis for an electrostatic Einzel lens that improves the electron beam path and emittance. In this inquiry, we have taken significant strides in designing a variety of electrostatic lenses with remarkable performance enhancements. This study explores key parameters, including the outer diameter, length of the third electrode, and the electron path within the third electrode. Significant improvements were achieved, including reduced beam emittance and a minimized cross-over radius of the paraxial trajectory.

In this study, the suggested lens was designed using SIMION 8.0 software. Calculation included the axial field, potential distribution, equipotential lines, and a LUA program to identify the trajectory of the electron beam and emittance parameters. SIMION 8.0 is mainly used to calculate electric fields based on electrode formations with specified voltages, as well as to simulate the trajectories of charged particles under various conditions, including RF effects, magnetic fields, and collisions. More details about this software can be found in the printed SIMION manual, additional electronic literature, and various resources available on the SIMION.com website. To our knowledge, no earlier research has investigated the effect of third electrode geometry on the transmittance of the electron beam and the cross-over radius of the paraxial trajectory using SIMION simulations.

2. Geometrical Design and Calculation Procedure

A key requirement for ES lenses is that they operate within a well-maintained vacuum environment to minimize the risk of electrical discharge and system failure. In the past, personnel adopted a numerical computer program that utilized the electrode geometry in either rectangular or cylindrical coordinates to calculate electric potential and field distribution. In this study, the proposed lens was designed using SIMION8. The computations included the axial field, potential distribution, and equipotential lines. A LUA program was used to determine the trajectory of the electron beam and emittance parameters [10]. Figure 2 shows the design of the Einzel lens, which comprises three electrodes. Two electrodes have both a potential of V_1=0 volts, and the central electrode has a potential of V_2=10 volts. The first and second electrodes have identical dimensions (10 x 3 mm), and the third electrode has dimensions of 3 × 3 mm.

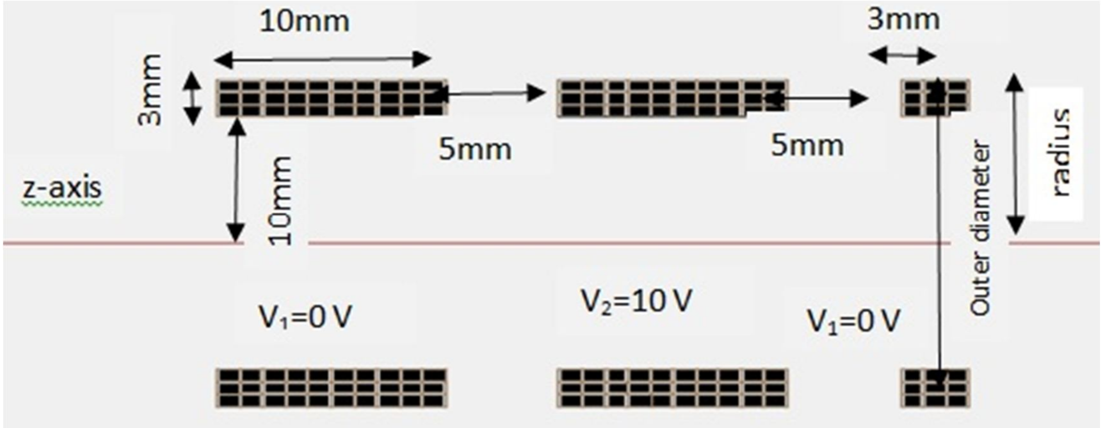

FIG. 2. Cross-sectional representation displaying the configuration and size proportions of a tripolar Einzel lens.

The axial electric field distribution is simulated after creating the electrode geometry and completing the electrical configuration of the lens. The Laplace equation is solved to determine the potential values and establish the boundary conditions, following Gauss's theorem as described by the equation:

$$\nabla.\vec{E} = 0 \tag{3}$$

The axial electric field distribution is calculated using numerical techniques, specifically the finite difference method (FDM). This entails selecting the electric field values through Poisson's equation and calculating the electron beam paths (r) using Lorentz's and Maxwell's equations [11]:

$$\nabla.E = \frac{\sigma}{\varepsilon_o} \tag{4}$$

$$\vec{F} = G(\vec{E} + V \times \vec{B}) \tag{5}$$

where E is the electric field, σ is the charge density, ε_o is the vacuum permittivity, and B is the magnetic field (set to 0).

Electrostatic fields are treated as solutions to the boundary value problem of Laplace's equation using FDM within SIMION 8.0. The trajectory of the electron beam and the emittance parameters are then computed using a LUA program that employs the Monte Carlo numerical method [12].

The structured steps for optimizing the third electrode are organized as follows:

2.1 Effect of Increasing the Outer Diameter of the Third Electrode

Figure 3 depicts the distribution of equipotential surfaces within the lens. The figure shows how these surfaces change as the outer radius of the third electrode varies (R = 13, 16, 19, 22, 25, and 28 mm). Increasing the diameter of the third electrode (iron material = 18 mm) reduces flux leakage from the lens toward the electron beam exit, compared to a smaller electrode diameter (iron material = 3 mm). This contrast results in a growing intensity of the flux lines within the lens as R increases. This, in turn, leads to a special behavior of the electron beam within the lens, ultimately impacting the path and emittance of the electron beam. This characteristic will serve as a conclusive factor in determining the additional optical properties of the Einzel lens [7]. Figure 4 shows a contrast between the axial electric field and the distribution of electric potential, calculated for different outer radius values of the third electrode (R) as a function of the z-axis. This graph illustrates the axial field distribution of an Einzel lens, where the middle electrode has a higher voltage than the two outer electrodes. Notably, the potential distribution V(z) stays constant at the boundaries, and the electric field E (z), given by the first derivative $V'(z)$, where $E = -\nabla V$, is zero. This observation suggests the absence of an electric field outside the lens, creating a region without a field that spans from the lens terminals. In this region, the trajectory of charged particle beams remains straight due to the absence of any external forces acting upon them [13].

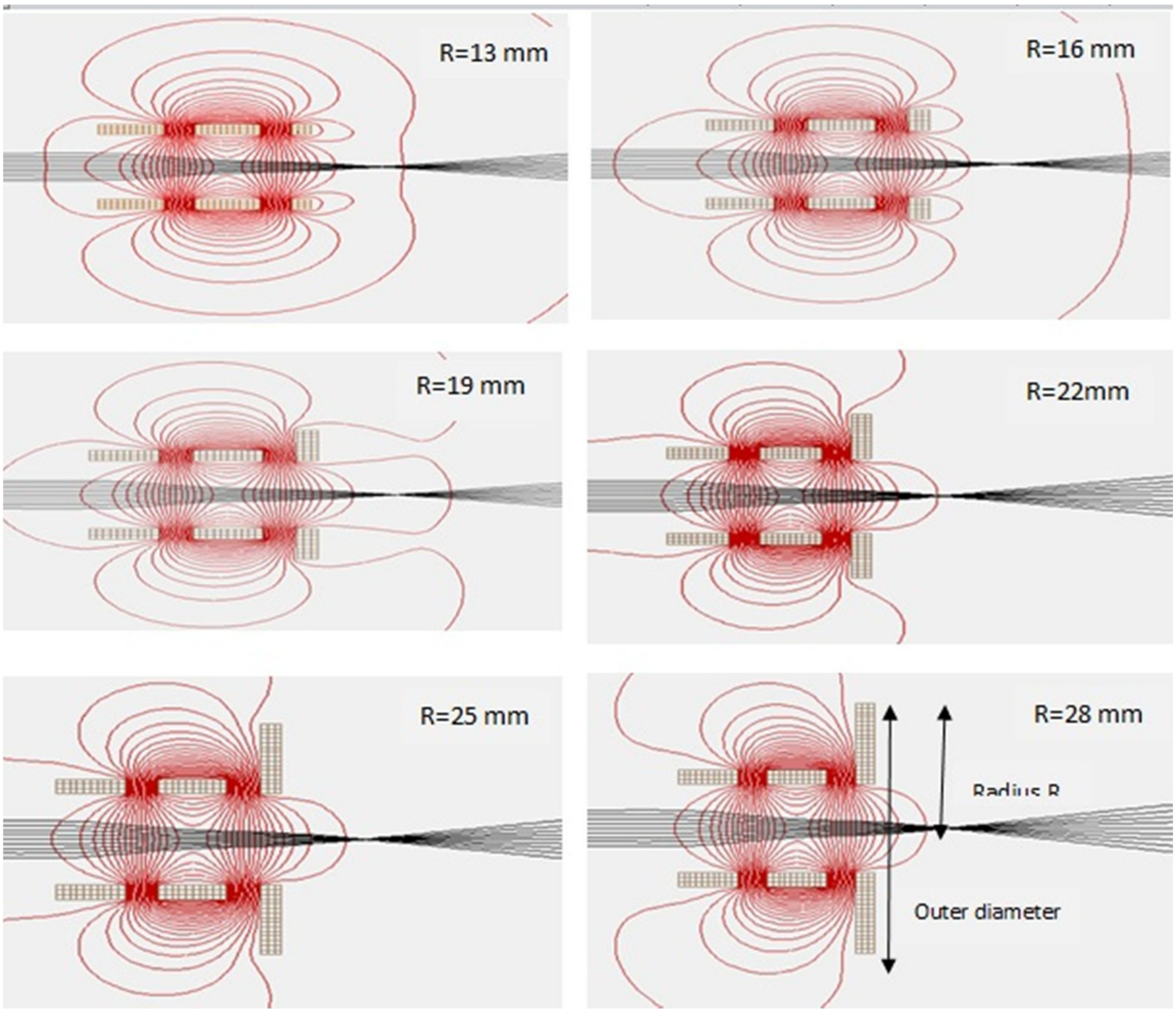

FIG. 3. Changes in the trajectory of the equipotential lines with the outer radius (R) of the third electrode. Increasing the electrode's iron material to 18 mm reduces leakage.

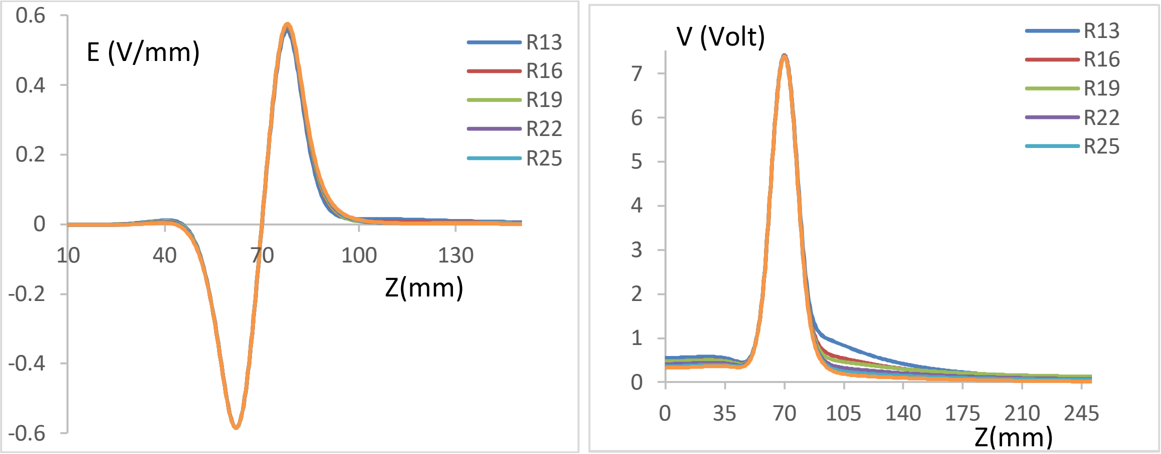

FIG. 4. Differences in the electric field (E) and axial potential distribution (V) along the z-axis for various radius values (R = 13, 16, 19, 22, 25, and 28 mm).

The electrons' trajectories (r) are plotted in Fig. 5, illustrating the disparity of the electron beam path (r) with outer radius (R) as a function of Z. The figure shows that increasing the outer radius of the third electrode improves the electron trajectories and reduces the radius at the focal point. Also, the path of the electron beam and emittance are plotted in Fig. 6 as a function of outer radius (R). From this figure, it is evident that the outer radius of the third electrode (R=19 mm) has a better focal length point (r =0.039 mm) and lower emittance (Ɛ=2.839 mm.rad). So, increasing the outer radius of the third electrode and controlling the stray electric equipotential lines outside the lens represent significant advancements. These discoveries open new oppor r (mm) achieving higher beam quality, precision, and efficiency in charged particle optics applications.

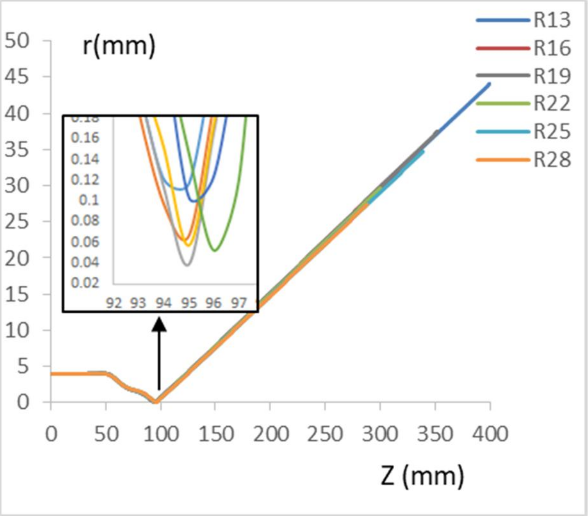

FIG. 5. The path of the electron beam (r) with respect to the z-axis for varying values of R.

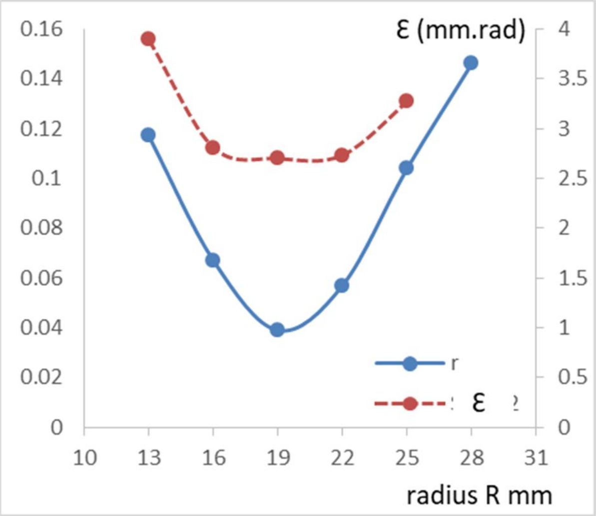

FIG. 6. The path of the electron beam (r) and emittance Ɛ as a function of radius R.

2.2 The of Effect Third Electrode Length

In the present study, we adopted a cylindrical shape for the third electrode, serving as a cover for the first and second electrodes, and investigated the impact of increasing its length. The effect of extending the cylindrical third electrode (S) was analyzed for the optimal lens configuration identified in the previous section (R = 19 mm). Figure 7 illustrates the changes in the equipotential field distribution within the lens as the electrode length increases (S = 5, 10, 15, 20, 25, and 30 mm). It is evident that lengthening the cylindrical third electrode reduces flux leakage and increases the density of flux lines inside the lens. This results in a more regular distribution of the equipotential lines, leading to improvements in the paraxial ray trajectory as well as in the shapes of the electric field and electric potential distribution curves, as shown in Fig. 8.

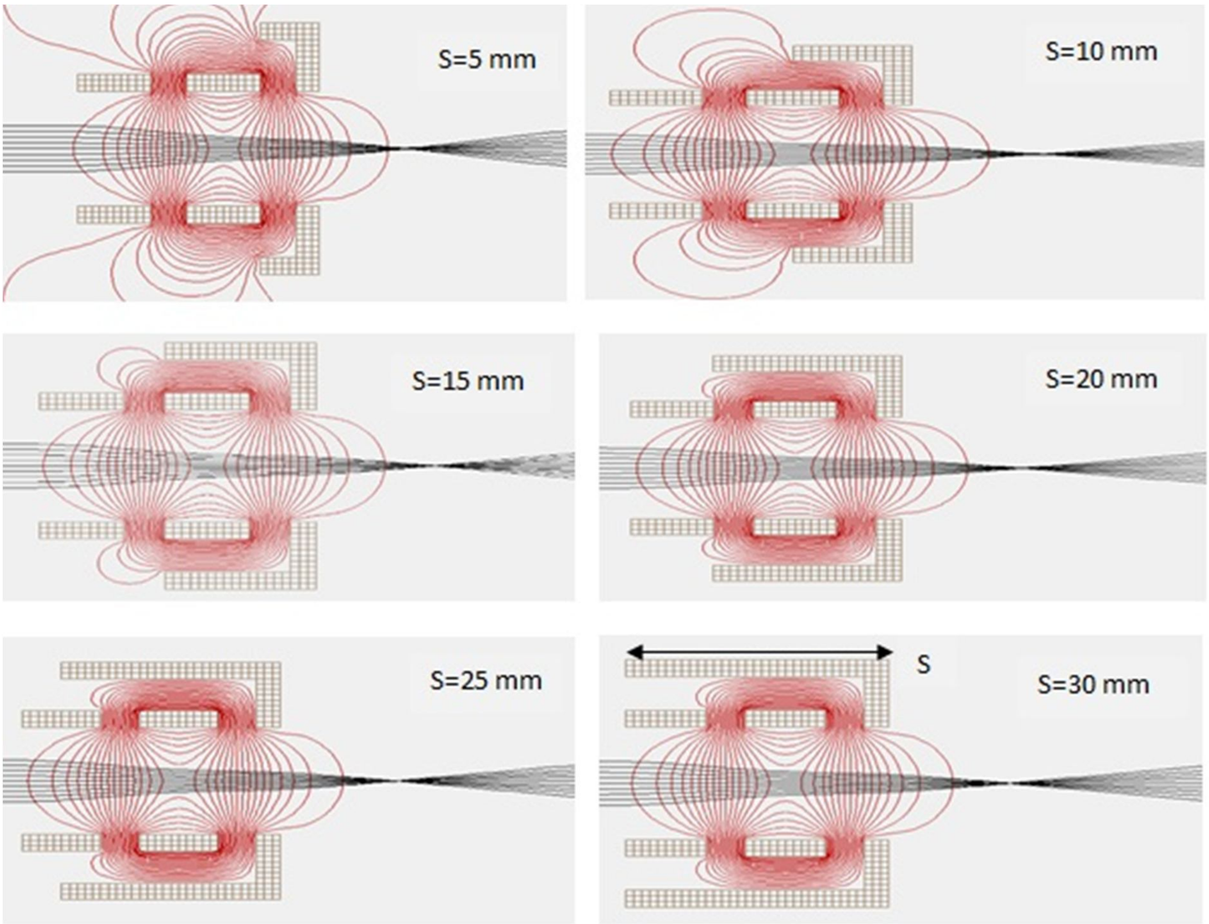

FIG. 7. Changes in the trajectory of equipotential lines with variations in the length of the third electrode (S = 5, 10, 15, 20, 25, and 30 mm).

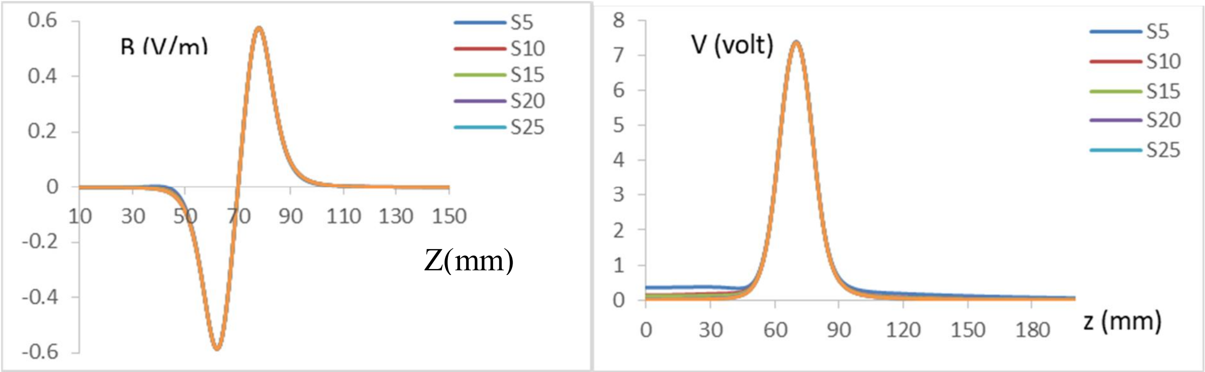

FIG. 8. Differences in the electric field (E) and axial potential distribution (V) concerning the z-axis for different values of the third electrode length (S = 5, 10, 15, 20, 25, and 30 mm).

The trajectory of the electron beam through the designed lens at different S values along the z-axis is depicted in Fig. 9. The figure demonstrates that as the length of the third electrode value increases (S = 25 and 30 mm), the gradient of the electron beam's path decreases. This results in an improved path of the electron beam and a reduction in the focal point diameter. Figure 10 shows the electron beam path (r) and the beam emittance (Ɛ) as a function of the third electrode length (S). Both parameters drop significantly at S=25 mm. These results indicate that the third electrode's cylindrical shape, which encapsulates the first and second electrodes, outperforms the traditional cylindrical design. This innovative configuration provides superior beam control and focusing capabilities, leading to enhanced lens efficiency.

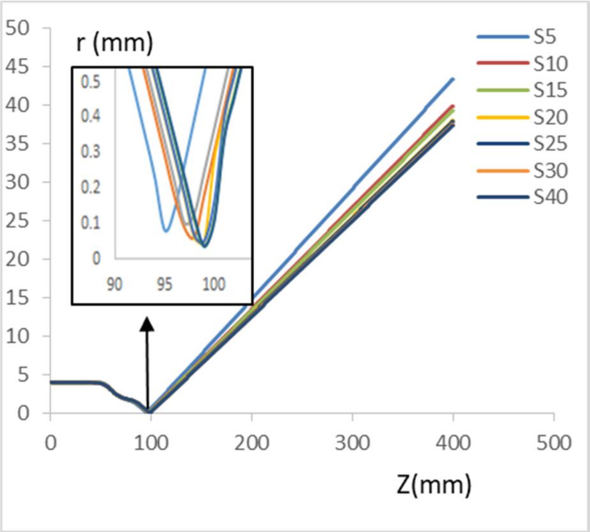

FIG. 9. The electrons' trajectories as a function of the z-axis for different values of length S.

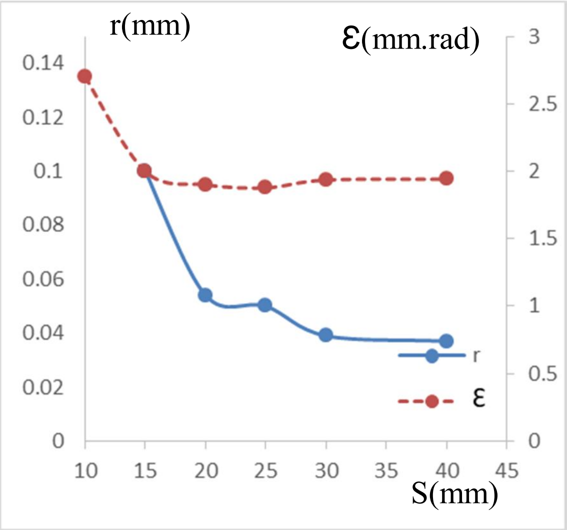

FIG. 10. The path of the electron beam (r) and emittance Ɛ as a function of length S.

2.3 The Length of the Electron Path within the Third Electrode

The initial beam particles' arrangement is created to observe their motion when projected paraxially with an initial energy from a distant source. This process provides insight into the optical characteristics of the electrodes making up the lens [14]. In this research, the effect of the length of the electron path within the third electrode was studied for various values of the length (L=2, 4, 6, and 8 mm). Figure 11 shows the distribution of the equipotential surface of the lens at values of L= 2, 4, 6, and 8 mm, radius R=19mm, and the length of the third electrode S= 30 mm. We can see that increasing the electron path length within the third electrode does not affect the distribution of the equipotential surfaces. Thus, the distributions of the field (E) and the electrical potential (V) are not affected, as illustrated in Fig. 12.

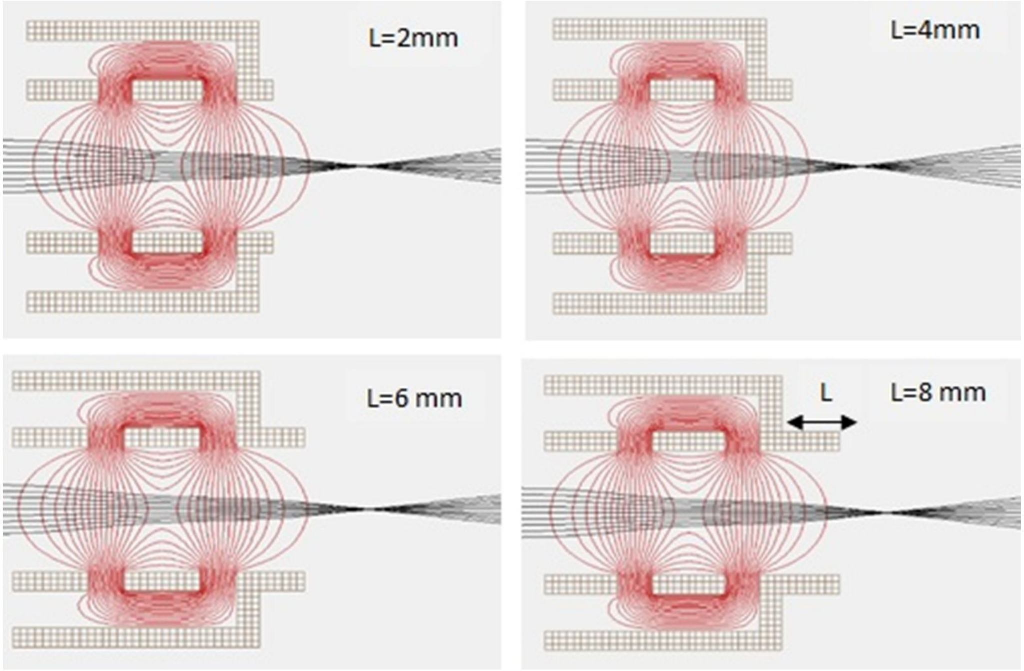

FIG. 11. The equipotential lines trajectory with variation of the length of the electron path within the third electrode (L = 2, 4, 6, and 8 mm), at constant value of R = 19mm & S = 30mm.

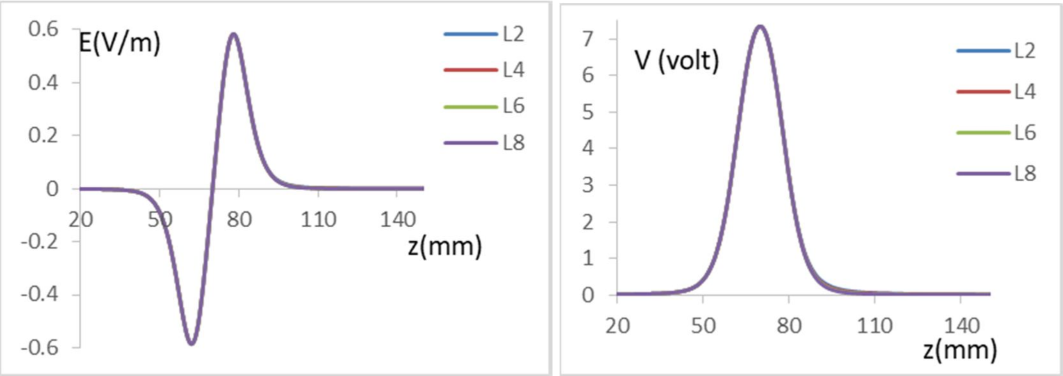

FIG. 12. Differences in the electric field (E) and axial potential distribution (V) along the z-axis for varying lengths of the electron path within the third electrode (L).

Figure 13 depicts the trajectory of the electron beam (r) within the lens at various lengths of the electron pathway inside the third electrode (L) along the z-axis. It is clear from this figure that increasing the length of the electron path with the third electrode length (L), produces a drop in radius of the focal point, reaching r = 0.065 mm at L = 6 mm. This increase in L also causes reduced beam emittance, as shown in Fig. 14, where the emittance decreases to Ɛ = 1.94 mm.rad. The electrostatic lens aberrations depend on the path taken by charged particles, and these aberrations are minimized when the particle trajectory is shorter. Furthermore, it was observed that the length of the electron beam's path within the third electrode has a scant impact on the propagation of the electron beam. The primary influence on the overall trajectory comes from other parameters.

Figure 15 illustrates the eventual configuration of the electrostatic Einzel lens and its optimized measurements. This depiction presents a 3D representation of the supplemented design of the third electrode of the electrostatic Einzel lens.

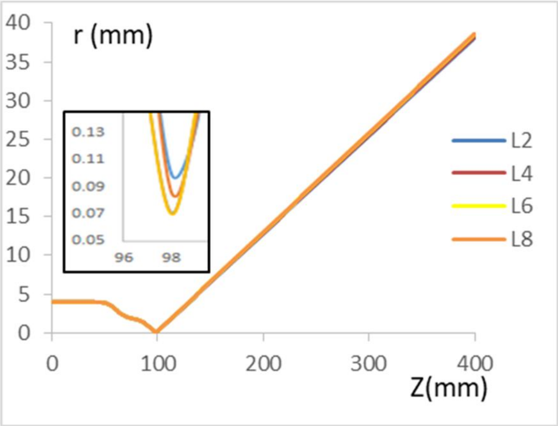

FIG. 13. The electron beam path (r) as a function of the z-axis for different values of L.

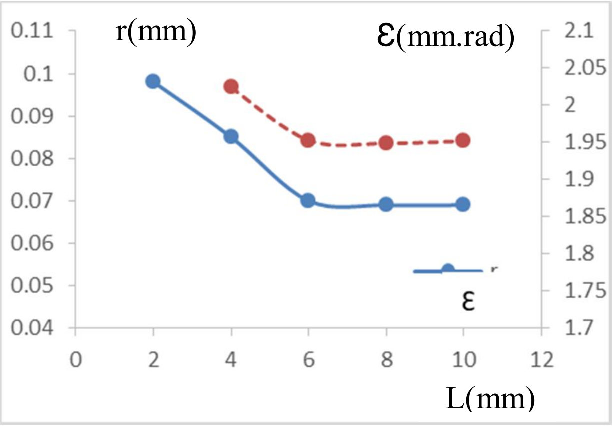

FIG. 14. The electron beam path (r) and emittance Ɛ as a function of L.

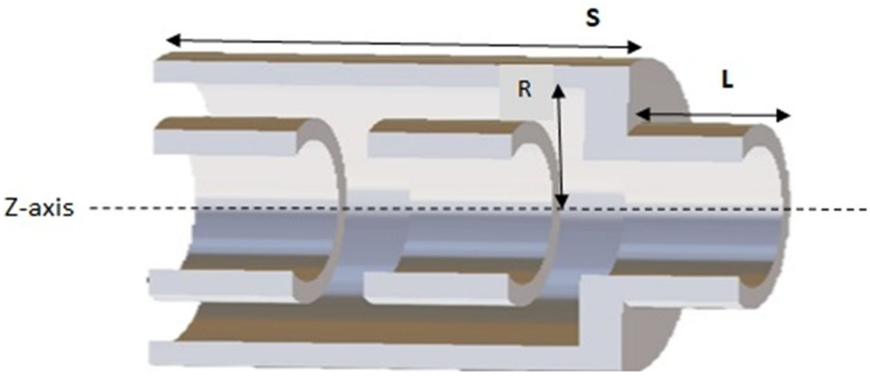

FIG. 15. Three-dimensional visualization of the finalized design of the proposed third electrode.

3. Results and Discussion

This investigation has made significant progress in designing various electrostatic lenses, with remarkable functioning enhancements. Through an overall exploration of parameters, such as the outer diameter and length of the third electrode, as well as the length of the electron path within the third electrode, we have achieved substantial improvements in lens properties.

3.1 The Effect of Increasing the Outer Diameter of the Third Electrode

A key finding of this study is that the existence of stray electric equipotential lines outside the Einzel lens impacts electron beam emittance and beam radius negatively. To reduce leakage of the electric flux towards the exit of the lens, the diameter of the third electrode must be increased. These improvements include a reduction of beam emittance values by 73% and a decrease in the cross-over radius of the paraxial trajectory by 27%. This highlights the decisive role of proper design and electric field shaping within the lens to achieve optimal performance.

3.2 The Effect of Third Electrode Length

Furthermore, the results suggest that the third electrode's cylindrical shape, which encapsulates the first and second electrodes, outperforms the traditional cylindrical shape. Increasing the length of the iron material of the third electrode limits flux leakage outside the lens. High density and regularity of flux lines optimized the paraxial ray trajectory by 37%, and reduced emittance by 76%. This creative configuration provides superior beam control and focusing capabilities, leading to enhanced lens efficiency.

3.3 The Length of Electron Path within the Third Electrode

Finally, it was noted that the length of the electron ray within the third electrode has a limited impact on the propagation of the electron beam from the lens. While the overall trajectory is mainly affected by previous parameters, this factor contributes to a more complete understanding of the electron beam's behavior within the lens system. As such, this research contributes to the development of cutting-edge technologies in various fields involving electron and ion beam systems, particle accelerators, and advanced microscopy.

Acknowledgment

I would like to express my thanks and appreciation to the University of Mosul, Iraq, for its valuable support and contributions to the completion of this research. I also appreciate the academic guidance provided by the university staff, and I extend my thanks to everyone who contributed to this study.

References

[1] Hinterberger, F., "Ion Optics with Electrostatic Lenses", Helmholtz-Institut für strahlem-und Kernphysik, (University of Bonn, Germany, 2005).

[2] Alsheikh Essa, A.A., Kheder, K.Q., and Alabdullah, A.I., "An Investigation of the Link between Radius and Energy Resolution Capability in Hemispherical Electron Energy Analyzer", (2023), Under publication.

[3] Kanaan, M.I., Alabdullah, A.I., and Al-Ahmad, A., Rafidain J. Sci., 32 (2) (2023) 30.

[4] Ahmad, A.A., Rafidain J. Sci., 25 (3) (2014) 70.

[5] Rashid, M.H., Proc. DAE Symp. Nucl. Phys., 56, (2011).

[6] Sulaiman, M.I., M.Sc. Thesis, University of Mosul, (2022), Iraq.

[7] Abdullah, R.T. and Hussein, O.A., J. Phys.: Conf. Ser., 1530 (2020) 012128.

[8] Hawkes, P. and Kasper, E., "Emittance, Principles of Electron Optics", 2nd Ed., (Sciencedirect.com, 2018),

[9] Jaechung, K., "Beam emittance", (Department of Nuclear Engineering, Seoul Natianal university, 2017),

[10] Alabdullah, A.I.M., Optik, 268 (2022) 169761.

[11] Halliday, D. and Resnick, R., "Fundamentals of Physics", 10th Ed., Extended Ed., (QC21.3.H35, book, 2014).

[12] Kanaan, M.I. and Alabdullah, A.I., Rafidain J. Sci., 32 (3) (2023) 55.

[13] Al-Ani, M.M., M.Sc. Thesis, College of Science of Al-Nahrain University, Baghdad, (2007), Iraq.

[14] Li, C., Huang, W., Du, Y., Yan, L., and Tang, C., Proc. IPAC, San Sebastian, Spain, (2011).

Volume 18, Number 3, 2025. pp. 319-328

Jordan Journal of Physics

ARTICLE

Heat Treatment Route Impact on 6063 Al-Mg-Si Alloy: Implications for Mechanical Properties

Mazen A. Madanat[a], **Qutaibah Al-Masri**[a], **Ayeh Arabiat**[a],
Saad S. Alrwashdeh[b] and **Marwan S. Mousa**[c]

[a] *Metallurgy and Materials Technology Research Unit, Advanced Research Centre, Royal Scientific Society, Amman 11941, Jordan.*
[b] *Mechanical Engineering Department, Mutah University, Al-Karak 61710, Jordan.*
[c] *Department of Renewable Energy Engineering, Jadara University, Irbid 21110, Jordan.*

Doi: **https://doi.org/10.47011/18.3.6**

Received on: 10/02/2024; *Accepted on: 27/08/2024*

Abstract: The industrial 6063 Al-Mg-Si alloy was subjected to solution heat treatment, water quenching, and ageing at different heat treatment times and temperatures, such as natural ageing (NA) at room temperature, pre-ageing (PA) at elevated temperatures of 80-120 °C, and artificial ageing (AA) at 180 °C. This study investigates how clusters and precipitates formed during various ageing processes impact the mechanical properties of 6063 Al-Mg-Si alloy. The results showed that the PA temperature plays a crucial role in the formation of clusters, while AA is critical for the formation of hardening precipitates (β''). PA at ≤ 100 °C produced clusters similar to those formed during NA, while PA at 120 °C produced more stable clusters (pre-hardening precipitates) (β'' nuclei). PA followed by AA at 180 °C for 6 hours increased the hardness and the tensile strength to values similar to AA without prior PA for PA ≤ 100 °C. AA after PA at 120 °C resulted in higher values of hardness and tensile strength. A good correlation was found between Vickers hardness, yield strength, and tensile strength, which agrees with the literature.

Keywords: Natural ageing, Pre-ageing, Artificial ageing, Al-Mg-Si alloys, Mechanical properties.

Introduction

The 6xxx series aluminium alloys are widely used industrial alloys due to their formability, high strength-to-weight ratio, and corrosion resistance. The standard process for producing the alloy involves solution heat treatment (SHT) at ~540°C, followed by water quenching (WQ) to create a supersaturated solid solution (SSSS) with good formability due to its low strength. This is followed by artificial ageing (AA) at 180°C to strengthen the alloy via β'' precipitates. However, in practice, there is often an unavoidable natural ageing (NA) step at room temperature between SHT and AA. To enhance the NA effect on the AA response, two approaches have been proposed: pre-ageing (PA) and microalloying with elements such as Sn.

The addition of Sn [1–4] helps control the clustering process by binding with vacancies and facilitating precipitation during AA [5]. The PA step is applied at temperatures higher than 67°C to form PA clusters that may grow into β'' precipitates during AA. The PA temperature has been suggested [6] as a transition temperature where clusters formed at higher temperatures can only grow into β'' precipitates during AA. The effect of different PA temperatures on the

Corresponding Author: Mazen A. Madanat **Email**: madanatmazen@yahoo.com

mechanical properties of the different aluminium alloys has been studied by several researchers [1, 7–12]. In the current work, the PA effect on the 6063aluminium alloy under specific and systematic times and temperatures is presented. The term “PA clusters” is used to label clusters formed during the PA step, regardless of the different notations used for different types of clusters in the literature [13–19].

This study investigates the impact of different heat treatment routes on the mechanical properties of the 6063 alloy. In addition, the tensile properties were estimated through correlations between Vickers hardness, yield strength, and tensile strength. The different PA time and temperature have shown different effects on the mechanical properties, due to differences in cluster formation and growth within the alloy.

Materials and Methods

Industrial ternary 6063 (Al-04Mg-0.5Si-(Fe)) aluminium alloy was provided by the Arab Aluminium Industry Co. Ltd (ARAL), Jordan. Samples with dimensions of 1 × 10 × 10 mm^3 were prepared for hardness measurements. Samples were ground, polished to a mirror-like finish, and ultrasonically cleaned. Tensile samples were prepared using a CNC machine in accordance with ASTM E8 for aluminium alloys, with a gauge length of 50 mm and a width of 12.5 mm.

Solution heat treatment (SHT) was performed at 540 °C for 1 h, followed by water quenching (WQ) at room temperature. Two heat treatment routes were then applied (see Fig. 1): (A) immediate artificial ageing (AA) at 180 °C for various times, or natural ageing (NA) at room temperature for 2 weeks followed by AA; (B) immediate pre-ageing (PA) at 80-120 °C for various times, or PA followed by 2 weeks NA, or PA + 2 weeks NA followed by AA at 180 °C for 6 hours. Samples were quenched after each PA or AA step.

Tensile measurements were carried out according to the international standard ASTM E8 using a Shimadzu machine. Vickers micro-hardness measurements were performed with a load of 200 gf (HV0.2), and the average of eight indentations was used for each measurement.

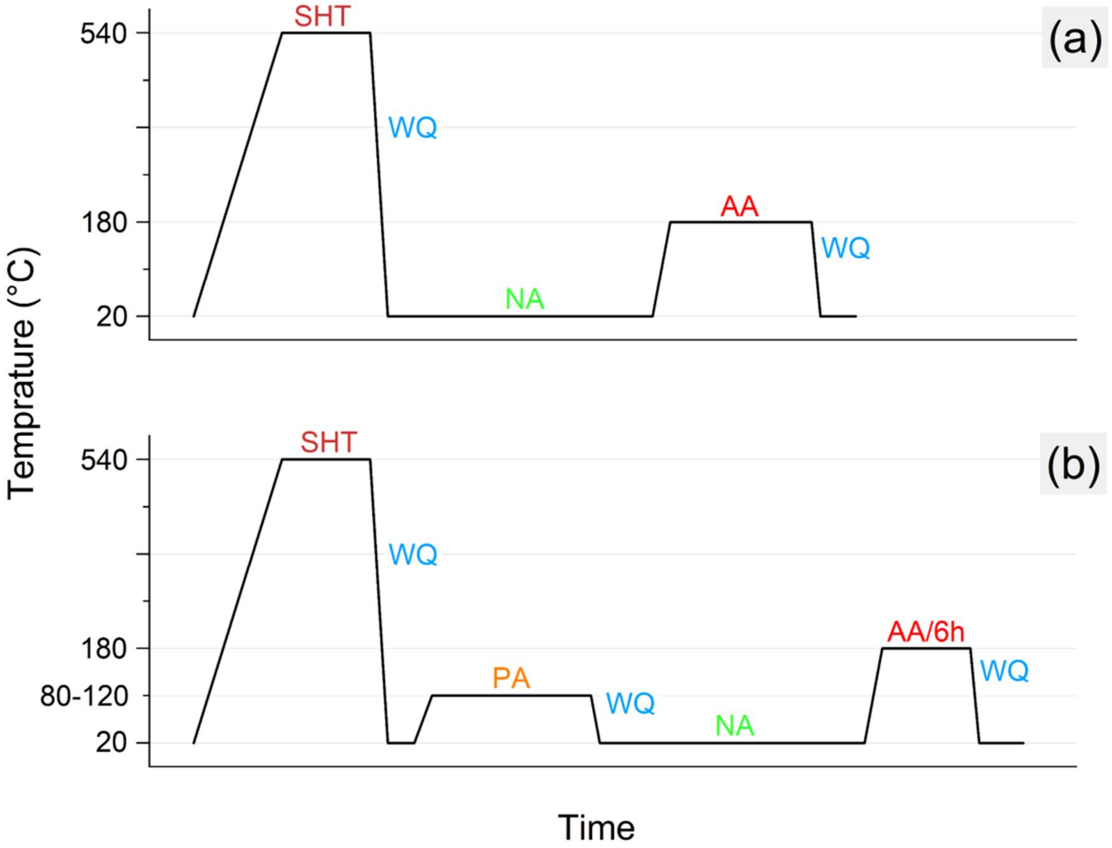

FIG. 1. Temperature profiles used in this work: (a) without PA and (b) with PA. SHT – 1 h at 540 °C, WQ at 20 °C, NA - 2 weeks at 20 °C, PA – various times at 80-120 °C, AA - various times at 180 °C in (a) and for 6 h in (b).

Results

Hardness

Figures 2(a)-2(d) present the evolution of hardness after different heat treatments. The hardness value immediately after solutionizing (SHT) and quenching (WQ) was 33 HV. Natural ageing (NA) for 2 weeks increased the hardness to 47.1 HV (red line). Artificial ageing (AA) for various times after NA reached a maximum hardness of ~88 HV after 12 hours of AA (green line). Immediate AA after SHT increased the hardness to a maximum of 61.5 HV after 8 hours of AA, but longer AA times decreased the hardness (black line). Pre-ageing (PA) at 80°C (dark blue line) and 100°C, indicated by the orange line in Fig. 2(b), showed no change in hardness up to 14 hours, while PA at 120°C (blue line) increased hardness to ~50 HV after 12 h and ~45 HV after -14 h. PA samples were then set to 2 weeks of NA, as shown in Fig. 2(c), and hardness increased to ~45 HV for the entire PA set at 100°C (orange line) and 120°C (blue line). Final AA at 180°C for 6 hours after PA and NA, illustrated in Fig. 2(d), increased the hardness to ~80 and 90 HV for PA at 100 °C and 120 °C, respectively. NA clusters retrogression or reversion was observed after AA, resulting in a slight decrease in hardness during the first minutes, due to cluster dissolution during AA [20–25].

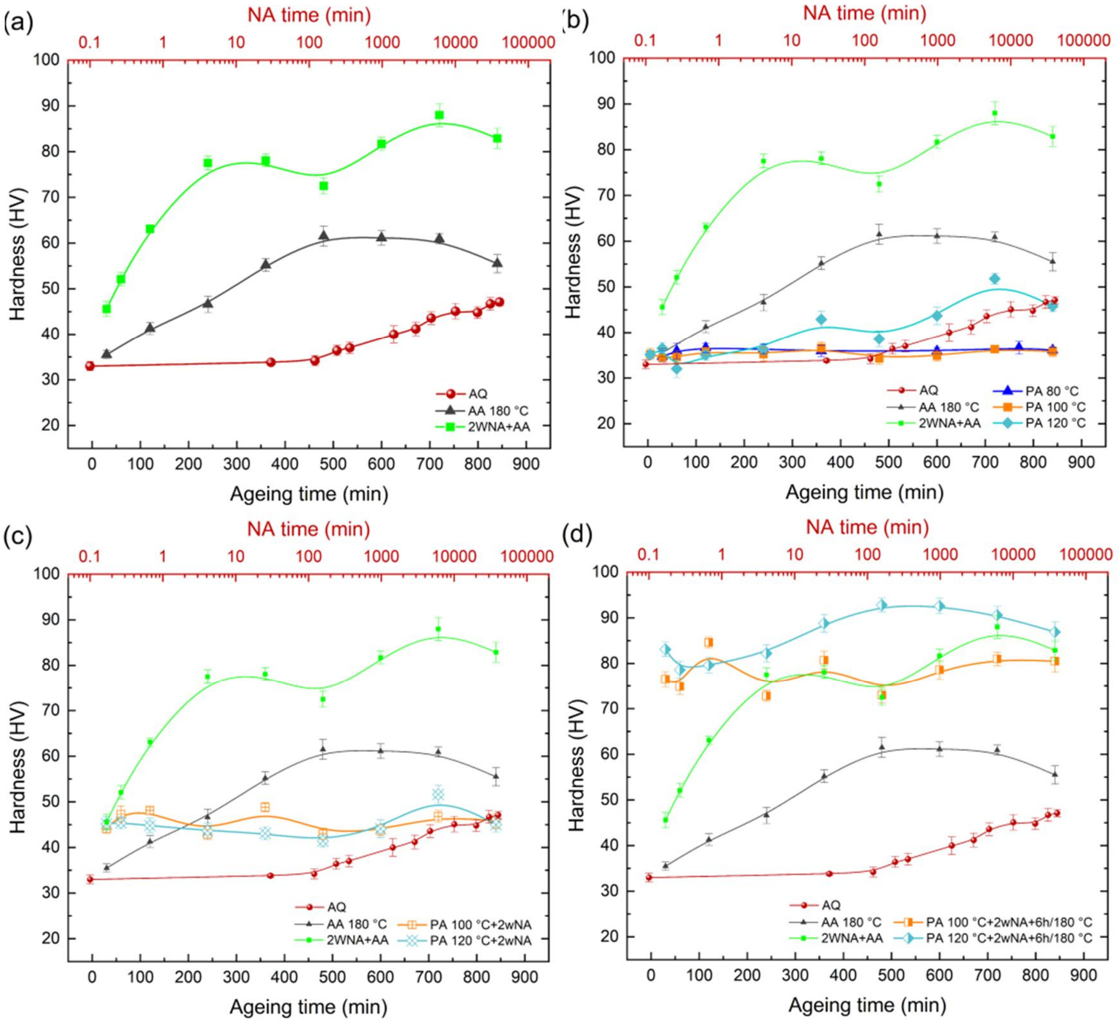

FIG. 2. Evolution of hardness (HV0.2) after different thermal treatments. The X-axis corresponds to hardness values, the upper Y-axis corresponds to NA time, and the lower Y-axis corresponds to ageing (PA or AA) times. (a–d) The red line shows the NA behavior after SHT and WQ. The black line corresponds to AA at 180°C for various times. The green line corresponds to samples subjected to NA for 2 weeks, followed by AA at 180°C for various times. (b) Hardness after PA at 80°C for various times (dark blue line), after PA at 100°C (orange line), and after PA at 120°C (blue line). (c) Hardness after PA and 2 weeks of NA. (d) Hardness after PA + 2 weeks of NA + AA at 180°C for 6 h.

Tensile measurements (PA at 120°C)

Figure 3(a) shows that the yield strength (YS) of the alloy increased from approximately 38 MPa in the AQ state to 79 MPa after 2 weeks of NA. AA at 180°C on samples that underwent NA for two weeks increased the YS from 70 MPa after 30 minutes of AA to 190 MPa after 4 hours of AA. For AA durations over 4 hours, the YS remained between 190-212 MPa up to 14 hours of AA.

PA for 30 minutes at 120°C decreased the YS to 44 MPa, but it slowly increased to 64 MPa after 6 hours of PA. The YS continued to increase and reached 104 MPa after 14 hours of PA.

2 weeks of NA after PA at 120°C showed a slight increase in the YS compared to PA without NA for PA durations up to 6 hours, with a YS of approximately 70 MPa. For longer PA durations, the YS values were similar in both cases (PA and PA + 2 weeks NA), with a maximum of 101 MPa after 14 hours of PA. Final AA after PA + 2 weeks NA affected the YS values based on the previous PA duration. PA for 4 hours or less increased the YS value to approximately 210 MPa, while PA for 6 hours or more further increased the YS value to approximately 240 MPa.

The results of the tensile strength (UTS) of the tested samples are presented in Fig. 3(b). The UTS of the AQ sample was ~118 MPa and increased to ~160 MPa after 2 weeks of NA. AA for 30 minutes resulted in a UTS of 160 MPa, which increased to a maximum of 235 MPa after 4 hours of AA. The UTS continued to increase up to 14 hours of AA. PA for 30 minutes resulted in a minimum UTS of 121 MPa, which increased to a maximum of 164 MPa after 14 hours of PA.

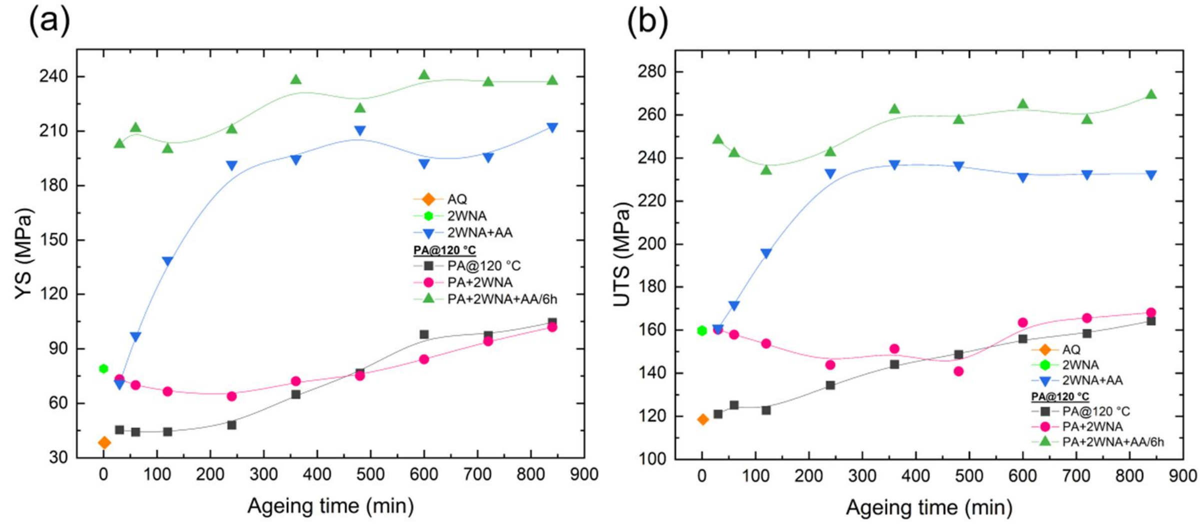

FIG. 3. (a) Evolution of yield strength (YS) and (b) ultimate tensile strength (UTS) after various heat treatment routes.

Following 2 weeks of NA after PA had a positive effect on the UTS for PA times less than 6 hours, with a UTS of 160 MPa after 30 minutes of PA and 2 weeks of NA. For PA times longer than 6 hours, the UTS values were similar for PA with and without 2 weeks of NA. Final AA at 180°C for 6 hours after PA and NA resulted in a significant increase in UTS values. AA after 30 minutes of PA and 2 weeks of NA doubled the UTS to 245 MPa. The UTS remained high at ~240 MPa for PA times up to 4 hours and had an average value of ~260 MPa for longer PA times.

Discussion

Behavior of Strength and Hardness

Without Pre-ageing

Immediately after the solution heat treatment (SHT) and quenching, a supersaturated solution forms, and solute atoms begin to diffuse and form clusters with the help of quench-in vacancies. Zurob and Seyedrezai have proposed a model for the movements of these vacancies and solute atoms [26]. They postulate that the rate of clustering is highest immediately after the SHT and quenching, due to the high concentration of mobile vacancies. The subsequent NA process reduces the level of supersaturation and consumes vacancies until they reach thermal equilibrium, leading to slower clustering kinetics.

Figures 2(a)-2(d) depict an increase in the hardness (red curve) over 2 weeks of NA (upper Y-axis). A plateau is observed up to 120 minutes, which is linked to the size of the formed clusters. Hardness is a sensitive measure of cluster size, and a change in hardness reflects changes in the critical cluster size. In this case, the size has stabilized after 120 minutes of NA. Further increases in hardness are observed over longer NA times and have been documented by several researchers [5, 24, 25, 27–32].

Immediate AA at 180°C after quenching creates a high driving force for the solute atoms and vacancies, resulting in the formation of stable clusters and precipitates. Madanat *et al.* [27, 33] studied the impact of different heating media on Al-Mg-Si alloys immediately after quenching. They found that a shorter AA time leads to faster cluster and precipitate formation, regardless of the heating medium used. Figure 2 displays the systematic increase in the AA curve (black line). The hardness continues to increase up to a maximum after 480 minutes of AA, followed by a decrease due to over-aging and the formation of coarse precipitates. The initial increase is a result of the formation of clusters and the pre-β'' phase and the following strengthening phase β''. The final decrease is due to over-aging and the formation of β' phase.

Tensile measurements, indicated by the blue line in Fig. 3(a) and 3(b), display a systematic increase in yield strength (YS) and ultimate tensile strength (UTS), similar to the results observed in the hardness measurements. Cao *et al.* [32] used atom probe tomography (APT) to explain this behavior and found that NA alone results in a high fraction of solutes aggregating into small solute aggregates, while NA + AA leads to a slight increase in large aggregates and a good amount of small aggregates. In a recent article by Engler *et al.* [24], they reported an increase in the size of clusters and precipitates and a decrease in their number density after NA (28 days) and AA (180°C). This supports our findings, as the increase in the size of clusters and precipitates leads to an increase in hardness and strength.

With Pre-ageing

Figures 2(b)-2(d) display the hardness results after different PA treatments. Hardness changes during PA are linked to cluster formation during PA itself. According to literature, a PA temperature of 100°C is a critical temperature for cluster formation [12, 34]. Zhu *et al.* [34] reported that PA at 100°C results in low-density, small, and intermediate-sized Mg-Si co-clusters. This aligns with the tensile results shown in Figs. 3(a) and 3(b), as YS and UTS after PA have low values following PA at 100°C. For industrial use, the upper limit for YS is 130 MPa [35]. With high elongation and low strength, PA alloys exhibit low spring-back, allowing the formation of complex shapes with high dimensional accuracy during sheet metal forming processes.

The change in mechanical properties after PA is linked to cluster size. PA at 120°C for 4 hours or more increases cluster size, raising hardness. However, YS and UTS remain largely unaffected because cluster density has not yet reached an effective threshold. Hardness saturation after 10 hours at 120°C confirms this. Subsequent NA after PA can result in either new NA cluster formation or attachment to pre-existing PA clusters. Zi *et al.* [12] studied the impact of PA time and temperature on subsequent NA using resistivity, DSC, and PALS measurements. They observed an increase in resistivity during NA after PA and a dissolution trough in the DSC signal, indicating new NA cluster formation. This is consistent with other studies [6, 9, 36]. APT analysis [37] shows that cluster number density affects resistivity more than size. Researchers [10, 12] found that resistivity changes minimally after PA at 80°C and 100°C, suggesting that PA clusters grow in size rather than number. Zandbergen *et al.* [13] confirmed via APT that PA at 80°C for 2 hours increases cluster size more than density. However, [12] found that AA response is not solely improved by cluster size, indicating that other factors contribute to AA behavior after PA.

Figure 4 shows the hardening coefficient (n-values) calculated from tensile tests. The n-value indicates the material's formability and is critical to consider before the final AA step. A higher n-value corresponds to better formability (acceptable range: 0.1-0.5 [38]). The n-value is calculated from the slope of the true strength-strain curve within the plastic region using its logarithmic form.

Samples in the AQ state (Fig. 4, orange dots) and after 2 weeks of NA (Fig. 4, green dots) have high n-values of ~0.45, indicating good formability due to incomplete cluster formation. Samples after PA and PA + NA have lower n-values of ~0.38, indicating cluster formation and reduction in formability; however, they remain within the acceptable n-value limits [38, 39].

In contrast, artificial aging has a more noticeable impact as bigger clusters form. PA at 120°C reduces the n-value to ~0.38 (Fig. 4, black curve), while PA + 2 weeks NA (Fig. 4, pink curve) slightly increases the n-value. PA stabilizes clusters during subsequent NA, thus the formability (n-value) is expected to be similar.

The increase in hardness after AA is shown in Fig. 2(a), whereas the corresponding increase in strength is shown in Figs. 3(a) and 3(b). The effect of prior PA and NA is evident, with a greater increase in values seen in samples with prior PA. The formation of clusters and precipitates requires vacancies, and a reduction in vacancy concentration after PA and NA is noted. According to Pogatscher *et al.* [21], the quenched-in vacancies play a critical role in the formation of clusters and precipitates after AA. The authors argue that most of the excess quenched-in vacancies from the PA step should be either annihilated or trapped, leaving only mobile thermal equilibrium vacancies. After AA at 180°C, there will be a new and higher equilibrium vacancy concentration, which is estimated to equilibrate in about 1 minute or less [42, 43]. Thus, the PA temperature is not a factor in this process.

In such a case, it is likely that the Mg:Si ratio of clusters formed at higher PA temperature (120°C in this case) is closely related to the strengthening precipitates (β'' nuclei), enabling their easy transformation into fully coherent β'' phase upon AA. This explains the observed high hardness, YS, UTS, and low n-values after AA with a prior short PA time (30 min).

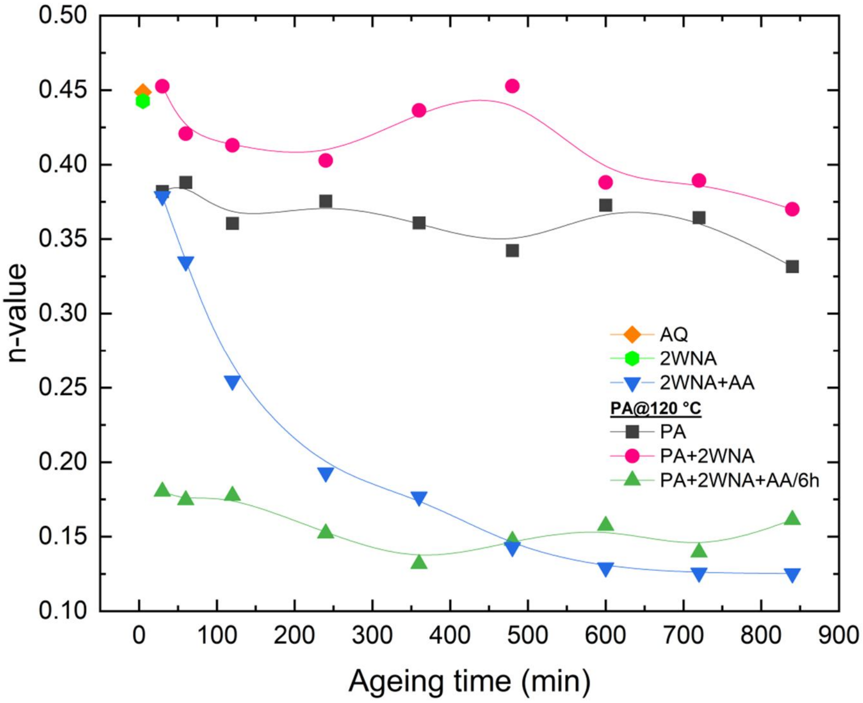

FIG. 4. Evolution of n-value before and after PA at 120°C for various times.

The chemical composition of clusters and precipitates, particularly their Mg:Si ratio, is critical in determining the outcome of heat treatment [13, 15, 23, 40, 41]. Clusters with higher Mg:Si ratios are favored at elevated temperatures [13]. These clusters are more ordered, which facilitates their transformation into β''-type strengthening precipitates during AA.

Consequently, performing PA at 100°C or 120°C leads to an increase in hardness and YS after a subsequent NA step, as the Mg:Si ratio approaches a critical value. Subsequent AA further enhances hardness and YS. Among these conditions, PA at 120°C produces the highest AA response, indicating the formation of clusters with a higher Mg:Si ratio, closer in composition to the β''-phase.

Short preliminary annealing times lead to the formation of more clusters, while longer annealing times result in the growth of both cluster size and chemical composition. In this study, no change in hardness was observed at 80°C and 100°C after up to 14 hours of PA, while at 120°C, the hardness increased with increasing PA time. After approximately 10 hours of PA, the hardness stabilized, indicating that the critical size and chemical composition had been reached.

Correlation between Strength and Hardness

Determining yield strength and tensile strength from hardness measurements is of significant interest.

The Vickers hardness (HV) is calculated by dividing the applied load by the contact area under the indenter, resulting in a relationship with the mean pressure under the indenter (P_m). This relationship can be expressed as:

$$HV = 0.927 \cdot P_m \tag{1}$$

where $$P_m = C \cdot \sigma_Y \tag{2}$$

where σ_Y represents the tensile yield strength and HV is the Vickers hardness in MPa. The constraint factor, C, has been extensively studied by various researchers [42–45] with values ranging from 2.8 to 3. These values apply to materials that have undergone full hardening. In our study, the alloy was pre-aged (at 120°C), which strongly suppressed work hardening; thus, we assumed a fully hardened alloy and used C = 3 for comparison purposes.

By combining Eqs. (1) and (2) we get:

$$\sigma_Y = \frac{H_V}{0.927 \cdot C} \tag{3}$$

After rearranging Eq. (3) to calculate the slope,

$$\frac{\sigma_Y}{HV} = \frac{1}{0.927 \cdot C} \tag{3.1}$$

By using C = 3, the slope is equal to $\frac{\sigma_Y}{HV} = 0.365$

Experimentally, the relationship between the Vickers hardness and tensile yield strength was found to be described by a linear fit with the equation:

$$\sigma_Y = \beta_1 \cdot HV + \beta_0 \tag{4}$$

where β_1 is the slope and β_0 is the Y-intercept.

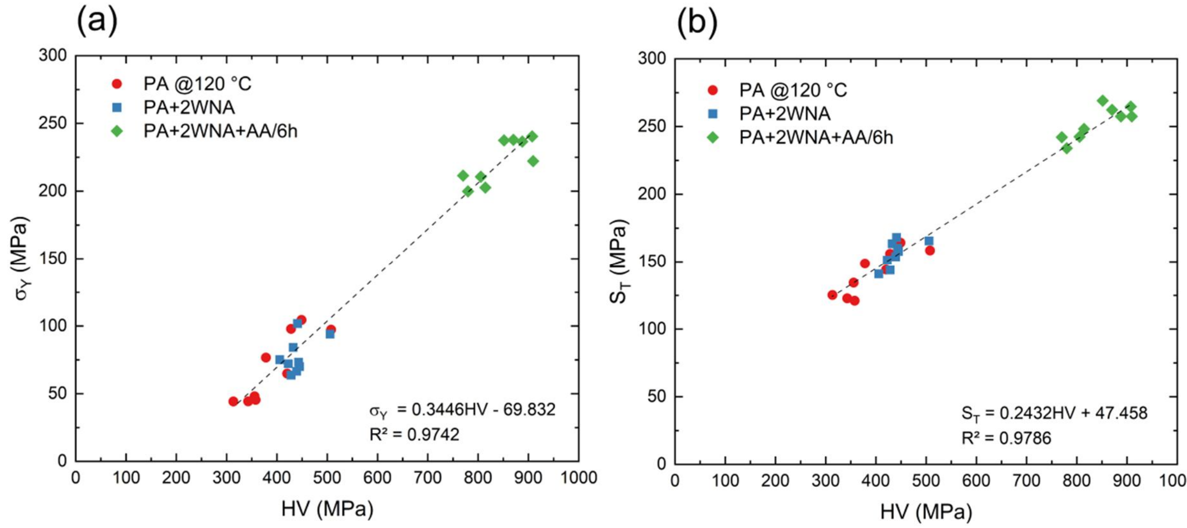

FIG. 5. Vickers hardness versus (a) yield strength and (b) tensile strength for samples investigated in this work after PA at 120°C. In this work, Vickers hardness is reported in MPa, which is found by multiplying the traditional Vickers number by the gravitational acceleration.

Figure 5(a) shows the relation between yield strength and hardness measurements. Applying a linear fit, Eq. (4) can be found as:

$$\sigma_Y = 0.345HV - 69.8 \tag{4.1}$$

The slope value of 0.345 is closely aligned with the calculated and literature value of 0.365, with a high coefficient of determination $R^2 = 0.974$. Tiryakioglu [44] attributed the negative y-intercept to the increase in strength under the indenter, resulting from work hardening, until it reaches the characteristic strain in the Vickers hardness test.

On the other hand, Fig. 5(b) shows the relation between Vickers hardness and tensile strength. The linear fit line has the equation:

$$S_T = 0.243HV + 47.5 \tag{4.2}$$

The R^2 shows a value of 0.979 with a slope equal to 0.243, which is similar to the value of 0.247 for alloy 7010 reported in literature [44].

In conclusion, Eqs. (4.1) and (4.2) provide the relationship between Vickers hardness and tensile yield strength, and between hardness and tensile strength, respectively.

In summary, the final mechanical properties are not only related to the final AA step but also to the earlier aging steps, namely the PA and NA. The AA after PA leads to an increase in strength due to clusters and precipitate formation, where the PA temperature is critical. PA at 120°C affects the size, density, and chemical composition of clusters, which, after subsequent AA, produce the strongest ageing response, resulting in increased strength and hardness.

Conclusion

In this study, a combination of hardness and tensile measurements was performed to examine the behavior of the age-hardening 6063 aluminum alloy in industrial applications under various thermal treatments. Samples were subjected to heat treatment at different durations and temperatures. The results indicated that:

- The pre-aging and natural aging significantly affect the alloy's mechanical and chemical properties.
- A critical PA temperature is required before the final AA step to achieve the desired microstructure.
- Pre-aging prior to natural aging has a positive effect on the alloy, as strength increases after pre-aging and aging.
- Pre-aging at 120°C is required for enhancing the final mechanical properties of the alloy by the formation of stable clusters (β'' nuclei), which transform into fully coherent hardening precipitates (β'') during subsequent aging.
- The relationship between Vickers hardness and yield strength is given by: $\sigma_Y = 0.345\,HV - 69.8$, with a slope of 0.345 closely matching literature values using a constraint factor of 3. Meanwhile, the relationship between hardness and tensile strength is: $S_T = 0.243HV + 47.5$.

Future work

Future studies will explore more complex heat treatment routes, including combinations of PA, NA, and AA, on the same alloy as well as on different alloys to determine the optimal heat treatment route with minimal energy requirements and optimal mechanical properties.

Acknowledgment

The authors would like to thank the Arab Aluminium Industry Co. Ltd (ARAL) for providing the alloy for this work.

This research did not receive any specific grant from funding agencies in the public, commercial, or not-for-profit sectors.

CRediT

Mazen Madanat: Conceptualization, Data curation, Formal analysis, Writing - original draft; Writing - review & editing, Supervision; *Qutaibah Al-Masri:* Experimental work, Data curation, Formal analysis; *Ayeh Arabiat:* Experimental work, Data curation, Formal analysis; *Saad S. Alrwashdeh:* Writing - review & editing; *Marwan S. Mousa:* Writing - review & editing.

Data Availability

The data that support the findings of this study are available from the corresponding author upon reasonable request.

References

[1] Zhang, X., Liu, M., Wang, J., Li, J., and Banhart, J., J. Mater. Sci., 57 (2022) 2149.

[2] Zhang, X., Liu, M., Sun, H., and Banhart, J., Materialia, 8 (2019) 100441.

[3] Schmid, F., Uggowitzer, P.J., Schäublin, R., Werinos, M., Ebner, T., and Pogatscher, S., Materials, 12 (11) (2019) 1801.

[4] Liu, M. *et al*., Materialia, 6 (2019) 100261.

[5] Pogatscher, S. *et al*., Appl. Phys. Lett., 112 (2014) 225701.

[6] Saga, M., Sasaki, Y., Kikuchi, M., Yan, Z., and Matsuo, M., Mater. Sci. Forum, 217 (1996) 821.

[7] Zhen, L. and Kang, S.B., Scr. Mater., 36 (10) (1997) 1089.

[8] Zhen, L., Kang, S.B., and Kim, H.W., Mater. Sci. Technol., 13 (11) (1997) 905.

[9] Birol, Y., Mater. Sci. Eng. A, 391 (1–2) (2005) 175.

[10] Ding, L., Weng, Y., Wu, S., Sanders, R.E., Jia, Z., and Liu, Q., Mater. Sci. Eng. A, 651 (2016) 991.

[11] Takaki, Y., Masuda, T., Kobayashi, E., and Sato, T., Mater. Trans., 55 (8) (2014) 1257.

[12] Yang, Z., Liang, Z., Leyvraz, D., and Banhart, J., Materialia, 7 (2019) 100413.

[13] Zandbergen, M.W., Xu, Q., Cerezo, A., and Smith, G.D.W., Acta Mater., 101 (2015) 136.

[14] Zandbergen, M.W., Cerezo, A., and Smith, G.D.W., Acta Mater., 101 (2015) 149.

[15] Serizawa, A., Hirosawa, S., and Sato, T., Metall. Mater. Trans. A, 39A (2008) 245.

[16] Edwards G.A., Stiller, K., Dunlop, G.L., and Couper, M.J., Acta Mater., 46 (11) (1998) 3893.

[17] Murayama, M. and Hono, K., Acta Mater., 47 (5) (1999) 1537.

[18] Marioara, C.D., Andersen, S.J., Jansen, J., and Zandbergen, H.W., Acta Mater., 51 (3) (2003) 789.

[19] Banhart, J., Chang, C.S.T., Liang, Z.Q., Wanderka, N., Lay, M.D.H., and Hill, A.J., Adv. Eng. Mater., 12 (7) (2010) 559.

[20] Gupta, A.K., Lloyd, D.J., and Court, S.A., Mater. Sci. Eng. A, 301 (2) (2001) 140.

[21] Pogatscher, S., Antrekowitsch, H., Leitner, H., Ebner, T., and Uggowitzer, P.J., Acta Mater., 59 (9) (2011) 3352.

[22] Yan, Y., Liang, Z.Q., and Banhart, J., Mater. Sci. Forum, 794–796 (2014) 903.

[23] Aruga, Y., Kozuka, M., Takaki, Y., and Sato, T., Mater. Sci. Eng. A, 631 (2015) 86.

[24] Engler, O., Marioara, C.D., Aruga, Y., Kozuka, M., and Myhr, O.R., Mater. Sci. Eng. A, 759 (2019) 520.

[25] Liu, M., Čížek, J., Chang, C.S.T., and Banhart, J., Acta Mater., 91 (2015) 355.

[26] Zurob, H.S. and Seyedrezai, H., Scr. Mater., 61 (2) (2009) 141.

[27] Madanat, M., Liu, M., Zhang, X., Guo, Q., Čížek, J., and Banhart, J., Phys. Rev. Mater., 4 (6) (2020) 063608.

[28] Yang, Z. *et al*., Scr. Mater., 190 (2021) 179.

[29] Yang, Z. and Banhart, J., Acta Mater., 215 (2021) 117014.

[30] Dumitraschkewitz, P., Gerstl, S.S.A., Stephenson, L.T., Uggowitzer, P.J., and Pogatscher, S., Adv. Eng. Mater., 20 (10) (2018) 1800255.

[31] Tu, W. *et al*., Mater. Des., 198 (2021) 109307.

[32] Cao, L., Rometsch, P.A., and Couper, M.J., Mater. Sci. Eng. A, 571 (2013) 77.

[33] Madanat, M.A., Ph.D. thesis, Technische Universität Berlin, Germany, (2018).

[34] Zhu, S., Shih, H.-C., Cui, X., Yu, C.-Y., and Ringer, S.P., Acta Mater., 203 (2021) 116455.

[35] Kleiner, S., Henkel, C., Schulz, P., and Uggowitzer, P.J., Int. Aluminium J., 77 (3) (2001) 185.

[36] Panseri, C. and Federighi, T., Acta Metall. Mater., 8 (4) (1960) 217.

[37] Esmaeili, S., Vaumousse, D., Zandbergen, M.W., Poole, W.J., Cerezo, A., and Lloyd, D.J., Philos. Mag., 87 (25–27) (2007) 3797.

[38] Prillhofer, R., Rank, G., Berneder, J., Antrekowitsch, H., Uggowitzer, P.J., and Pogatscher, S., Materials, 7 (7) (2014) 5047.

[39] Castany, P., Diologent, F., Rossoll, A., Despois, J.-F., Bezençon, C., and Mortensen, A., Mater. Sci. Eng. A, 559 (2013) 558.

[40] Aruga, Y., Kim, S., Kozuka, M., Kobayashi, E., and Sato, T., Mater. Sci. Eng. A, 718 (2018) 371.

[41] Torsaeter, M. et al., J. Appl. Phys., 108 (7) (2010).

[42] Shield, R.T., Proc. R. Soc. Lond. A., 233 (1193) (1955) 267.

[43] Shaw, M.C. and DeSalvo, G.J., J. Eng. Ind., 92 (2) (1970) 480.

[44] Tiryakioğlu, M., Robinson, J.S., Salazar-Guapuriche, M.A., Zhao, Y.Y., and Eason, P.D., Mater. Sci. Eng. A, 631 (2015) 196.

[45] Tabor, D., Proc. R. Soc. Lond. A, 192 (1029) (1948) 247.

Volume 18, Number 3, 2025. pp. 329-347

Jordan Journal of Physics

ARTICLE

A Comprehensive Review on the Formation Mechanism of Zinc Oxide Nanoparticles Using Plant Extracts

Banaz S. Haji[a], **Azeez A. Barzinjy**[b,c], **Marwan S. Mousa**[d], **Ahmad W Al Shaer**[e] and **Samir M. Hamad**[f],

[a] *Medical Radiology Imaging,College of Health Sciences,Lebanese French University, Kurdistan Region,Erbil, Iraq.*

[b] *Department of Physics, Faculty of Science, Soran University, Kurdistan Region, Iraq.*

[c] *Department of Physics Education, Faculty of Education, Tishk International University-Erbil, Kurdistan Region, Iraq.*

[d] *Department of Renewable Energy Engineering Jadara University, Irbid 21110, Jordan.*

[e] *School of Engineering, University of Central Lancashire, Fylde Road, Preston, PR1 2HE, The United Kingdom.*

[f] *Scientific Research Center, Soran University, Kurdistan Region, Iraq.*

Doi: **https://doi.org/10.47011/18.3.7**

Received on: 09/02/2024; *Accepted on: 31/07/2024*

Abstract: Nanotechnology is an emerging field of science that concerns the industrial use of nanoparticles (NPs), typically ranging in size from 1 to 100 nm, which are classified into different classes such as inorganic, organic, ceramic, and carbon-based nanoparticles. Zinc oxide (ZnO) NPs are utilized in medicine, pharmaceuticals, cosmetics, sunscreens, water treatment, sensors, textiles, agriculture, and the food industry, making them the focus of this review. Since producing NPs using chemical and physical methods is often expensive and potentially harmful to both the environment and the user, there has been an increasing interest in using biological or green methods to produce metal and metal oxide NPs. Recently, researchers started to utilize green synthesis methods for producing different NPs; however, the mechanisms of NP formation using plant extracts are still under investigation. Consequently, more in-depth studies are needed on how NPs are formed in the plant extract medium. This review highlights the most robust mechanisms of ZnO NPs formation using plant extracts and covers the commonly used plants for ZnO NP synthesis over the last fourteen years. This review will help researchers in understanding the formation mechanisms proposed for nanoparticle synthesis using plant extracts and in identifying knowledge gaps in this field.

Keywords: Nanoparticles, Green synthesis, ZnO nanoparticles, Plant extract, Formation mechanism.

1. Introduction

The field of nanotechnology is one of the important fields of investigation in contemporary materials science. It is developing rapidly and continuously, influencing nearly every sector of human life. This field also generates an increasing interest in life sciences, especially in medical procedures and biotechnology [1]. The word "Nanoparticles" refers to particles having sizes between 1 and 100 nm, while "Nanotechnology" is defined as the field of technology that uses nanomaterials in practical applications, such as in medical devices, coating,

Corresponding Author: Azeez A. Barzinjy **Email**: azeez.azeez@soran.edu.iq

surface modification, etc. The Greek word "nano" means "dwarf" or "small things", and it relates to one billionth of a meter (10^{9} m) [2]. Nowadays, metallic NPs have attracted countless scientific attention due to their special optoelectronic, physical, and chemical properties with applications in fields such as molecular diagnostics [3], drug delivery [4], imaging [5], solar cells [6], catalysis [7], and sensing [8].

In recent years, the focus on zinc oxide nanoparticles (ZnO NPs) and their applications has increased dramatically as a result of their outstanding properties [9]. ZnO NPs are the most broadly used nanoparticles in numerous applications, including smart UV sensors [10], targeted drug delivery [11], antioxidant activity [12], anticancer activity [13], biosensors [14], environmental remediation [15], water purification [16], and even as agents that enhance drought tolerance and serve as nutrient source of crops [17].

NPs synthesis is normally conducted by means of three main approaches: physical, chemical, and green/biological approaches (as shown in Fig. 1) [18]. Each of these methods possesses its own identifiable special properties. Physical and chemical methods have greater efficacy for producing stable nanostructures of a similar size; however, they do not meet the purpose of obtaining long-term sustainability [19]. The most important step in the NPs synthesis method is the selection of eco-friendly solvents as good reducing, capping, and safe stabilizing agents. Yet, physical and chemical methods often rely on using hazardous materials, require advanced equipment, and have a negative impact on the environment. In contrast, the biological or green technique, which uses microorganisms such as bacteria, fungi, yeast, and plant extracts, offers a safer, affordable, dependable, and eco-friendly way to create many kinds of nanomaterials. There is a rising demand for the development of an environmentally friendly NPs synthesis technique that does not use harmful ingredients [20].

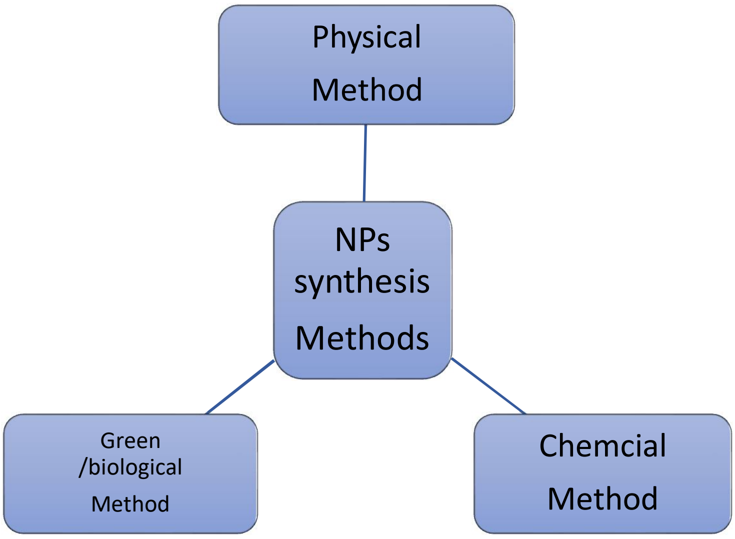

FIG. 1. Methods of synthesizing NPs.

Various studies have been conducted for synthesizing ZnO NPs, using different methods, including green synthesis with plants, algae, bacteria, fungi, and other biological sources. This is owing to the fact that green synthesis is considered the most eco-friendly, affordable, safe, and straightforward method. Plants, in particular, are favored because they enable large-scale production of stable nanoparticles in diverse shapes and sizes, using environmentally friendly, simple, and inexpensive extracts along with other natural components [21]. Owing to the presence of phytochemicals, which act as reducing, capping, and stabilizing agents, various plant parts, including leaves, fruits, roots, stems, and seeds, have been employed to produce NPs. The size and morphology of the resulting NPs can be controlled by the existing phytochemicals, tailoring them for a number of applications [22].

Instead of using toxic chemicals or energy-intensive machines, the green method of nanoparticle synthesis has been proposed. For ZnO NPs, green synthesis is particularly attractive due to its low toxicity and minimal impact on human health and the environment. Compared with microorganism-mediated synthesis, the use of plant extracts is a very straightforward technology to produce ZnO NPs on a large scale, making it one of the most promising green methods.

Although there are numerous contemporary scientific studies on the green synthesis of nanoparticles using different plant extracts, the underlying mechanisms of nanoparticle formation have not yet been extensively addressed [23, 24]. This review aims to fill this gap by focusing specifically on the formation mechanisms of ZnO NPs synthesized using plant extracts. ZnO NPs were selected because of their unique physical and chemical properties and their wide range of advanced applications in medicine, food, healthcare, wastewater treatment, anticancer therapies, and various industrial fields. The novelty of this review lies in its critical evaluation of green synthesis mechanisms, with the goal of advancing understanding of how ZnO NPs are formed, identifying knowledge gaps, and highlighting current and future trends in their production.

2. Role of Phytochemicals in Synthesizing ZnO NPs

Phytochemicals are natural compounds present in plants and are categorized into primary and secondary metabolites based on their function in plant metabolism. Primary metabolites, such as amino acids, proteins, lipids, purines, and pyrimidines of nucleic acids, are required for plant life. Secondary metabolites, by contrast, are not directly involved in basic plant life functions; hence, they do not play a role in the growth and development of plants. The secondary metabolites are categorized into five major classes, according to their compound structure: carbohydrates, terpenoids, phenolics, alkaloids, and polyketides [25].

Over the past decade, plant extracts have been widely used for the creation of numerous metal and metal oxide NPs. Particularly, they have been investigated for the synthesis of zinc oxide nanoparticles. The primary process in the production of zinc oxide NPs using plant extracts is the reduction of zinc ions by phytochemicals and enzymes that are easily found in the extracts [24]. Generally, the green nanoparticle manufacturing process proceeds through three steps: reduction phase, growth phase, and stabilization phase. The first and most essential step is the reduction phase, in which phytochemicals of plant extracts can interact with metal ions. These interactions allow metal ions to be reduced to metal atoms, and then nucleation of the reduced metal atoms occurs [26]. Next, during the growth phase, individual metal atoms unite through the coarsening process to form big particles of a stable size and shape. As the growth phase lengthens, NPs can develop into diverse morphologies such as nanorods, nanotubes, hexahedrons, prisms, and others [27]. The stabilization phase is the last step in the biosynthesis of nanoparticles. When nanoparticles are covered with plant metabolites, they gradually obtain their most favorable and stable form [28]. Typically, the final product is subjected to heat treatment. Differential scanning calorimetry (DSC) reveals a strong exothermic peak around 500 °C, corresponding to the crystallization of ZnO NPs. Figure 2 illustrates the mechanism of ZnO NP formation via plant-based green synthesis.

3. Mechanism of the Formation of ZnO NPs from Plant Extracts

Biosynthesis of nanoparticles offers a promising alternative to chemical and physical methods. Recently, green methods using plant extracts have been developed to synthesize metal oxide NPs. Phytochemicals in plants, such as polysaccharides, polyphenols, flavonoids, vitamins, amino acids, alkaloids, tannins, saponins, and terpenoids, are usually utilized as reducing and capping agents that react with zinc salt solution to form zinc oxide nanoparticles [29]. Plants are often favored in green nanoparticle synthesis because plant substrates are thought to be less expensive, easier to process, and less harmful than other microorganisms. Additionally, there are no health and safety issues imposed on humans due to the use of harmful microorganisms during the process [30].

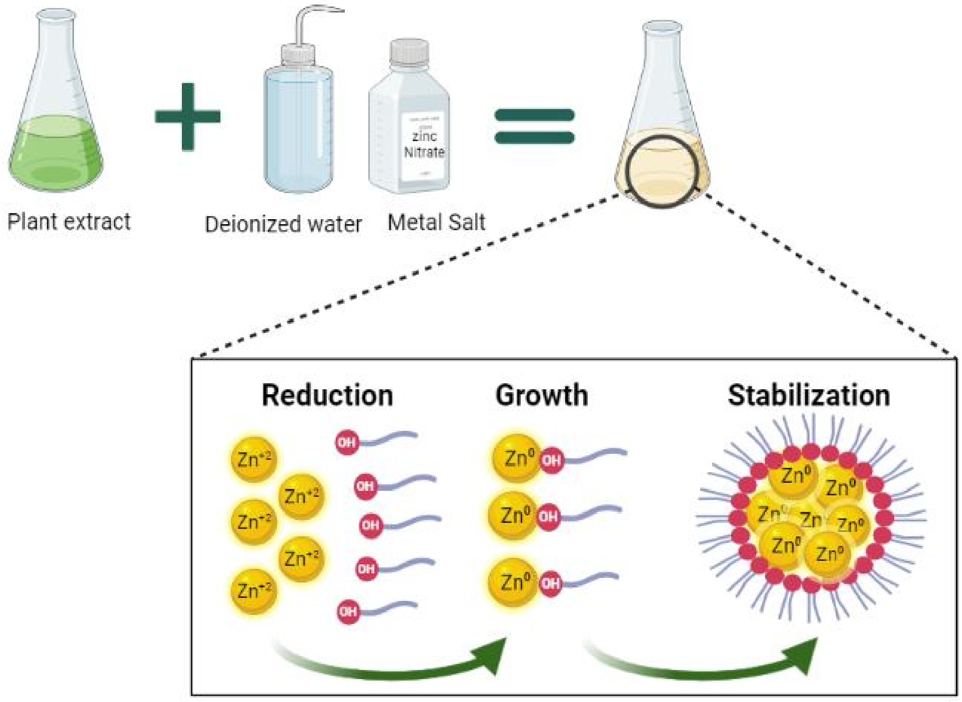

FIG. 2. Proposed mechanism for the green synthesis of ZnO NPs.

Although there are numerous studies showing the benefit of green synthesis in producing metal and metal oxide NPs, the formation mechanism of NPs is not yet clear and requires further investigation. We believe that the real problem lies in the lack of consensus among chemists, physicists, and biologists. An integrated explanation of the nanoparticle formation mechanism requires taking all aspects together rather than viewing this issue from one angle. Consequently, in this study, we summarize the current studies related to the mechanism of formation of zinc oxide nanoparticles utilizing different fragments of plant extracts.

In 2011, Gunalan *et al.* [31] synthesized zinc oxide nanoparticles using *Aloe barbadensis miller* leaf extract. It was found that various terpenoids, phenolic compounds, or proteins adhered to the surface of ZnO NPs and remained there after several washings. Free amino and carboxyl groups that were attached to the zinc surface were believed to be responsible for the stability of the ZnO NPs. However, heterocyclic chemicals that form functional group bonds such as -CO-C-, -CO-O-, and -C=C-, as well as amide domains formed from proteins found in leaf extracts, act as a capping agent around the NPs. Additionally, the presence of the proteins in the medium helps to stabilize the metal nanoparticles by producing a coat around them and preventing agglomeration. Overall, this research provides insights into the formation mechanism of zinc oxide nanoparticles and highlights the role of some phytochemicals in stabilizing the nanoparticles, although there remain some uncertainties associated with unclear scientific explanations.

In 2014, Brajesh *et al.* [32] prepared zinc oxide nanoparticles from *Citrus paradisi* peel extracts and investigated the mechanism of NPs formation. They found that flavonoids, limonoids, and carotenoids with free OH/COOH groups could interact with zinc sulfate to produce ZnO NPs. Based on these findings, they proposed a plausible formation mechanism, illustrated in Fig. 3. To our understanding, this extensive study provides a new technique to explain the formation mechanism of zinc nanoparticles through visual illustration; however, the evidence provided is still insufficient for readers to fully understand all steps of zinc nanoparticle formation.

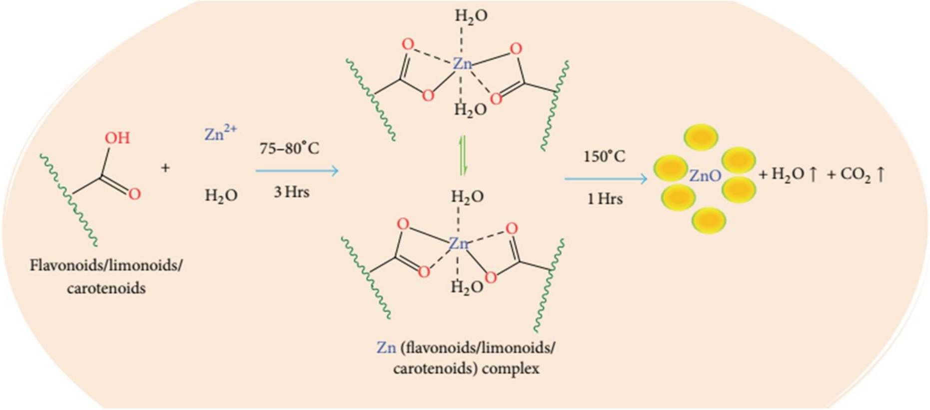

FIG. 3. The possible mechanism of ZnO NPs formation proposed by Ref. [32].

In 2015, Buazar *et al.* synthesized zinc oxide nanoparticles by utilizing potato extracts and explored the formation mechanism [33]. It was shown that potato is a high-carbohydrate crop that is mostly made up of starch, a natural polymer. The presence of a large number of hydroxyl groups in starch can help the complexation of zinc ions with the molecular matrix, whereas the aldehyde terminals assist in the reduction of Zn(II) ions to Zn(0). Beyond these mechanistic roles, starch offers several advantages as a renewable protective agent. First of all, starch may be dispersed in H_2O; as a result, organic solvents can be avoided totally. Second, the starch-metal nanoparticle binding relationship is a bit weak compared with the interactions between NPs and typical thiol-based protective groups; this indicates that the protection should be simply changeable at comparatively above-average temperatures, allowing for particle separation. Using the multifunctional (reducing and capping) characteristics of starch-rich potato extract, Buazar *et al.* proposed a streamlined technique of organic phase synthesis of zinc oxide nanoparticles through a green approach (Fig. 4). This study provided a comprehensive explanation of the formation mechanism of ZnO NPs and highlighted the role of starch in both complexation and reduction. However, while weak starch–nanoparticle binding is advantageous for particle recovery, it may pose challenges in applications requiring stronger stabilization, where insufficient binding could compromise nanoparticle stability.

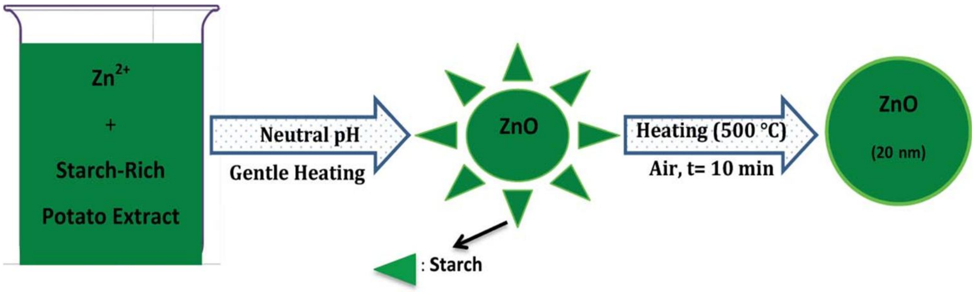

FIG. 4. Plant extract as both reducing and stabilizing agent of ZnO NPs [33].

In 2016, Prasanta *et al.* synthesized zinc oxide nanoparticles by utilizing tomato (*Lycopersicon esculentum*) extracts and investigated the mechanism of NPs formation [34]. Their study demonstrated that tomato extract through ascorbic acid is reducing Zn^{+2} ions and forms ZnO NPs. Ascorbic acid initially changes into a free radical ion known as "semihydro-ascorbic acid" and then oxidizes to become dehydro-ascorbic acid. Also, ascorbic acid behaves as a stable (electron + proton) donor during interactions. Therefore, ascorbic acid was capped with zinc ions, and Zn^{2+} was reduced within the nanoscale template to generate Zn(0) atoms.

In 2017, Senthilkumar *et al.* synthesized zinc oxide nanoparticles from *Tectona Grandis* leaf extracts [35]. It was shown that the primarily available chemical elements in the *Tectona Grandis* leaf extracts are phenols and flavonoids. It was clarified that through the available phenols and flavonoids in the aqueous leaf extract, the manageable size of ZnO NPs can be produced. The OH groups in phenols and flavonoids act as reducing and capping agents. Secondary metabolites were found in almost all medicinal plants, including phenols and flavonoids, which have been studied for their role as bio-reducing agents of metallic ions in aqueous medium. These phytochemicals also have a wide range of biological roles, ranging from antioxidants to anti-carcinogenic properties. Also, it was explained that the detected vibrational bands in the Fourier-transform infrared spectrum show the functional groups responsible for the reducing, capping, and stabilizing agents. To the best of our knowledge, the aptitude of these secondary metabolites to bind to zinc surfaces and induce nanoparticle formation is an essential step towards understanding the basic mechanisms of NPs formation. Likewise, the remark of these compounds as potential capping agents and their ability to control the size of the nanoparticles offers a new view of these compounds and the size of ZnO NPs. However, more technical information about the actual chemical events might help us understand the phenomena better.

In 2018, Joghee *et al.* synthesized ZnO NPs from *Costus pictus D. Don* leaf extract and investigated their formation mechanism presented in Fig. 5 [36]. They believed that zinc oxide nanoparticles are formed by diosgenin ($C_{27}H_{42}O_3$), a phyto-steroid sapogenin. It was explained that when diosgenin reacts with a metal nitrate, weak hydrogen bonds produce a complex (for example, a metal-diosgenin complex). This complex solution is then put in a high-temperature oven for eight hours to be transformed into hydroxide forms. The bio-synthesized hydroxide complex material is calcined to generate metal oxide NPs. Although *Costus pictus* leaf extracts contain numerous phytochemicals, the study focused specifically on a diosgenin compound because it easily attracts metals due to its phenolic content. According to our understanding, a more detailed description of this mechanism might improve comprehension of the process. While the formation of the metal–diosgenin complex was described, the precise chemical interactions and pathways were not fully elaborated. Additionally, although the authors emphasized the role of phenolic content in metal attraction, they did not clarify why phenolic groups are critical in this process.

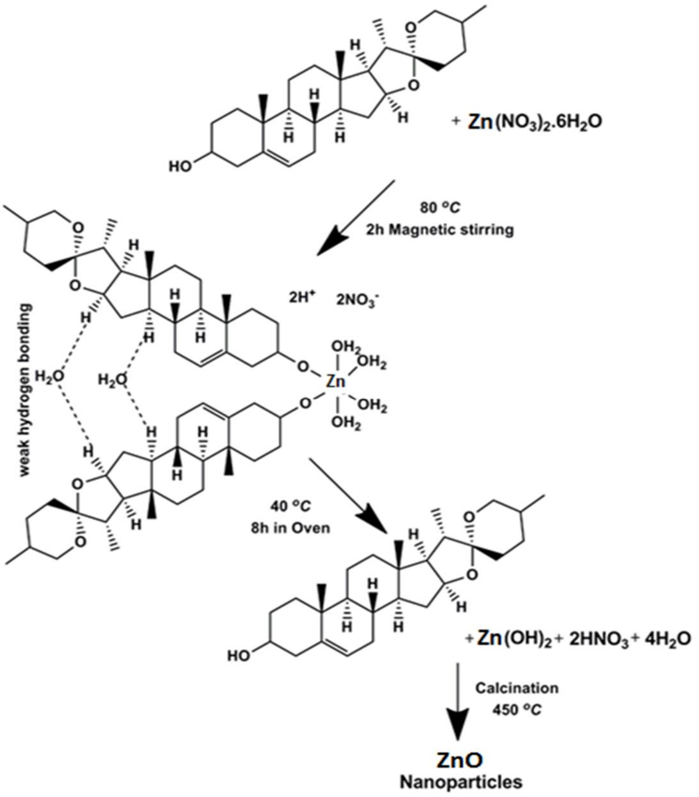

FIG. 5. Proposed mechanism of formation ZnO NPs [36].

In 2018, Luque *et al.* [37] produced zinc oxide nanoparticles using orange (*Citrus sinensis*) peel extract and explored the mechanism of the NPs formation. It was proposed that the synthesis process of ZnO NPs using *C. sinensis* peel extract can potentially occur through a reaction mechanism. This mechanism involves the interaction between the functional molecules present in the orange peels and the zinc precursor. Within these components, certain aromatic hydroxyl groups possess the ability to bind with zinc ions, thereby forming zinc-ellagate structures. Upon heat treatment at 400 °C, these structures undergo direct decomposition, leading to the liberation of the freshly synthesized ZnO nanoparticles. Figure 6 displays the mechanism of zinc oxide nanoparticle formation utilizing *C. sinensis* peel extract. However, the information provided appears insufficient to fully elucidate the mechanism of NPs synthesis. In particular, specific details regarding the key phytochemicals responsible for reduction, capping, and stabilization were not addressed.

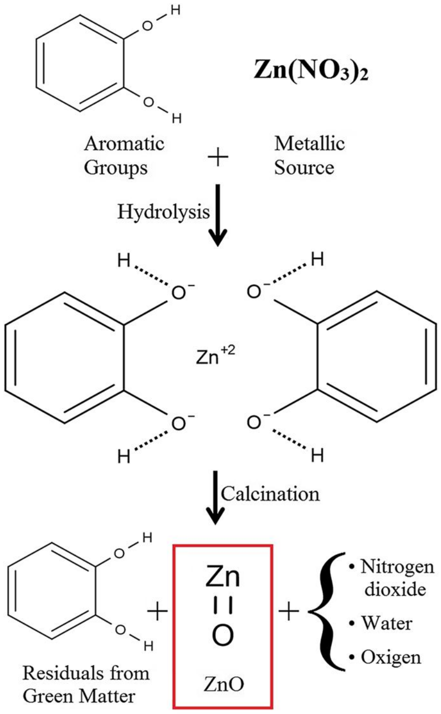

FIG. 6. Proposed mechanism of formation of ZnO NPs from Ref. [37].

In the same year, Mina *et al.* [38] prepared zinc oxide nanoparticles using *Thymus vulgaris* leaf extracts and investigated their synthesizing mechanism. It was reported that the presence of phenol byproducts (thymol and flavonoid) in the leaf extract works as a size reducer throughout the zinc oxide NPs producing process, preventing further development of ZnO crystals. The OH/COOH groups found in phenol are bonded to the surface of zinc oxide particles and behave as surfactants, stabilizers, and size-reducing agents. As a result, they prevent overreaction, the formation of additional compounds, and the growth of ZnO. Figure 7 depicts the possible mechanism of this process.

$$Zn\,(NO_3)_2.6H_2O+2NaOH \xrightarrow{\Delta} Zn\,(OH)_2 + 2NaNO_3$$

$$Zn\,(OH)_2 + NaNO_3 \xrightarrow{Thymus\ leaf\ extract} ZnO\ \text{nanoparticles}$$

Basically, this study highlighted the essential role of OH/COOH groups in phenol as reducing and stabilizing agents. These findings may guide further research toward plants rich in such functional groups for more effective green synthesis of ZnO nanoparticles.

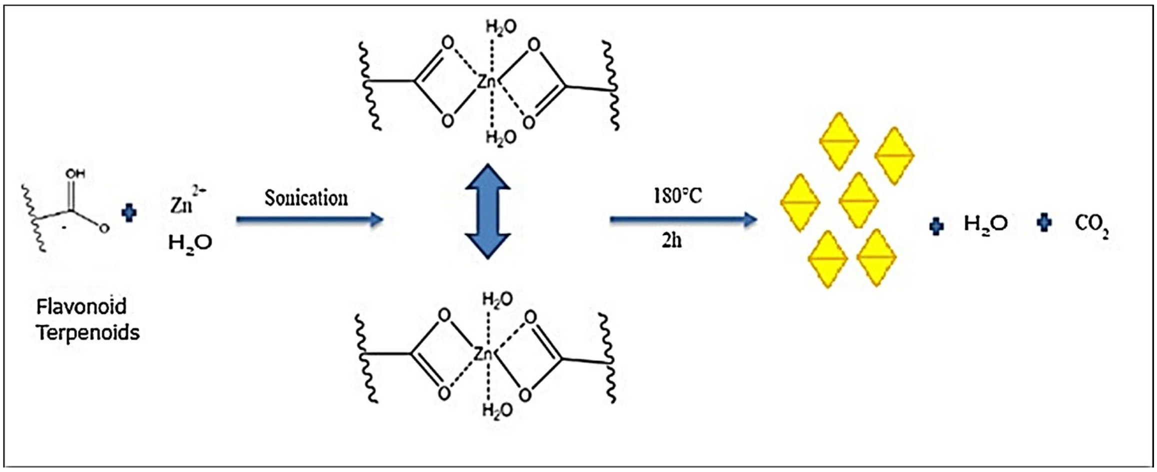

FIG. 7. Possible mechanism of ZnO NPs synthesis and formation using Ref. [38].

In 2020, Vijayakumar *et al.* prepared zinc oxide NPs by utilizing *Acalypha fruticosa L.* leaf extracts and explained the mechanism of ZnO NPs construction [39]. It was shown that *A. fruticosa* leaf extract contained nine chemicals, six of which were flavonoids, one terpenoid, and two glycosides. It was explained that only flavonoids are taken into account because they contribute to the structure of the dominant chemicals found in the extracts, namely 2-Methyl-5,7-dihydroxyl chromone, 9,12-Octadecadienoic acid, Kaempferol-3-Orutinoside, Quercetin, Acalyphin, and Apigenin. The proposed mechanism involves the reaction of 2-Methyl-5,7-dihydroxylchromone with zinc acetate dihydrate [Zn $(CH_3COO)_2$:$2H_2O$], where oxidation by free radicals in the extract leads to the formation of dehydro-2-Methyl-5,7-dihydroxylchromone.
Electrostatic attraction between these free radicals and zinc cations facilitates reduction and nucleation. Figure 8 depicts the formation mechanism of ZnO NPs. While flavonoids were emphasized due to their key functional groups acting as reducing agents, it is also important to consider the roles of glycosides and terpenoids, which likely contribute to capping, preventing aggregation, and ensuring long-term nanoparticle stability.

In 2019, Barzinjy *et al.* synthesized ZnO NPs using pomegranate (*Punica granatum*) juice extract and explored their formation mechanism [40]. The extract was shown to be rich in polyphenols, which possess phenolic rings with multiple hydroxyl groups (Fig. 9). These groups act as reducing and capping agents, enabling interaction with Zn^{+2} ions to form zinc hydroxide complexes. Upon annealing, these complexes are converted into ZnO nanoparticles. This study presented a clear and straightforward mechanism that is accessible even to readers without extensive knowledge of phytochemicals.

Subsequently, in 2020, Barzinjy *et al.* reported another study, this time utilizing *Eucalyptus globulus Labill.* leaf extracts for the synthesis of ZnO NPs [41]. They proposed the following possible mechanism of formation:

$$nZn^{2+} + 2Ar - (OH)_n \rightarrow nZn^0 + 2nAr = O + 2nH^+$$

$$2(x + 1)\, Zn^0 + 2Ar = O + yO_2 \rightarrow 2(ZnO - Zn_xO_y - Ar = O)$$

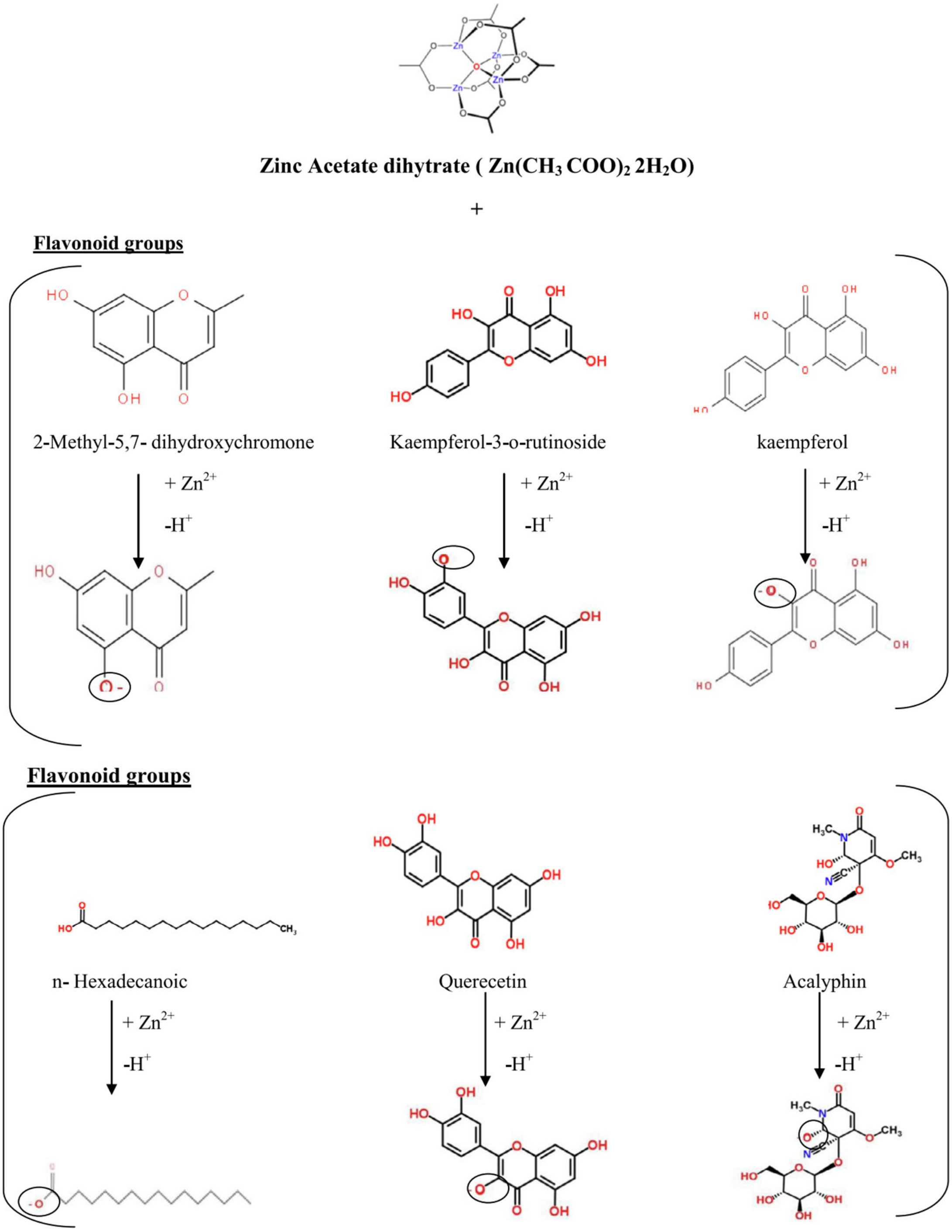

FIG. 8. Proposed mechanism of ZnO NPs formation, adapted from Ref [39].

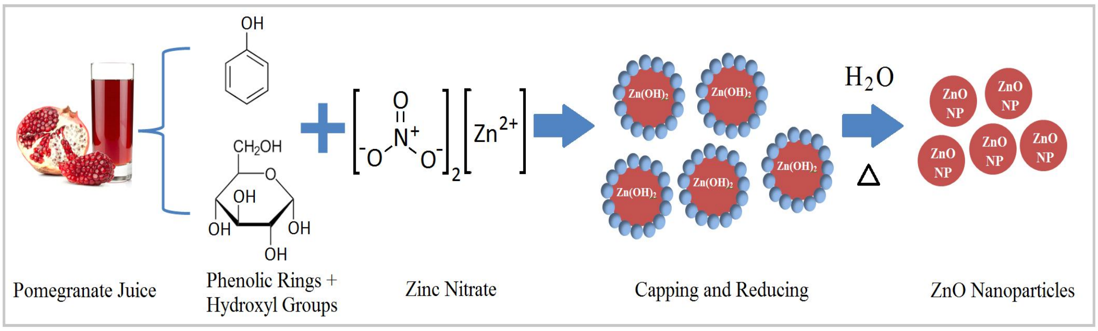

FIG. 9. Proposed mechanism of ZnO NPs formation, adapted from Ref [40].

The natural compounds found in *Eucalyptus globulus* leaf extracts, such as tannins and flavonoids (Ar-$(OH)_n$), play a crucial role in ZnO nanoparticle formation. These biomolecules have the ability to release electrons, thereby aiding in the efficient reduction of Zn^{2+} ions to Zn^0. This process creates a Zn^0-phenolate complex due to a chelating effect, which promotes the nucleation and growth of nanoparticles at a temperature of 60 °C. As the temperature increases to 100 °C in the presence of air, this complex directly decomposes, leading to the formation of Zn nanoparticles. Consequently, the natural phenolic compounds demonstrate a positive influence on the ZnO NPs preparation. From our perspective, this highlights the positive role of natural phenolic compounds in the ZnO nanoparticle synthesis process. Also, this might offer a clear understanding of the potential benefits of utilizing plant extracts in nanomaterial production. However, the formation of a Zn^0-phenolate complex and its subsequent decomposition, possibly, does not provide a complete scenario of the underlying chemical mechanisms for readers who are not knowledgeable in this field.

In 2021, Vishnu *et al.* published an article in which they prepared ZnO NPs by using *Scoparia Dulcis* leaf extracts and explained the mechanism of formation [42]. They reported that several phytochemicals in the extract act as both stabilizers and reducing agents. Specifically, the hydroxy and oxo substituents of plant metabolites interact with Zn^{2+} ions, enabling the reduction process. Figure 10 presents the plausible mechanism for ZnO NP formation mediated by *S. dulcis* phytochemicals. To propose the mechanism, the authors selected 2-hydroxy-2H-1,4-benzoxazol-3-one, an active compound found in all parts of the plant. The mechanism involves deprotonation of the hydroxyl group, generating a negatively charged oxygen center. Zinc ions are then chelated at this site, leading to complex formation and ultimately the generation of ZnO nanoparticles. In our assessment, this study demonstrates that hydroxy and oxo substituents play a central role in Zn^{2+} interaction. However, the specificity of these interactions remains unclear. Furthermore, clearer descriptions of the roles of individual phytochemicals would greatly enhance readers' understanding of the proposed mechanism.

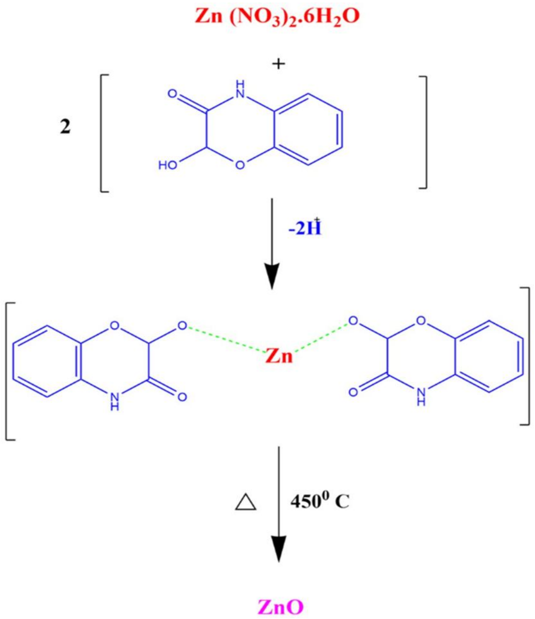

FIG. 10. Proposed mechanism of ZnO NPs formation, adapted from Ref. [42].

In 2022, Supin *et al.* prepared ZnO NPs using *Lepidagathis ananthapuramensis (LA)* leaf extract and explained the mechanism of formation [43]. It was shown that the *LA* leaves extracts contain flavonoids, alkaloids, phenols, and quinones, which participate in producing ZnO NPs via chemical reduction and oxidation processes. These phytochemicals function not only as reducing and oxidizing agents but also as effective capping agents during the formation process. Also, it was mentioned that the actual mechanism for synthesizing ZnO nanoparticles from leaf extracts is not totally understood. Nevertheless, they proposed that two main steps are sufficient to explain the likely formation process, as follows:

1. Zn $(OH)_2$ is formed from the corresponding Zn $(NO_3)_2.6H_2O$ salt.
2. Calcination of the resulting intermediate produces ZnO NPs.

During the process, Zn^{2+} ions available in the zinc electrolytic solution [Zn $(NO_3)_2.6H_2O$ solution] are reduced to the stabilized compound by chelating to phytochemicals, including polyphenols and flavonoids contained in the leaf extract. Through extracting a proton from the phytochemicals, the anionic component of thezinc salt is removed as the corresponding acid. Water molecules attempt to transfer their protons to the corresponding phytochemicals. As a result, the hydroxyl group in the reaction mixture (biomolecule or solution) forms a bond with the stabilized metal species, resulting in the formation of zinc hydroxide (Zn $(OH)_2$). All of these procedures take place at the same time, as illustrated in Fig. 11. According to our assessment, this study aimed to explain the formation mechanism in detail. However, the authors acknowledged that the process is not yet fully understood. Further improvements could include specifying the exact phytochemicals involved, elaborating their roles, and providing a step-by-step description of the formation mechanism to help other researchers address these gaps.

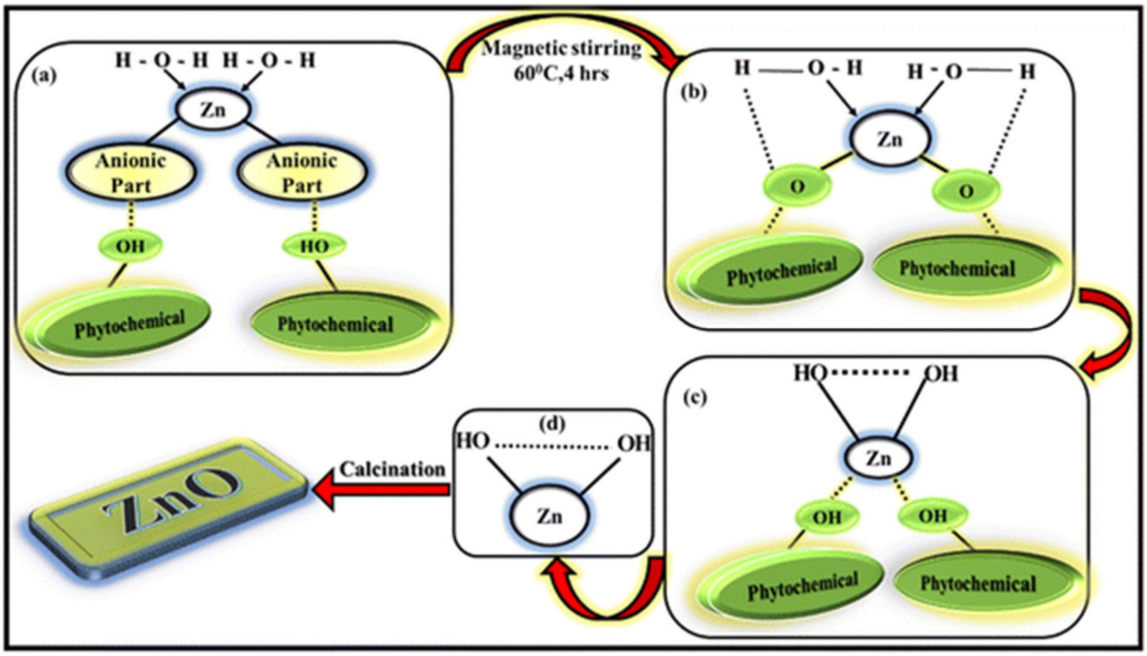

FIG. 11. Proposed mechanism of ZnO NPs formation, adapted from Ref. [43].

In 2023, Maymounah *et al.* synthesized ZnO nanoparticles using *Ziziphus jujuba* leaf extracts and clarified the formation mechanism [44]. The study revealed that *Ziziphus jujuba* plants contain a rich variety of phytochemicals, including terpenoids, tannins, phenolic compounds, saponins, alpha-tocopherol, beta-carotene, flavonoids, alkaloids, sterols, and fatty acids, which work as both reducing and capping agents to avoid ZnO NPs agglomeration, likely due to the presence of long-chain natural products in the extract. These compounds may convert Zn^{2+} to Zn^0, which may then be oxidized to ZnO NPs during the heating process. Moreover, complexation may occur between Zn^{2+} ions and phytochemicals such as polyphenols, leading to the formation of zinc hydroxide (Zn $(OH)_2$) hydrolysis. Upon heating, the complex decomposes to yield stable ZnO nanoparticles. However, the study did not specify which phytochemicals play the most dominant role in the formation process, leaving some uncertainty about the key contributors.

4. Zinc Oxide Nanoparticles Synthesis from Plant Extracts

Plant extracts have recently been used as green media for nanoparticle synthesis because they act as natural chemical factories that are cost-efficient and require minimal maintenance. Various parts of plants, including flowers, leaves, fruits, stems, and roots, have been widely utilized in green synthesis due to the presence of bioactive phytochemicals. These compounds, such as terpenoids, alkaloids, phenols, tannins, and vitamins, simultaneously act as stabilizing and reducing agents during nanoparticle formation [45].

Numerous plants have been reported so far for synthesizing zinc oxide nanoparticles. Ravindra *et al.* were the first to use the milky latex of the plant *Calotropis procera* to successfully biosynthesize ZnO NPs [46]. Their research showed that the ZnO nanoparticles have a spherical shape, and the nanoparticle sizes were in the range of 5-40 nm. The synthesized ZnO NPs were characterized by UV–Vis spectroscopy, scanning electron microscope (SEM), transmission electron microscopy (TEM), X-ray diffraction (XRD), and photoluminescence (PL). Their research also highlighted the potential applications of these nanoparticles in biosensing devices and nanoelectronics due to their environmentally friendly characteristics.

In another study, Gunalan *et al.* prepared ZnO nanoparticles by utilizing *Aloe barbadensis Miller* leaf extracts and obtained stable spherical ZnO NPs [31]. Moreover, the biosynthesis of ZnO NPs produced polydisperse NPs, with the average particle sizes of 25 to 45 nm. Niranjan *et al.* prepared zinc oxide nanoparticles by utilizing *Hibiscus subdariffa* leaf extracts by dissolving 1 g of zinc acetate in 50 mL of distilled water, gradually adding the solution to 20 mL of plant extract preheated at 50 °C for 10 minutes [47]. After 30 minutes of stirring, the mixture reduced to zinc hydroxide, which was then vacuum-dried at 30 °C. Additional samples were dried at 60 °C and 100 °C. SEM analysis revealed that the drying temperature influenced the morphology: irregular surfaces were observed at 30 °C, spherical structures at 60 °C, and dumbbell-shaped, more crystalline structures at 100 °C.

Javed *et al.* biosynthesized ZnO NPs by utilizing *Elaeagnus angustifolia L.* leaf extracts and explored their multiple in vitro biological applications [48]. UV–Vis spectroscopy confirmed the synthesis, showing a surface plasmon resonance (SPR) peak at 399 nm. The resulting nanoparticles were spherical with an average size of around 26 nm. The study demonstrated that ZnO NPs exhibited strong antibacterial, antifungal, antioxidant, biocompatibility, anticancer, and enzyme inhibition activities. Sangeetha and Thambvani compared two approaches for ZnO NP synthesis: a chemical method using sodium hydroxide and zinc acetate precursors, and a biological method using *Coriandrum sativum* leaf extract with zinc acetate [49]. SEM and XRD analyses showed that the biosynthesized ZnO NPs had an average size of 66 nm, whereas the chemically synthesized ones were slightly larger at 81 nm. The authors concluded that the green method was superior due to its eco-friendly and cost-effective nature.

Suresh *et al.* reported the synthesis of ZnO NPs using *Cassia fistula* extracts through a green synthesis method aimed at harnessing antioxidant and antibacterial properties [50]. TEM and XRD analyses revealed nanoparticles with sizes ranging from 5 to 15 nm and a hexagonal wurtzite structure. The ZnO NPs showed high efficiency in degrading methylene blue dye under both UV and sunlight exposure. They also exhibited excellent antioxidant activity, effectively scavenging DPPH free radicals, and demonstrated antibacterial activity against *Plasmodium desmolyticum*, *Klebsiella aerogenes*, *Staphylococcus aureus*, and *Escherichia coli*.

Barzinjy *et al.* synthesized ZnO NPs using *Euphorbia petiolata* leaf extracts mixed with an aqueous zinc nitrate solution [51]. The reaction resulted in the reduction of zinc ions and the formation of ZnO nanoparticles, confirmed by UV–Vis spectroscopy (SPR peak at 360 nm). XRD analysis revealed a hexagonal wurtzite structure with average particle sizes of 55–60 nm. In another study, Barzinjy and Himdad synthesized ZnO NPs from *Eucalyptus globulus Labill.* leaf extracts combined with zinc nitrate hexahydrate [41]. The mixture, stirred continuously at 60 °C, changed color from light green to yellowish paste, indicating nanoparticle formation. The ZnO NPs were spherical with average sizes between 27 and 35 nm. Characterization showed a band gap of 2.67 eV, high stability (zeta potential and BET surface area of 23.481 m^2/g), and thermal behavior confirmed by DSC, which revealed two endothermic peaks (water evaporation and zinc hydroxide conversion) and an exothermic peak (ZnO crystallization and organic material degradation).

Farjana *et al.* produced zinc oxide nanoparticles with an average size of 16.6 nm from the leaf extracts of *Cocos nucifera* through an easy, inexpensive, and green process [52]. Various techniques, including UV-Vis spectroscopy, XRD, FTIR, EDX, and SEM investigations, were utilized to identify and characterize the produced NPs. According to UV-Vis spectroscopy measurements, the aqueous solution of the produced zinc oxide nanoparticles displayed absorption maxima, λ_{max}, at 370 nm. XRD analysis showed that the produced ZnO NPs have a hexagonal wurtzite shape. The produced nanoparticles showed strong photocatalytic activity and modest antioxidant activity. Based on these findings, the authors concluded that the produced zinc oxide nanoparticles could be utilized in biological, therapeutic, and pharmacological applications, as well as used as photocatalysts in the dye degradation process. Recently, Muthu Kathija *et al.* used *Pisonia alba* leaf extract to prepare zinc oxide nanoparticles [53]. In this investigation, XRD, UV–Vis, FTIR, XPS, and FESEM with EDS were utilized to study the morphological and structural characteristics of the produced ZnO NPs. The highest absorbance was observed at 375 nm, corresponding to an energy gap of 2.96 eV. The average particle size, according to XRD analysis, was 48 nm. In addition, green ZnO NPs showed antimicrobial efficacy against both Gram-positive (*S. aureus*) and Gram-negative (*K. pneumoniae*) bacteria. Table 1 lists 80 different plants reported in the literature for the green synthesis of ZnO nanoparticles.

TABLE 1. Plant extracts used for synthesizing ZnO NPs.

Plant name	Plant part	NPs Size (nm)	Morphology	Surface Plasmon Resonance (SPR)	Year	Reference
Cicer arietinum	Seeds	20–30	spherical	401, 482 and 524	2010	[54]
Aloe barbadensis Miller	Leaves	25-40	Spherical	375	2011	[31]
Physalis alkekengi L	roots, leaves, stems, and fruits	72.5	triangular and elongated	-	2011	[55]
Sedum alfredii Hance	-	53.7	pseudo-spherical	-	2011	[56]
Calotropis procera	Milky latex	5-40	Spherical, granular	368	2011	[46]
Teucrium polium L	Flower	-	elongated	250 to 380	2013	[57]
Parthenium hysterophorus L.	Leaves	27 ± 5 and 84 ± 2	spherical and hexagonal	374 and 370	2013	[58]
P. trifoliate	Fruit	21.12	spherical	327	2013	[59]
Calotropis gigantea	Leaves	30–35	Spherical	-	2013	[60]
Corriandrum sativum	Leaves	66	Cubic	-	2013	[49]
Sargassum myriocystum	Leaves	36	Spherical	-	2013	[61]
Camellia sinensis	Leaves	16	hexagonal	325	2014	[62]
Hibiscus rosa-sinensis	Leaves	30-35	Spongy	-	2014	[63]
Tabernaemontana Divaricate	Leaves	36 ± 5	Spherical	-	2014	[64]
Murraya koeininggi	Leaves	30-35	Hexagonal	-	2014	[65]
Plectranthus amboinicus	Leaves	88	a rod	390	2015	[66]
Pongamia pinnata	Leaves	100	spherical	358	2015	[67]
Solanum nigrum	Leaves	20–30	wurtzite hexagonal	358	2015	[68]
Vitex trifolia L	Leaves	28	spherical	372.56	2015	[69]
Murraya koenigii	Leaves	12	spherical	373	2015	[70]
Azadirachta indica	Leaves	9.6-25.5	spherical	377	2015	[71]
Corymbia citriodora	Leaves	64	polyhedron	386	2015	[72]
Trifolium pratense	Flower	100–190	-	283	2015	[73]
Laurus nobilis	Leaves	47.27	hexagonal	338	2016	[74]
Potato	Roots	20∓1.2	Hexagonal	-	2016	[33]
Ocimum tenuiflorum	Leaves	15 -132 ± 10	rod	380	2016	[75]
Carissa edulis	Fruits	50–55	flower	358	2016	[76]
Limonia acidissima L	Leaves	12-53	spherical	374	2016	[77]
Boswellia ovalifoliolata	Stems	20	spherical	240	2016	[78]
Lycopersicon esculentum	Fruits	50 and 90	spherical	360	2016	[34]

Plant name	Plant part	NPs Size (nm)	Morphology	Surface Plasmon Resonance (SPR)	Year	Reference
Ruta graveolens (L.)	Stems	~28	spherical	355	2016	[12]
Passiflora caerulea	Leaves	70	spherical	380	2017	[79]
Tectona grandis (L.)	Leaves	54	spherical	360	2017	[35]
Sechium edule	Leaves	36.2	a spherical	362	2017	[80]
Musa paradisiaca	Leaves	23.3	spherical	338	2017	[81]
Ziziphus nummularia	Leaves	17.33	spherical/irregular	370	2017	[82]
Imperata cylindrica L	Leaves	11.9	wurtzite hexagonal	359	2017	[83]
Calotropis procera	Leaves	15–25	hexagonal wurtzite	397	2017	[84]
Ipomoea pes-caprae	Leaves	2–20	hexagonal wurtzite	322	2017	[85]
Melia dubia	Leaves	13.39	hexagonal wurtzite	-	2017	[86]
Citrus aurantifolia	Peel	50	Hexagonal	-	2017	[87]
Bauhinia tomentosa	Leaves	22–94	hexagonal	370	2018	[88]
Aristolochia indica	Leaves	22.5	quasi-spherical	367	2018	[89]
Andrographis paniculata	Leaves	96–115 and 57 ± 0.3	spherical and hexagonal	375	2018	[90]
Vaccinium arctostaphylos L	Fruits	-	spherical	420	2018	[91]
Crinumlatifolium	Leaves	10–30	hexagonal and spherical	320	2018	[92]
Coccinia abyssinica	Tuber	10.4	hexagonal	365	2018	[93]
Lawsonia inermis	Leaves	75-100	hexagonal	-	2018	[94]
Citrus sinensis	Peel	-	hexagonal wurtzite	-	2018	[37]
Costus pictus D. Don	Leaves	40	Hexagonal and spherical	-	2018	[36]
Justicia wynaadensis	Leaves	~39	hexagonal wurtzite	329	2019	[95]
Papaver somniferum L	Pod	48	irregular and spherical	360	2019	[96]
Costus igneus	Leaves	26.55	hexagonal wurtzite	365	2019	[97]
Ocimum americanum	-	21	spherical	316	2019	[98]
Pandanus odorifer	Leaves	~90	spherical	~399	2019	[99]
Plectranthus amboinicus	Leaves	88	Spherical	-	2019	[100]
Thymus vulgaris	Leaves	50−60	Irregular	~ 370	2019	[38]
Euphorbia petiolata	Leaves	55-60	hexagonal-wurtzite	360	2019	[51]
Laurus nobilis L	Leaves	21.49-25.26	spherical	350	2019	[101]
Mentha spicata	Leaves	11 to 88	spherical	-	2020	[102]
Sesbania grandiflora	Leaves	70–150	spherical and flakes	375–378	2020	[103]
Punica granatum	Fruits	~60	hexagonal wurtzite	364	2020	[104]
Eucalyptus globulus Labill	Leaves	27 and 35	hexagonal	375	2020	[41]
orange	Fruit Peel	10–20	Spherical	-	2020	[105]
Azadirachta indica	Leaves	20–30	Spherical	-	2020	[106]
Acalypha fruticosa L	Leaves	55	dispersion and spherical	310	2020	[39]
Capparis zeylanica	Leaves	32 to 40	Spherical	356	2020	[21]
Aquilegia pubiflora	Leaves	34.23	Spherical	-	2021	[107]

Plant name	Plant part	NPs Size (nm)	Morphology	Surface Plasmon Resonance (SPR)	Year	Reference
Knoxia sumatrensis	Leaves	50–80	rod	354	2021	[108]
Syzygium Cumini	Leaves	11.35	hexagonal packing	375	2021	[109]
R. tuberosa	Leaves	40–50	rod	320	2021	[110]
Syzygium cumini	Leaves	30	spherical	320	2021	[111]
Carica papaya	Leaves	15-50	semi-spherical, non-spherical, and flower	360	2021	[112]
Lantana Camara	Leaves	35	Spherical	-	2022	[113]
Pelargonium odoratissimum (L.)	Leaves	21.6	spherical and hexagonal	370	2022	[114]
Cocos nucifera	Leaves	16.6	hexagonal wurtzite	370	2022	[52]
Ailanthus altissima	Leaves	13.27	Spherical	327	2023	[115]
Camellia sinensis	Leaves	19.380 ± 2.14	hexagonal	509	2023	[116]
Lepidagathis ananthapuramensis	Leaves	10–15	hexagonal	372	2023	[43]
Pisonia Alba	Leaves	48	hexagonal	378	2023	[53]

Plants have numerous biological properties, and their parts, such as roots, leaves, seeds, stems, and fruits, are excellent resources for nanoparticle production. Extracts derived from these parts act as reducing, capping, and stabilizing agents, with their effectiveness influenced by parameters such as pH, temperature, reaction time, salt concentration, and the available phytochemicals, which control the quality, stability, and quantity of the synthesized nanoparticles. In addition, it was documented that different parts of the same plant can produce different nanoparticle shapes and sizes depending on the type of phytochemicals present [117]. Different groups of phytochemicals were noted by Pawan *et al.* in different parts of *Calendula officinalis L.* as shown in Fig. 12 [118]. Based on our analysis of Table 1, approximately 78% of studies have relied on leaf extracts for ZnO nanoparticle synthesis (Fig. 13). Leaves are relatively easy to obtain and typically contain a wide range of phytochemicals—such as chlorophyll, flavonoids, tannins, alkaloids, carotenoids, phenolic acids, and terpenoids—which play crucial roles as reducing, capping, and stabilizing agents in nanoparticle synthesis [119]. Moreover, because the concentrations of these bioactive compounds vary among different types of leaves, the specific chemical composition of leaf extracts significantly impacts the biosynthesis of nanoparticles [120].

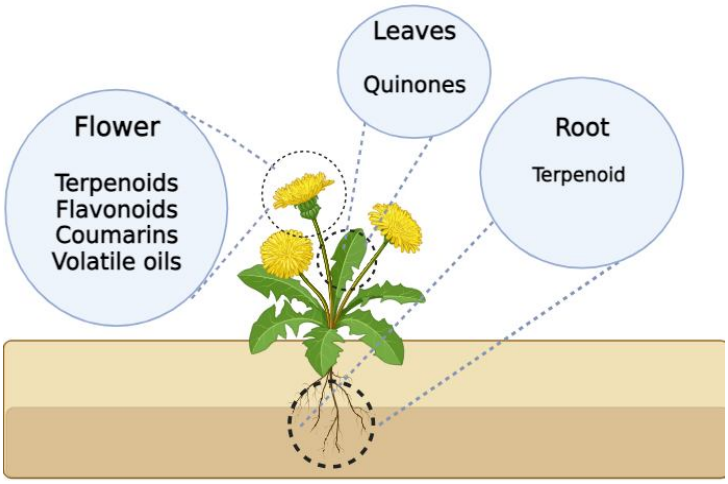

FIG. 12. Different phytochemicals present in the *Calendula officinalis* extract.

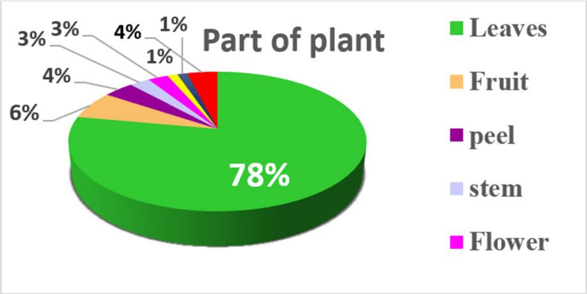

FIG. 13. Contribution of different plant parts in ZnO NPs formation.

5. Conclusions

This investigation aimed to summarize recent research on the biosynthesis of zinc oxide nanoparticles utilizing plant extracts as reducing, capping, and stabilizing agents. Although the complexity of phytochemical structures remains a challenge in evaluating the biosynthesis of nanoparticles, more research on the mechanism of formation of the biosynthesized zinc oxide nanoparticles is required to obtain a better understanding of the chemical processes and reactions that occur during the synthesis. This review includes a comprehensive analysis of 14 distinct articles that offer detailed insights into the green synthesis of ZnO nanoparticles. This review also critically discusses the information available in recent investigations regarding the formation mechanism of biosynthetic ZnO nanoparticles. Moreover, this study covers most of the important plants used in the synthesis of ZnO NPs of various sizes and shapes. Therefore, we believe this review will assist researchers in choosing a suitable plant to modify the NPs' properties for diverse applications. Last but not least, the results of this research showed that about 78% of innovative researchers used the plant leaf extract instead of other parts to synthesize zinc oxide NPs.

Acknowledgement:

The authors would like to thank Soran University and Tishk International University for their continuous support. Special thanks are extended to Dr. David M. W. Wawa (Tishk International University) for his excellent proofreading of this manuscript.

Conflict of interest:

The authors report no conflicts of interest.

Reference:

[1] Aithal, P., Int. J. Manag. IT Eng., 6 (1) (2016) 182.

[2] Bocca, B. *et al.*, Sci. Total Environ., 630 (2018) 922.

[3] Kang, B.-H. *et al.*, ACS Nano, 15 (6) (2021) 10194.

[4] Desai, N. *et al.,* Expert Opin. Drug Deliv., 18 (9) (2021) 1261.

[5] Huang, Y.-C. *et al.*, ACS Photonics, 8 (2) (2021) 592.

[6] Samajdar, D., Sol. Energy, 190 (2019) 278.

[7] Sápi, A. *et al.*, Catal. Lett., 151 (2021) 2153.

[8] Haick, H., J. Phys. D: Appl. Phys., 40 (23) (2007) 7173.

[9] Khan, A.U., Khan, M., and Khan, M.M., BioNanoScience, 9 (2019) 597.

[10] Sosna-Głębska, A. *et al.*, Mater. Today Proc., 20 (2020) 25.

[11] Fahimmunisha, B.A. *et al.*, J. Drug Deliv. Sci. Technol., 55 (2020) 101465.

[12] Lingaraju, K. *et al.*, Appl. Nanosci., 6 (2016) 703.

[13] Majedi, S. *et al.*, New J. Chem., 47 (2023) 16809.

[14] Hwa, K.-Y. and Subramani, B., Biosens. Bioelectron., 62 (2014) 127.

[15] Singh, J. *et al.*, J. Nanobiotechnol., 16 (1) (2018) 1.

[16] Azeez, H.H. and Barzinjya, A.A., Desalination Water Treat., 190 (2020) 179.

[17] Pokhrel, L.R. and Dubey, B., Sci. Total Environ., 452 (2013) 321.

[18] Nagajyothi, P.C. *et al*., Crit. Rev. Environ. Sci. Technol., 50 (24) (2020) 2617.

[19] Khan, M.M. *et al*., Bull. Korean Chem. Soc., 33 (8) (2012) 2592.

[20] Rauwel, P. *et al*., Adv. Mater. Sci. Eng., 2015 (2015) 1.

[21] Nilavukkarasi, M., Vijayakumar, S., and Prathipkumar, S., Mater. Sci. Energy Technol., 3 (2020) 335.

[22] Becker, J., Manske, C., and Randl, S., Curr. Opin. Green Sustain. Chem., 33 (2022) 100562.

[23] Mondal, A. *et al*., Curr. Pharm. Biotechnol., 22 (13) (2021) 1782.

[24] Ahmed, S., Chaudhry, S.A., and Ikram, S., J. Photochem. Photobiol. B, 166 (2017) 272.

[25] Hussein, R.A. and El-Anssary, A.A., Herbal Med., 1 (3) (2019).

[26] Makarov, V. *et al*., Acta Naturae, 6 (1) (2014) 35.

[27] Ingham, B. *et al*., Chem. Mater., 23 (14) (2011) 3312.

[28] Xu, L. *et al*., Chem. Rev., 118 (7) (2018) 3209.

[29] Liu, Y., Li, J., and Chen, Z., Technol. Water Treat., 45 (2019) 6.

[30] Ahmed, S. *et al*., J. Adv. Res., 7 (1) (2016) 17.

[31] Sangeetha, G., Rajeshwari, S., and Venckatesh, R., Mater. Res. Bull., 46 (12) (2011) 2560.

[32] Kumar, B. *et al*., Bioinorg. Chem. Appl., 2014 (2014).

[33] Buazar, F. *et al*., J. Exp. Nanosci., 11 (3) (2016) 175.

[34] Sutradhar, P. and Saha, M., J. Exp. Nanosci., 11 (5) (2016) 314.

[35] Senthilkumar, N. *et al*., New J. Chem., 41 (18) (2017) 10347.

[36] Suresh, J. *et al*., Adv. Nat. Sci.: Nanosci. Nanotechnol., 9 (1) (2018) 015008.

[37] Luque, P. *et al*., J. Mater. Sci.: Mater. Electron., 29 (2018) 9764.

[38] Zare, M. *et al*., Mater. Res. Bull., 109 (2019) 49.

[39] Vijayakumar, S. *et al*., Mater. Today Proc., 23 (2020) 73.

[40] Barzinjy, A.A. *et al*., Micro Nano Lett., 15 (6) (2020) 415.

[41] Barzinjy, A.A. and Azeez, H.H., SN Appl. Sci., 2 (5) (2020) 991.

[42] Sivasankarapillai, V.S. *et al*., Appl. Nanosci., 2022 (2022) 1.

[43] Supin, K., PM, P.N., and Vasundhara, M., RSC Adv., 13 (3) (2023) 1497.

[44] Alharthi, M.N. *et al*., Separations, 10 (2) (2023) 78.

[45] Kuppusamy, P. *et al*., Saudi Pharm. J., 24 (4) (2016) 473.

[46] P Singh, R. *et al*., Adv. Mater. Lett., 2 (4) (2011) 313.

[47] Bala, N. *et al*., RSC Adv., 5 (7) (2015) 4993.

[48] Iqbal, J. *et al*., Sci. Rep., 11 (1) (2021) 20988.

[49] Gnanasangeetha, D. and SaralaThambavani, D., Res. J. Mater. Sci., 2320 (2013) 6055.

[50] Suresh, D. *et al*., Mater. Sci. Semicond. Process., 31 (2015) 446.

[51] Barzinjy, A., Eurasian J. Sci. Eng., 4 (3) (2019) 74.

[52] Rahman, F. *et al*., R. Soc. Open Sci., 9 (11) (2022) 220858.

[53] MuthuKathija, M., Badhusha, M.S.M., and Rama, V., Appl. Surf. Sci. Adv., 15 (2023) 100400.

[54] Pandey, A.C., Sanjay, S.S., and Yadav, R.S., J. Exp. Nanosci., 5 (6) (2010) 488.

[55] Qu, J. *et al*., Environ. Pollut., 159 (7) (2011) 1783.

[56] Qu, J., Luo, C., and Hou, J., Micro Nano Lett., 6 (3) (2011) 174.

[57] Ansari, M. *et al*., Int. J. Pharm. Investig., 3 (4) (2013) 188.

[58] Rajiv, P., Rajeshwari, S., and Venckatesh, R., Spectrochim. Acta A Mol. Biomol. Spectrosc., 112 (2013) 384.

[59] Nagajyothi, P. *et al*., Mater. Lett., 108 (2013) 160.

[60] Vidya, C. *et al*., Int. J. Curr. Eng. Technol., 1 (1) (2013) 118.

[61] Nagarajan, S. and Kuppusamy, K.A., J. Nanobiotechnol., 11 (2013) 1

[62] Senthilkumar, S. and Sivakumar, T., Int. J. Pharm. Pharm. Sci., 6 (6) (2014) 461.

[63] Devi, R.S. and Gayathri, R., Int. J. Curr. Eng. Technol., 4 (4) (2014) 2444.

[64] Sivaraj, R. *et al*., Int. Conf. Adv. Agric. Biol. Environ. Sci., (2014).

[65] Divyapriya, S., Sowmia, C., and Sasikala, S., World J. Pharm. Pharm. Sci., 3 (12) (2014) 1635.

[66] Fu, L. and Fu, Z., Ceram. Int., 41 (2) (2015) 2492.

[67] Sundrarajan, M., Ambika, S., and Bharathi, K., Adv. Powder Technol., 26 (5) (2015) 1294.

[68] Ramesh, M., Anbuvannan, M., and Viruthagiri, G., Spectrochim. Acta A Mol. Biomol. Spectrosc., 136 (2015) 864.

[69] Elumalai, K. *et al*., Adv. Powder Technol., 26 (6) (2015) 1639.

[70] Elumalai, K. *et al*., Mater. Sci. Semicond. Process., 34 (2015) 365.

[71] Bhuyan, T. *et al*., Mater. Sci. Semicond. Process., 32 (2015) 55.

[72] Zheng, Y. *et al*., Green Chem. Lett. Rev., 8 (2) (2015) 59.

[73] Dobrucka, R. and Długaszewska, J., Saudi J. Biol. Sci., 23 (4) (2016) 517.

[74] Vijayakumar, S. *et al*., Biomed. Pharmacother., 84 (2016) 1213.

[75] Sushma, N.J. *et al*., Appl. Phys. A, 122 (2016) 1.

[76] Fowsiya, J. *et al*., J. Photochem. Photobiol. B Biol., 162 (2016) 395.

[77] Patil, B.N. and Taranath, T.C., Int. J. Mycobacteriol., 5 (2) (2016) 197.

[78] Supraja, N. *et al*., Appl. Nanosci., 6 (2016) 581.

[79] Santhoshkumar, J., Kumar, S.V., and Rajeshkumar, S., Resour.-Effic. Technol., 3 (4) (2017) 459.

[80] Elavarasan, N. *et al*., Res. Chem. Intermed., 43 (2017) 3361.

[81] Vijayakumar, S. *et al*., Limnologica, 67 (2017) 1.

[82] Padalia, H. and Chanda, S., Artif. Cells Nanomed. Biotechnol., 45 (8) (2017) 1751.

[83] Saputra, I. and Yulizar, Y., IOP Conf. Ser. Mater. Sci. Eng., (2017).

[84] Gawade, V. *et al*., J. Mater. Sci. Mater. Electron., 28 (2017) 14033.

[85] Venkateasan, A., Prabakaran, R., and Sujatha, V., Nanotechnol. Environ. Eng., 2 (2017) 1.

[86] Prabhu, S. *et al*., IET Nanobiotechnol., 11 (1) (2017) 62.

[87] Çolak, H. and Karaköse, E., J. Alloys Compd., 690 (2017) 658.

[88] Sharmila, G. *et al*., J. Nanostruct. Chem., 8 (2018) 293.

[89] Steffy, K. *et al*., J. Infect. Public Health, 11 (4) (2018) 463.

[90] Rajakumar, G. *et al*., Bioproc. Biosyst. Eng., 41 (2018) 21.

[91] Bayrami, A. *et al*., Artif. Cells Nanomed. Biotechnol., 46 (4) (2018) 730.

[92] Jalal, M. *et al*., Artif. Cells Nanomed. Biotechnol., 46 (sup1) (2018) 912.

[93] Safawo, T. *et al*., OpenNano, 3 (2018) 56.

[94] Upadhyaya, H. *et al*., Am. J. Plant Sci., 9 (6) (2018) 1279.

[95] Hemanth Kumar, N.K., Devabrath Andia, J., Manjunatha, S., Murali, M., Amruthesh, K.N., and Jagannath, S., Biocatal. Agric. Biotechnol., 18 (2019) 101024.

[96] Wali Muhammad, N.U., Haroona, M., and Abbasi, B.H., RSC Adv., 9 (51) (2019) 29541.

[97] Viswanathan Vinotha, A.I., Thaya, R., Govindarajan, M., Alharbi, N.S., Kadaikunnan, S., Khaled, J.M., Al-Anbr, M.N., and Vaseeharan, B., J. Photochem. Photobiol. B Biol., 197 (1011-1344) (2019) 11541.

[98] Narendra Kumar, H.K. *et al.*, SN Appl. Sci., 1 (6) (2019) 651.

[99] Afzal Hussaina, M.O., Alajmi, M.F., Hussainc, I., Amird, S., Ahmede, J., Rehmana, M.T., El-Seedif, H.R., and Ali, I., RSC Adv., 9 (27) (2019) 15357.

[100] Zheng, Y., Huang, Y., Shi, H., and Fu, L., Inorg. Nano-Met. Chem., 49 (9) (2019) 277.

[101] Fakhari, S., Jamzad, M., and Fard, H.K., Green Chem. Lett. Rev., 12 (1) (2019) 19.

[102] Abdelkhalek, A. and Al-Askar, A.A., Appl. Sci., 10 (15) (2020) 5054.

[103] Mahalakshmi, S., Hema, N., and Vijaya, P.P., BioNanoScience, 10 (1) (2020) 112.

[104] Barzinjy, A.A., Hamad, S.M., Esmaeel, M.M., Aydın, S.K., and Hussain, F.H.S., Micro Nano Lett., 15 (6) (2020) 349.

[105] Thi, T.U.D., Nguyen, T.T., Thi, Y.D., Thi, K.H.T., Phan, B.T., and Pham, K.N., RSC Adv., 10 (40) (2020) 23899.

[106] Saravanan, P. *et al.*, Mater. Today Proc., 33 (2020) 3160.

[107] Jan, H. *et al.*, Oxid. Med. Cell. Longev., 2021 (2021) 4786227.

[108] Loganathan, S. *et al.*, Toxicol. Rep., 8 (2021) 64.

[109] Sadiq, H. *et al.*, J. Mol. Liq., 335 (2021) 116567.

[110] Vasantharaj, S. *et al.*, J. Environ. Chem. Eng., 9 (4) (2021) 105772.

[111] Arumugam, M. *et al.*, Environ. Technol. Innov., 23 (2021) 101653.

[112] Dulta, K. *et al.*, J. Clust. Sci., 33 (2) (2022) 603.

[113] Surendra, B.S. *et al.*, Sens. Int., 3 (2022) 100176.

[114] Abdelbaky, A.S. *et al.*, Antioxidants, 11 (8) (2022) 1444.

[115] Shabbir Awan, S. *et al.*, Saudi J. Biol. Sci., 30 (1) (2023) 103487.

[116] Yassin, M.T. *et al.*, Micromachines, 14 (1) (2023) 209.

[117] Ravindran, C., Manokari, M., and Shekhawat, M.S., World Sci. News, 2016 (28) (2016) 18.

[118] Verma, P.K. *et al.*, Pharm. Biomed. Res., 4 (2) (2018) 1.

[119] Shafey, A.M.E., Green Process. Synth., 9 (1) (2020) 304.

[120] Mukunthan, K. and Balaji, S., Int. J. Green Nanotechnol., 4 (2) (2012) 71.

Volume 18, Number 3, 2025. pp. 349-363

Jordan Journal of Physics

ARTICLE

Comparative Analysis of the Effect of Polystyrene Coating on the Field Emission Characteristic of Tungsten and Carbon Fiber Emitters

Marwan S. Mousa[a], **Ildiko Tulbure**[b,c,d], **Moneeb T. M. Shatnawi**[e], **Saleh H. Fawaeer**[f], **Alexandr Knápek**[g], **Vlasta Sedláková**[h], **M-Ali H. Al-Akhras**[i], **Mo'tasem Alabth**[e], **Mohmmad M. Allaham**[g,h], **Ammar Al Soud**[f,h], **Samer I. Daradkeh**[f], **Kipkurui Ronoh**[f,j], **Wala' M. Al-Qaisi**[f] and **Dinara Sobola**[f,i,j]

[a] *Department of Renewable Energy Engineering, Jadara University, Irbid 21110, Jordan.*
[b] *University "1 Decembrie 1918", Alba Iulia 510009, Romania.*
[c] *Technical University of Cluj-Napoca, Cluj-Napoca 400114, Romania.*
[d] *Clausthal University of Technology, Clausthal-Zellerfeld 38678, Germany.*
[e] *Department of Physics, The University of Jordan, Amman 11942, Jordan.*
[f] *Central European Institute of Technology, Brno University of Technology, Purkyňova123, Brno 612 00, Czech Republic.*
[g] *Institute of Scientific Instruments of Czech Academy of Sciences, Královopolská 147, Brno 612 00, Czech Republic.*
[h] *Department of Physics, Faculty of Electrical Engineering and Communications, Brno University of Technology, Technická 2848/8, Brno 616 00, Czech Republic.*
[i] *Department of Physics, Jordan University of Science and Technology, Irbid 22110, Jordan.*
[j] *Academy of sciences ČR, Institute of Physics of Materials, Žižkova 22, Brno 616 00, Czech Republic.*

Doi: **https://doi.org/10.47011/18.3.8**

Received on: 22/02/2024; *Accepted on: 02/06/2024*

Abstract: Achieving high initial emission currents at relatively low operating voltages is essential for field electron emission sources utilized in equipment reliant on focused electron beams. Coating these emitters with a dielectric layer has the potential to enlarge their effective emission region, thereby increasing the initial emission current value while simultaneously reducing the operating voltage. This study compares and contrasts the effects of a dielectric polystyrene coating on field electron emission characteristics, drawing on two investigations of polystyrene-coated emitters. The study provides a brief analysis of the field electron emission characteristics obtained from carbon fiber and tungsten emitters, both prepared using electrochemical etching and subsequently coated with polystyrene. Both studies are thoroughly reviewed and contextualized, emphasizing the advantageous attributes of this emitter type. The focus of the study lies in the current-voltage characteristic, Murphy-Good analysis plot, and field electron emission images obtained from both emitters, with particular attention to how the coating influences emissivity. The investigation into the emission characteristics of coated tungsten indicates a significant improvement over coated carbon fiber emitters, with performance enhanced several times.

Keywords: Carbon fiber emitter, Dielectric polystyrene coating, Field electron emission, Murphy-good plot, Tungsten emitter.

Corresponding Authors: Marwan S. Mousa **Email**: m.mousa@jadara.edu.jo
Saleh H. Fawaeer **Email**: saleh.hekmat@ceitec.vutbr.cz

1. Introduction

In recent years, the rapid advancement of nanofabrication technology [1–3] has reignited interest in nano-field electron emission (FEE) emitters, particularly sharp-point emitters designed for high current density applications [4–7]. Cold field electron emission from a metal source coated with a dielectric layer has attracted considerable attention due to its relevance for electron-beam-based equipment. Such applications require a high-quality source of free electrons that is intense and capable of providing high current density while operating in less-than-ideal vacuum conditions [8–11]. To meet these demands, experimental coated FEE-emitters based on sharp emitters such as tungsten (W) [12, 13], molybdenum (Mo) [14], tantalum (Ta) [1], and carbon fibre (CF) [15], featuring a metal oxide-dielectric structure, have emerged as promising candidates [8].

The advantages of coated FEE sources are noteworthy: (I) Minimal demagnification is required to achieve a probe with a diameter as small as 1 nm, thanks to the small virtual source size starting from a few nanometers [2, 3]. (II) The presence of minimal energy spread allows operation at low accelerating voltages. Consequently, exceptionally sharp, high-contrast images can be obtained without inducing considerable damage. (III) The coating layer facilitates operation in a relatively low-quality vacuum ($\leq 10^{-6}$ Pa), thereby mitigating ion-bombardment and the sorption of residuals on the emitter's surface. Maintaining a lower vacuum level also enables quicker sample manipulation [9, 13].

The need for a deeper comprehension of FEE phenomena and the advancement of field electron emission theories for dielectric-coated emitters serve as the driving force for further investigation into the behavior of coated emitters [4, 16–18]. Therefore, numerous comprehensive experimental studies have been conducted to simulate this type of FFE-tips by fabricating and characterizing various kinds of sharp emitters to investigate their FEE-behavior before and after covering with a dielectric material. These studies revealed that coated FEE-tips exhibit several promising operational properties compared to the performance of well-known uncoated emitters [11, 12, 15, 19, 20]. Additionally, certain dielectric coatings enhance FEE at low fields (<V/nm) when applied to emitter surfaces [9, 12, 15, 19, 21]. Indeed, cold field electron emission occurs once an electric field is applied to the coated emitter, resulting in a higher emission current at significantly lower voltage compared to the uncoated emitter. Cycling of the voltage yields reproducible current-voltage ($\mathrm{I}-\mathrm{V}$) characteristics with enhanced stability and brighter spot [22–27].

Following these promising findings, two experimental studies were conducted on two different kinds of electron sources coated with polystyrene (PS) dielectric material [26, 27]. In these studies, a thin coat of PS material was applied to CF and W emitters with different thicknesses ($\leq$ 350nm). The objective was to evaluate the FEE characteristics and capabilities of these coated emitters as field-electron emission sources, studying the effect of PS-coating on their emission properties. The Murphy-Good (MG) plot was employed as an advanced method to analyze the acquired $\mathrm{I}-\mathrm{V}$ data, providing a more precise characterization of emitter behavior. This plot serves as a graphical representation of the MG equation, which was developed to characterize emitter behavior based on an advanced mathematical understanding of Fowler-Nordheim theory [16, 17, 28–30]. Both studies presented results from FEE sources, specifically CF and W emitters, both before and after being coated with PS. Their findings demonstrated that coated emitters exhibit several promising properties compared to uncoated emitters. These coated emitters showed significant enhancements in the electron emission process, including higher emission current values, lower threshold voltages, brighter emission images, and more intense electron beams [26, 27].

This study provides a brief analysis of the field emission behavior of two experimental emitters: PS-coated CF and W emitters, as presented in two distinct works. By compiling data from their $\mathrm{I}-\mathrm{V}$ characteristic curves, MG analysis plots, FEE images, and scanning electron micrographs, this study investigates and elucidates the similarities and differences in how PS coatings influence the performance of CF versus W emitters.

2. Materials and Methods

2.1. Emitter Fabrication

In the first study, experiments were carried out using polyacrylonitrile VPR-19 carbon fibre (7 µm in diameter), while in the second study, high-purity polycrystalline tungsten wire with a diameter of 0.1 mm was used. These choices were made due to the distinctive features of CF and W, such as their high melting points (3970 K for CF and 3650 K for W), high work function (4.95 eV for CF and 4.55 eV for W), as well as their high hardness, strength, and heat resistance at elevated temperatures [12, 13, 15].

For the fabrication of FEE-emitters, they are typically shaped into sharp emitters with an emitter-apex radius of a few nanometers [3, 4]. In both works [26, 27], the sharp emitters used as a substrate for the PS-coating layer were fabricated using the same method based on electrolytic etching [12, 15]. A solution of 0.1 molar sodium hydroxide (NaOH) was employed to etch the CF [25], while a solution of 2 molar NaOH was used to etch the W wire [23]. The etching process of the emitters was controlled by selecting an appropriate initial etching current to produce sharp emitters on the solution surface. Approximately 35 µA of current was applied for CF etching, while 4 mA was applied for W-wire etching [24]. Following the etching process, the samples (i.e., the etched tips) were cleaned in water for a few minutes, utilizing a sonicator to remove contaminants arising from the electrolytic etching [9].

Since polystyrene $(C_8H_8)_n$ has a high melting point [3] and a low work function (4.22 eV) [31], its solution has been used as a dielectric coating for etched tips. In both works, PS-pellets (as the solute) and toluene (as the solvent) were used to prepare a PS-coating solution with different concentrations. The covering process in both works involved dipping the emitter into the PS-coating solution and ensuring its apex was coated with a layer as homogeneous as possible. In the first work, the CF-emitter was dipped several times into a solution of 0.16 g/mL PS, forming a layer that was approximately 50-75 nm thick, while in the second work, the W-emitter was also dipped several times into a solution of 0.8 g/mL PS, resulting in a 100–150 nm thick layer [26, 27]. The variation in coating thickness was due to differences in solution concentration and the number of dipping cycles.

In both works, the emitter was subsequently subjected to a curing cycle, and the PS-layer underwent a glass transition, transforming into a hard and relatively brittle "glassy" material [9]. In the first work, the CF-emitter was baked directly in the FEE-vacuum chamber during the degassing procedure, whereas in the second work, the W-emitter was cured in an electric furnace. The curing process involved two stages: heating for 10 minutes at 100 °C to remove solvents, followed by another 10 minutes at 120 °C to complete the curing process [26, 27].

Figures 1 and 2 show the emitters from both works using scanning electron microscopy (SEM), which was employed in both cases before and after PS coating. This was done to determine the radius of the FEE-tip apex resulting from the etching process, and subsequently followed by the coating process. By subtracting these two values, the thickness of the dielectric PS-coating layer formed on top of the etched tip could be determined [23, 25]. Additionally, the SEM images reveal the slight difference in surface contrast between the dielectric PS-coating layer and the core tip, providing insights into the fine structure of the composite emitter.

Since it is a complementary method and provides different information about the etched tip and the coating layer, Fig. 1 presents SEM-images of the first and second carbon fibre samples (labelled as CF^1 and CF^2) with a tip apex radius of 41.3 and 63.4 nm, respectively, (a) before and (b) after coating with a dielectric PS-layer of 92.5 and 54.3 nm thickness, respectively [26]. Similarly, SEM-images of the first and second tungsten samples (labelled as W^1 and W^2) with a tip apex radius of 161 and 170 nm, respectively, are shown in Fig. 2: (a) before and (b) after coating with a dielectric PS-layer of thickness 142 and 105 nm, respectively [27].

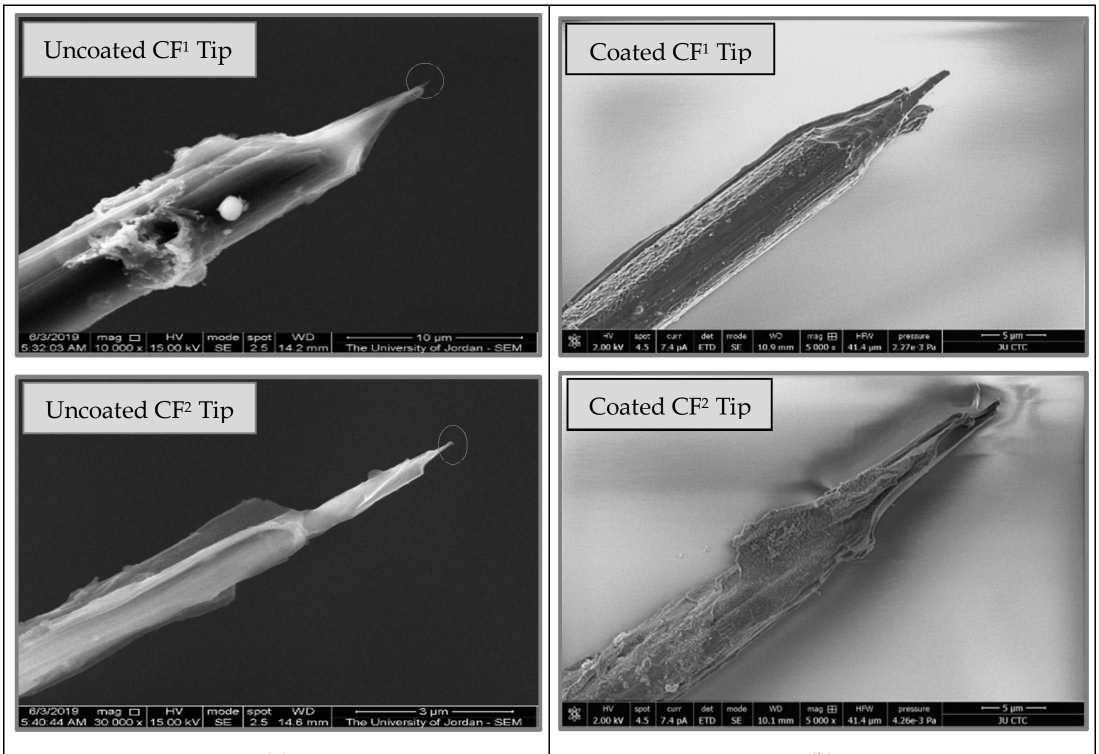

(a) (b)

FIG. 1. Scanning electron microscope images for the first and second carbon fibre tips (CF^1 and CF^2) (a) before and (b) after polystyrene coating [26].

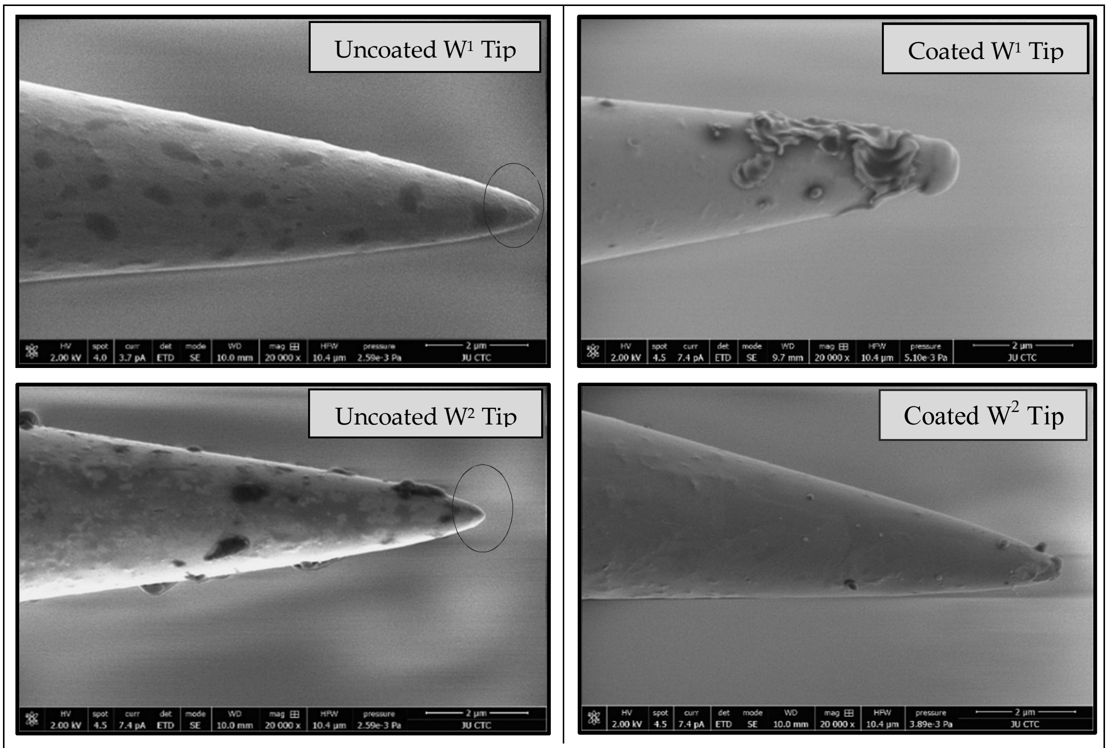

(a) (b)

FIG. 2. Scanning electron microscope images for the first and second tungsten tips (W^1 and W^2) (a) before and (b) after polystyrene coating [27].

2.2. Analytical Facility

In both FEE studies, the most important results obtained from coated emitters were the $I-V$ characteristics [8, 19, 22–25], which were analyzed by applying analytical MG plots [16, 17, 28]. The $I-V$ data were acquired utilizing a home-built field emission microscope (FEM).

Inside a high-vacuum chamber, the emitter (acting as a cathode) was positioned 1 cm away from a phosphorus screen (serving as an anode), which was grounded by picometers to measure the emission current. The emitter was connected to a high-voltage power source to induce electron emission after applying a voltage across the emitter. The specific setup and measurement procedures were described in detail in [26, 27]. The summary provided in this work pertains to investigations conducted under high vacuum conditions at a pressure ranging from 10^{-6} to 10^{-8} mbar. This vacuum was achieved inside the chamber with the help of a slow baking process of the system at 140−170 °C, followed by a rapid cooling process with liquid nitrogen to maintain the vacuum for as long as possible [26, 27]. This high vacuum is crucial to diminish the ion-bombardment rate of gas molecules on the emitter surface and to keep it from being damaged [9,20].

3. Results and Discussion

This part shows the results acquired from the CF and W-tips before and after PS coating, highlighting similarities and differences in their FEE characteristics. These findings encompass the $I - V$ characteristics and FEM images [26, 27].

3.1. Analysis of the Emission Characteristics Obtained from Coated Emitters

3.1.1 Current-voltage ($I - V$) Characteristics

The current-voltage curve was used to model the behavior of the FEE emitter during operation. Additionally, the MG plot was used to characterize the emitter behavior by interpreting the $I - V$ data and analyzing it graphically. The rationale behind using the MG plot was to derive an approximate linear relationship from the practical FEE data. Improvements in emitter behavior after coating were assessed by the extent to which the linearity of the data was enhanced [16, 28, 30].

3.1.1.1 Polystyrene−Coated Carbon Fibre Emitters

For the first and second uncoated CF samples presented in Fig. 1(a), emission was observed to initiate after applying an initial operating voltage across the emitter at 440 V and 590 V, respectively. This resulted in an initial emission current of 96 nA and 41 nA, respectively. With increasing applied voltage, the I–V characteristics (curve A) for the uncoated CF1 and CF2 emitters were obtained, as shown in Figs. 3(a) and 4(a) , respectively. These curves extended over a wide voltage range, up to 900 V and 910 V, with current values of 1.15 μA and 1.74 μA, respectively. When the voltage applied across the emitter was lowered to threshold values of 320 V and 360 V, the FEE behavior followed a trend like curve B, as shown in Figs. 3(a) and 4(a), for the uncoated-CF^1 and CF^2-samples, respectively.

Murphy-Good plots of the current-voltage characteristics (curves A and B) for the uncoated-CF-samples were found to be approximately linear in the region of emission currents < 10^{-7} A, as shown in Figs. 3(b) and 4(b) for the uncoated CF^1 and CF^2 emitters, respectively. However, significant linear deviations were observed in the region with higher emission current values. This property is known and related to this type of emission process [23–25].

In Figs. 5(a) and 6(a), curve A represents the current-voltage characteristics of the first and second CF samples coated with 92.5 and 54.3 nm of PS, respectively, as shown in Fig. 1(b). Compared with curve A in Figs. 3 and 4, the initial operating voltages applied across the PS-coated CF^1 and CF^2 emitters decreased slightly to 350 V and 540 V, respectively, while their initial emission current values increased to 81 nA and 102 nA. Moreover, an additional hysteresis appeared, shifting the $I - V$ characteristics slightly towards higher emission current values when the applied voltage across the PS-coated CF^1 and CF^2 emitters was increased to the range of 900-950 V, with an emission current value of 1880 nA. When the voltage applied across the PS-coated CF^1 and CF^2 emitters was lowered to threshold values of 330 and 400 V, respectively, their FEE behavior followed a pattern similar to curve B, as shown in Figs. 5(a) and 6(a).

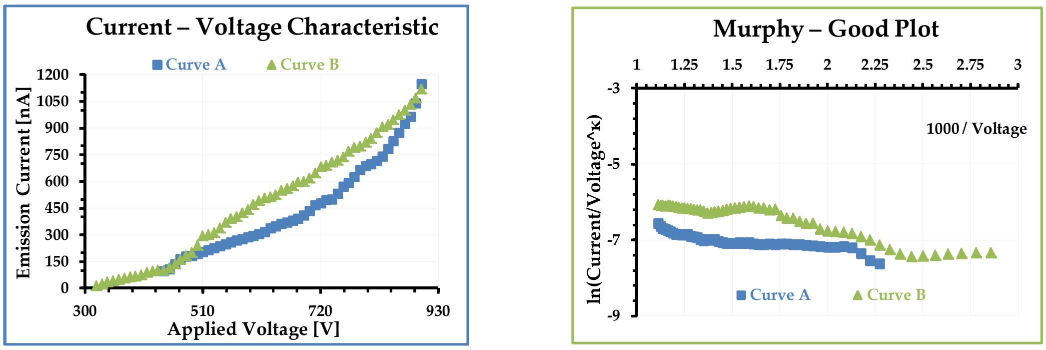

(a) (b)

FIG. 3. Current-voltage characteristic of the uncoated CF^1 emitter with an apex radius of 41.3 nm: (a) emission behavior during increasing (curve A) and decreasing (curve B) voltage cycles; (b) corresponding Murphy–Good plots for the same tip under both cycles.

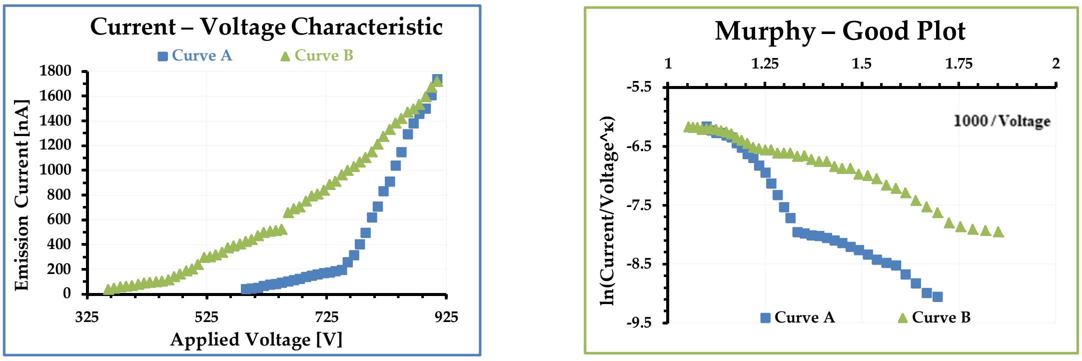

(a) (b)

FIG. 4. Current-voltage characteristic of the uncoated CF^2 emitter with an apex radius of 63.4 nm: (a) emission behavior during increasing (curve A) and decreasing (curve B) voltage cycles; (b) corresponding Murphy–Good plots for the same tip under both cycles.

Figures 5(b) and 6(b) display the Murphy-Good plots of the current-voltage data for the PS-coated CF^1 and CF^2 emitters, respectively. Comparing the MG-plot of the current-voltage characteristics of the uncoated and coated CF samples reveals a noticeable difference in the low-field region. Specifically, the slopes of the approximately linear relations are slightly lower for the PS-coated emitters (Figs. 5 and 6) than for the uncoated ones (Figs. 3 and 4). This reduction in slope suggests that the coating layer enhanced the effective emissive area of the emitters by lowering the work function of the composite coated tips. As a result, a lower-potential Schottky–Nordheim barrier was formed at reduced applied fields. Once this barrier was sufficiently suppressed by the applied voltage, electrons from states near the Fermi level could tunnel through, generating a denser electron beam with higher emission current at a lower extraction voltage. Consequently, the FEE characteristics of the coated emitters were significantly improved compared with those before coating [12, 21]. Similar effects have been reported and discussed in previous works [9, 22–25].To provide perspective on the variability in the FEE performance of this type of CF-tip, Table 1 summarizes the compiled current-voltage data for CF^1 and CF^2 tips before and after coating with PS.

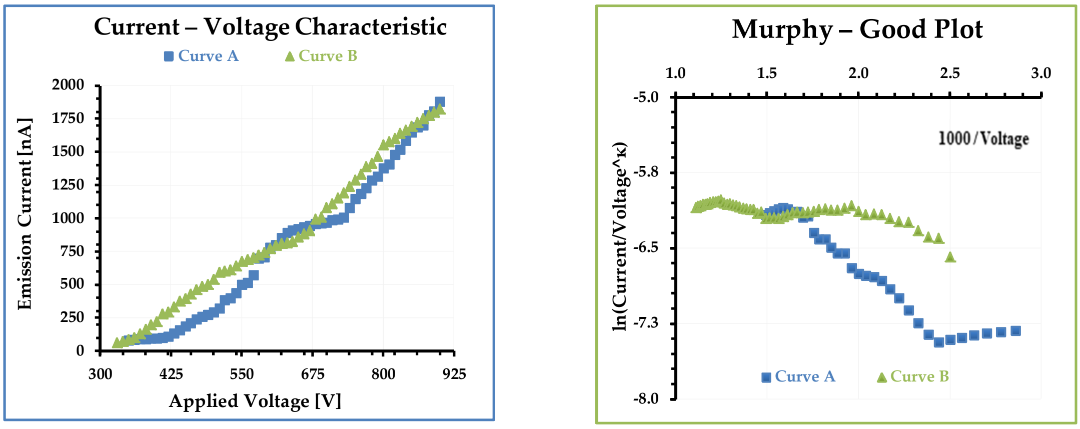

(a) (b)

FIG. 5. Current-voltage characteristic of a CF^1 emitter with a tip radius of 41.3 nm coated with a 92.5 nm PS layer during (a) increasing (curve A) and decreasing (curve B) cycles. (b) Murphy–Good plot of the same tip for the increasing and decreasing cycles.

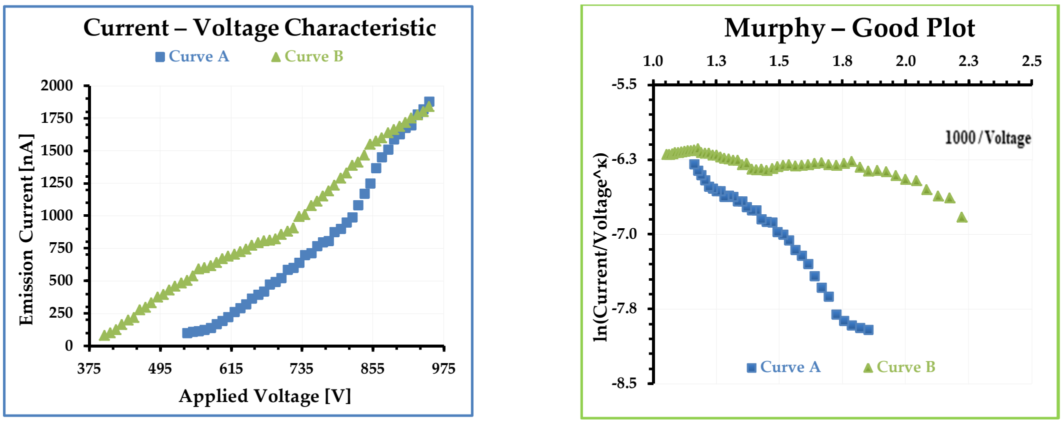

(a) (b)

FIG. 6. Current-voltage characteristic of a CF^2 emitter with a tip radius of 63.4 nm coated with a 54.3 nm PS layer during (a) increasing (curve A) and decreasing (curve B) cycles. (b) Murphy–Good plot of the same tip for the increasing and decreasing cycles.

TABLE 1. Compiled current-voltage data for CF^1 and CF^2 tips before and after they were covered with PS.

Sample	Radius (nm)	Cycle	Voltage range (V)	Emission current (nA)
Uncoated CF^1 – tip	41.3	Increasing Voltage	440 – 900	96 – 1151
		Decreasing Voltage	900 – 320	1120 – 13
CF^1 – tip coated with a PS layer 92.5 nm thick	133.8	Increasing Voltage	350 – 900	81 – 1880
		Decreasing Voltage	900 – 330	1820 – 63
Uncoated CF^2 – tip	63.4	Increasing Voltage	590 – 910	41 – 1741
		Decreasing Voltage	910 – 360	1770 – 38
CF^2 – tip coated with a PS layer 54.3 nm thick	117.7	Increasing Voltage	540 – 950	102 – 1880
		Decreasing Voltage	950 – 400	1840 – 79

3.1.1.2 Polystyrene−Coated Tungsten Emitters

For the first and second uncoated W samples presented in Fig. 2(a), their current−voltage measurements are represented in Figs. 7 and 8, respectively. Part (a) shows the I − V characteristics, while part (b) displays the MG-plot of the I − V data. From curves A and B of the uncoated W emitters, it can be observed that their FEE behavior follows a somewhat similar trend to that of the uncoated CF emitter curves, although they cover a wider range of extraction voltages. As shown in Figs. 7 and 8, emission for the uncoated W1 and W2 emitters began at initial operating voltages of 750 and

1050 V, respectively, with emission current values of 30 and 1 nA. Subsequently, when the voltage applied across the emitters was increased to 2000 and 2150 V, the emission current values reached 4000 and 800 nA, respectively. Upon reducing the applied voltage across the uncoated W^1 and W^2 emitters to threshold values of 900 and 1000 V, respectively, the FEE behavior followed a trend similar to curve B, as shown in Figs. 7(a) and 8(a), respectively.

The Murphy-Good plots in Figs. 7(b) and 8(b) indicate that the I – V data for the uncoated W samples followed almost the same approximately linear relation as that of the MG plots for the uncoated CF samples, with a slight difference in the slope value. This slight difference in the emission I – V characteristics for both emitters is mainly due to the different chemical structure (CF vs. W), different work function, and tip sharpness, as they all influence and contribute to the formation of a low-potential Schottky-Nordheim barrier, which in turn affects the field electron emission characteristics from the emitter. Several studies have explained these effects on emissivity in more detail [8, 22–25].

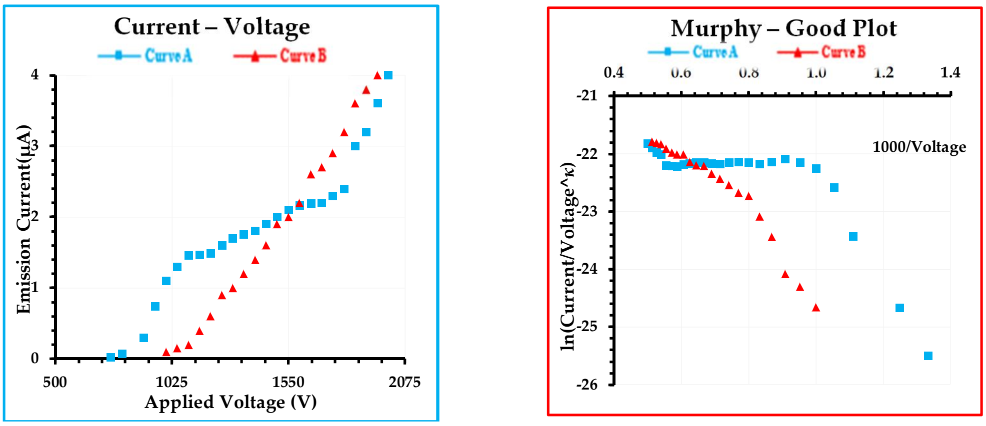

(a) (b)

Fig. 7. Current-voltage characteristic of an uncoated W^1 tip with an apex radius of 161 nm during (a) increasing (curve A) and decreasing (curve B) cycles. (b) Murphy–Good plot for the same tip during the increasing and decreasing cycles.

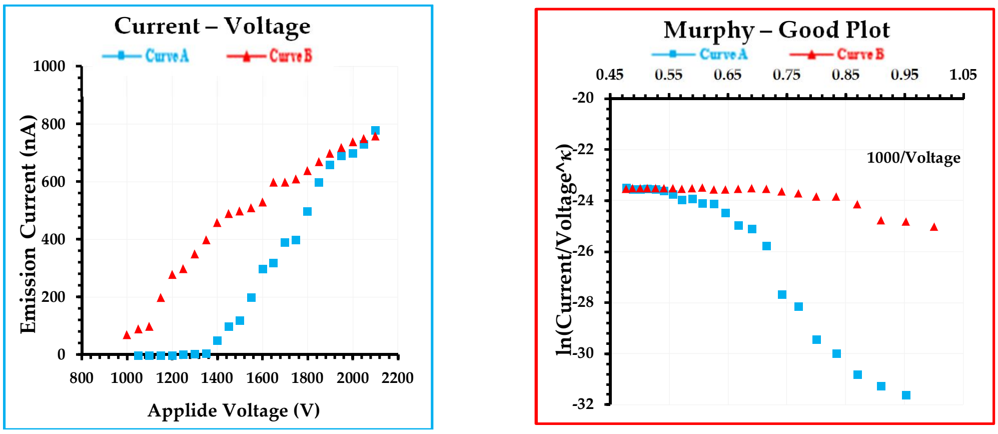

(a) (b)

Fig. 8. Current-voltage characteristic of an uncoated W^2 tip with an apex radius of 170 nm during (a) increasing (curve A) and decreasing (curve B) cycles. (b) Murphy–Good plot for the same tip during the increasing and decreasing cycles.

For the first and second W samples coated with a PS layer with thicknesses of 142 and 105 nm, as presented in Fig. 2(b), a distinctive behavior was observed compared to the PS-coated CF emitters when the voltage applied across the coated W tip was increased. This behavior included the phenomenon known as the 'switch-on'. The 'switch-on' refers to the sudden appearance of a high emission current, referred to as the 'saturation' current (I_{SAT}), usually in microamperes, at a certain voltage termed the 'switch-on voltage' (V_{SW}) during voltage ramp-up [11–13, 32]. In this case, the initiation of field electron emission was noticed after applying a switch-on voltage across the PS-coated W^1 and W^2 emitters at 3000 and 3700 V, respectively, which produced saturation current values of 16 and 18 μA, respectively, and was maintained at lower voltages. After the current stabilized, lowering the voltage applied across the emitter to a threshold voltage of 1100 and 500 V produced the $I-V$ characteristic (curve B) and the MG analysis-plot for this case, as shown in Figs. 9 and 10 for the PS-coated W^1 and W^2 emitters, respectively.

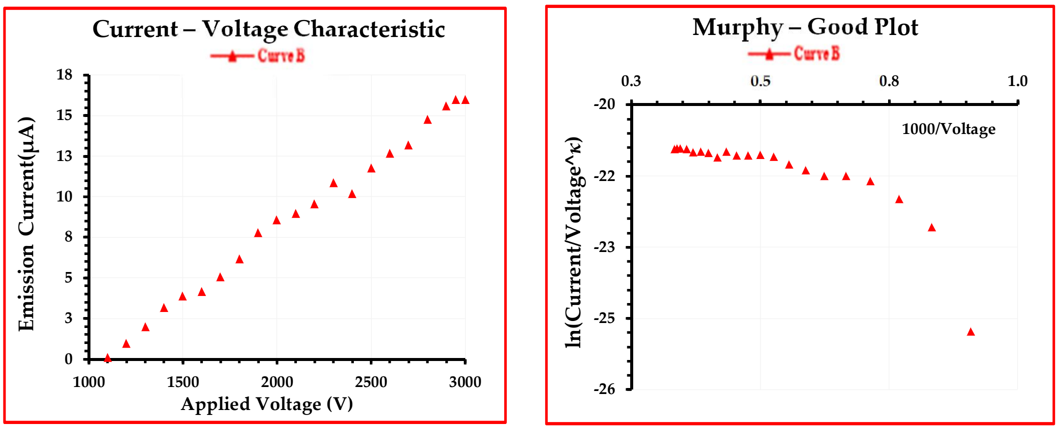

(a) (b)

Fig. 9. (a) $I-V$ characteristic (curve B) of a W^1 emitter with an apex radius of 161 nm, coated with a 142 nm thick PS layer. (b) Corresponding MG plot during the first voltage decrease.

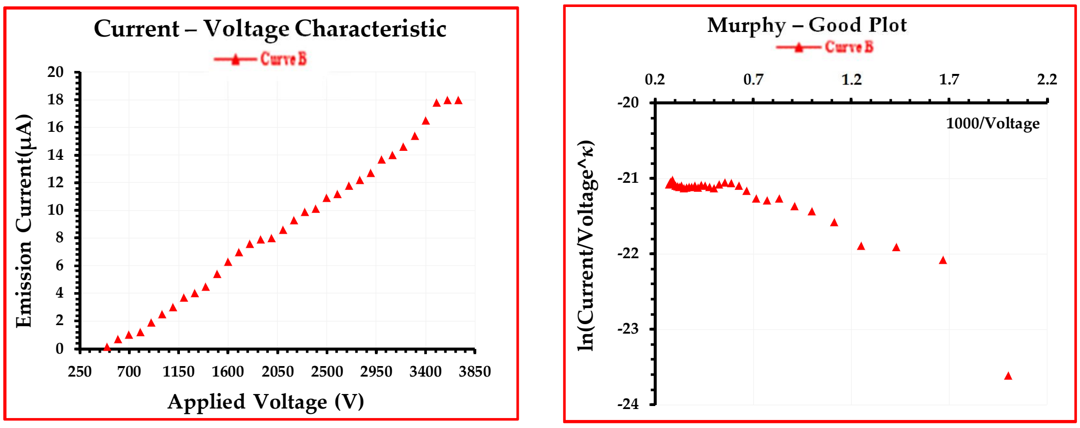

(a) (b)

Fig. 10. (a) $I-V$ characteristic (curve B) of a W^2 emitter with an apex radius of 170 nm, coated with a 105 nm thick PS layer; (b) corresponding MG plot during the first decreasing voltage cycle.

Then, a complete voltage cycle was applied across the coated W samples to produce the $I-V$ characteristics for their FEE behavior during operation, as shown in Figs. 11(a) and 12(a) for the PS-coated W^1 and W^2 emitters, respectively. Compared to the uncoated W emitters (curve A in Figs. 7 and 8), the PS-coated W^1 and W^2 samples exhibited higher initial emission current values of 100 and 900 nA at applied voltages of 1000 and 500 V, respectively. It is also evident that an additional hysteresis occurred, causing the $I-V$ characteristic to shift slightly towards higher emission current values when the applied voltage across the PS-coated W^1 and W^2 samples was increased to 2000 and 2500 V, resulting in emission current values of 7000 and 11000 nA, respectively. When lowering the voltage applied across the PS-coated W^1 and W^2 emitters to a threshold voltage, the FEE performance followed a trend similar to curve B, as shown in Figs. 11(a) and 12(a), respectively.

In the Murphy-Good plot of the current-voltage data for the PS-coated W^1 and W^2 emitters shown in Figs. 11(b) and 12(b), respectively, a certain similarity can be observed with the MG-plot shown in Figs. 5(b) and 6(b). This similarity arises from the fact that the $I-V$ data obtained from the PS-coated W emitter followed the same approximately linear relation with lower slope values than the uncoated W emitter, similar to the effect observed with the coated CF emitter. This implies that the effect of the PS-coating layer on FEE behavior for both coated emitters was the same. However, comparing the MG plots of the PS-coated W emitters with those of the PS-coated CF emitters also shows a difference in slope values. This difference arises primarily from variations in chemical structure (PS-coated CF vs. PS-coated W), work function, and coating thickness, all of which influence the field electron emission characteristics. These effects have been discussed in detail in previous studies [9, 22, 23]. Table 2 provides a perspective on the variability in FEE performance observed for this type of W-tip.

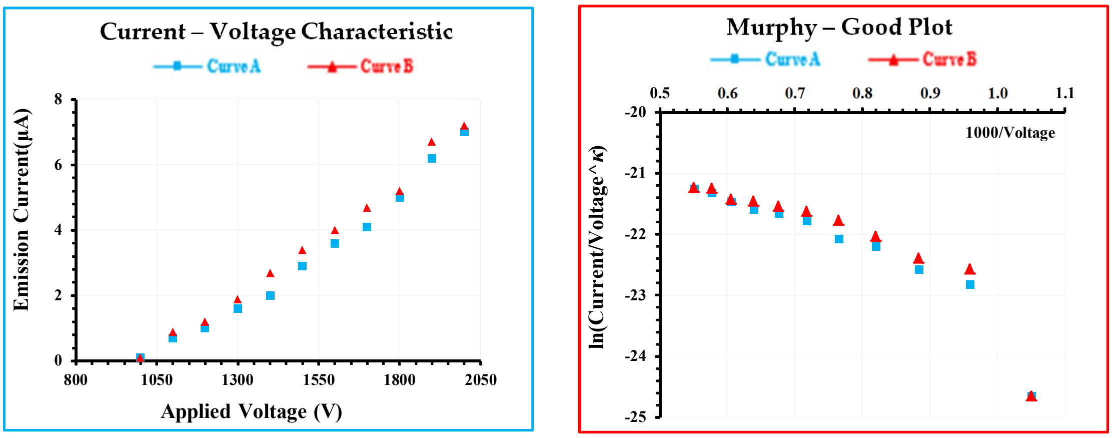

(a) (b)

FIG. 11. Current-voltage characteristic of a W^1 emitter with a tip radius of 161 nm, coated with a 142 nm thick PS layer, during (a) increasing (curve A) and decreasing (curve B) voltage cycles. (b) Murphy–Good plot for the same emitter showing the corresponding increasing and decreasing cycles.

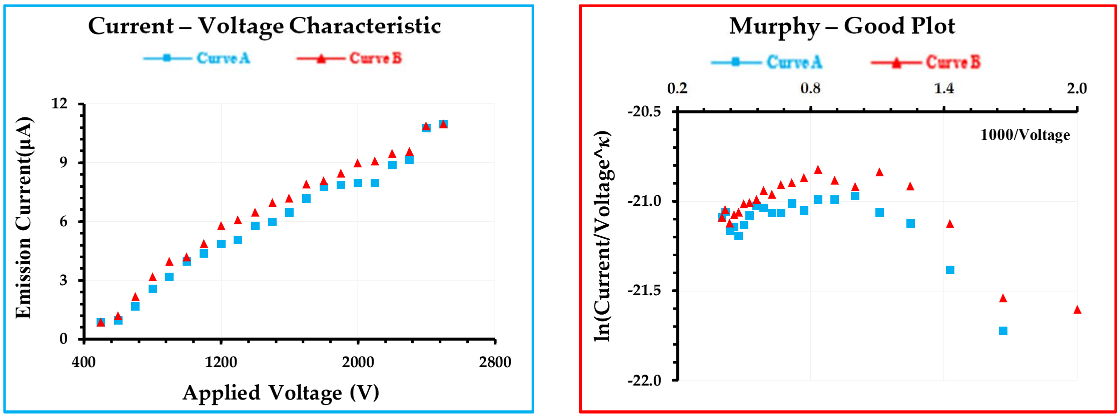

(a) (b)

FIG. 12. Current-voltage characteristic of a W^2 emitter with a tip radius of 170 nm covered by a 105 nm thick PS layer during (a) increasing (curve A) and decreasing (curve B) cycles. Murphy–Good plot for the same emitter during (b) the increasing and decreasing cycles.

TABLE 2. Compiled data from current–voltage measurements for W^1 and W^2 tips, before and after they were covered by PS.

Sample	Radius (nm)	First Decreasing Cycle		Cycle	Voltage Range (V)	Emission Current (nA)
		Switch-on Voltage	Saturated Emission Current			
Uncoated W^1 tip	161	No “switch-on” phenomenon		Increasing Voltage Decreasing Voltage	750 – 2000 1950 – 900	30 – 4000 4000 – 60
W^1 tip coated with 142 nm PS layer	303	Voltage Range: (3 – 1.1) KV 3 KV	Current Range: (16 – 0.1) µA 16 µA	Increasing Voltage Decreasing Voltage	1000 – 2000 2000 – 1000	100 – 7000 7200 – 100
Uncoated W^2 tip	170	No “switch-on” phenomenon		Increasing Voltage Decreasing Voltage	1050 – 2150 2100 – 1000	1 – 800 760– 70
W^2 tip coated with 105 nm PS layer	275	Voltage Range: (3.7 – 0.5) KV 3.7 KV	Current Range: (18 – 0.12) µA 18 µA	Increasing Voltage Decreasing Voltage	500 – 2500 2500 – 500	900 – 11000 11000 – 900

3.1.2 Emission Images Characteristics

The emission image that appears on the FEM phosphor screen, which is used to display the field electron emission shape, is also referred to as an emission pattern due to its geometric arrangement. In both studies, a photograph of the FEE image was captured to analyze the emission pattern from the uncoated and coated emitters. This analysis aimed to investigate the effect of coating on the FEE characteristic by comparing the differences between the two patterns.

3.1.2.1 Polystyrene– Coated Carbon Fibre and Tungsten Emitters

Figures 13(a) and 13(b) show the emission images of the uncoated CF^1 and CF^2 emitters, while Figs. 13(c) and 13(d) show those of the corresponding PS-coated emitters. Figures 14(a) and 14(b) present the uncoated W^1 and W^2 emitters, and Figs. 14(c) and 14(d) show the PS-coated emitters. All images were obtained during the voltage-up cycle corresponding to the I–V characteristic (curve A) discussed in the subsections on PS-coated CF and W emitters [26, 27]. The FEE images obtained from the uncoated CF and W emitters, shown in Figs. 13(a) and 14(c) display the active emission region on the emitter surface. The emission appears as a multicenter spot, where the densely packed centers within the spot (i.e., sharper regions of the tip surface) have a lower work function than the surrounding areas (i.e., less sharp, atomically rough regions). As a result, bright centers appear against a dimmer background.

By contrast, the FEE images of the PS-coated emitters in both studies, presented in Figs. 13(b) and 14(d) show a concentric emission area, appearing as a single, highly bright central spot. Unlike the uncoated emitters, which exhibit multiple bright spots due to a background structure, the coated emitters display a more uniform and concentrated emission.

The FEM images also reveal that the electron beams from uncoated CF and W emitters were unstable, with individual spots flickering in intensity and randomly switching on and off under applied voltage. This instability is attributed to the adsorption of residual gas contaminants on the uncoated emitter surfaces, which reduces both emission concentration and stability. In contrast, the FEM images of the PS-coated CF and W emitters show a more concentrated and stable beam. Consequently, the FEM images appear significantly brighter and more focused for the coated emitters.

This enhancement can be attributed to the protective role of the PS coating, which shields the emitter surface from ionized gas bombardment and reduces surface adsorption. In doing so, the PS coating helps preserve the chemical structure of the emitter surface and improves emission stability [9, 19, 22–25].

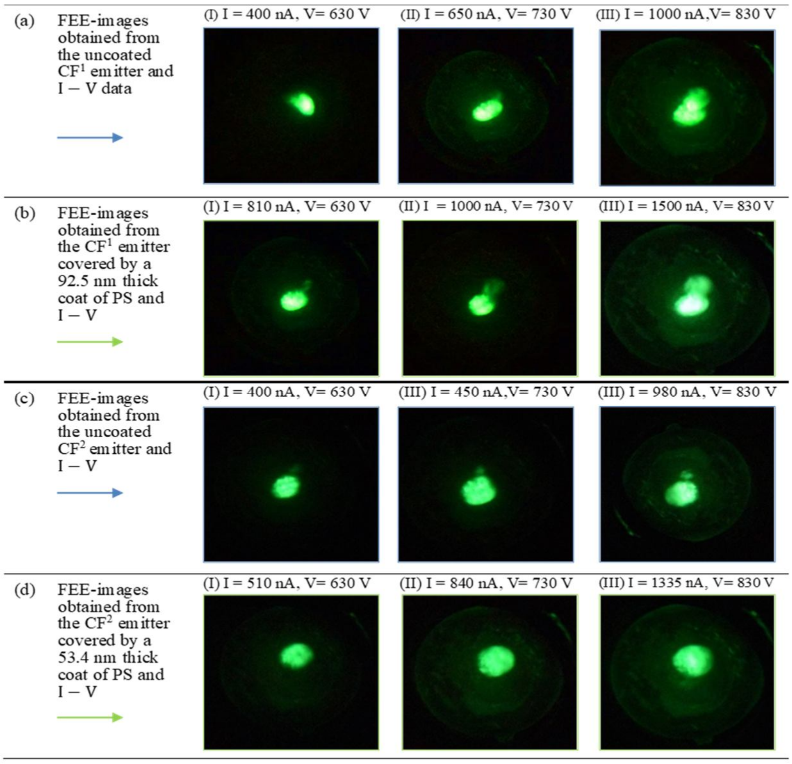

FIG. 13. Series of FEM images from CF^1 tips (a) uncoated and (b) coated with a 92.5 nm PS layer, and CF^2 tips (c) uncoated and (d) coated with a 53.4 nm PS layer. Spot size and brightness increase with applied voltage. All images were recorded under identical conditions: the same tip-to-screen distance and a 10-minute interval between exposures.

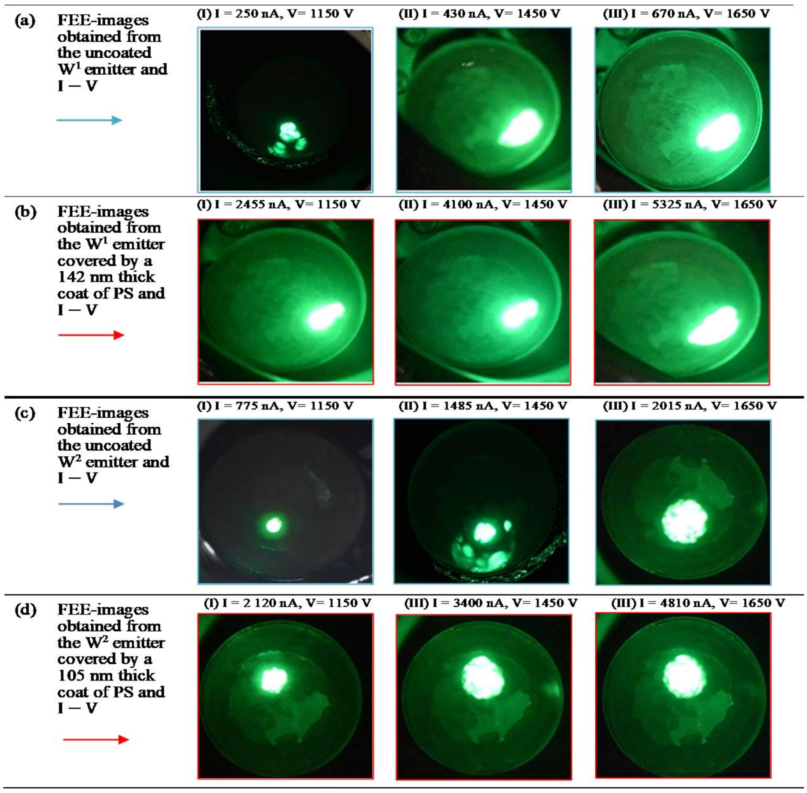

FIG. 14. Series of FEM images from W^1 tips (a) uncoated and (b) coated with a 142 nm PS layer, and W^2 tips (c) uncoated and (d) coated with a 105 nm PS layer. Spot size and brightness increase with applied voltage. All images were recorded under identical conditions: the same tip-to-screen distance and a 10-minute interval between exposures.

In general, when comparing the current-voltage characteristic obtained from the two kinds of emitters, it is observed that the PS-coated CF and W emitters exhibit greater variation in their $I-V$ curves compared to the uncoated ones. This variation stems from the PS-coated emitters' ability to emit at lower voltages with higher currents, indicating higher efficiency compared to the uncoated emitters. However, the impact of the PS coat on the FEE behavior differs between the two emitters, as evidenced by comparing the results before and after coating in Tables 1 and 2. Key agreements highlighting the contribution of the PS coating layer to the production of an improved, current-stabilized coated emitter include: (I) The PS coating layer improves the field electron emission initiation voltage for the coated emitter samples in both studies. This improvement manifests as a decrease in the starting voltage or an increase in the initial emission current, or both. (II) Additionally, the PS coating layer enhances the operating voltage range of the coated emitter during voltage increasing-and-decreasing cycles. This enhancement is characterized by starting at a lower voltage and reaching a higher voltage, and vice versa, thereby reducing the threshold voltage and increasing the operating voltage gap.

Coating both CF and W emitters with a PS layer proved highly beneficial, reducing the required supply voltage for emission initiation and yielding more condensed electron beams. However, marked differences were observed in the FEE characteristics of PS-coated CF and W emitters, evident from the results in Tables 1 and 2, including: (I) PS-coated W emitters exhibited a distinct 'switch-on' phenomenon. When the applied voltage was slowly increased, the emission current abruptly jumped from nearly zero to a large ISAT value. This behavior is attributed to PS optimizing the chemical structure of W, forming an effective composite that enables this effect. (II) Differences in sample geometry also contributed. Variations in radius and coating thickness, as measured from SEM images, affected the emission properties. PS-coated W emitters showed a larger built-in $I-V$ hysteresis between the up and down cycles, requiring higher initiation and threshold voltages and operating over a wider voltage range than the coated CF emitters. (III) Murphy–Good plots of the current-voltage data revealed similar linearity in the low-field region for both coated CF and W emitters, but the slope for W was smaller. This indicates greater stability and compatibility of W with the PS coating, improving performance in this region.

Figures 13 and 14 further demonstrate these differences. The PS-coated W emitters produced more concentrated beams than the PS-coated CF emitters, with FEM images showing brighter, more intense spots. This enhanced brightness is attributed to a combination of chemical structure, tip sharpness, and coating thickness. These factors not only increased the spot brightness of the PS-coated W samples but also contributed to higher emission current and overall stability.

In general, significant differences in the profiles and structures—size, shape, and chemical composition—were observed between uncoated and coated CF and W emitters. These differences directly influenced electron beam emission, resulting in variations in brightness [8, 16, 18, 23–25, 28]. Both coated and uncoated emissions are governed by field electron emission theory and its associated models. For coated emitters, the emission process follows the metal–insulator–vacuum regime [12, 13, 21, 32]. In this regime, penetration of the electric field into the dielectric reduces the Schottky–Nordheim barrier, allowing electrons to tunnel from the metal substrate into the dielectric conduction band and then through the surface barrier into vacuum without thermal excitation [10, 11, 18, 20]. The sharpness of the emitter tip and the dielectric coating collectively lower the effective work function of the coated composite emitter. This ensures that even at relatively low extraction voltages, internal electrons can tunnel efficiently, producing higher emission currents. The work function of PS-coated W emitters is lower than that of PS-coated CF emitters, leading to a more pronounced reduction of the potential barrier and improved emission characteristics. Consequently, the coated emitters deliver higher emission currents at lower extraction voltages. Furthermore, the stability and concentration of the electron beam from coated emitters are attributed to the field-induced formation of an emission channel through the dielectric layer at the emitter apex, concentrating the beam into a single bright spot. Differences in the composition structure of PS-coated CF and W samples could contribute to variations in the shape and size of the emission channel and, consequently, the concentration and beam stability [8, 9, 22, 23]. In summary, the coated composite emitter structure of the W sample proves to be more suitable and stable, emitting a brighter, more intense, and more concentrated beam.

4. Conclusions

This work provides a brief analysis of two similar studies, highlighting their shared features and confirming the excellent field electron emission behavior of dielectric-coated emitter tips. Such emitters hold strong potential as advanced electronic field sources. From a technological standpoint, polystyrene-coated carbon fiber and tungsten emitters offer several advantages over uncoated emitters. Particularly noteworthy are their low operating voltages and high current values, enabling higher current densities for the same applied electric fields. Furthermore, the polystyrene coating serves as a protective barrier, guarding the emission plane surface against undesired chemical or physical sorption of ions that could lead to tip bombardment. This protection allows the emitter to operate stably at lower vacuum levels compared to conventional field electron emission emitters. Moreover, the polystyrene coat significantly enhances the concentration and stability of the emitted electron beam, resulting in more stable, concentrated, condensed, and brighter field-emission microscope current-distribution images compared to those obtained with uncoated emitters. Overall, the polystyrene coating layer, as demonstrated in both studies, leads to high source brightness, low emission threshold voltage, low operating voltage, and stable high emission current under high vacuum conditions. Polystyrene, as a coating material that yields enhanced results, stands as a viable option alongside epoxy resins and metal oxides for covering field electron emission emitter sources.

Acknowledgments

We acknowledge CzechNanoLab Research Infrastructure, supported by MEYS CR (LM2018110). Knápek and Allaham would like to acknowledge financial support from the Czech Academy of Sciences (RVO:68081731).

References

[1] Baig, N., Kammakakam, I., and Falath, W., Mater. Adv., 2 (2021) 1821.

[2] Khursheed, A., Ultramicroscopy, 128 (2013) 10.

[3] Bronsgeest, M.S., Barth, J.E., Swanson, L.W., and Kruit, P., J. Vac. Sci. Technol. B, 26 (3) (2008) 955.

[4] Swanson, L.W. and Schwind, G.A., "A Review of the Cold-Field Electron Cathode", In: "Advances in Imaging and Electron Physics", (Elsevier, 2009) pp. 63–100.

[5] Lee, H.R., Lee, S.W., Shikili, C., Kang, J.S., Lee, J., and Park, K.C., J. Nanosci. Nanotechnol., 16 (2016) 12053.

[6] Lei, W., Li, C., Cole, M.T., Qu, K., Ding, S., Zhang, Y., Warner, J.H., Zhang, X., Wang, B., and Milne, W.I., Carbon, 56 (2013) 255.

[7] Nirantar, S., Ahmed, T., Bhaskaran, M., Han, J.-W., Walia, S., and Sriram, S., Adv. Intell. Syst., 1 (2019) 1900039.

[8] Burda, D., Allaham, M.M., Knapek, A., Sobola, D., and Mousa, M.S., 2021 34th Int. Vacuum Nanoelectron. Conf., IVNC 2021. (2021).

[9] Mousa, M.S., Knápek, A., and Grmela, L., Jordan J. Phys., 13 (2020) 171.

[10] Mousa, M.S. and Kelly, T.F., Ultramicroscopy, 95 (2003) 125.

[11] Mousa, M.S., Surf. Interface Anal., 39 (2007) 102.

[12] Latham, R.V. and Mousa, M.S., J. Phys. D Appl. Phys., 19 (1986) 699.

[13] Mousa, M.S., J. Phys. Colloques, 48 (1987) C6-109.

[14] Miller, M.K., Kenik, E.A., Mousa, M.S., Russell, K.F., and Bryhan, A.J., Scr. Mater., 46 (2002) 299.

[15] Mousa, M.S., Appl. Surf. Sci., 94–95 (1996) 129.

[16] Allaham, M.M., Forbes, R.G., Knápek, A., Sobola, D., Burda, D., Sedlák, P., and Mousa, M.S., Mater. Today Commun., 31 (2022) 103654.

[17] Forbes, R.G., R. Soc. Open. Sci., 6 (2019) 190912.

[18] Knápek, A., Allaham, M.M., Burda, D., Sobola, D., Drozd, M., and Horáček, M., Mater. Today Commun., 34 (2023) 105270.

[19] Knápek, A., Dallaev, R., Burda, D., Sobola, D., Allaham, M.M., Horáček, M., Kaspar, P., Matějka, M., and Mousa, M.S., Nanomaterials, 10 (2020) 1294.

[20] Mousa, M.S. and Kelly, T.F., Surf. Interface Anal., 36 (2004) 444.

[21] Mousa, M.S., Surf. Sci., 231 (1990) 142.

[22] Al Soud, A., Knápek, A., and Mousa, M.S., Jordan J. Phys., 13 (2020) 191.

[23] Al-Qudah, A.A., Mousa, M.S., and Fischer, A., IOP Conf. Ser. Mater. Sci. Eng., 92 (2015) 1.

[24] Alnawasreh, S.S., Al-Qudah, A.M., Madanat, M.A., Ali, E.S.B., Almasri, A.M., and Mousa, M.S., Appl. Microsc., 46 (2016) 227.

[25] Almarsi, A.M., Hagmann, M.J., and Mousa, M.S., Appl. Microsc., 47 (2017) 55.

[26] Fawaeer, S.H., Shatnawi, M.T.M., Allaham, M.M., and Mousa, M.S., Adv. Mater. Process. Technol., 8 (2021) 2775.

[27] Alabth, M., Shatnawi, M.T.M., Allaham, M.M., Burda, D., and Mousa, M.S., Ultramicroscopy, 244 (2023) 113643.

[28] Madanat, M., Al Share, M., Allaham, M.M., and Mousa, M.S., J. Vac. Sci. Technol. B, 39 (2021) 024001.

[29] Popov, E.O., Filippov, S.V., Kolosko, A.G., and Knápek, A., J. Vac. Sci. Technol. B, 40 (2022) 024201

[30] Allaham, M.M., Forbes, R.G., and Mousa, M.S., Jordan J. Phys., 13 (2) (2020) 101.

[31] Higashitani, K., Makino, H., and Matsusaka, S., "Powder Technology Handbook", 4th ed., (CRC Press, Boca Raton, FL: Taylor & Francis Group, LLC, 2019).

[32] Mousa, M.S., J. Phys. Colloques, 48 (1987) C6-115.

Volume 18, Number 3, 2025. pp. 365-374

Jordan Journal of Physics

ARTICLE

The Quantum Harmonic Oscillator with $\lambda\delta'(x)$ Potential

M. A. Dalabeeh

Physics Department, Faculty of Science, Al-Balqa Applied University, Al-Salt, Jordan.

Doi: **https://doi.org/10.47011/18.3.9**

Received on: 19/03/2024; Accepted on: 22/04/2024

Abstract: In this work, the problem of the quantum harmonic oscillator with a delta-derivative potential $\lambda\delta'(x)$, where λ is a coupling constant, is solved using the Green's function technique. A transcendental equation that governs the energy eigenvalues of the problems for each coupling constant is obtained. The eigenfunctions and their first derivative are proved to be discontinuous at the origin. The values of the discontinuity jumps are found to agree with the requirements of having a self-adjoint extension Hamiltonian. In the large coupling limit, the even energy eigenvalues and eigenfunctions for the quantum harmonic oscillator are annihilated, and only the odd parts survive. The dependence of the energy eigenvalues and eigenfunctions on the sign of λ was made clear. A mapping between the sign of λ and the positions of the particle was used to explain the discontinuity of the solution. In the large-λ regime, an educated guess for the wave functions was proposed. The proposed solutions led to the correct energy eigenvalues and obeyed the required conditions to have a self-adjoint extension Hamiltonian.

Introduction

The quantum harmonic oscillator potential is among the most popular and important potentials in quantum mechanics; this comes from the fact that it is an approximate solution to many systems around their minimum potential. Moreover, the simplicity of obtaining its exact solution using various approaches, such as the analytic and algebraic techniques, is useful in presenting quantum mechanics ideas and formalisms [1]. On the other hand, the Dirac delta derivative potential describes a point-like or contact interactions that appear in many applications in physics. The interest in this model of contact potential goes back to the early days of quantum mechanics. After the pioneering paper of Berezin and Faddeev [2], a lot of works on this subject have been published. It was shown that contact or singular potential of different physical systems could be represented using the Dirac delta function and its derivatives, such as spectral filters [3, 4], supersymmetry [5], quantum waveguides [6, 7], thin sheets [8, 9], an entanglement of polymers [10], Bose-Einstein condensation in a harmonic trap [11], and propagation of a light [12]. Also, this contact potential is of particular importance in the nanoscale quantum devices [13].

The interpretation of the $\delta'(x)$ potential is unclear, and there are many discussions about its physical meaning. For example, in many works [14–19], this potential is used as boundary conditions on the wave function or its first derivative; in other works [20, 21], it is considered as a dipole-dipole interaction [22–24], or as a zero limit of a smooth potential [25, 26]. A discussion of these interpretations can be found in [27].

Solving the Schrödinger equation for a Hamiltonian with a contact potential is usually challenging compared to other regular Hamiltonians and has attracted considerable attention, including some controversy. One difficulty related to this potential is that the

Corresponding Authors: M. A. Dalabeeh **Email**: madalabeeh@bau.edu.jo

Hamiltonian is not self-adjoint unless the solutions are allowed to be discontinuous, with specific discontinuity jumps required to ensure self-adjointness.

Janev *et al.* [28] determined the perturbed spectrum of a three-dimensional harmonic oscillator potential with an added singular δ-type potential centered at the origin. In the work of Gadella *et al.* [29], the authors studied the one-dimensional harmonic oscillator with a singular potential given in terms of the Dirac delta function and its first derivative, namely, $-a\delta(x)+b\delta'(x)$, where $a,b>0$. They used the Lippman-Schwinger Green's function technique to obtain the energy eigenvalues for the problem. Many interesting works, based on the physical applications and models related to this type of potential, have been published since then [30–37].

In our work, we deal with a closely related singular potential, namely, $\lambda\delta'(x)$, which uses part of the potential studied by Gadella *et al.* [29]. The motivation behind this is that problems involving singular potentials are susceptible to our choice of the involved parameters and the applied techniques as well. For example, we can find many examples in the literature where the obtained results directly depend on the way the authors followed in dealing with the singular potential, especially in the regularization technique [38]. On the other hand, it is not straightforward to simply set $a=0$ in the general expression $a\delta(x)+b\delta'(x)$ to obtain the correct result for $b\delta'(x)$ alone. This ambiguity is particularly evident in the Klauder phenomenon [39], where $H=H_0+\lambda H'$ does not converge to H_0 when the positive real parameter λ of the singular perturbation H' tends to zero.

In contrast, the Green's function approach used in this work is independent of the specific potential of the problem as long as the solutions without the contact potential are known. This method was followed by Atkinson [40] and Chair [41] to obtain the solution and the exact eigenvalues for problems involving contact potential. In this method, the completeness and the orthonormality properties of the exact solutions are used as an expansion basis for the solution of the problem with the $\lambda\delta'(x)$ potential. For the Hamiltonian operator to be self-adjoint, both $H^\dagger = H$ and the domains of $H^\dagger$ and H should be equal, that is:

$$<\phi|H\psi> - <H^\dagger\phi|\psi> = 0 \qquad (1)$$

is satisfied for all ϕ and ψ in the same domain. In the one-dimensional case, the Hamiltonian is given by

$$H = -\frac{d^2}{dx^2} + \lambda\delta'(x) \qquad (2)$$

Kurasov's theorem states that there is a one-to-one correspondence between the set of self-adjoint extensions of such Hamiltonians and the wave functions' boundary conditions [42]. For the harmonic oscillator with a Dirac delta-derivative potential Hamiltonian, namely, $H=-\frac{d^2}{dx^2}+x^2+\lambda\delta'(x)$, we adopt Griffiths' [43] method to find the boundary conditions on the solutions to ensure the self-adjointness of the Hamiltonian.

General Outline

The bound state problem in one dimension with a potential that involves a delta function derivative $\lambda\delta'(x)$, where λ is a coupling constant, has an exact solution whenever the exact solutions to the problem without $\lambda\delta'(x)$ potential are known and complete. In the following, we will outline the procedure, then apply it to the problem under consideration. The Schrödinger equation in the presence of $\delta'(x)$ is given by:

$$[-\frac{\hbar^2}{2m}\frac{d^2}{dx^2} + U(x) + \lambda\delta'(x)]\psi(x) = \epsilon\psi(x). \quad (3)$$

If for $\lambda=0$ the set of eigenfunctions $\psi_n(x)$ corresponding to the energy eigenvalues ϵ_n, that is

$$[-\frac{\hbar^2}{2m}\frac{d^2}{dx^2} + U(x)]\psi_n(x) = \epsilon_n\psi_n(x), \qquad (4)$$

are complete

$$\sum_n \psi\,(x)^*_n\psi_n(x') = \delta(x-x') \qquad (5)$$

and orthonormal

$$\int \psi(x)^*_n\psi_m(x)dx = \delta_{nm}, \qquad (6)$$

then we can expand the solution $\psi(x)$ using these eigenfunctions

$$\psi(x) = \sum_{n=0} c_n\,\psi_n(x). \qquad (7)$$

Substituting this into Eq. (3), we obtain

$$\sum_{n\geq 0}[\,c_n\epsilon_n\psi_n(x) + \lambda\delta'(x)c_n\psi_n(x)] = \epsilon\sum_{n\geq 0} c_n\,\psi_n(x). \qquad (8)$$

Using the orthonormality of the eigenfunctions $\psi_n(x)$

$$\int_{-\infty}^{\infty} \psi_n(x)\psi_m(x)dx = \delta_{nm} \qquad (9)$$

and the following property of the $\delta'(x)$ proposed by Kurasov [44] when applied to a function with discontinuity jump at the origin and a discontinuity jump in its first derivative at the origin,

$$f(x)\delta'(x) = \bar{f}(0)\delta'(x) - \bar{f}'(0)\delta(x), \qquad (10)$$

where

$$\bar{f}(0) = \frac{f(+0)+f(-0)}{2}, \bar{f}'(0) = \frac{f'(+0)+f'(-0)}{2} \qquad (11)$$

are the averages of the function and its first derivative at $x = 0$, respectively[1], leads to the following expression of the expansion coefficient c_n:

$$c_n = \lambda \frac{[\overline{\psi'}(0)\psi_n^*(0)+\overline{\psi}(0)\psi_n'^*(0)]}{\epsilon_n-\epsilon}. \qquad (12)$$

From Eq. (7), the solution $\psi(x)$ now is given by:

$$\psi(x) = \lambda \sum_{n\geq 0} \frac{[\overline{\psi'}(0)\psi_n^*(0)+\overline{\psi}(0)\psi_n'^*(0)]}{\epsilon_n-\epsilon} \psi_n(x). \qquad (13)$$

The assumption that the sum is convergent for all values of $x \neq 0$, while for $x \to 0$ it converges to $\psi(\bar{0})$, leads us to an implicit equation for the eigenvalues ϵ and the coupling constant λ:

$$\frac{1}{\lambda} = \frac{\overline{\psi'}(0)}{\overline{\psi}(0)} \sum_{n\geq 0} \frac{|\psi_n(0)|^2}{\epsilon_n-\epsilon} + \sum_{n\geq 0} \frac{\psi_n'^*(0)\psi_n(0)}{\epsilon_n-\epsilon}. \qquad (14)$$

After obtaining the energy eigenvalues ϵ, the corresponding eigenfunctions $\psi(x)$ can be found using Eq. (13). The ratio $\frac{\overline{\psi'}(0)}{\overline{\psi}(0)}$ can be determined by normalizing the wave function $\psi(x)$ using:

$$\int_{-\infty}^{\infty} |\psi(x)|^2 dx = 1, \qquad (15)$$

and by implying that the first derivative of the wave function $\psi'(x)$ can be obtained using Eq. (13), that is:

$$\psi'(x) = \lambda \sum_{n\geq 0} \frac{[\overline{\psi'}(0)\psi_n^*(0)+\overline{\psi}(0)\psi_n'^*(0)]}{\epsilon_n-\epsilon} \psi_n'(x). \qquad (16)$$

In the following, we are going to apply this technique to the quantum harmonic oscillator problem $U(x) = \frac{1}{2}m\omega^2x^2$ to solve the Schrödinger equation with the added delta-derivative potential.

Schrödinger Equation for the Harmonic Oscillator with $\lambda\delta'(x)$

The Schrödinger equation for the harmonic oscillator with a delta-derivative potential is given by:

$$[-\frac{\hbar^2}{2m}\frac{d^2}{dx^2} + \frac{1}{2}m\omega^2x^2 + \lambda\delta'(x)]\psi(x) = \epsilon\psi(x), \qquad (17)$$

where m is the particle's mass, $\omega = \sqrt{\frac{k}{m}}$ is the angular frequency of the oscillator, and k is the force constant. By applying the Green's function technique [45, 46], we obtain the solutions in the following linear combination:

$$\psi(x) = \sum_{n\geq 0} c_n \psi_n(x), \qquad (18)$$

where $\psi_n(x)$ are the eigenfunctions of the problem with $\lambda = 0$, that is:

$$[-\frac{\hbar^2}{2m}\frac{d^2}{dx^2} + \frac{1}{2}m\omega^2x^2]\psi_n(x) = \epsilon_n\psi_n(x). \qquad (19)$$

The energy eigenvalues in this case are given by $\epsilon_n = (n + \frac{1}{2})\hbar\omega$. The eigenfunctions of $\psi_n(x)$ are given explicitly by:

$$\psi_n(x) = \frac{1}{\sqrt{2^n n!}}(\frac{mw}{\pi\hbar})^{1/4} e^{-mwx^2/2\hbar} H_n(\sqrt{\frac{mw}{\hbar}}x). \qquad (20)$$

Here, $H_n(x)$ are the Hermite polynomials [47]. To simplify the calculations, we will use the following scale for length and energy. In this scale, the energy is measured in units of $\hbar\omega/2$ while the length is measured in units of $\sqrt{\hbar/m\omega}$. Using this scale, the Schrödinger equation for the harmonic oscillator becomes:

$$[-\frac{d^2}{dx^2} + x^2]\psi_n(x) = \epsilon_n\psi_n(x), \qquad (21)$$

and the eigenvalues ϵ_n are given by $\epsilon_n = 2n + 1$.

---

[1] For a continuously differentiable function $f(x)$, the equation $f(x)\delta'(x) = f(0)\delta'(x) - f'(0)\delta(x)$ holds. This equation can be extended to discontinuous functions. In Kurasov [44], the values and derivatives at $x = 0$ were replaced with the average values of the left- and right-hand limits at the discontinuity point, using the generalized definition of the δ function $\int \delta(x-a)f(x)dx = \frac{f(a-0)+f(a+0)}{2}$.

The Self-Adjoint Extension of the Hamiltonian

The presence of the contact potential $\lambda\delta'(x)$ in the Hamiltonian

$$H = -\frac{d^2}{dx^2} + x^2 + \lambda\delta'(x) \tag{22}$$

requires imposing additional conditions on the domain of H, such that the domains of H and its hermitian conjugate $H^\dagger$ coincide. In one dimension, the self-adjointness of a Hermitian operator requires that

$$\int_{-\infty}^{\infty} \psi^* \, H\phi dx - \int_{-\infty}^{\infty} (H^\dagger\psi^*)\phi dx = 0, \tag{23}$$

hold for any pair of functions ψ and ϕ sharing the same domain. The process of adding the required conditions to the domain of a Hermitian operator to ensure that Eq. (23) is satisfied is called self-adjoint extension. In the case of the one-dimensional Hamiltonian given by $H = -\frac{d^2}{dx^2} + \lambda\delta'(x)$, the wave function and its first derivative according to Kurasov's theorem [42] should satisfy the following boundary conditions at the origin

$$\begin{pmatrix}\psi(+0)\\ \psi'(+0)\end{pmatrix} = \begin{pmatrix}\frac{2+\lambda}{2-\lambda} & 0\\ 0 & \frac{2-\lambda}{2+\lambda}\end{pmatrix}\begin{pmatrix}\psi(-0)\\ \psi'(-0)\end{pmatrix}. \tag{24}$$

Now these boundary conditions require that the discontinuity jumps $\Delta\psi = \psi(+0) - \psi(-0)$ and $\Delta\psi' = \psi'(+0) - \psi'(-0)$ are equal to $\lambda\overline{\psi}(0)$ and $-\lambda\overline{\psi'}(0)$, respectively. In our case, we can find the conditions on the wave function and its first derivative by following the procedure used by Griffiths [43]. First, we integrate the Shrödinger equation for the harmonic oscillator in the presence of $\lambda\delta'(x)$ from η to $-\eta$:

$$-\int_{-\eta}^{\eta}\frac{d^2}{dx^2}\psi(x)dx + \lambda\int_{-\eta}^{\eta}\delta'(x)\psi(x)dx + \int_{-\eta}^{\eta}x^2\,\psi(x)dx = \epsilon\int_{-\eta}^{\eta}\psi(x)dx. \tag{25}$$

The first integral gives $\psi'(+\eta) - \psi'(-\eta)$, which is the discontinuity jump at $x = 0$ of the first derivative that is $\Delta\psi'$ when we take the limit $\eta \to 0$. The second integral can be computed using integration by parts:

$$\lambda\int_{-\eta}^{\eta}\delta'(x)\psi(x)dx = \lambda\delta(x)\psi(x)|_{-\eta}^{\eta} - \lambda\int_{-\eta}^{\eta}\delta(x)\psi'(x)dx. \tag{26}$$

The term $\delta(x)\psi(x)|_{-\eta}^{\eta}$ is zero, while the integral $\int_{-\eta}^{\eta}\delta(x)\psi'(x)dx$ can be computed by considering $\delta(x)$ and $\psi'(x)$ as distributions [42], and the result is:

$$\int_{-\eta}^{\eta}\delta(x)\psi'(x)dx = \bar{\psi}'(0). \tag{27}$$

The integrals $\int_{-\eta}^{\eta}\psi(x)dx$ and $\int_{-\eta}^{\eta}x^2\,\psi(x)dx$ in Eq. (25) vanish in the limit $\eta \to 0$, and we end up with the following boundary condition:

$$\Delta\psi' = -\lambda\bar{\psi}'(0). \tag{28}$$

This matches the boundary condition on the first derivative of the eigenfunctions obtained in [43] and [42] for the simpler Hamiltonian $H = -\frac{d^2}{dx^2} + \lambda\delta'(x)$. To obtain the second boundary condition, we integrate the Schrödinger equation from $-l$ to x with l positive this time:

$$-\int_{-l}^{x}\frac{d^2}{dy^2}\psi(y)dy + \lambda\int_{-l}^{x}\delta'(y)\psi(y)dy + \int_{-l}^{x}y^2\,\psi(y)dy = \epsilon\int_{-l}^{x}\psi(y)dy. \tag{29}$$

The first integral gives $\psi'(x) - \psi'(l)$. The second, via integration by parts, yields

$$\int_{-l}^{x}\delta'(y)\psi(y)dy = \delta(y)\psi(y)|_{-l}^{x} - \int_{-l}^{x}\delta(y)\psi'(y)dy, \tag{30}$$

Now, for $x < 0$, the integral $\int_{-l}^{x}\delta(y)\psi'(y)dy$ is zero. For $x \geq 0$ the integral can be found as before by regarding $\delta(y)$ and $\psi'(y)$ as distributions:

$$\int_{-l}^{x}\delta'(y)\psi(y)dy = \delta(x)\psi(x)|_{-l}^{x} - \theta(x)\bar{\psi}'(0) = \delta(x)\psi(x) - \theta(x)\bar{\psi}'(0), \tag{31}$$

where $\theta(x)$ is the Heaviside step function given by:

$$\theta(x) = \begin{cases} 0 & x < 0\\ 1 & x \geq 0\end{cases}$$

Substituting these results into Eq. (29), then integrating again from $-\eta$ to η, we obtain:

$$-\int_{-\eta}^{\eta}(\psi'(x) - \psi'(l))dx, + \lambda\int_{-\eta}^{\eta}(\delta(x)\psi(x) - \theta(x)\bar{\psi}'(0))dx = \int_{-\eta}^{\eta}\left(\int_{-l}^{x}(\epsilon - y^2)\psi(y)dy\right)dx \tag{32}$$

integrating the left-hand side and taking the limit $\eta \to 0$ yields $-\Delta\psi + \lambda\bar{\psi}(0)$. As the right-hand side integral is zero in the limit $\eta \to 0$, we conclude that the wave function $\psi(x)$ is discontinuous and the discontinuity jump is

$$\Delta\psi = \lambda\overline{\psi}(0). \tag{33}$$

This is again the same condition found for the kinetic energy operator with a singular potential $\lambda\delta'(x)$.

The Energy Eigenvalues

The energy eigenvalues ϵ for the quantum harmonic oscillator with $\lambda\delta'(x)$ are determined using Eq. (14), which gives

$$\frac{1}{\lambda} = \frac{\overline{\psi'}(0)}{\overline{\psi}(0)}\sum_{n\geq 0}\frac{|\psi_{2n}(0)|^2}{\epsilon_{2n}-\epsilon}, \tag{34}$$

where the second term in Eq. (14) has no contribution to ϵ since $\psi_n(0)=0$ for odd n, while $\psi_n'(0)=0$ for even n. By a process of analytic continuation, this sum can be found as follows. First, note that $\psi_{2n}(0)$ is given by [48]:

$$\psi_{2n}(0) = (-1)^n\sqrt{\frac{(2n)!}{\pi^{1/2}2^{2n}(n!)^2}} = (-1)^n\sqrt{\frac{1}{\pi}\frac{\Gamma(n+\frac{1}{2})}{\Gamma(n+1)}}. \tag{35}$$

If we assume temporarily that $\epsilon < 1$, the following integral representation can be used to evaluate the sum

$$\frac{1}{\lambda} = -\frac{\overline{\psi'}(0)}{4\pi\overline{\psi}(0)}\int_0^1 x^{-(\epsilon+3)/4}\sum_{n\geq 0}x^n\frac{\Gamma(n+\frac{1}{2})}{\Gamma(n+1)}dx. \tag{36}$$

The asymptotic behavior of the ratio of gamma functions $\frac{\Gamma(n+\frac{1}{2})}{\Gamma(n+1)}$ can be obtained using Stirling's formula

$$\Gamma(az+b) \sim \sqrt{2\pi}e^{-az}(az)^{az+b-(1/2)}, a > 0,\ b \in C, \tag{37}$$

then

$$\frac{\Gamma(n+\frac{1}{2})}{\Gamma(n+1)} \sim n^{-1/2}, n \to \infty. \tag{38}$$

This ensures the convergence of the series that appeared in Eq. (36) (after doing the integration). Using the Taylor series expansion of the function $\frac{1}{\sqrt{1-x}}$, the sum can be found as

$$\sum_{n\geq 0}x^n\frac{\Gamma(n+\frac{1}{2})}{\Gamma(n+1)} = \frac{\pi^{1/2}}{(1-x)^{1/2}}. \tag{39}$$

Substituting this back into Eq. (36), the integral can be easily computed using the beta functions expressed in terms of gamma functions:

$$\int_0^1\frac{x^{-(\epsilon+3)/4}}{(1-x)^{1/2}}dx = B(\tfrac{1}{4}-\tfrac{\epsilon}{4},\tfrac{1}{2}) = \frac{\Gamma(\frac{1}{4}-\frac{\epsilon}{4})\Gamma(\frac{1}{2})}{\Gamma(\frac{3}{4}-\frac{\epsilon}{4})}. \tag{40}$$

where $\Gamma(\frac{1}{2}) = \sqrt{\pi}$. By analytic continuation, we can extend the result of Eq. (40) for small ϵ to include all values of $\epsilon \neq 4n+1$. Using Eq. (34), the energy eigenvalues are determined by the following transcendental equation:

$$\frac{1}{\lambda} = -\frac{\overline{\psi'}(0)}{4\overline{\psi}(0)}\frac{\Gamma(1/4-\epsilon/4)}{\Gamma(3/4-\epsilon/4)}. \tag{41}$$

The scale $\frac{\overline{\psi'}(0)}{\overline{\psi}(0)}$ may be computed numerically using the normalization condition together with Eq. (16) evaluated at $x=0$. Using the transcendental equation, exact numerical values of the energy eigenvalue ϵ of the problem can be obtained. For each given λ, an infinite set of eigenvalues ϵ exists. In Tables 1 and 2, the ground state and the first five excited-state energy eigenvalues for different positive and negative coupling constant is given. The purpose of the figure and tables is to provide an outline of the general behavior of the energy spectrum. The $\lambda = 0$ case recovers the eigenvalues energy for the even states of the original problem without $\lambda\delta'(x)$.

TABLE 1. Energy eigenvalues of the harmonic oscillator in the presence of the $\lambda\delta'(x)$ potential for different values of the negative scaled coupling constant $\lambda_s = \lambda\frac{\overline{\psi'}(0)}{4\overline{\psi}(0)}$.

λ_s	E_0	E_2	E_4	E_6	E_8	E_{10}
0	1	5	9	13	17	21
-0.1	0.75577	4.88620	8.91510	12.9293	16.9382	20.9111
-0.2	0.47073	4.77166	8.83015	12.8587	16.8765	20.8889
-0.5	-	4.44153	8.58245	12.6515	16.6946	20.7248
-0.8	-	4.16109	8.35827	12.4588	16.5229	20.5684
-1	-	4.0095	8.22685	12.3419	16.4166	20.4703
-2	-	3.57029	7.77759	11.9073	16.0006	20.0724
-5	-	3.23098	7.33826	11.4155	15.4776	19.5301
- 10	-	3.12994	7.17024	11.2116	15.2457	19.2753

TABLE 2. Energy eigenvalues of the harmonic oscillator in the presence of the $\lambda\delta'(x)$ potential for different values of the positive scaled coupling constant $\lambda_s = \lambda\frac{\overline{\psi'}(0)}{4\overline{\psi}(0)}$.

λ_s	E_0	E_2	E_4	E_6	E_8	E_{10}
0.1	0.75577	4.88620	8.91510	12.9293	16.9382	20.9111
0.2	1.38757	5.21886	9.16676	13.1397	17.1225	21.1105
0.5	1.78548	5.50928	9.40039	13.3398	17.3001	21.2717
0.8	2.04393	5.74525	9.60541	13.5219	17.4652	21.4235
1	2.16779	5.87417	9.72459	13.6313	17.5664	21.5180
2	2.50638	6.28378	10.1423	14.0407	17.9627	21.9001
5	2.78401	6.67640	10.5984	14.5357	18.4826	22.4365
10	2.88937	6.83036	10.7922	14.7581	18.7284	22.6962

From Fig. 1, we notice that the energy eigenvalues increase with increasing λ in the positive region. For negative λ, however, the energy decreases as the magnitude of λ increases. For sufficiently large λ, these energy eigenvalues converge to the energy eigenvalues of the odd states of the original problem without the contact interaction $\lambda\delta'(x)$. The convergence depends on the sign of λ. If λ is positive, the energy converges to the next odd state energy, whereas for negative λ, it converges to the odd eigenvalue of the previous state. In the first table, we neglected the values of ϵ in the negative region, since the transcendental equation is derived for positive values of ϵ.

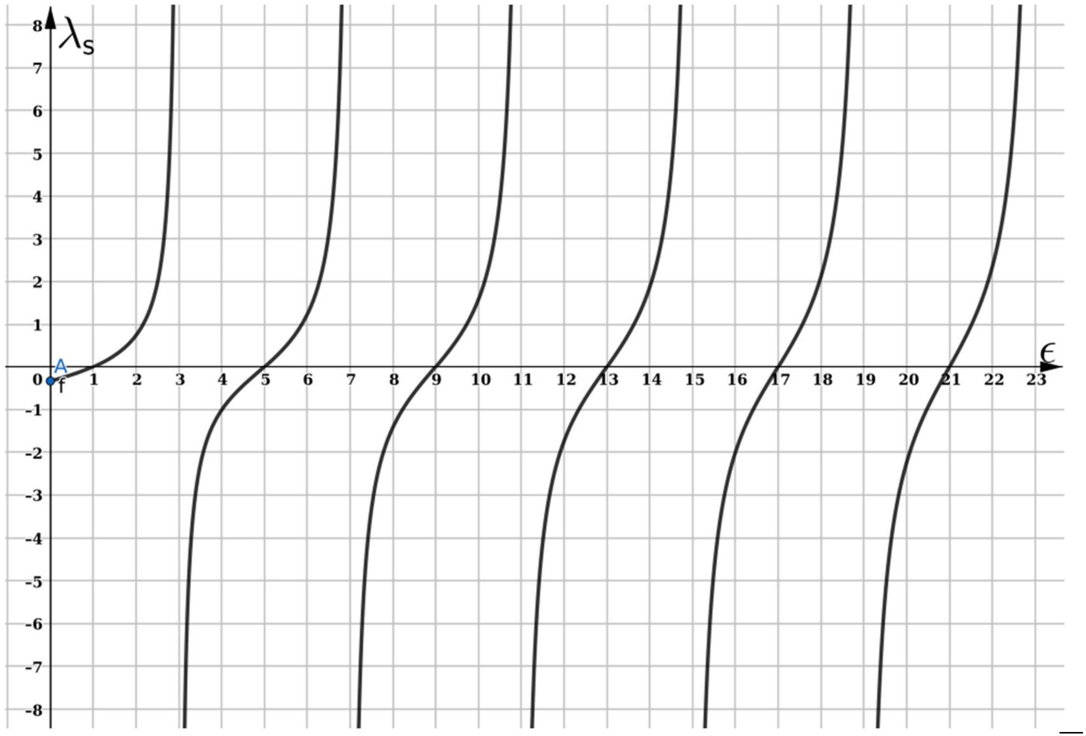

FIG. 1. A plot of Eq. (41) with the coupling constant λ replaced by the scaled coupling constant $\lambda_s = \lambda\frac{\overline{\psi'}(0)}{4\overline{\psi}(0)}$.

The behavior of the energy eigenvalues can be explained using the gamma function identity

$$\Gamma(z)\Gamma(1-z) = \frac{\pi}{\sin(\pi z)} \quad (42)$$

together with Stirling's formula

$$\Gamma(az+b) \sim \sqrt{2\pi}e^{-az}(az)^{az+b-(1/2)}, a > 0,\ b \in C. \quad (43)$$

For large ϵ, the ratio that appears in Eq. (40) can be written as:

$$\frac{\Gamma(\frac{1}{4}-\frac{\epsilon}{4})}{\Gamma(\frac{3}{4}-\frac{\epsilon}{4})} = \frac{\Gamma(\frac{1}{4}+\frac{\epsilon}{4})\sin\pi(\frac{3}{4}-\frac{\epsilon}{4})}{\Gamma(\frac{3}{4}+\frac{\epsilon}{4})\sin\pi(\frac{1}{4}-\frac{\epsilon}{4})} \sim \frac{\sqrt{\epsilon}}{2}\tan\frac{\pi}{4}(\epsilon-1). \quad (44)$$

This asymptotic behavior is periodic under the shift $\epsilon \rightarrow \epsilon + 4$. Moreover, as $\epsilon \rightarrow 2n + 1$, the ratio diverges to infinity. This behavior is clearly reflected in Tables 1 and 2 and in Fig. 1.

The Energy Eigenfunctions

The Green's function technique is used to obtain exact implicit results concerning the energy eigenvalues of the system under consideration. Using this technique, we can go further and try to get the energy eigenfunctions of the system. From Eq. (13) and the transcendental Eq. (41), the solution to the Schrödinger equation of the quantum harmonic oscillator in the presence of the Dirac delta derivative potential can be written as an infinite sum:

$$\psi(x) = \frac{4\overline{\psi}(0)}{\overline{\overline{\psi'}}(0)} \frac{\Gamma\left(\frac{3}{4}-\frac{\epsilon}{4}\right)}{\Gamma\left(\frac{1}{4}-\frac{\epsilon}{4}\right)} \times \sum_{n\geq 0} \frac{[\overline{\psi'}(0)\psi_n^*(0)+\overline{\psi}(0)\psi_n'^*(0)]}{\epsilon-\epsilon_n}\psi_n(x). \qquad (45)$$

Since $\psi_{2n+1}(0)$ and $\psi'_{2n}(0)$ are both zeros, we can simplify the sum above by splitting it into two sums, one over the odd values of n and another over even n as follows:

$$\psi(x) = \frac{4\Gamma\left(\frac{3}{4}-\frac{\epsilon}{4}\right)}{\Gamma\left(\frac{1}{4}-\frac{\epsilon}{4}\right)} \times \begin{bmatrix} \overline{\psi}(0)\sum_{n\geq 0}\frac{\psi_{2n}^*(0)}{\epsilon-\epsilon_{2n}}\psi_{2n}(x) \\ +\frac{\overline{\psi}^2(0)}{\overline{\overline{\psi'}}(0)}\sum_{n\geq 0}\frac{\psi_{2n+1}'^*(0)}{\epsilon-\epsilon_{2n+1}}\psi_{2n+1}(x) \end{bmatrix}. \qquad (46)$$

Using the recursion relation

$$\psi'_n(x) = \sqrt{\frac{n}{2}}\psi_{n-1}(x) - \sqrt{\frac{n+1}{2}}\psi_{n+1}(x) \qquad (47)$$

together with the identity Eq. (35), the wave function can be written as:

$$\psi(x) = \frac{4\Gamma(3/4-\epsilon/4)}{\sqrt{\pi}\Gamma(1/4-\epsilon/4)}\sum_{n\geq 0}(-1)^n \frac{\sqrt{\Gamma(n+\frac{1}{2})}}{\sqrt{\Gamma(n+1)}} \times \left[\frac{\overline{\psi}(0)\psi_{2n}(x)}{(\epsilon-\epsilon_{2n})} + \sqrt{4n+2}\,\frac{\frac{\overline{\psi}^2(0)}{\overline{\overline{\psi'}}(0)}\psi_{2n+1}(x)}{(\epsilon-\epsilon_{2n+1})}\right]. \qquad (48)$$

This wave function is supposed to be discontinuous at the origin. We can check this by noting that there is a one-to-one correspondence between the solution in the positive and the negative regions and the sign of the coupling constant λ. Specifically, the solution in the positive region, $\psi_+(x)$, is equal to the solution in the negative region, $\psi_-(x)$, with λ replaced by $-\lambda$. To see this, we write the Shrödinger equation in the positive and the negative regions:

$$[-\frac{d^2}{dx^2} + x^2 + \lambda\delta'(x)]\psi(x) = \epsilon\psi(x), x > 0 \qquad (49)$$

$$[-\frac{d^2}{dx^2} + x^2 + \lambda\delta'(x)]\psi(x) = \epsilon\psi(x), x < 0 \qquad (50)$$

Since the Hamiltonian $-\frac{d^2}{dx^2} + x^2 + \lambda\delta'(x)$ is odd only on $\delta'(x)$, Eq. (50) can be rewritten as:

$$[-\frac{d^2}{dx^2} + x^2 - \lambda\delta'(|x|)]\psi(x) = \epsilon\psi(x), x < 0. \qquad (51)$$

This equation is similar to Eq. (49) with the opposite sign of λ. This means that the solution in the negative region can be obtained by solving the Schrödinger equation in the positive region for the opposite sign of λ. This one-to-one correspondence is transitive to the energy eigenvalues. Let us denote the roots of the transcendental Eq. (41) for $\pm\lambda$ by $\epsilon_{m_\pm}$. Then the solutions in both regions are related to each other by replacing the energy eigenvalues from $\epsilon_{m_+} \rightarrow \epsilon_{m_-}$. In the case of $\lambda = 0$, the energy eigenvalues satisfy $\epsilon_{m_+} = \epsilon_{m_-}$, and the solutions in both regions are the same. This recovers the original solution of the quantum harmonic oscillator. Our solution now can be rewritten in a way that emphasizes its discontinuity as follows:

$$\psi_m(x) = \begin{cases} \frac{4\Gamma(3/4-\epsilon_{m_+}/4)}{\sqrt{\pi}\Gamma(1/4-\epsilon_{m_+}/4)}\sum_{n\geq 0}(-1)^n\frac{\sqrt{\Gamma(n+\frac{1}{2})}}{\sqrt{\Gamma(n+1)}}[\frac{\overline{\psi}(0)\psi_{2n}(x)}{(\epsilon_{m_+}-\epsilon_{2n})} + \frac{\sqrt{4n+2}\frac{\overline{\psi}^2(0)}{\overline{\overline{\psi'}}(0)}\psi_{2n+1}(x)}{(\epsilon_{m_+}-\epsilon_{2n+1})}], & x > 0 \\ \frac{4\Gamma(3/4-\epsilon_{m_-}/4)}{\sqrt{\pi}\Gamma(1/4-\epsilon_{m_-}/4)}\sum_{n\geq 0}(-1)^n\frac{\sqrt{\Gamma(n+\frac{1}{2})}}{\sqrt{\Gamma(n+1)}}[\frac{\overline{\psi}(0)\psi_{2n}(x)}{(\epsilon_{m_-}-\epsilon_{2n})} + \frac{\sqrt{4n+2}\frac{\overline{\psi}^2(0)}{\overline{\overline{\psi'}}(0)}\psi_{2n+1}(x)}{(\epsilon_{m_-}-\epsilon_{2n+1})}], & x < 0. \end{cases} \qquad (52)$$

Using Cramér's inequality [49]

$$|\psi_n(x)| \leq \pi^{1/4}, \qquad (53)$$

we notice that the sums in the wave function $\psi_m(x)$ depend critically on the denominators $\epsilon_{m_\pm} - \epsilon_{2n}$ and $\epsilon_{m_\pm} - \epsilon_{2n+1}$. Thus, the dominant sum is chosen regarding the eigenvalues $\epsilon_{m_\pm}$. For small λ, the values of $\epsilon_{m_\pm}$ lie between the odd and even original eigenvalues of the problem (without the added contact interaction), namely, $\epsilon_{2m+1} > \epsilon_{m_+} > \epsilon_{2m}$, and $\epsilon_{2m+1} < \epsilon_{m_-} < \epsilon_{2m}$. So for small λ, both the even and the odd sums contribute to the wave function $\psi_m(x)$. On the other hand, for a large value of λ, the eigenvalues $\epsilon_{m_\pm}$ tend to $\epsilon_{2m\pm1}$ as we can see from Eq. (44), so the odd part of the sums above will dominate the even contribution and hence, the solution will be represented by the odd wave function of the problem before adding the contact interaction. In the following section, we will give an educated solution for the large λ situation.

Large Coupling Constant Solutions

The asymptotic behavior of the energy eigenvalues, as given in Eq. (44) and shown in Fig. 1, motivates us to write the solutions in the large coupling constant regime. Since the eigenvalues in this limit shift to the odd energy levels of the quantum harmonic oscillator, we suggest that the eigenfunctions approach the odd oscillator wave functions $\psi_{2n\pm1}(x)$. The shift in ϵ, evident from Fig. 1, depends on the sign of λ. Since $\delta'(x)$ is an odd function of x, the sign of λ can be transferred to the variable x. Hence, the behavior of the energy eigenvalues ϵ now depends on the sign of x. This implies that the wave functions differ on either side of the singular point $x = 0$, consistent with the discontinuity condition established in Sec. IV and the discussion in Sec. VI. Taking these facts into account, we propose the following form for the wave functions in the large-λ region.

$$\psi_n(x) = \begin{cases} \psi_{2n+1}(x) + \phi_+(x) & \text{if } x > 0, n = 0,1,2,3\cdots \\ \psi_{2n-1}(x) + \phi_-(x) & \text{if } x < 0, n = 1,2,3\cdots \\ \phi_-(x) & \text{if } x < 0, n = 0 \end{cases} \tag{54}$$

Since the eigenfunctions $\psi_{2n\pm1}(x)$ are zeros at $x = 0$, we add the functions $\phi_\pm(x)$. The functions $\phi_\pm(x)$ are chosen to decay rapidly and to satisfy both the boundary conditions on the wave function and its derivative. Moreover, for $x << 1$, they must satisfy the Schrödinger equation, where the harmonic potential x^2 can be neglected. A good choice of $\phi_\pm(x)$ comes from the bound-state solution of the Schrödinger equation in the presence of the $\lambda\delta'(x)$ potential:

$$[-\frac{\hbar^2}{2m}\frac{d^2}{dx^2} + \lambda\delta'(x)]\phi(x) = \epsilon\phi(x), \tag{55}$$

The solutions to this problem, for the bound state case, were obtained in [41] and are given by:

$$\phi_\pm(x) = \frac{\lambda}{2}(\frac{\overline{\psi'}(0)}{\kappa} \pm \overline{\psi}(0))e^{\mp\kappa x}. \tag{56}$$

The ± stands for the solution on the positive (negative) x-axis. The eigenvalue κ is related to the coupling constant λ by:

$$\frac{1}{\lambda} = \frac{\overline{\psi'}(0)}{2\kappa\overline{\psi}(0)}. \tag{57}$$

The solutions $\phi_\pm$ were shown to satisfy the required boundary conditions on the wave function and its first derivative. As $\psi_{2n\pm1}(x)$ are zero at the origin and as the boundary conditions on our work are similar to the conditions on the solution $\phi_\pm$, we conclude that Eq. (54) provides valid approximate solutions for the Schrödinger equation of the harmonic oscillator with the additional $\lambda\delta'(x)$ potential in the large coupling region.

Conclusion

In this work, we found that exact solutions of the quantum harmonic oscillator with the addition of a point interaction represented by the $\lambda\delta'(x)$ centred at the origin can be obtained using Green's method. The values of the energy eigenvalues are determined using a transcendental equation. The numerical values of the energy eigenvalues can be determined exactly whenever the solutions are normalized. We showed that, for a large coupling constant, the energy eigenvalues tend to be the odd eigenvalues of the quantum harmonic oscillator. The conditions required for a self-adjoint extension of the Hamiltonian were obtained following the method of Griffiths. Both the wave function and its first derivative were found to be discontinuous at the singular point $x = 0$, with discontinuity jumps consistent with the results previously derived by Kurasov and Griffiths for simpler Hamiltonians. These boundary conditions appear to be a general feature whenever such contact potentials are present. The results in the large coupling constant region show that only the odd solutions of the harmonic oscillator were available. Furthermore, for large λ, it was easy to guess the solution that meets the behavior of the energy eigenvalues and the conditions on the solution. Finally, expressing the exact solutions, which are represented as infinite series, in terms of elementary functions remains a challenging mathematical problem. Successfully doing so would enable full normalization of the wave functions, exact computation of energy eigenvalues, and deeper physical insight into the problem.

The authors have no conflicts to disclose.

References

[1] Bloch, S.C., "Introduction to Classical and Quantum Harmonic Oscillators", (Wiley, 1997).

[2] Berezin, F.A. and Faddeev, L.D., Dokl. Akad. Nauk. SSSR, 137 (5) (1961) 1011.

[3] Turek O. and Cheon, T., EPL, 98 (2) (2012) 20004.

[4] Turek, O. and Cheon, T., J. Math. Phys., 54 (3) (2013) 033508.

[5] Diaz, J.I., Negro, J., Nieto, L.M., and Rosas-Ortiz, O., J. Phys. A Math. Gen., 32 (48) (1999) 8447.

[6] Albeverio, S., Cacciapuoti, C., and Finco, D., J. Math. Phys., 48 (5) 052103.

[7] Cacciapuoti, C. and Exner, P., J. Phys. A Math. Theor., 40 (26) (2007) F511.

[8] Zolotaryuk, A.V. and Zolotaryuk, Y., J. Phys. A Math. Theor., 48 (33) (2015) 335302.

[9] Zolotaryuk, A.V., Phys. Rev. A, 87 (6) (2013) 062115.

[10] Lin, M.C. and Jao, R.F., Phys. Rev. E, 74, 74 (4) (2006) 046608.

[11] Uncu, H., Tarhan, D., Demiralp, E., and Müstecaplıoğlu, Ö.E., Phys. Rev. A, 76 (1) (2007) 013618.

[12] Zurita-Sanchez, R. and Halevi, P., Phys. Rev. E, 61 (5) (2000) 5805.

[13] Cheon, T., Exner, P., and Seba, P., Phys. Lett. A, 277 (1) (2000) 7.

[14] Albeverio, S., Gesztesy, F., Høegh-Krohn, R., and Kirsch, W., J. Oper. Theory, 12 (1) (1984) 101.

[15] Albeverio, S., Gesztesy, F., and Holden, H., J. Phys. A Math. Gen., 26 (16) (1993) 3903.

[16] Albeverio, S., Brzeźniak, Z., and Dąbrowski, L., J. Phys. A Math. Gen., 27 (14) (1994) 4933.

[17] Coutinho, F.A.B., Nogami, Y., and Perez, J.F., J. Phys. A Math. Gen., 30 (11) (1997) 3937.

[18] Coutinho, F.A.B., Nogami, Y., and Perez, J.F., J. Phys. A Math. Gen., 32 (11) (1999) L133.

[19] Coutinho, F.A.B., Nogami, Y., and Tomio, L., J. Phys. A Math. Gen., 32 (26) (1999) 4931.

[20] Coutinho, F.A.B., Nogami, Y., and Tomio, L., Rev. Bras. Ens. Fís., 31 (4) (2009) 4302.

[21] Patil, S.H., Phys. Scr., 49 (5) (1994) 645.

[22] Christiansen, P.L. et al., Journal of Physics A: Mathematical and General, 36 (27) (2003) 7589.

[23] Christiansen, P.L., Low Temperature Physics/ Fizyka Nyzkykh Temperatur, 48 (12) (2022) 1169.

[24] Zolotaryuk, A.V., Christiansen, P.L., and Iermakova, S.V., J. Phys. A Math. Gen., 39 (30) (2006) 9329.

[25] Golovaty, Y., Integral Equ. Oper. Theory, 75 (3) (2013) 341.

[26] Golovaty, Y.D. and Hryniv, R.O., J. Phys. A Math. Theor., 43 (15) (2010) 155204.

[27] Lange, R.-J., J. Math. Phys., 56 (12) (2015) 122105.

[28] Janev, R.K. and Marić, Z., Phys. Lett. A, 46 (5) (1974) 313.

[29] Gadella, M., Glasser, M.L., and Nieto, L.M., Int. J. Theor. Phys., 50 (7) (2011) 2144.

[30] Gadella, M., Hernandez-Munoz, J., Nieto, L.M., and San Millan, C., Symmetry, 13 (2) (2021) 350.

[31] Zolotaryuk, A.V. and Zolotaryuk, Y., J. Phys. A Math. Theor., 54 (3) (2021) 035201.

[32] Nieto, L.M., Gadella, M., Mateos-Guilarte, J., Munoz-Castaneda, J.M., and Romaniega, C., "On the Schrödinger Equation with Dirac Delta Potentials", In: "Geometric Methods in Physics xxxviii", (Birkhäuser, 2020), pp. 127–140.

[33] Conde-Vazquez, R., Barrera-Figueroa, V., and Rabinovich, V. S., J. Phys.: Conf. Ser., 1540 (1) (2020) 012028.

[34] Erman, F., Gadella, M., and Uncu, H., Front. Phys., 8 (2020) 65.

[35] Fassari, S. and Rinaldi, F., Nanosyst. Phys. Chem. Math., 10 (6) (2019) 608.

[36] Zolotaryuk, A.V., Ukr. J. Phys., 64 (11) (2019) 1021.

[37] Golovaty, Y., Front. Phys., 7 (2019) 70.

[38] Zolotaryuk, A.V., Phys. Lett. A, 374 (15-16) (2010) 1636.

[39] DeFacio, B. and Hammer, C.L., J. Math. Phys., 15 (7) (1974) 1071.

[40] Atkinson, D.A. and Crater, H.W., Am. J. Phys., 43 (4) (1975) 301.

[41] Chair, N. and Dalabeeh, M.A., Eur. J. Phys., 42 (5) (2021) 055404.

[42] Kurasov, P., J. Math. Anal. Appl., 201 (1) (1996) 297.

[43] Griffiths, D.J., J. Phys. A Math. Gen., 26 (9) (1993) 2265.

[44] Kurasov, P.B., Scrinzi, A., and Elander, N., Phys. Rev. A, 49 (6) (1994) 5095.

[45] Roach, G.F., "Green's Functions", 2nd Ed., (Cambridge University Press, 1982).

[46] Byron, F.W. and Fuller, R.W., "Mathematics of Classical and Quantum Physics", (New York: Dover Publications, 1992).

[47] Griffiths, D.J., "Introduction to Quantum Mechanics", 2nd Ed., (Pearson Prentice Hall, 2004).

[48] Arfken, G.B. and Weber, H.J., "Mathematical Methods for Physicists", 6th Ed., (Academic Press, 2005).

[49] Bateman, H. and Erdélyi, A., "Higher Transcendental Functions", Vol. 1, (McGraw-Hill Book Company, 1953).

Volume 18, Number 3, 2025. pp. 375-388

Jordan Journal of Physics

ARTICLE

Natural Radioactivity and Estimation of Radiation Doses in Some Northern Jordanian Buildings

Talal S. M. Haimur[a], **Saleh R. Al-Bashaish**[a] and **Marwan S. Mousa**[b]

[a] *Department of Allied Sciences, Faculty of Arts and Sciences, Al-Ahliyya Amman University, P.O. Box 19328 Amman, Jordan.*

[b] *Department of Renewable Energy Engineering, Jadara University, Irbid 21110, Jordan.*

Doi: **https://doi.org/10.47011/18.3.10**

Received on: 27/03/2024; *Accepted on: 03/09/2024*

Abstract: The radioactivity of different types of building materials used in Jordan was analyzed using a high-purity germanium detector (HPGe). The measured activity concentrations of ^{238}U, ^{235}U, ^{232}Th, ^{226}Ra, and ^{40}K in Bq.kg^{-1} were found in ranges of 1.7-66.1, 0.02-1.7, 0.3-11, 1.22-65.8, and 8.1-69.4, respectively. The radium equivalent activity (R_{eq}) ranged from 87.36 to 3.46 Bq.kg^{-1}. Mean values of the radium equivalent activity, hazard indices, absorbed dose rate, and annual effective dose were calculated. The results obtained in this investigation were analyzed and compared with data reported from other countries. With one exception, the findings are consistent with the recommended limits of the International Commission on Radiological Protection.

Keywords: Natural radioactivity, Building materials, Gamma-ray spectroscopy, Jordan, Hazard indexes.

1. Introduction

The radiological hazards of construction materials used in buildings due to the presence of natural radioactivity have been extensively investigated over the past 45 years. Several studies have been carried out to estimate the radiological hazards and annual dose contributions of natural radioactivity in buildings [1], both in Jordan and worldwide. Since people spend nearly 80% of their lives indoors [2], understanding the accumulation of radioactive nuclei in construction components is crucial for evaluating radiation exposure. Among the different radio-nuclides, $^{40}K_{19}$ and members of the natural radioactive series starting with $^{238}U_{92}$, $^{235}U_{92}$, and $^{232}Th_{90}$, are to be considered [3]. These radionuclides are found geologically in soils and hard rocks and are widely distributed in the environment [4]. Building materials derived from such ores and raw resources inevitably contain varying levels of these radionuclides, thereby increasing the absorbed dose of residents through external exposure [5, 6]. The γ-rays, as has been largely recognized, can seriously cause a great deal of damage to the human body [7]. High radium exposure could cause immune suppression, anemia, cataracts, and tooth frailty. These health impacts are realized only through extreme exposure to radium in the workplace [3]. Health risks might exist in many forms: accumulation of the radio-nuclide dust through mining, aggregation in the kidneys and bones, or cancer [8]. For this reason, there is a growing need to control the use of soil-derived materials, such as cement, ceramic, granite, and decorative stones. These materials can serve as an additional source of radiation exposure to people [9].

In this study, gamma radiation measurements are reported for a variety of naturally occurring rocks in Jordan, marketed under different commercial names. These results are of general interest since such rocks are globally used as building and ornamental materials. A standard

Corresponding Author: Talal S. M. Haimur **Email**: thaimur@ammanu.edu.jo

high-purity germanium detector was used for these measurements, but advanced gamma detection systems that use high-resolution, coincidence/anti-coincidence, and thorough background analyses to suppress background and detect weak radionuclides can also be useful for studies of radiological hazards [10-14].

2. Materials and Methods

2.1. Sample Collection

Thirty-one samples of different types of construction components used in the northern area of Jordan were collected. It was noted that some construction materials are directly used in construction, primarily hard limestone. These materials are usually uprooted and drawn as they are, and then taken directly for uses in building construction, a fact that is confirmed in the natural formation of this type of building material. In this study, ten samples (group 1) were taken from these materials and then cut into parallel slices of known thickness to fit the detector system. The characteristics of these natural construction materials are presented in Table 6.

Materials of the second type have been processed in the laboratory as a concrete mixture (cement, aggregate, sand, and water). These materials have been prepared and processed manually in the laboratory. Five concrete mixtures (group 2), equipped with specific components, were packed and sealed using polyethylene Marinelli beakers and stored to dry for twelve hours and then dipped in water for a period of thirty-six hours. Then the samples were put under the sunlight to dry naturally for five days. The details of these processed samples are given in Table 7.

Finally, the third type included factory-processed construction materials: six tiles (group 3), five bricks (group 4), and five ceramic samples (group 5). These materials were collected from different factories, where they were manufactured and equipped for use as building materials. Their compositions and manufacturing methods were used to characterize these man-made products. The specifications of these samples are summarized in Table 8.

Samples under investigation were put in sealed plastic bags for one month before starting the process of measuring the radioactivity contents of these samples within the device (high-pure germanium detector and computer system), in order to assess the status of internal stability between ^{226}Ra and ^{231}Th and their progeny.

2.2. Spectroscopic Analysis

The activity concentrations of natural radionuclides in the prepared samples were measured at the Radiation Measurements Laboratory, Al-Balqa Applied University, Jordan. For energy calibration and efficiency evaluation, standard reference materials (RGU-1, RGTh-1, RGK-1), certified by the International Atomic Energy Agency [15], were used.

The detection system consisted of a p-type well-type high-purity germanium detector (GWL) with a standard energy resolution of 2.09 keV and a relative efficiency of 56.9% at 1.33 MeV of ^{60}Co. The detector was cylindrical, with dimensions of 3 inches in diameter and 3 inches in thickness, made of 99.99999998% pure germanium crystal. To minimize background radiation, the detector was surrounded by a 15-cm-thick lead shield. The shield was mounted directly on a liquid nitrogen cylinder, which cooled the detector to the operating temperature of liquid nitrogen (77 ^{40}K). The software, Gamma Vision (Model A66-B32, Version 5 [16], has been readily supplied with the detector system. Absolute errors in the measured values were estimated, based upon the Gaussian distribution, using the uncertainty in the number of counts given by the software [7]. Gamma ray spectra were analyzed for photo peaks of uranium, thorium daughter products, and ^{40}K. The ^{226}Ra radio-nuclide level has been estimated from photo peaks of ^{214}Pb at 295.22 keV (19.30%), 351.93 keV (37.6%), photo peaks of ^{214}Bi at 609.31 keV (46.1%), and 1764.49 keV (15.4%), and photo peaks of ^{234}Pa at 1001.3 keV (0.838%), and 766.36 keV (0.317%). Similarly, ^{232}Th radio-nuclide level was estimated from photo peaks of ^{228}Ac at 911.2 keV (25.8%), 968.97 keV (15.8%), and 338.32 keV (11.27%), photo peaks of ^{208}Tl at 2614.53 keV (35.64%), 583.19 keV (30.72%), photo peaks of ^{212}Bi at 727.33 keV (6.67%), 39.86 keV (27.7%), and the 238.6 keV (43.6%) photo peak of ^{212}Pb. Finally, the ^{40}K radio-nuclide level was measured directly using the (1460.72 keV) (10.7%) gamma photo peak.

2.3. The Design of Detector Shielding

The purpose of detector shielding is to reduce the amount of radiation from background sources reaching the detector. This background derives from radioactive nuclides within the environment, primarily ^{40}K in natural potassium and the uranium decay chain nuclides. Adequate reduction in the external gamma radiation intensity is not the only criterion that must be considered. As the atomic number of an absorber increases, the importance of Compton scattering as the primary interaction decreases relative to photoelectric absorption and pair production. If a shield is made of lead rather than iron, fewer gamma-rays will be Compton scattered as opposed to being absorbed. That, in turn, means that there will be fewer scattered gamma-rays to penetrate the shielding from outside and, perhaps more importantly, fewer backscattered gamma-rays from within the shield. Conventionally, detector shielding consists of 100 mm of lead. Although a greater thickness of lead would provide a greater reduction in background peak heights, the greater mass of lead available for interaction with cosmic rays would lead to an increase in the overall background continuum level. Therefore, 100-150 mm of lead is regarded as optimum. The detector is mounted within a thin aluminum retaining sleeve, which also serves as the outer contact with the detector. The core contact is made with either a conical pin or a spring-loaded pin extending within the hollow core. This arrangement is fixed to a pedestal, which is connected to the copper cold finger extending through the cryostat to the liquid nitrogen reservoir. The complete assembly is then covered by the end cap to form a sealed chamber. The upper part of the detector housing is evacuated and thermally insulated from the rest of the housing. A pack of charcoal or molecular sieve absorbent is mounted in the detector chamber to absorb traces of gases left after evacuation when the detector is cooled. Beneath the detector pedestal, preamplifier field-effect transistors (FETs) are secured and cooled for stable operation [17].

Figures 1-3 show the electronic structure of the high-purity germanium detector and the liquid nitrogen reservoir.

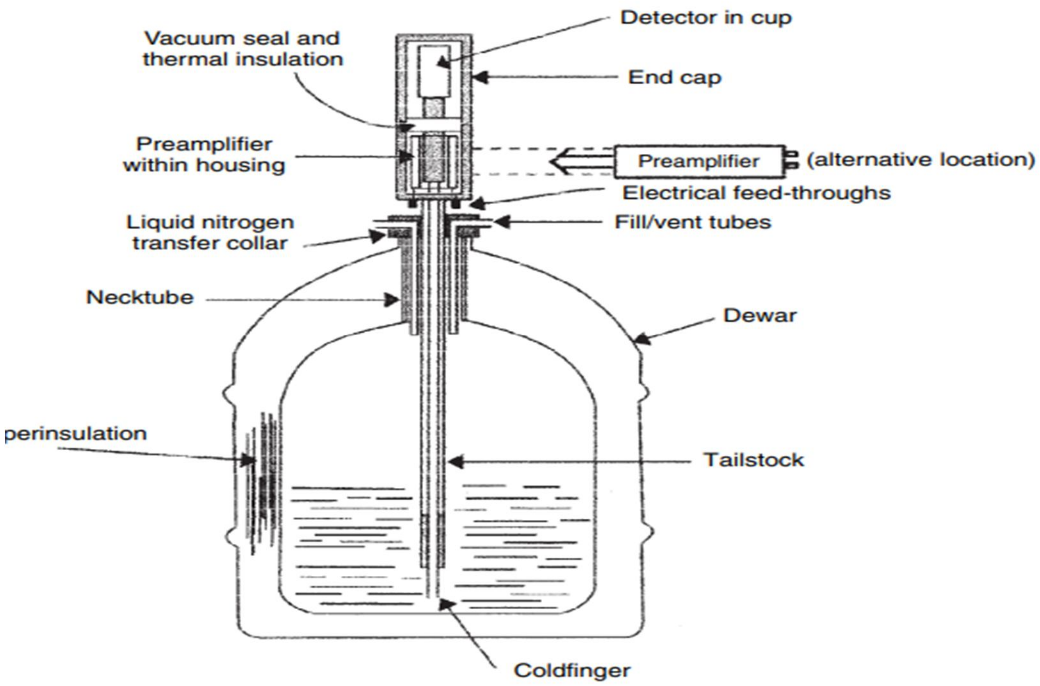

FIG. 1. A typical germanium detector, including the cryostat and liquid nitrogen reservoir.

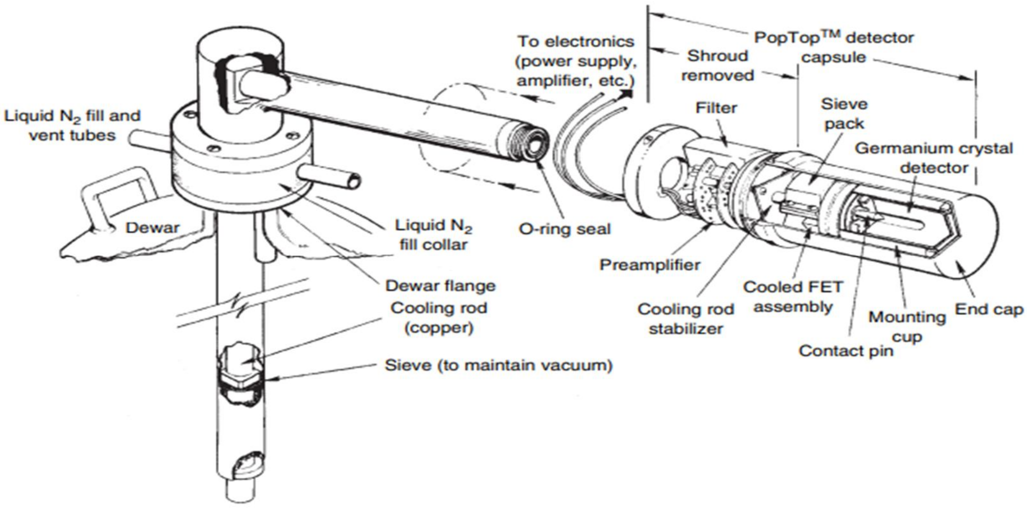

FIG. 2. A modern arrangement of detector and preamplifier within the cryostat housing – an exploded view of the ORTEC Pop-Top™ detector capsule with a horizontal dipstick cryostat and a 20 l Dewar. Reproduced by permission of ORTEC.

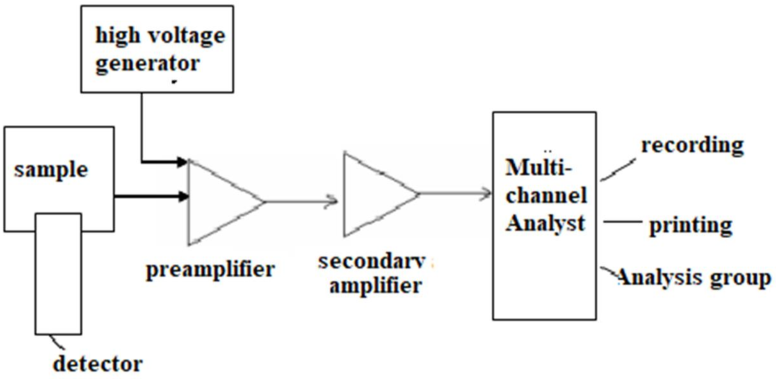

FIG. 3. Electronic structure of a high-purity germanium detector

3. Calculations

3.1 Radioactive Nuclei Accumulation

The calculations of the activity concentration (A_{Ei}) values of ^{235}U, ^{238}U, ^{232}Th series, and ^{40}K in the samples were carried out by using the following equation [18]:

$$A_{Ei} = N_{Ei} / (\varepsilon_E)\,(t)\,(\gamma_d)\,(m) \qquad (1)$$

where A_{Ei} represents the nucleus i-activity at energy Ei, N_{Ei} represents the number of peak photos at energy Ei, ϵ_E is the detection efficiency of energy Ei, t represents the counting time, γ_d represents the gamma emission resulting from each disintegration at the energy Ei of this nucleus, and m represents the mass sample in kg.

The determination of $^{238}U_{90}$ was performed indirectly through its gamma-emitting daughter nuclides, assuming that they exist in secular equilibrium with their precursors [18]. The contribution of ^{226}Ra at the energy peak (186.21 keV) can be calculated from ^{214}Pb at the energy line (295.2 keV).

The $^{235}U_{90}$ activity in building materials is rarely reported due to difficulties in gamma-ray spectrometry. The only usable photopeak for ^{235}U is at 185.72 keV [18, 19], which is recorded in the same region as the peak of ^{226}Ra (186.21 keV, 3.59%).

3.2. Radium Equivalent Activity (Ra_{eq})

Due to the irregular distributions of radionuclides ^{226}Ra, ^{232}Th, and ^{40}K in samples under investigation, it is possible to calculate the radium equivalent activity (Ra_{eq}), which is defined according to the estimation that 1 Bq.kg^{-1} of ^{226}Ra, 0.7 Bq.kg^{-1} of ^{232}Th, and 13Bq.kg^{-1} of ^{40}K produce the same gamma ray dose [20-22, 1]:

$$Ra_{eq} = A(Ra) + 1.43\,A(Th) + 0.077\,A(K) \qquad (2)$$

where A(Ra), A(Th), and A(K) are the specific activities of ^{226}Ra, ^{232}Th and ^{40}K in Bq.kg^{-1}, respectively. The maximum value of Ra_{eq} in building constructions must be less than 370 for safe use [23].

3.3. Hazard Indices

To consider radiological hazards from building materials as negligible, the external and internal gamma radiation doses should be limited to 1mSvy^{-1}. Thus, we can calculate the external and internal hazard indices when the safety requirements for building structures are being satisfied. Hence, the external dose should not exceed 1.5 mSv. y^{-1} [23].

For samples under investigation, the external hazard index (H_{ex}) and the internal hazard index (H_{in}) can be calculated by using the following equations [4, 19, 21, 22]:

$$H_{ex} = A(^{226}Ra)/370 + A(^{223}Th)/259 + A(^{40}K)/4810 \leq 1 \quad (3)$$

$$H_{in} = A(^{226}Ra)/185 + A(^{232}Th)/259 + A(^{40}K)/4810 \leq 1 \quad (4)$$

where $A(^{226}Ra)$, $A(^{90}Th)$, and $A(^{40}K)$ are the specific activities of ^{226}Ra, ^{232}Th, and ^{40}K, respectively.

3.4. Estimation of Gamma Absorbed Dose Rate (D)

The conversion factor used for calculating the absorbed gamma dose rate D (in nGy·h^{-1}) corresponds to 0.92 nGy·h^{-1} per Bq·kg^{-1} for ^{226}Ra, 1.1 nGy·h^{-1} per 1 Bq·kg^{-1} for ^{232}Th, and 0.08 nGy·h^{-1} per 1 Bq·kg^{-1} for ^{40}K. For samples under investigation, it is possible to calculate (D) by using the equation [1, 24, 25]:

$$D\ (nGy.\ h^{-1}) = 0.08\ A(K_{19}) + 0.092A(Ra_{88}) + 1.1\ A(Th_{90}) \quad (5)$$

Here, $A(K_{19})$, $A(Ra_{88})$, and $A(Th_{90})$ are specific activities (in Bq.kg^{-1}) of $^{40}K_{19}$, $^{226}Ra_{88}$, and $^{232}Th_{90}$, respectively.

3.5. Annual Effective Absorbed Dose (AED)

The annual effective absorbed dose (H_E) in mSv.y^{-1} can be calculated by the formula [4, 21]:

$$H_E\ (mSv.y^{-1}) = D(nGy.h^{-1}) \times T \times F \quad (6)$$

where T is the indoor occupancy time, which is approximately 80% of the year (8760 hy^{-1}), and F is the gamma conversion factor (0.7×10^{-6} SvGy^{-1}).

4. Results and Discussion

4.1. Activity Concentrations of ^{238}U, ^{35}U, ^{232}Th, ^{226}Ra, and ^{40}K

The specific activity concentrations of ^{238}U, ^{35}U, ^{232}Th, ^{226}Ra, and ^{40}K in the collected samples, including associated uncertainties (Bq.kg^{-1}), are listed in Table 1. Figure 4 illustrates the average radioactive nuclei accumulation for ^{232}Th, ^{226}Ra, and ^{40}K in the investigated construction materials used in Jordan.

The maximum activity concentrations for ^{238}U were 65.9±2.21 Bq/kg in the tile sample 3-T6, and the minimum was 1.7 ± 0.05 Bq/kg in brick sample 4-B1. For ^{235}U, the maximum concentration was 1.72 ± 0.01 in sample 4-B4, and the minimum concentration was 0.03±0.01 in ceramic sample 5-Cc1. For ^{232}Th, the maximum concentration was 11.00 ± 4.41 Bq/kg in ceramic sample 5-Cc3, while the minimum concentration was 0.30±0.01 Bq/kg in brick sample 4-B2. For ^{226}Ra, the maximum concentration was 66.10±2.31 Bq/kg in tile sample 3-T6, while the minimum concentration was 1.03±0.04 Bq/kg in brick sample 4-B1. For ^{40}K, the maximum concentration was 692.10±16.90 Bq/kg in ceramic sample 5-Cc4, while the minimum was 9.10±1.21 Bq/kg in brick sample 4-B4.

From these results, it can be seen that the building materials of type three (factory-processed materials, group (B), bricks) have the minimum average concentrations among all material types. Additionally, we found that specific activity concentration due to ^{40}K contributed the most to the total radioactivity for all samples (Figure 4). In general, the average activity concentrations of natural radionuclides in all samples were below the world averages of 50 Bq.kg^{-1} for ^{226}Ra and ^{232}Th, and 500 Bq.kg^{-1}for ^{40}K [27], except for four samples: ^{226}Ra in tile sample 3-T6 that reached 66.10 ± 2.31 Bq/kg and ^{40}K in ceramic samples 5-Cc3, 5-Cc4, and 5-Cc5 that reached 518.80± 22.20, 692.10± 16.90, and 536.5 0± 9.61, respectively.

TABLE 1. The radioactive nuclei accumulation measured for samples under investigation on average (in Bq kg-^{1}).

Sample code	^{238}U	^{235}U	^{232}Th	^{226}Ra	^{40}K
1-R1(stone)	10.29 ± 1.18	0.16 ± 0.08	5.90 ± 1.61	10.20 ± 1.31	120.90 ± 9.21
1-R2(stone)	07.10 ± 0.80	0.30 ± 0.07	1.00 ± 0.00	06.98 ± 1.92	031.80 ± 6.32
1-R3(stone)	04.00 ± 0.68	0.10 ± 0.05	2.19 ± 1.11	04.00 ± 0.81	032.90 ± 5.70
1-R4(stone)	11.50 ± 0.85	0.10 ± 0.06	4.10 ± 3.01	11.20 ± 0.91	073.10 ± 6.33
1-R5(stone)	12.50 ± 1.00	0.14 ± 0.06	7.40 ± 4.22	12.40 ± 1.20	084.90 ± 15.80
1-R6(stone)	14.50 ± 1.39	0.13 ± 0.09	1.40 ± 0.71	14.40 ± 1.51	064.00 ± 6.21
1-R7(stone)	10.10 ± 2.70	0.40 ± 0.11	1.20 ± 0.70	09.70 ± 2.92	036.80 ± 3.11
1-R8(stone)	09.40 ± 3.58	0.51 ± 0.21	1.20 ± 1.00	08.90 ± 3.90	033.70 ± 1.83
1-R9(stone)	16.30 ± 1.20	0.20 ± 0.08	8.50 ± 2.32	16.20 ± 1.22	047.00 ± 9.31
1-R10(stone)	19.00 ± 0.10	0.10 ± 0.01	10.10 ± 3.21	19.00 ± 0.05	050.00 ± 8.91
2-Ct1(cement)	10.90 ± 3.22	0.20 ± 0.11	5.70 ± 1.41	10.70 ± 1.81	220.00 ± 17.04
2-Ct2(cement)	12.00 ± 1.21	0.13 ± 0.08	6.40 ± 1.21	11.80 ± 1.32	128.70± 14.22
2-Ct3(cement)	13.50 ± 0.31	0.05 ± 0.03	7.90 ± 1.71	13.50 ± 0.41	400.00 ± 18.90
2-Ct4(cement)	13.10 ± 1.51	0.12 ± 0.01	7.00 ± 2.20	13.00 ± 1.60	268.70± 16.41
2-Ct5(cement)	10.47 ± 1.72	0.31 ± 0.02	5.00 ± 0.51	10.20 ± 1.81	223.80± 17.22
3-T1(cement)	14.80 ± 0.12	0.10 ± 0.01	1.00 ± 0.30	14.70 ± 0.12	212.00 ± 18.82
3-T2(tile)	24.90 ± 0.31	0.10 ± 0.01	5.50 ± 3.60	25.00 ± 0.41	214.60± 15.91
3-T3(tile)	33.40 ± 0.59	0.10 ± 0.04	0.90 ± 0.10	33.40 ± 0.70	133.50± 17.63
3-T4(tile)	15.40 ± 0.51	0.10 ± 0.02	1.00 ± 0.15	15.40 ± 0.52	148.00 ± 17.68
3-T5(tile)	14.50 ± 0.62	0.02 ± 0.00	1.00 ± 0.20	14.50 ± 0.61	201.00 ± 13.88
3-T6(tile)	65.90 ± 2.21	0.32 ± 0.01	1.20 ± 0.20	66.10 ± 2.31	259.10± 12.52
4-B1(brick)	01.70 ± 0.05	0.65 ± 0.01	0.50 ± 0.10	01.03 ± 0.04	022.40 ± 3.51
4-B2(brick)	05.10 ± 0.51	0.70 ± 0.03	0.31 ± 0.01	04.40 ± 0.51	043.40 ± 4.71
4-B3(brick)	08.30 ± 1.92	1.62 ± 0.11	0.40 ± 0.10	06.70 ± 3.42	029.60 ± 1.93
4-B4(brick)	05.10 ± 1.17	1.72 ± 0.01	0.45 ± 0.21	03.40 ± 1.28	009.10 ± 1.21
4-B5(brick)	05.02 ± 1.14	1.18 ± 0.01	0.40 ± 0.10	03.81 ± 0.60	025.71 ± 1.70
5-Cc1(ceramic)	08.70 ± 0.21	0.03 ± 0.01	0.62 ± 0.20	08.70 ± 0.11	209.70 ± 19.01
5-Cc2(ceramic)	06.50 ± 0.28	0.40 ± 0.03	6.10 ± 0.31	06.10 ± 0.22	313.20 ± 32.02
5-Cc3(ceramic)	26.80 ± 1.20	0.40 ± 0.08	11.00 ± 4.41	26.40 ± 1.89	518.80± 22.20
5-Cc4(ceramic)	22.30 ± 0.31	0.40 ± 0.02	4.20 ± 1.22	22.00 ± 0.31	692.10± 16.90
5-Cc5(ceramic)	26.50 ± 0.62	0.33 ± 0.03	5.50 ± 2.91	26.20 ± 0.62	536.5 0± 9.61

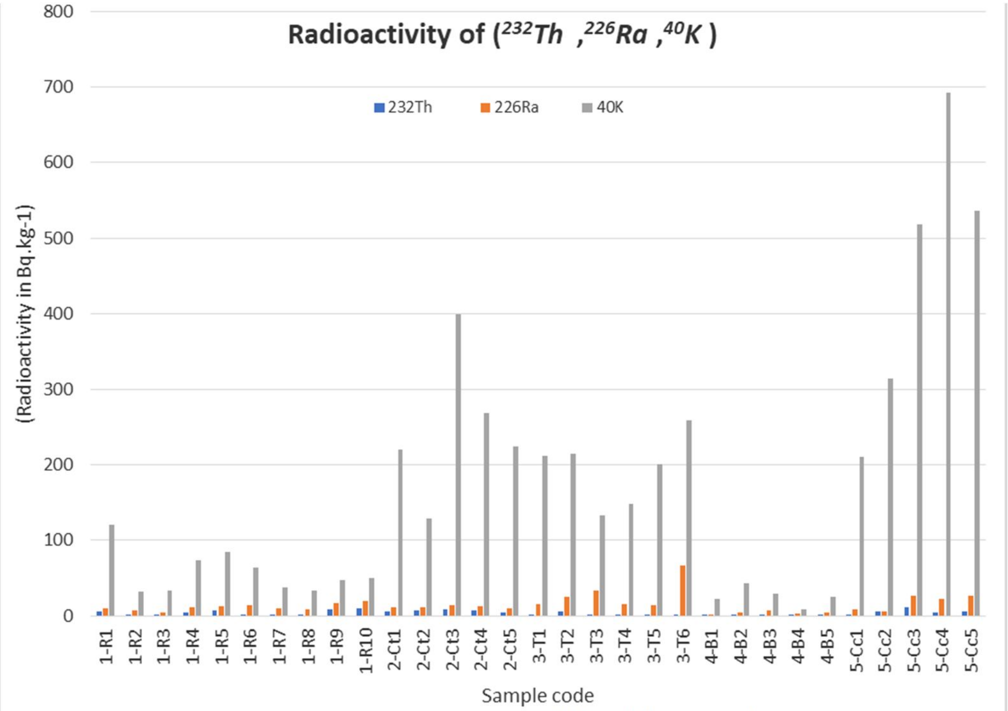

FIG. 4. The radioactive nuclei accumulation in average for ^{226}Ra, ^{232}Th, and ^{40}K of construction components used in Jordan.

4.2. Radium Equivalent Activity (Ra_{eq} in $Bq.kg^{-1}$) and Hazard Indices

The calculated values of radium equivalent (**Ra_{eq}**), external and internal hazard indices (H_{ex}, H_{in}), absorbed dose rate, and effective dose (D, HE) for all samples are summarized in Table 2. The range of radium equivalent activity from a maximum of 87.359 $Bq.kg^{-1}$ for tile sample 3-T6 to a minimum of 3.4598 $Bq.kg^{-1}$ for brick sample 4-B1 has been illustrated in Fig. 5. All samples exhibited Ra_{eq} values below the recommended upper limit of 370 $Bq.kg^{-1}$ for safe use in building materials. Hazard indices ranged from a maximum of 0.2925 for ceramic sample 5-Cc3 to a minimum of 0.0126 4-B for brick sample. The recorded absorbed dose rate presents a range from a maximum of 82.4840 $nGy\ h^{-1}$ for tile sample 3-T6 to a minimum of 3.28040 $nGy\ h^{-1}$ for brick sample. The effective dose ranges from a maximum of 0.4046 $mSvy^{-1}$ for the tile sample to 0.0161 $mSvy^{-1}$ for brick sample 4-B1. All values are below the recommended average indoor dose rate of 84 $nGyh^{-1}$ suggested for construction materials [23], indicating negligible radiological risk for humans, whether at home or in the workplace [36].

TABLE 2. Radium equivalent, external and internal hazard indexes, absorbed dose rate, and effective dose of absorption per year calculated for all samples.

Sample code	Ra_{eq} *(Bq.kg^{-1})*	H_{ex}	H_{in}	*D (nGy h^{-1})*	*HE (mSvy^{-1})*
1-R1(stone)	27.954	0.0754	0.1031	25.5540	0.1254
1-R2(stone)	10.894	0.0294	0.0484	10.1000	0.0496
1-R3(stone)	09.687	0.0261	0.0370	08.7400	0.0429
1-R4(stone)	22.684	0.0612	0.0916	20.6540	0.1013
1-R5(stone)	29.527	0.0797	0.1132	26.3480	0.1293
1-R6(stone)	21.330	0.0576	0.0966	19.9080	0.0977
1-R7(stone)	14.188	0.0383	0.0646	13.1240	0.0644
1-R8(stone)	13.234	0.0357	0.0598	12.2280	0.0600
1-R9(stone)	31.974	0.0863	0.1302	28.0140	0.1374
1-R10(stone)	37.293	0.1006	0.1521	32.5900	0.1599
2-Ct1(cement)	35.791	0.0966	0.1256	33.7140	0.1654
2-Ct2(cement)	30.885	0.0833	0.1153	28.2160	0.1384
2-Ct3(cement)	55.597	0.1500	0.1866	53.1100	0.2605
2-Ct4(cement)	43.723	0.1180	0.1532	41.1800	0.2020
2-Ct5(cement)	34.598	0.0934	0.1210	32.8040	0.1609
3-T1(cement)	32.454	0.0877	0.1274	31.5840	0.1549
3-T2(tile)	49.42	0.1334	0.2011	46.2500	0.2269
3-T3(tile)	45.082	0.1218	0.2121	42.5180	0.2086
3-T4(tile)	28.226	0.0762	0.1179	27.1080	0.1330
3-T5(tile)	31.407	0.0848	0.1240	30.5200	0.1497
3-T6(tile)	87.359	0.2360	0.4136	82.4840	0.4046
4-B1(brick)	3.4598	0.0093	0.0121	3.28040	0.0161
4-B2(brick)	8.1708	0.0221	0.0340	07.8500	0.0385
4-B3(brick)	9.5512	0.0258	0.0439	08.9720	0.0440
4-B4(brick)	4.6672	0.0126	0.0218	04.2710	0.0210
4-B5(brick)	6.4211	0.0175	0.0279	06.0934	0.0298
5-Cc1(ceramic)	25.7566	0.0696	0.0931	25.4860	0.1250
5-Cc2(ceramic)	38.924	0.1050	0.12160	37.3620	0.1833
5-Cc3(ceramic)	81.862	0.2209	0.2925	77.6680	0.3810
5-Cc4(ceramic)	81.2438	0.2194	0.2789	80.1720	0.3933
5-Cc5(ceramic)	75.4602	0.2037	0.2746	73.1620	0.3589

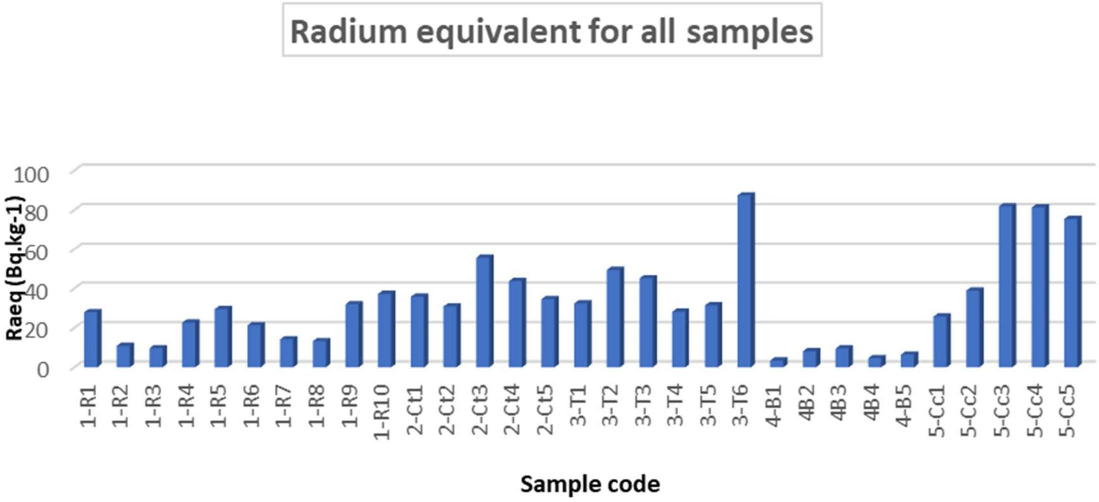

FIG. 5. Radium equivalent activity Ra_{eq} in average for the studied samples.

To compare the five studied groups—building hard rocks (stones), concrete, tiles, bricks, and ceramics—Tables 3, 4a, and 4b, along with Figs. 6–8, summarize and illustrate the results.

It is observed that the ceramics group (5-Cc) had the maximum average radium equivalent Ra_{eq} (60.64 Bq.kg^{-1}), maximum average external index H_{ex} (0.16372), maximum average internal index H_{in} (0.2121), maximum average absorbed dose rate (58.8 nGy. h^{-1}), and maximum average annual effective dose rate (0.288302 mSv. y^{-1}). The bricks group (4-B) had the minimum average radium equivalent Ra_{eq} (06.46 Bq.kg^{-1}), minimum average external index H_{ex} (0.01745), minimum average internal index H_{in} (0.02795), minimum average absorbed dose rate (06.1 nGy. h^{-1}), and minimum average annual effective dose rate (0.029892 mSv. y^{-1}).

Regarding radionuclide concentrations, the tiles group (3-T) had the highest averages for ^{226}Ra (28.12 ± 7.670 Bq kg-^{1}) and ^{238}U (28.183 ± 0.717 Bq kg-^{1}). The concrete group (2-Ct) recorded the maximum average for ^{232}Th (6.40 ± 1.40 Bq kg-^{1}), while the ceramics group (5-Cc) showed the highest average concentration of ^{40}K (453.6 ± 19.76 Bq kg-^{1}).

The bricks group (4-B), on the other hand, had the lowest average radionuclide concentrations across most isotopes: 5.05 ± 0.583333 Bq kg-^{1} for ^{238}U, 3.88 ± 1.567 Bq kg-^{1} for ^{226}Ra, 0.41 ± 0.11Bq kg-^{1} for ^{232}Th, and 25.88 ± 2.745 for ^{40}K. Ultimately, we found that it also had the highest average concentration of ^{235}U (1.1675 ± 0.035 Bq kg-^{1}).

TABLE 3. Average radiological hazard indices for radionuclides in selected building material groups under study.

Group name	Number of shambles	Average Radium equivalent activity Ra_{eq} (Bq.kg^{-1})	Average External index H_{ex}	Average Internal index H_{in}	Average Absorbed Dose Rate (nGy. h^{-1})	Average Annual Effective Dose Rate (mSv. y^{-1})
Hard rocks (stones)	10	21.88	0.02159	0.08964	19.7	0.096768
Concrete	5	40.12	0.10825	0.14035	37.8	0.185455
Tiles	6	45.67	0.12332	0.19934	43.4	0.212955
Bricks	5	06.46	0.01745	0.02795	06.1	0.029892
Ceramics	5	60.64	0.16372	0.2121	58.8	0.288302
Min		06.46	0.01745	0.02795	06.1	0.029892
Max		60.64	0.16372	0.2121	58.8	0.288302

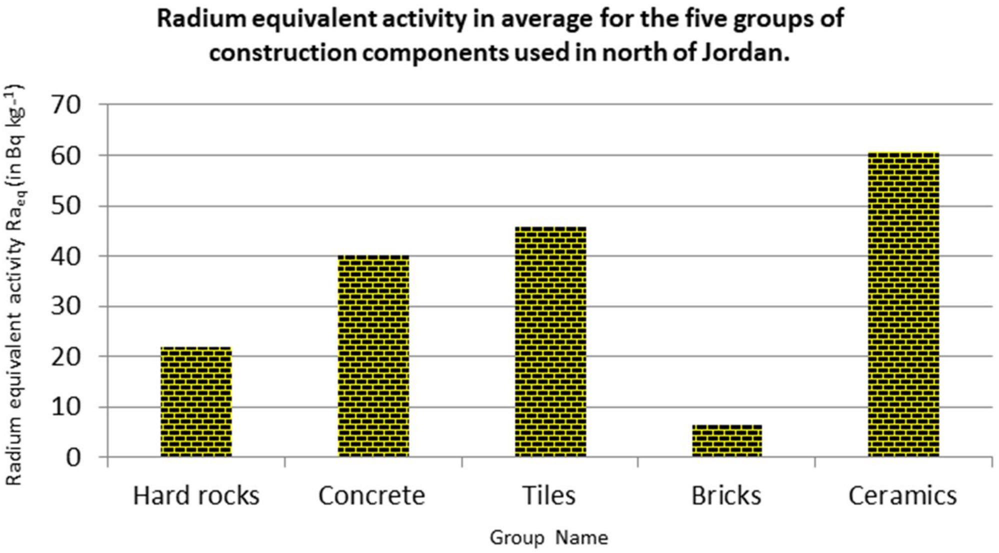

FIG. 6. Radium equivalent activity Ra$_{eq}$ in average for the five groups of construction components used in Jordan.

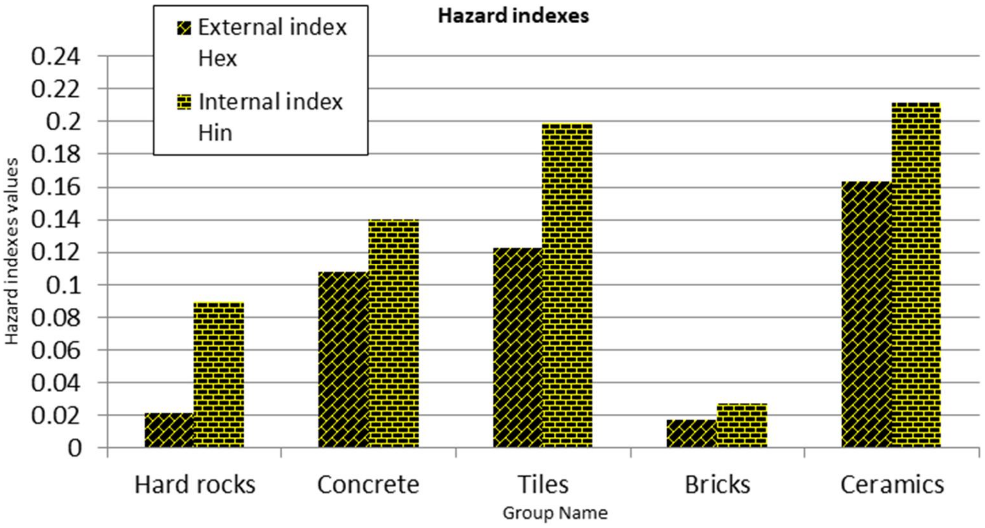

FIG. 7. Hazard indexes in average for the five groups of construction components used in Jordan.

TABLE 4a. Average activity concentrations (Bq·kg^{-1}) of radionuclides in selected building material samples from northern Jordan, representing each group.

radionuclide	^{238}U			^{235}U		
Group name	Average activity concentration (Bq kg-$^{1)}$	Minimum Average activity concentration (Bq kg-$^{1)}$	Maximum Average activity concentration (Bq kg-$^{1)}$	Average activity concentration (Bq kg-$^{1)}$	Minimum Average activity concentration (Bq kg-$^{1)}$	Maximum Average activity concentration (Bq kg-$^{1)}$
Hard rocks (stones)	11.470 ± 1.350	4 ± 0.7	19 ± 0.050	0.215 ± 0.0783	0.1 ± 0.003	0.51 ± 0.200
Concrete	11.994 ± 1.580	10.47 ± 1.700	13.50 ± 0.300	0.162 ± 0.044	0.05 ± 0.020	0.31 ± 0.010
Tiles	28.183 ± 0.717	14.50 ± 0.600	66.10 ± 2.200	0.123 ± 0.020	0.02 ± 0.010	0.32 ± 0.010
Bricks	5.050 ± 0.583	1.70 ± 0.050	8.30 ± 1.900	1.1675 ± 0.035	0.65 ± 0.004	1.70 ± 0.006
Ceramics	18.160 ± 0.520	6.50 ± 0.300	26.80 ± 1.200	0.312 ± 0.032	0.03 ± 0.010	0.40 ± 0.020

TABLE 4b (continued). Average activity concentrations (Bq·kg^{-1}) of radionuclides in selected building material samples from northern Jordan, representing each group.

Radio-nuclide	^{226}Ra			^{232}Th			^{40}K		
Group name	Average activity concentration (Bq kg-$^{1)}$	Minimum Average activity concentration (Bq kg-$^{1)}$	Maximum Average activity concentration (Bq kg-$^{1)}$	Average activity concentration (Bq kg-$^{1)}$	Minimum Average activity concentration (Bq kg-$^{1)}$	Maximum Average activity concentration (Bq kg-$^{1)}$	Average activity concentration (Bq kg-$^{1)}$	Minimum Average activity concentration (Bq kg-$^{1)}$	Maximum Average activity concentration (Bq kg-$^{1)}$
Hard rocks (stones)	11.3 ± 1.565	4 ± 0.8	19 ± 0.05	4.3 ± 1.78	1 ± 0.0	10.1 ± 3.2	57.5 ± 7.26	31.8 ± 6.3	120.90 ± 9.20
Concrete	11.84 ± 1.380	10.20 ± 1.80	13.50 ± 0.40	6.40 ± 1.40	5 ± 0.5	7.9 ± 1.7	248.4 ± 16.79	128.7 ± 14.2	400 ± 18.90
Tiles	28.12 ± 7.670	14.50 ± 0.60	65.70 ± 2.30	1.77 ± 0.79	0.9 ± 0.1	5.5 ± 3.8	195 ± 16.066	133.5 ± 17.5	259.1 ± 12.50
Bricks	3.88 ± 1.567	1.02 ± 0.05	6.70 ± 4.40	0.41 ± 0.11	0.3 ± 0.02	0.5 ± 0.1	25.88 ± 2.745	8.1 ± 1.00	43.40 ± 4.70
Ceramics	17.88 ± 0.480	6.10 ± 0.20	26.40 ± 1.20	5.48 ± 1.80	0.62 ± 0.2	11 ± 4.4	453.6 ± 19.76	209.7 ± 19	691.4 ± 16.90

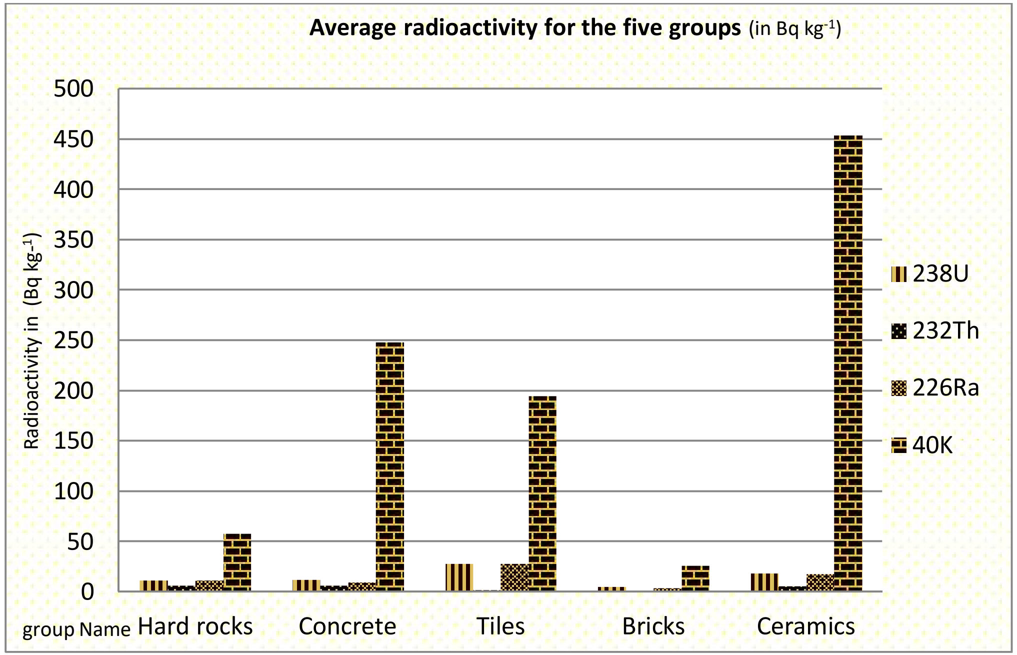

FIG. 8. Average activity concentrations of ^{238}U, ^{232}Th, ^{226}Ra, and ^{40}K in the five groups of construction components used in Jordan.

TABLE 5. Characteristics of the collected samples of natural construction materials used directly without processing.

Sample code	material	Type	Origin	Dimensions (mm)	Weight (kg)	Counting time (s)
1-R1	stone	Walls White Stone	Ajloun /Jordan	30*100*100	0.9921	92435.36
1-R2	stone	Walls Red Stone	Hayyan /Jordan	30*98*98	0.6359	88268
1-R3	stone	Walls White stone	Hayyan / Jordan	28*100*100	0.7199	252915.9
1-R4	stone	Walls White stone	Halabat / Jordan	30*100*100	0.7584	255509.8
1-R5	stone	Walls Blue stone	Halabat / Jordan	30*100*100	0.8007	84689.3
1-R6	stone	Walls White Stone	Irbid / Jordan	30*100*100	0.9921	172016.6
1-R7	stone	Walls White Stone	Irbid / Jordan	60*100*100	1.743	170597.5
1-R8	stone	Walls White Stone	Irbid / Jordan	90*100*100	2.486	343162.6
1-R9	stone	Walls White Stone	Souf / Jordan	30*100*100	0.9891	84993.9
1-R10	stone	Walls White Stone	Souf / Jordan	30*100*100	1.002	87718.7

TABLE 6. Characteristics of laboratory-processed construction material samples.

Sample code	Material	Components	Components weight (gm)	Sample weight (kg)	Counting time (s)
2-Ct1	Cement 1	Coarse aggregate	212	0.638	81580.96
		Fine aggregate	214		
		Sand (silica)	106		
		Cement	107		
		Silt clay	107		
2-Ct2	Cement 2	Coarse aggregate	229.4	0.5735	253992.40
		Fine aggregate	1147		
		Cement	114.7		
		Silt clay	114.7		
2-Ct3	Cement 3	Coarse aggregate	116.3	0.4652	88107.30
		Fine aggregate	116.3		
		Sand (silica)	116.3		
		Cement	116.3		
2-Ct4	Cement 4	Coarse aggregate	275.9	0.578	1011069.1
		Sand (silica)	100		
		Cement	100		
		Silt clay	100		
2-Ct5	Cement 5	Coarse aggregate	366.5	0.6665	67698.18
		Fine aggregate	100		
		Sand (silica)	100		
		Cement	100		

TABLE 7. Characteristics of the collected samples of factory-processed construction materials.

Sample code	Material	Type	Origin	Counting time (s)
3-T1	Tile	Floor tile	Ma'am / Jordan	84381.48
3-T2	Tile	Floor tile	Jarash/Jordan	86416.6
3-T3	Tile	Floor tile	Turkey	88672.72
3-T4	Tile	Floor tile	Irbid/Jordan	84980.62
3-T5	Tile	Floor tile	Irbid /Jordan	87614.3
3-T5	Tile	Dubaa floor tile	Dubaa /Jordan	256407.5
4-B1	Brick	Brick walls 10 cm	Jarash/Jordan	82694.5
4-B2	Brick	Brick walls 15 cm	Jarash/Jordan	76897.96
4-B3	Brick	Brick walls 20 cm	Jarash/Jordan	172387.5
4-B4	Ribs Brick	Ceiling ribs 15cm	Jarash/Jordan	352183.5
4-B1	Ribs Brick	Ceiling ribs 15cm	Jarash/Jordan	711213.5
5-Cc1	Ceramic	Floor ceramic	Egypt	168271
5-Cc2	Ceramic	International floor ceramic	Jordan	82405.73
5-Cc3	Ceramic	Diamond floor ceramic	Jordan	80978.32
5-Cc4	Ceramic	Egyptian wall ceramic	Egypt	99888.36
5-Cc5	Ceramic	International wall ceramic	Jordan	256198.9

4.3. Comparison of the Radioactivity Concentrations with Other Research

By comparing the three studies carried out in Jordan and mentioned in this work for stone samples, we noticed that $^{226}Ra_{88}$ was reported as 18.36 Bq.kg^{-1} in [9], 27.7 Bq.kg^{-1} in [27], and 11.3 Bq.kg^{-1} in the present study. This was less than the value reported from studies from Croatia [28], which was 35 Bq.kg^{-1}. For $^{232}Th_{90}$, the reported values were 2.77 Bq.kg^{-1} in [9], 5.9 Bq.kg^{-1} in [27], and 2.77 Bq.kg^{-1} in the present study, while in Slovakia it was 25.35 Bq.kg^{-1}, which was higher than in Jordan. For ^{40}K, the reported values were 32.7 in [9], 38.6 Bq.kg^{-1} in [27], and 32.7 Bq.kg^{-1} in the present study. These results are close to one another across the Jordanian studies. For ceramic samples in the present study, the average activity concentrations were 17.9 Bq.kg^{-1}, 5.5 Bq.kg^{-1}, and 453.6 Bq.kg^{-1} for ^{226}Ra, ^{232}Th, and ^{40}K, respectively. These values are generally lower than those reported in other referenced studies, with the exception of potassium, which exceeds the world average of 370 Bq.kg^{-1} [27].

For cement and brick samples, the activity concentrations were also lower than the corresponding values reported in other studies.

Overall, Table 8 demonstrates that the average activity concentrations for all studied samples are below the recommended world averages, except for ^{40}K in ceramic samples. In comparison with data from other countries, the measured activity concentrations of $^{226}Ra_{88}$, $^{232}Th_{90}$, and $^{40}K_{19}$ fall within the reported ranges, confirming consistency with international findings.

TABLE 8. Comparison of average radioactive nuclei accumulation (Bq.kg^{-1}) in selected building material samples with previous studies.

Building material	*Average Radioactivity concentration (Bq.kg^{-1})*			*Country*	*Reference*
	^{226}Ra	^{232}Th	^{40}K		
Hard rocks (Limestone)	11.3	4.3	57.5	Jordan	(present study)
Limestone	10.5	0.67	3.7	Jordan	[7,37]
Hard rock Halabat	27.7	5.9	38.6	Jordan	[27]
Stone (Hard rocks)	40.8-47.7	13.7-35.0	340.0-363.3	Jordan	[36]
Limestone	10	13.4	115	Austria	[28]
Limestone	35	7.8	57	Croatia	[28]
Stone	8-16	12-18	230-803	Bangladesh	[29]
Stone	4.98	25.35	370.06	Slovakia	[30]
Stone	18.36	2.77	32.7	Jordan	[9]
Stone					
Ceramic	17.9	5.5	453.6	Jordan	(present study)
	32.6	28.3	413.5	Jordan	[7.37]
	28.7	6.2	42.3	Jordan	[27]
	140.5	101.1	570.1	Jordan	[36]
	47.4	42.84	313.6	Egypt	[31]
	38	47	697	China	[32]
	58	51	473	Italia	[33]
	73.7	58.2	624	Palestine	[34]
	71.3	86.5	522	Saudi Arabia	[5]
	17-80	10-54	207-655	Bangladesh	[29]
Cement (Concrete)	11.8	6.4	248.6	Jordan	(present study)
	9.5	4.13	29.9	Jordan	[7,36]
	38	6	138	Jordan	[27]
	43.2-49.1	11.2-13.5	11.9-265.1	Jordan	[36]
	20	13	241	Greece	[34]
	28.5	7.6	167.4	Saudi Arabia	[6]
	23	9.3	118	Austria	[28]
	59	18.9	187	Croatia	[28]
	15-34	14-24	231-426	Bangladesh	[29]
	56.65	46.65	368.58	Federal University of Gusau	[31]

Building material	*Average Radioactivity concentration ($Bq.kg^{-1}$)*			*Country*	*Reference*
	^{226}Ra	^{232}Th	^{40}K		
Brick	3.9	0.4	25.9	Jordan	(Present study)
	6.5	1.3	6.5	Jordan	[7,37]
	35	45	710	Greece	[35]
	41	89	681	Australia	[20]
	8.7	8.6	271.2	Saudi Arabia	[6]
	7.16	46.07	705.16	Slovakia	[30]
	55.05	77.93	238.65	Federal University of Gusau	[31]

5. Conclusions

In this study, the radioactive nuclei accumulation of $^{238}U_{92}$, $^{235}U_{92}$, $^{232}Th_{90}$, $^{226}Ra_{88}$, and $^{40}K_{19}$ was measured in 31 construction material samples commonly used in northern Jordan by means of gamma-ray spectroscopy.

Measurement of the radionuclide activity of $^{238}U_{92}$, $^{235}U_{92}$, $^{232}Th_{90}$, $^{226}Ra_{88}$, and $^{40}K_{19}$ indicates that their values in the studied samples are less than the corresponding world average values, with the exception of the mean values of $^{40}K_{19}$ concentration in ceramic samples. The radium equivalent activities obtained using the concentrations of these nuclides were below the allowable level of 370 Bq/kg [20] in all studied samples. All hazard indexes are less than unity.

The quantitative results indicate that brick samples have the minimum values of radiation contents and the smallest values of dose indices, while ceramic samples have the highest. As causes of radiation hazards, most construction materials used in the northern area of Jordan can be safely considered insignificant.

References

[1] Morteza, I., Mohammademad, A., Amin, S., Ghazaleh, A., Ali, Y., Erika, K., Edit, T.-B., and Tibor, K., Environ. Sci. Pollut. Res., 28 (2021) 41492.

[2] Marlet, L. and Enn, R., Proc. Est. Acad. Sci., 61 (2012) 107.

[3] Evan, R.D., Health Phys., 17 (2) (1969) 229.

[4] Rati, V., Mahur, A., Sonkawde, R., Suhail, M.A., Azam, A., and Prasad, R., Indian J. Pure Appl. Phys., 48 (7) (2010) 473.

[5] Khan, K., Aslam, A., Orifi, S.D., and Khan, H.M., J. Environ. Radioact., 58 (1) (2002) 59.

[6] Safia, Q., Amidalddin, Alzahrani, J.H., Aamudy, Fakeha. Z., M., A., Al-Habeadi, H., and Ibrahim, N., Life Sci. J., 12 (2015).

[7] Awadallah, M.I. and Imran, M.M.A., J. Environ. Radioact., 94 (3) (2007) 129.

[8] Darby, S., Hill. D., and Doll, R., Ann. Oncol., 12 (2001) 1341.

[9] Saleh, H., Hamideen, M., Al-Hwaiti, M., and Al-Kharoof, S., Jordan J. Phys., 11 (3) (2018) 193.

[10] Ababneh, E., Al-Amarat, S., Okoor, S., Imran, M., & Dababneh, S., Jordan J. Phys., 15(2), (2022) 149.

[11] Ababneh, E., Alzoubi, H., Qbelat, A. S., & Al-Bashaish, S. R., Journal of Physics Communications, 8(10) (2024) 105001.

[12] Ababneh, E., Qbelat, A. S., Imran, M. M., Al-Bashaish, S. R., Okoor, S., Darabee, A., & Mousa, M. S., Physica Scripta, 99 (8) (2024) 085303

[13] Ababneh, E., Mubayed, N., Okoor, S., Al-Bashaish, S. R., Qbelat, A. S., Sulieman, M., & Ershaidat, N. M., Radiation Detection Technology and Methods, 9(1) (2025) 132-144.

[14] Al-Bashish, S., Ababneh, E., Mousa, M. S., Okoor, S., Hyasat, M., Nusir, M., ... & Dababneh, S., Radiation Detection Technology and Methods, 5(3) (2021) 409-420.

[15] IAEA (International Atomic Energy Agency), Guidelines for Radioelement Mapping Using Gamma Ray Spectrometry Data, Vienna: IAEA. (IAEA-TECDOC-1363), (2003).

[16] EG&G Ortec, Gamma Vision-32, "Gamma-ray Spectrum Analysis and MCA Emulator". (EG&G Instruments Inc. Oak Ridge, Tennessee, 1999).

[17] Gilmore, G., “Practical Gamma-ray Spectrometry”, (John Wiley & Sons, Ltd, 2, 2008).

[18] Issa, S., Uosif, M., and Elsaman, R., Turkish J. Eng. Environ. Sci., 37 (2013) 109.

[19] Al-Hamarneh I., Dirasat, Pure Sci., 33 (1) (2006) 49.

[20] Beretka, J. and Mathew, P.J., Health Phys., 48 (1) (1985) 87.

[21] Thabayneh, K.M., Arab. J. Sci. Eng., 38 (2013) 201.

[22] Lyngkhoi, B. and Nongkynrih, P., Egypt. J. Basic Appl. Sci., 7 (1) (2020) 194.

[23] UNSCEAR, United Nations Scientific Committee on the Effect of Atomic Radiation, Report to the General Assembly, Annex A and B Vol. 1 (2000).

[24] EC (European Commission), Radiation Protection, (Directorate-General Environment, Nuclear Safety and Civil Protection: Luxembourg, Belgium, 112, 1999).

[25] Jose, A., Kumar, A.S., Govindarajan, K.N., and Manimaran, P., J. Med. Phys., 45 (3) (2020) 182.

[26] Vineethkumar, V., Akhil, R., Shimod, P.K., and Prakash, V., J. Radioanal. Nucl. Chem., 327 (2021) 189.

[27] Al-Jundi, J., Salah, W., Bawaaneh, M.S., and Afaneh, F., Radiat. Prot. Dosim., 118 (1) (2006) 93.

[28] Todorović, N., Bikit, I., Krmar, M., Mrđa, D., Hansman, J., Nikolov, J., Todorović, S., Forkapić, S., Jovančević, N., Bikit, K., and Mandić, L.J., Rom. J. Phys., 62 (2017) 817.

[29] Khatun, M.A., Ferdous, J., and Haque, M.M., J. Environ. Prot., 9 (10) (2018) 1034.

[30] Estokova, A., Singovszka, E.، and Vertal, M., Mater. Marian, 15 (2022) 6876.

[31] Uosif, M., Omer, M., Ali, N.A., El-Kamal, A.H., and Hefni, M.A., Int. J. Adv. Sci. Technol., 80 (2015) 19.

[32] Xinwei, L. and Xiaolan, Z., Radiat. Prot. Dosim., 128 (1) (2008) 77.

[33] Righi, S. and Bruzzi, L., J. Environ. Radioact., 88 (2) (2006) 158.

[34] Stoulos, S., Manolopoulou, M., and Papastefanou, C., J. Env. Rad., 69 (3) (2003) 225.

[35] Papaefthymiou, H. and Gouseti, O., Radiat. Meas., 43 (8) (2008) 1453.

[36] Matiullah, N.A. and Hussein, A.J.A., J. Environ. Radioact., 39 (1) (1998) 9.

[37] Awadallah, M.I. and Imran, M.M., Dirasat: Pure Sciences, 34 (1) (2007).

Volume 18, Number 3, 2025. pp. 389-398

Jordan Journal of Physics

ARTICLE

Ultraviolet Photodetectors Based on Nanostructured SnO_2 Thin Films/P-Si Heterojunctions Prepared by a Hydrothermal Method

Abd alhameed A. Hameed[a], **J. F. Mohammad**[b] and **Isam M. Ibrahim**[c]

[a] *Ministry of Education, Education Direction in Al-Anbar, Iraq.*

[b] *Physics Department, College of Education for Pure Sciences, University of Anbar, Iraq.*

[c] *Department of Physics, College of Science, University of Baghdad, Baghdad, Iraq.*

Doi: **https://doi.org/10.47011/18.3.11**

Received on: 31/03/2024; *Accepted on: 26/06/2024*

Abstract: The aim of this work is to investigate the possibility of using SnO_2 thin films as ultraviolet (UV) detectors. Films were grown on seed layer substrates of glass and p-type Si through the hydrothermal method at different pH values (3, 9, and 11). X-ray diffraction (XRD) pattern reveals that the films are polycrystalline with a tetragonal structure, and the structure has maximum intensity in the (110) direction. The crystallite size of the prepared samples was found to vary from 5.3 to 7.3 nm. FESEM indicated that the synthesized nanoparticles also underwent morphological transformations, changing from spherical to nanorod-like like structures depending on the pH value. Energy-dispersive X-ray spectroscopy (EDS) analysis revealed that there were no foreign particles or impurities in the films. Increasing the pH from 3 to 9 changed the characteristics of the synthesized films and led to a decrease in the optical band gap from 3.3 to 3.1 eV, along with reduced optical transmittance. Current-voltage (I-V) characteristics were found to exhibit Schottky-like characteristics where photocurrent increased exponentially with the increase of the bias voltage and light intensity. The photodetector response at the extraction wavelength of 370 nm displayed a reasonable level of sensitivity, reaching up to 42.77% for the sample prepared at pH 9. All films demonstrated rise and fall times of less than one second, confirming their suitability for high-speed UV detection.

Keywords: Photo sensor, Detector, Sensitivity, Seed layer, SnO_2.

1. Introduction

Over the last decade, there has been a substantial amount of research dedicated to the study of metal oxide thin films. This research has been motivated by the recognition of their potential applications across several domains, including but not limited to solar cells, optoelectronic devices, liquid crystal displays, heat mirrors, and gas sensors. The optical transparency of undoped and doped nonstoichiometric metal oxide thin films is significant in the visible spectrum, and their conductivity closely resembles that of metallic materials [1, 2]. The technical uses of semiconductor nanocrystals are of great interest and focus. The electrical, optical, and magnetic characteristics of these particles are greatly influenced by their size [3, 4]. Numerous studies have demonstrated that altering the pH value leads to changes in the shape and size of nanoparticles, which in turn enhances the applications of metal oxides in sensors and other fields [5, 6]. Recently, considerable effort has been devoted to the systematic improvement of semiconductor oxides with unique structures or

Corresponding Author: Abd alhameed A. Hameed **Email**: abd21u3009@uoanbar.edu.iq

morphologies [7-9]. Tin dioxide (SnO_2) is a Nano scale material that includes semiconductor materials. SnO_2 is commonly used as an essential material in the fabrication of solar cells [10], transparent conductive oxides (TCOs) [11], gas sensing devices [12], and photocatalysts [13]. SnO_2 has several advantages, including high transparency and high sensitivity to gas [14]. SnO_2 thin films typically exhibit n-type semiconductor behavior, characterized by a broad energy band gap, and are commonly found in a tetragonal rutile structure [15]. Each preparation method has its drawbacks, such as the requirement of a vacuum environment, complex procedures, or high temperatures, which can lead to reduced crystallinity, contaminants, or inadequate dispersion. The hydrothermal technique, a synthetic method that involves the bottom-up approach, has gained significant popularity as a preferred approach for the synthesis of nanomaterials. This is mostly due to its straightforward procedure, ability to produce high-quality crystals, convenient control over shape, efficient sintering activity, and low temperature requirements [16, 17]. In this work, nanostructured SnO_2 thin films with varying pH values were synthesized using a hydrothermal technique. The crystal structure, morphology, and photodetector characteristics were studied.

2. Experimental Methods

Tin dioxide thin films were fabricated using a hydrothermal technique on a seeded layer. First, the glass slides were thoroughly cleaned using distilled water and ethanol in an ultrasonic bath for ten minutes. The 0.01 M tin chloride solution was then agitated on a magnetic stirrer for 30 minutes to create the precursors, which served as the sources of tin ions. The p-type silicon wafer substrate was cleaned using a solution of hydrofluoric acid (HF) and ethanol (99%) in a 1:1 ratio. Tin chloride solution was sprayed on glass and silicon (p-type) substrates using chemical spray pyrolysis at 400°C. The spraying time was 5 seconds, followed by a stop time of 20 seconds. The growth solution was created by dissolving 0.1 M tin chloride, which acts as a tin ion source, in a mixture of 70% ethanol and deionized water in a 1:1 ratio. Furthermore, 0.1 M trisodium citrate ($Na_3C_6H_5O_7$) was dissolved in deionized water and agitated for 30 minutes. Next, the two solutions were combined and agitated for 30 minutes, with varying pH levels (3, 9, and 11) achieved by introducing NaOH. These solutions were then labeled S1, S2, and S3, respectively. The ultimate blend was moved to a stainless-steel autoclave coated with Teflon, where the substrates containing seeded layers were positioned vertically inside the Teflon container. In a digitally controlled oven, the autoclave was promptly sealed and maintained at a consistent temperature of 100°C for a duration of 6 hours. Following this, the autoclave was subjected to a process of natural cooling until it attained the ambient temperature. In order to remove any residual solid particles or unreacted atoms from the surface, the substrates underwent a rinsing process using deionized water. Following that, the samples underwent a drying process in an oven set at a temperature of 100°C for a duration of 30 minutes. The annealing process took place in a furnace over a period of 1 hour at a temperature of 400°C. After that, the films were prepared for characterization.

3. Results and Discussion

3.1 Structure and Morphological Properties

Figure 1 displays the X-ray diffraction (XRD) patterns of tin dioxide films synthesized using a hydrothermal method on glass substrates at different pH values. The films exhibited a polycrystalline tetragonal structure with a preferred orientation along the (110) plane, corresponding to a diffraction angle of 26.74°. Additional diffraction peaks were observed at approximately 34° and 51.9°, corresponding to the (101) and (211) planes, respectively. These observations are consistent with standard data (JCPDS card No. 00-001-0657) and agree with previously reported results [18, 19]. The Debye–Scherrer equation, $D = k\lambda/\beta\cos\theta$, is used for the calculation of crystal size. In this equation, k denotes the shape factor (0.94), β represents the full width at half-maximum (FWHM), θ is the angle of the diffraction peak, and λ=0.15405 nm is the wavelength of the X-ray source. The crystallite size was found to be in the range of 7.26 to 7.3 nm. The average crystal size decreased when the pH increased from 3 to 9, as shown in Table 1. The pH level regulates the degree of supersaturation by altering the ionic equilibrium, particularly through changes in hydroxide ion concentration. This, in turn, modifies the interaction with tin ions, thereby controlling the nucleation process and ultimately affecting the size and morphology of the crystallites [20]. Since supersaturation acts as a driving force for nucleation and crystal growth [21], its regulation is crucial for tailoring nanostructures. At pH 11, however, the crystallite size increased again to 7.3 nm, which is consistent with the findings of other researchers [18, 22].

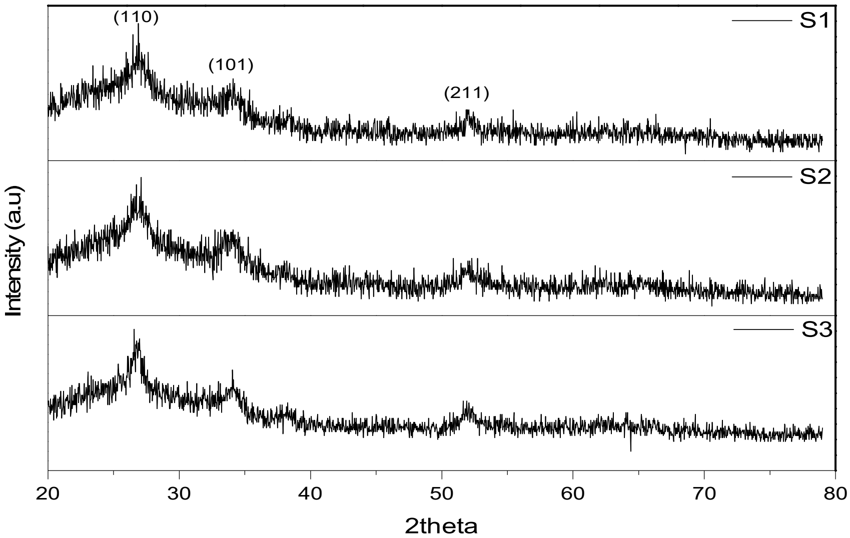

FIG. 1. XRD patterns of SnO_2: S1 (pH= 3), S2 (pH= 9), and S3 (pH= 11).

TABLE 1. Structure parameters of the prepared SnO_2 thin films at different pH values.

Sample	2θ (Exp.)	d_{hkl} Exp.(A)	d_{hkl} Std.(A)	FWHM	D (nm)	hkl	$D_{ave.}$ (nm)	System	Card No.
S1	26.74	3.21233	3.34000	1.8750	4.55	110	7.26	Tetragonal	00-001-0657
	34.06	2.55684	2.64000	1.1400	7.62	101			
	51.99	1.72646	1.75000	0.9600	9.62	211			
S2	26.74	3.20638	3.34000	1.8900	4.52	110	5.3	Tetragonal	00-001-0657
	33.94	2.56534	2.64000	1.4400	6.03	101			
	51.89	1.72963	1.75000	0.8100	5.34	211			
S3	26.74	3.21261	3.34000	1.4200	6.01	110	7.3	Tetragonal	00-001-0657
	34.09	2.55473	2.64000	1.2000	7.24	101			
	51.9	1.72827	1.75000	1.0800	8.55	211			

Figure 2 displays the field emission scanning electron microscopy (FESEM) images of tin dioxide samples prepared by the hydrothermal method at pH values of 3, 9, and 11 at a temperature of 100°C on glass substrates. The size and structure of SnO_2 nanoparticles were greatly affected by the pH of the reaction mixture, and the growth of nanoparticles depended on the pH of the solution. A variety of agglomerated particle shapes was discovered. At pH 3, the particles were spherical, with a size of 11.1 nm. Increasing the pH to 9 led to an increase in the particle size to 17.13 nm, and the shape changed to oval. Increasing the pH to 11 led to an increase in the particle size to 23.16 nm, and the particle shape became similar to that of nanorods or clustered worms. It is clear from above that changing the pH levels can inhibit agglomeration between molecules and lead to shape transformation [21].

The cross-sectional FESEM image is shown in Fig. 3. It is observed that the thickness of SnO_2 films is around 405.6 nm, calculated as follows:

Thickness = (422.8 + 429.5 + 364.5) / 3 = 405.6 nm

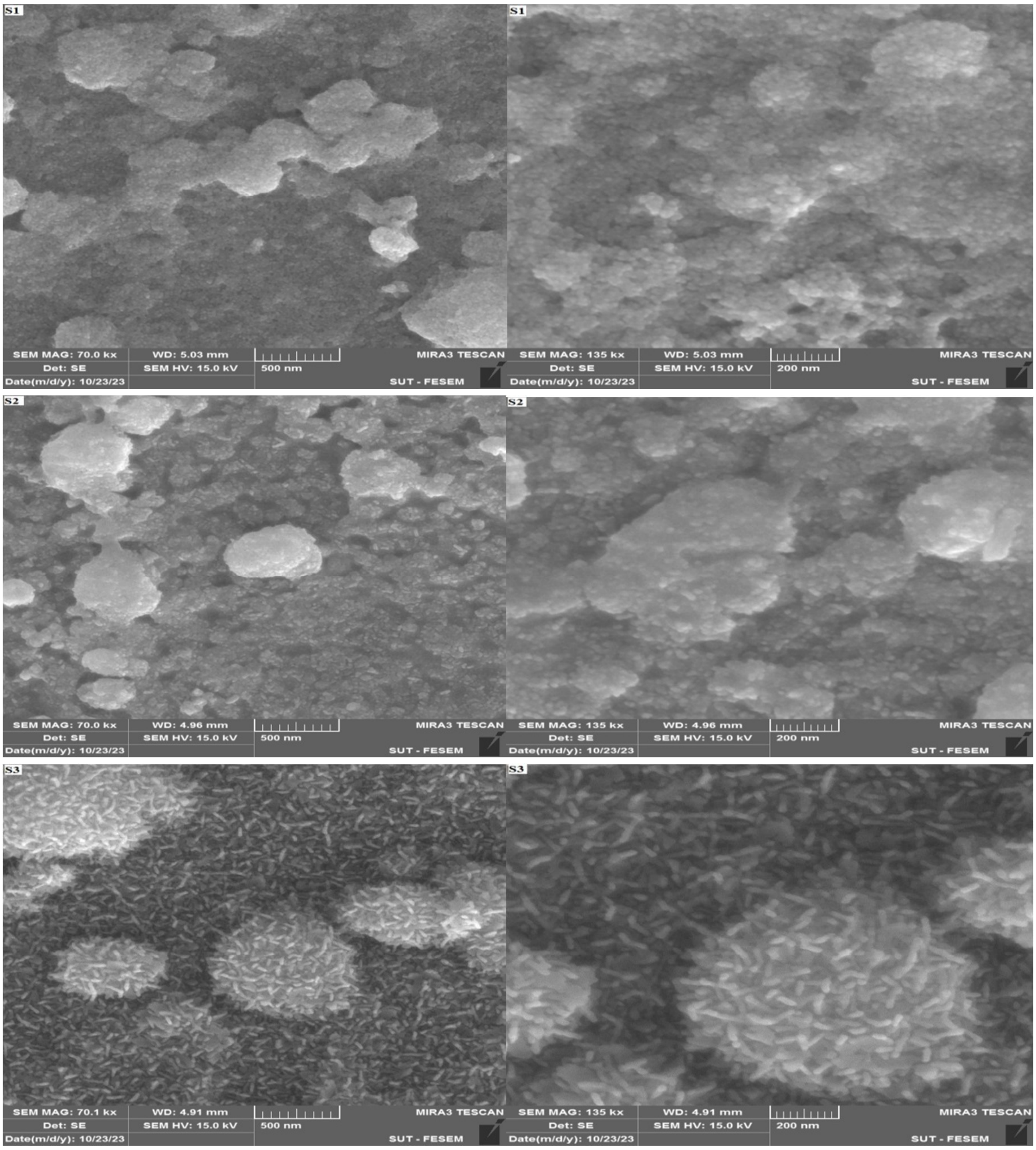

FIG. 2. FESEM images of tin dioxide thin films prepared from solutions S1 (pH = 3), S2 (pH = 9), and S3 (pH = 11).

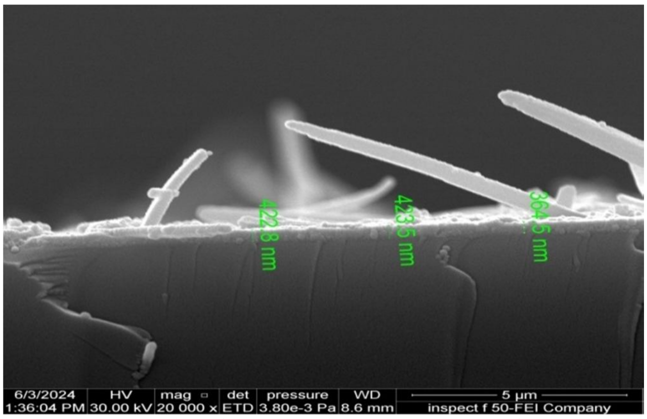

FIG. 3. Cross-sectional FESEM image for SnO_2 films at pH = 3.

Energy dispersive spectroscopy (EDS) analysis of the tin dioxide samples (S1, S2, and S3) indicated the presence of both tin and oxygen. Figures 4, 5, and 6 demonstrate that all samples exhibit a pure SnO_2 phase. The atomic ratios of tin and oxygen in the three samples were very similar, confirming the relatively homogeneous composition of the nanoparticles. The EDS results showed a strong correlation with the XRD findings. The gold peak observed originates from the gold coating that was applied to enhance conductivity during the FESEM examination.

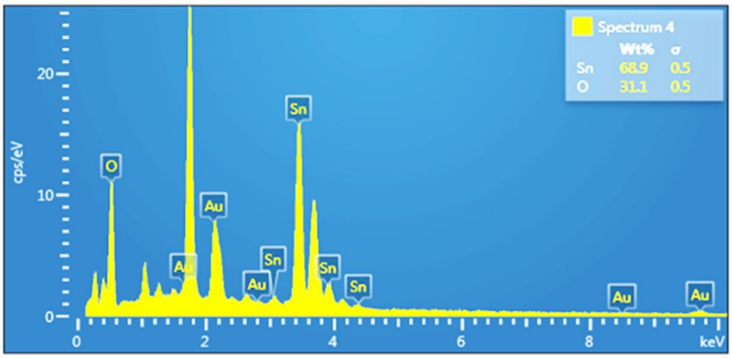

FIG. 4. EDS pattern of the tin dioxide thin film on sample S1.

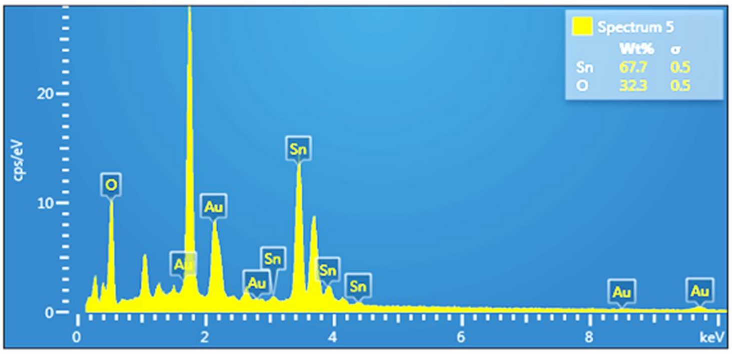

FIG. 5. EDS pattern of the tin dioxide thin film on sample S2

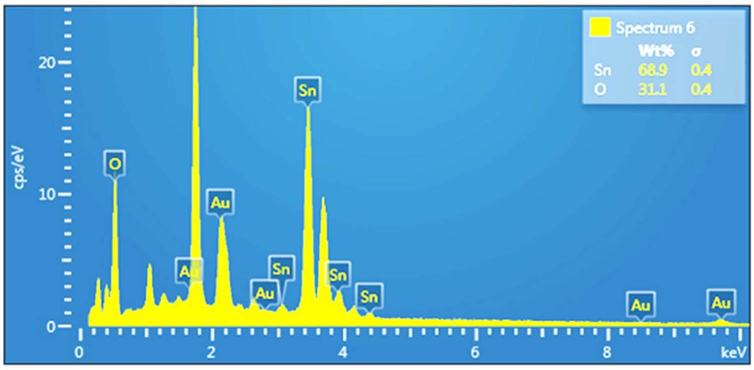

FIG. 6. EDS pattern of the tin dioxide thin film on sample S3.

3.2. Optical Properties

Optical transmittance analysis is important for various optoelectronic applications, including solar cells and photodetectors. Figure 7 displays the optical transmittance spectra of the tin dioxide thin films at pH values of 3, 9, and 11. All spectra have significant transmittance levels in the visible region, exceeding 60%. Overall, the curves exhibit good regularity, which is attributed to the uniformly distributed thickness of the film on the substrate. The decrease in transmittance is attributed to the increase in film thickness when the pH level rises. Enhanced nucleation and grain growth promoted the generation of additional Sn ions, which then reacted with oxygen ions to produce SnO_2, leading to an increase in the film thickness [19].

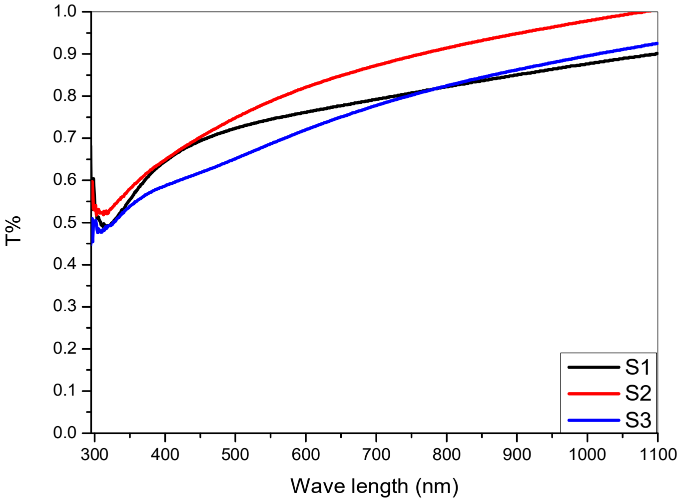

FIG. 7. Optical transmittance of SnO_2 films at varying pH values.

Figure 8 shows the optical energy gap of tin dioxide films, which was computed by extending the curve between (hv) and $(\alpha hv)^2$ using the following relation:

$$\propto hv = A(hv - E_g)^{1/2} \quad (1)$$

where ∝ represents the absorption coefficient, and A is a constant. The optical band gap values of S1, S2, and S3 were determined from the Tauc formula to be 3.3, 3.35, and 3.15 eV, respectively. These values align with the findings documented by other studies [23, 24]. The samples exhibit a reduced optical energy gap compared to tin dioxide [22, 25]. The reduced energy gap significantly contributed to the improved photocatalytic efficiency of these samples. Low-bandgap materials can absorb photons of higher wavelengths, including visible light, making them suitable as visible light-responsive photocatalysts [26].

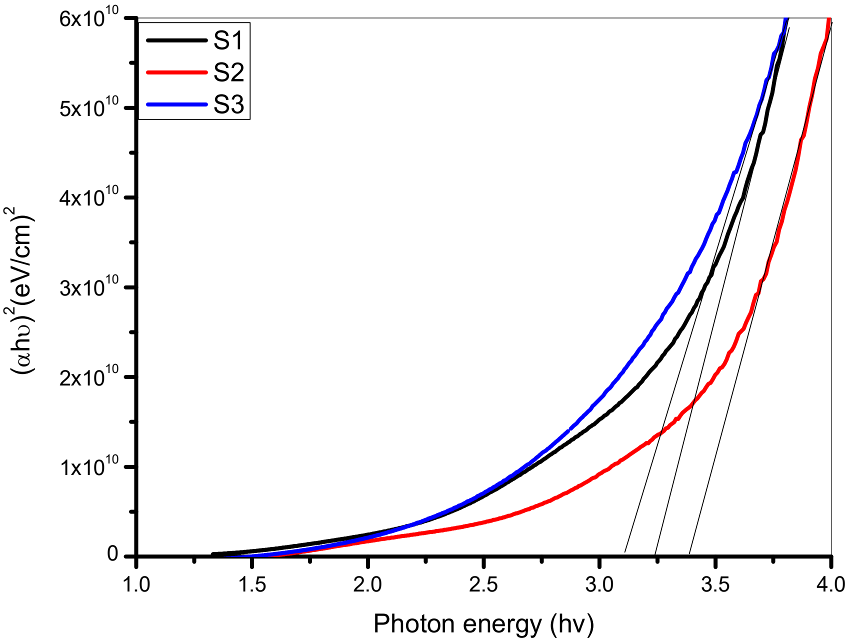

FIG. 8. Optical energy gap of SnO_2 films at varying pH values.

3.3. Current-Voltage Characteristics

The current-voltage (I-V) behavior is a crucial aspect of several interferometry techniques. Under the influence of a DC voltage sweep ranging from +1 to -1 V, the current-voltage characteristics of tin dioxide films prepared on p-Si substrates with varying pH levels (3, 9, and 11) were measured under both illuminated and dark conditions. A halogen lamp (Philips) with an intensity of 104.986 mW/cm² positioned 30 cm away from the film surface was used. The Keithley 2450 measurement unit was employed to measure the current and voltage difference, with inputs and outputs connected via aluminum electrodes deposited on the top of a film surface. Figure 9 illustrates the current-voltage characteristics under dark conditions. Two types of currents were identified: the forward dark current, driven by majority carriers, and the recombination current occurring in the low voltage region due to the concentration of both majority and minority carriers, which exceeds the intrinsic carrier concentration. Additionally, a slight increase in the recombination current was observed for sample S3 in the low voltage region, attributed to the excitation of electrons from the valence band to the conduction band. With increasing voltage, diffusion current dominated, resulting in an exponential increase in the current. The symmetrical and nearly linear I-V characteristics indicate that the contacts for samples S1 and S2 are ohmic or semi-ohmic [27]. This behavior can be attributed to the diffusion of aluminum into the nanostructure of the oxide, creating an easier path for electron flow instead of passing through the nanostructure.

Figure 10 presents the current-voltage characteristics under illumination. The films exhibit Schottky behavior of the junction in all the manufactured devices. These graphs demonstrate that as the forward bias voltage increased, the current also increased. Increasing the reverse bias voltage widened the depletion region, leading to the separation of electron-hole pairs and an increase in current. Incidental photons of light generated a photocurrent. The number of photogenerated charge carriers in the depletion and diffusion carrier zones increased as a consequence [28, 29]. The small increase in current under illumination confirms that the device generates charge carriers in response to light, albeit in small amounts.

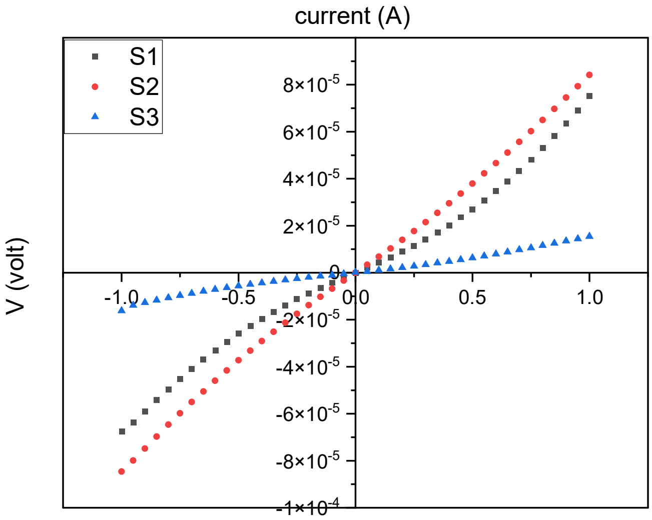

FIG. 9. I-V characteristics of SnO_2/Si-p-type materials in the dark at different pH values.

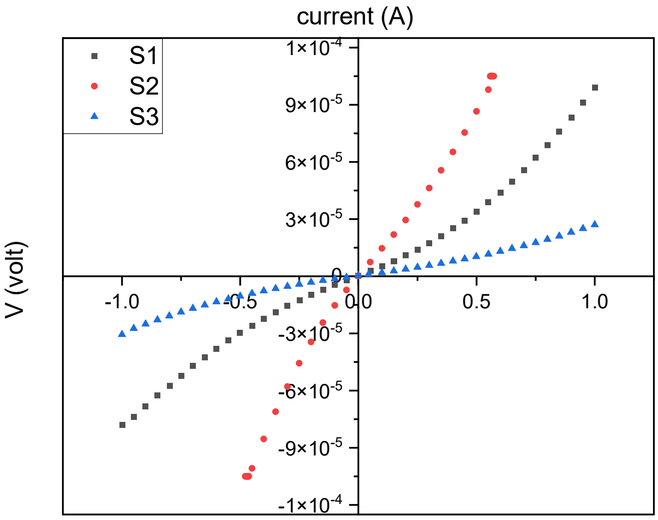

FIG. 10. I-V characteristics of the SnO_2/Si-p alloy at different pH under illumination (104.986 mW/cm^2).

3.4. Responsivity (R_λ)

The spectrum responsivity, denoted as R_λ, is a metric used to evaluate the efficiency of a system by quantifying the photocurrent produced per unit of power of the incident light intensity on the effective regions. In a photoconductive detector, the magnitude of the generated electrical signal is directly correlated with the intensity of the input light, which was approximately 0.0004 W/cm² at a wavelength of 370 nm. The determination of the spectrum responsivity of the tested detector involves calculating the ratio of the photocurrent density generated by the detector to the calculated power density, as represented by the following equation [30]:

$$R_\lambda = J_{ph}(\lambda) / P_{in}(\lambda). \quad (2)$$

Here, J_{ph} (λ) represents the density of the measured photocurrent emitted by the tested detector, whereas Pin (λ) denotes the magnitude of the incident power measurement obtained from the photoconductive detectors. Table 2 displays the spectral response values of the prepared samples, indicating that sample S2 exhibited the highest response. It is noted that this sample possesses the smallest crystallite size, as evidenced by X-ray analysis. According to the principle of quantum confinement, this suggests a heightened reactivity with the surface when exposed to light. Furthermore, the optical energy gap for this sample is approximately 3.35 eV, which aligns well with the wavelength of the ultraviolet radiation utilized.

3.5. Photosensitivity

The current-time characteristics of the prepared films were measured under irradiation in the ultraviolet region at a wavelength of 370 nm and an intensity of 0.0004 W/cm². The exposure of the thin film to light resulted in the formation of electron-hole pairs, hence causing an augmentation in the current. Once the light was turned off, the current reverted to its initial magnitude. Figure 11 shows the current-time characteristics of the films prepared on p-type silicon substrates. Figure 11 and Table 2 show that the photodetector sensitivity was approximately 2.48% for sample S1, approximately 42.77% for sample S2, and approximately 22.22% for sample S3. Additionally, the rise and fall times for all three samples were less than one second.

TABLE 2. Photo-sensitivity and responsivity (R_λ) as a function of wavelength for SnO_2/p-Si.

Sample	S% at 370 nm	R_λ (A/W)	T_{rise} (s)	T_{fall} (s)
S1 PH(3)	2.48	1.315943253	0.758	0.688
S2 PH(9)	42.77	2.532226606	0.803	0.803
S3 PH(11)	22.22	0.242888516	0.742	0.784

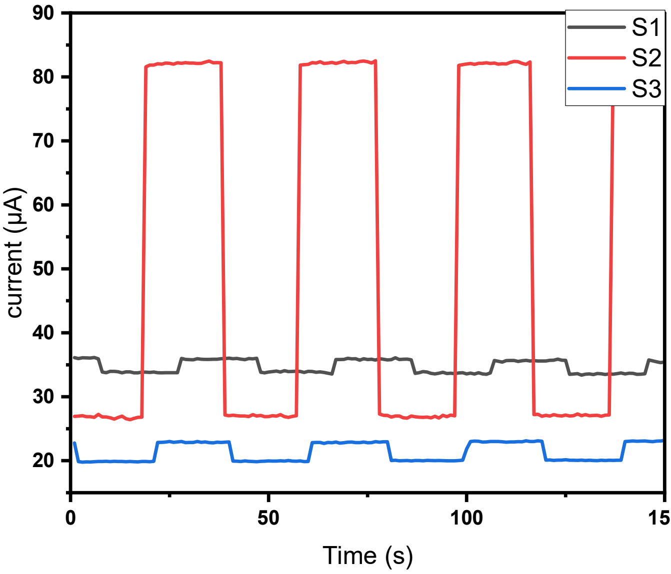

FIG. 11. Photoresponse time of SnO_2/Si-p at different pH values upon exposure to 370 nm light.

The responsivity of the devices directly depended on the photocurrent, since all three were exposed to identical optical powers. Two main factors influence the photocurrent: the absorption of incident light and the efficient transfer of charge carriers [31]. The creation of a shallow connection between SnO_2 and p-Si facilitated the reduction in carrier distance. Additionally, the heightened prevalence of defect states, specifically vacancies and voids inside nanostructures, disrupted the mobility of photogenerated charges, thereby negatively impacting the effective conduction cross section. In addition, surface states possess the ability to ensnare carriers and generate sites for recombination [32]. Consequently, there was a notable decrease in the conduction and accumulation of carriers. Hence, the decline in the sensitivity of SnO_2/p-Si in samples S1 and S3 can be ascribed to the diminished quantity of photogenerated carriers, caused by ineffective charge transfer arising from uneven growth and the formation of shallow junctions, as well as reduced conduction area due to the heightened presence of defect states. The superior performance of S2 over the other samples was clear. Thus, the architecture of S2 can be considered highly suitable for UV detection. Further research is required to fully evaluate the effectiveness of devices employing SnO_2.

Conclusion

The hydrothermal technique was used to successfully synthesize nanostructured SnO2 thin films on the seed layer. XRD measurements showed that the crystal size could be controlled by adjusting the pH. FESEM images revealed that the particle morphology varied with pH. The optical transmittance of the SnO_2 thin films at pH 3, 9, and 11 exceeded 60% in the visible region. The optical energy gaps of S1, S2, and S3 were found to be 3.3, 3.35, and 3.15 eV, respectively. The best sensitivity and responsivity of the SnO_2/p-Si photodetector were obtained for the sample prepared at pH = 9. All prepared samples showed rise and fall times of less than one second.

Acknowledgment

This research is funded by the Scientific Committee at the Department of Physics, College of Education for Pure Sciences, University of Anbar, and the Department of Physics, College of Science, University of Baghdad.

References

[1] Guneri, E. *et al.*, Optoelectron. Adv. Mater. Rapid Commun., 3 (4) (2009) 383.

[2] Du Ahn, B. *et al.*, J. Cryst. Growth, 309 (2) (2007) 128.

[3] Bargougui, R. *et al.*, Adv. Mater. Lett., 6 (9) (2015) 816.

[4] Ara, M.M. *et al.*, Optik, 123 (22) (2012) 2090.

[5] López-Ortiz, S. *et al.*, J. Nanomater., 2020 (2020) 1.

[6] Mamakhel, A. *et al.*, J. Supercrit. Fluids, 166 (2020) 105029.

[7] Gupta, V.K., Sadeghi, R., and Karimi, F., Sens. Actuators B Chem., 186 (2013) 603.

[8] Van Dang, T. *et al.*, ACS Appl. Mater. Interfaces, 8 (7) (2016) 4828.

[9] Liu, J. *et al.*, Sens. Actuators B Chem., 245 (2017) 551.

[10] Bittau, F. *et al.*, Thin Solid Films, 633 (2017) 92.

[11] Kim, A. *et al.*, Adv. Funct. Mater., 24 (17) (2014) 2462.

[12] Barsan, N., Rebholz, J., and Weimar, U., Sens. Actuators B Chem., 207 (2015) 455.

[13] Joshi, B.N., Yoon, H., and Yoon, S.S., J. Electrostat., 71 (1) (2013) 48.

[14] Susilawati *et al.* J. Phys.: Conf. Ser., 1572 (2020) 012085.

[15] Doyan, A. *et al.*, IOP Conf. Ser. Mater. Sci. Eng., 196 (2017) 012004.

[16] Zhao, J. *et al.*, Appl. Sci., 13 (4) (2023) 2048.

[17] Chen, L.-Y. *et al.*, J. Nanosci. Nanotechnol., 12 (9) (2012) 6921.

[18] Van Tuan, P., Tuong, H.B., and Khiem, T.N., Commun. Phys., 31 (4) (2021) 361.

[19] Azzahra, I. *et al.*, E3S Web Conf., 517 (2024) 10004.

[20] Kohli, N., Singh, O., and Singh, R.C., Sens. Actuators B Chem., 158 (1) (2011) 259.

[21] Habte, A.G., Hone, F.G., and Dejene, F.B., Phys. B Condens. Matter, 580 (2020) 411832.

[22] Mohammad, J., Sooud, M., and Abed, S., J. Ovoni. Res., 16 (2020) 107.

[23] Kumkale, V.Y. *et al.*, ES Energy Environ., 23 (2024) 1104.

[24] Chand, P., Optik, 181 (2019) 768.

[25] Kamble, V.B. and Umarji, A.M., AIP Adv., 3 (8) (2013) 082120.

[26] Zhang, H. *et al.*, Catalysts, 13 (4) (2023) 728.

[27] Çorlu, T. and Acar, S., Gazi Müh. Bilim. Derg., 9 (1) (2023) 93.

[28] Mishra, S.K. *et al.*, Opto-Electron. Rev., 18 (4) (2010) 467.

[29] Hathal, Y.R., Ibrahim, I.M., and Khalaf, M.K., Iraqi J. Appl. Phys., 20 (2B) (2024) 349.

[30] Hamdan, S. and Ali, I., Dig. J. Nanomater. Biostruct., (DJNB), 13 (3) (2018) 669.

[31] Ozel, K. *et al.*, J. Alloys Compd., 849 (2020) 156628.

[32] Mishra, M. *et al.*, ACS Omega, 3 (2) (2018) 2304.

Volume 18, Number 3, 2025. pp. 399-410

Jordan Journal of Physics

ARTICLE

Role of Solitary Waveform on the Reaction Rate of Slab Reactor Geometry for Different Neutron Absorbers Using GEANT4

Seyede Nasrin Hosseinimotlagh[a], **Kavoos Abbasi**[b] , **Mohammad Ali. Zarei**[c], **Abuzar Shakeri**[a], **Vahid Reza Rezaei**[a], **Jahangir Bayat**[a] and **Hamid Reza Vanaie**[d]

[a] *Department of Physics, Shi.C., Islamic Azad University, Shiraz, Iran.*
[b] *Department of Physics, College of Sciences, Yasouj University, Yasouj, 75918-74831, Iran.*
[c] *Department of Physics, Payame Noor University, Tehran, Iran.*
[d] *Department of Sciences, Bu.C., Islamic Azad University, Bushehr, Iran.*

Doi: **https://doi.org/10.47011/18.3.12**

Received on: 14/05/2024; *Accepted on: 14/08/2024*

Abstract: Graphite nuclear properties, such as moderating power and absorption cross-section, are not as good as those of heavy water. However, graphite can be prepared in a pure form. Its structural and thermal properties are good, and it has a high thermal conductivity. The thermal neutron in graphite performs an average of 1200 scattering collisions before it is absorbed. This very low absorption cross-section makes graphite an ideal material for applications in nuclear reactors. In the current research, graphite is assumed as a diffusive medium due to its low absorption cross-section (0.0035 barn) and its atomic mass being close to that of the neutron. In this medium, the neutron absorbers boron (^{10}B), cadmium (^{113}Cd), samarium (^{149}Sm), europium (^{151}Eu), hafnium (^{177}Hf), and gadolinium (^{157}Gd) are considered individually. The aim of this paper is to obtain the solitary waveform of the reaction rate in a graphite diffusive medium using these neutron absorbers. This work shows that hafnium has the longest transition time among the materials examined in this research. This means that, for a constant transition length, hafnium requires more time to reach a steady state. The efficiency of hafnium as a neutron absorber is determined not only by the magnitude of its thermal neutron absorption cross-section, but also by its exceptional capacity to absorb higher-energy neutrons over the energy range of their deceleration.

Keywords: Graphite, Neutron absorbers, Soliton theory, KdV equation, Inverse scattering transform, Nuclear reactor.

1. Introduction

A soliton wave is spread in the environment in such a way that its shape and size do not change with time, and it moves with group velocity in a reference frame. In fact, the soliton wave is a nonlinear wave and does not lose its structure due to interaction with other solitons.
Each soliton wave packet has a maximum value. Soliton waves have been seen in scientific fields, such as rising water levels and light intensity in fiber optics. If two solitons move in the opposite direction, they pass each other without any change. Solitons can be obtained, for example, by solving the Korteweg de-Vries (KdV) and nonlinear Schrödinger equations. Soliton-type solutions resulting from solving differential equations give useful information about the dynamics of these waves.

Corresponding Author: Abuzar Shakeri **Email**: Abuzar.Shakeri6845@gmail.com

In the 1800s, scientists discovered the existence of soliton waves. John Scott Russell observed solitons for the first time [1]. Russell considered the soliton wave important, while many scientists disagreed with his idea. Airy and Stokes tried to describe soliton-type waves, but unfortunately, they did not find justification. Following them, Bosinsek and Riley, in 1871 and 1876, respectively, were able to provide a theoretical justification for soliton-type waves. However, discussions about soliton-type waves continued until the presentation of the famous KdV equation [2]. Finally, a complete study on soliton waves was presented by Zabusky and Kruskal [3], who analyzed the KdV equation numerically and observed their particle-like behavior.

They found that these waves do not change their velocity and shape after collision and named these waves as solitons [4]. The inverse scattering transformation process (ISTP) about solitons [5] is one of the most important discoveries in physics and mathematics [6-8]. It is worth mentioning that until the ISTP was presented to find multi-soliton solutions, some nonlinear partial differential equations (NLDEs) could not be solved analytically, which emphasizes the importance of ISTP [9-12]. Therefore, the emergence of solitons and ISTP has created a formulation for solving NLDEs. Having soliton solutions for a nonlinear partial differential equation provides exact solutions [13].

The inverse scattering transform or IST acts in precisely the same way as the Fourier transform (FT) does in linear problems; namely, it transforms the dependent variable, which satisfies a given partial differential equation (PDE), to a set of new dependent variables whose evolution in time is described by an infinite sequence of ordinary differential equations (ODEs). For special classes of PDEs, these equations are separable and hence trivially integrable. Compared with the FT, IST differs in two key aspects. First, the basis is no longer fixed (like $e^{\pm ikx}$) but moves in a way that depends on the unknown variable. Second, the spectrum (and here we are considering partial differential equations over infinite spatial intervals) no longer simply consists of the continuum of real wavenumbers k but includes, in addition, a finite number of isolated complex wavenumbers. It is the complex wave-numbers which give rise to the entities known as solitons. They are truly nonlinear quantities and have no linear analogue. Soliton theory has caused a revolution in mathematics and physics, which has led to the creation of new issues in various scientific branches, such as quantum and classical physics.

The credit for the discovery of the soliton concept belongs to John Scott Russell, who observed a special wave in the shallow waters of the British Channel in 1834. A soliton, or a solitary wave, is a type of self-amplifying wave packet that continues to propagate at a constant speed. It retains its originality. Russell noticed that this wave stops due to the obstruction of the wave propagation by the boat, but continues to move at a constant speed without losing its shape. He followed a wave for about 8 miles and found that this wave traveled at a constant speed for up to 2 miles without losing its shape. In the continuation of his research, he stated the properties of transmission waves as: (i) Waves can travel long distances at a constant speed. (ii) Unlike ordinary waves, waves never merge. (iii) The speed of a wave depends on its size, its width, and the depth of the water. (iv) Higher waves travel faster than smaller waves. (v) The speed of these waves is determined by: $V = \sqrt{G(h + A)}$, where G is the acceleration due to gravity, A is the amplitude of the soliton wave, and H is the height of the shallow water channel.

Solitons have numerous applications in both pure and applied mathematics, particularly in areas such as differential equations, Lie groups, Lie algebras, and differential geometry. Through the inverse scattering transform (IST), multi-soliton solutions of many nonlinear partial differential equations (PDEs) that cannot be solved analytically can be obtained. For example, IST has been applied to solve the initial-value problem for the Korteweg–de Vries (KdV) equation, enabling the description of the time evolution of the corresponding scattering data.

The study of solitons, in conjunction with Hamiltonian theory, has revolutionized research in mathematical physics, giving rise to new concepts and theories in diverse fields, including classical mechanics, quantum mechanics, and Lie theory. Beyond mathematics, soliton theory has been applied in fluid dynamics, plasma physics, nonlinear optics, astrophysics, and molecular biology to address important practical problems. A prominent example is in optical fiber communications, where solitons are widely used for the long-distance transmission of digital signals with minimal distortion. Apart from being used in communications, solitons are also used in optical switches. The most active research topics in soliton theory are due to its significant potential applications in information and communication technology. [14-15].

Also, solitons play a special role in the study of plasma, biology, and neutron diffusion in nuclear reactors [16-20]. In this work, we investigate neutron diffusion in diffusive media as solitary waves using diffusion theory. In fission reactors, neutron absorbers (NAs) are used to control reactivity. The reaction rate of neutrons diffusing in a pure absorbing medium is similar to a solitary wave. In the solitary wave, the absorbing material atomic density and the neutron flux spatial shape do not change during burning. The velocity of the burning wave is a function of initial neutron flux per density of NA in the diffusive media. The reason for the generation of soliton waves is the non-linearity of the equations describing the flux and atomic density dependent on space and time in the environment under investigation. Graphite, beryllium, light water, and heavy water are the most important diffusion materials. Graphite nuclear properties, such as moderating power and absorption cross-section, are not as good as those of heavy water. But its pure form can be prepared. Its structural and thermal properties are good, and it has a high thermal conductivity.

The thermal neutron in graphite performs an average of 1200 scattering collisions before it is absorbed. This very low absorption cross-section makes graphite an ideal material for applications in nuclear reactors. In the current research, graphite is assumed as a diffusive medium due to its low absorption cross-section (0.0035 barn) together with its atomic mass being close to that of the neutron. In this medium, boron (^{10}B), cadmium (^{113}Cd), samarium (^{149}Sm), europium (^{151}Eu), hafnium (^{177}Hf), and gadolinium (^{157}Gd) are studied individually as neutron absorbers. The aim of this paper is to obtain the solitary waveform of the reaction rate in a graphite diffusive medium using these neutron absorbers. Therefore, to achieve this goal, the sections that are studied in this article are listed below.

Diffusive media are turbid media where propagation occurs in a diffusive regime. In fact, propagation is dominated by multiple scattering and photon scattering events before being detected. In this article, we study the soliton behavior of neutrons in the neutron diffusive media. The diffusion theory model of neutron transport plays a crucial role in reactor theory. Here, the neutrons are characterized by a single energy or speed, and the model allows preliminary design estimates. The mathematical methods used to analyze such a model are the same as those applied in more sophisticated methods, such as multi-group diffusion theory, and transport theory.

The selection of appropriate materials for neutron absorption and radiation shielding is crucial for both industrial and research applications. One of the main requirements is to protect personnel from radiation, and in most places, the principle is that below the limit, the dose received should be "acceptably low". When using radiation sources for applications in science and technology, the definition of collimated beams is often an important requirement, and this also requires effective absorbers [21].

Recent papers describe important criteria for the selection of neutron absorbers [22, 23]. Elements such as boron, gadolinium, and samarium that may be used in combination with various polymers in terms of neutron absorption and external radiation dose have been evaluated by Castley *et al.* [22]. A review of the wide range of different materials that can be used with instrumentation for neutron scattering is presented by Stone *et al.* [23].

In Section 2, the concept of solitary waves using the KdV equation is introduced. In Section 3, soliton-soliton interaction is reviewed. In Section 4, the properties of selected neutron-absorbing media are described. In Section 5, the solitary wave variables are described. In Section 6, the solving method of the soliton wave equations of the diffusive medium for determining the neutron reaction rate is presented. In Section 7, our selected geometry of a neutron diffusive and absorbing medium for determining the numerical values of neutron reaction rate is given, and in the final Section, the conclusions are presented.

2. KdV Equation

To confirm the creation of solitons, we examine the KdV equation. The KdV equation is not only a scattered waves equation but also a nonlinear evolution equation. In fact, Scott Russell [1] observed that:

i) A soliton wave propagates in a stationary form over a smooth area without breaking its geometry or speed.

Note that a single wave is a wave that does not interact with any other waves. If these waves do not change their shape and speed after impact and remain transparent, they are called solitons [24]. Also, certain sine waves are initially divided into several soliton waves.

ii) A soliton wave continues to travel after a stationary collision, retaining its geometry and momentum.

iii) The soliton wave probably experiences a change in phase and a time delay in the interval of the collision.

The issues mentioned above must be supported by solitons. The equation that so far introduces the properties of solitons well is the KdV equation [9]:

$$\partial_t u + \beta u \partial_x u + \partial_x^3 u = 0, x \in R \qquad (1)$$

where β is a real coefficient and βu is known as the velocity of propagation, which depends on the wave mode. The KdV equation accepts several exact solutions for the propagating waves as follows:

$$u = \frac{3c}{\beta} sech^2 \left[\frac{\sqrt{c}}{2} (x - ct) \right] \qquad (2)$$

Here, c is the wave propagation velocity. The above equation is known as the d'Alembert solution. The solitary wave solution must preserve soliton properties, which is verified if it obeys the following equation:

$$u = \frac{72}{\beta} \frac{3+4cosh(2x-8t)+cosh(4x-64t)}{\{3cosh(x-28t)+cosh(3x-36t)\}^2} \qquad (3)$$

The asymptotic solution for large t is given by:

$$u = \frac{12_{k_i}}{\beta} sech^2 \left[k_i \left(x - 4k_i^2 t \right) + \delta_i \right] \qquad (4)$$

where i = 1, 2 and $k_1 = 1, k_2 = 2$. Also, δ_i is a constant.

3. Soliton–Soliton Interaction

Research has shown that the interaction between two solitons is a function of their separation distance and relative phase [25]. Therefore, as a result of the interaction between two solitons, a bound state of two solitons may be formed. The main issue that should be mentioned here is that the relative phase of two solitons varies dynamically when the distance between them varies. When two solitons that initially have the same phase slowly get closer to each other, their relative phase varies, and therefore the force between them becomes repulsive.

On the other hand, if two solitons travel away from each other, the force they exert on each other becomes attractive and can complete its cycle. Knowing the concept that varies the relative phase between solitons is necessary to find their coupling properties. It should be noted that as the distance between solitons increases, the number of equilibrium points around which they can oscillate also increases. If the phase changes from 0 to π within half of the oscillation period, the interaction force alternates between attraction and repulsion.

It should also be emphasized that the completely “elastic” collision of solitons implies that there is no net energy exchange between them, and their fundamental parameters, such as amplitude and velocity, remain unchanged. One of the most important parameters in the dynamics of soliton–soliton interactions is the relative phase at the moment of collision. For instance, the maximum amplification amplitude observed during soliton collisions is determined by their phase synchronization. Phase synchronization also plays a crucial role in the formation of high-amplitude waves. Recent studies have analytically investigated phase synchronization in multi-soliton arrays [26–28].

4. Properties of Neutron Absorbing Media

Burnable absorbers or burnable neutron poisons are materials that are placed in the core of a fission reactor, which include fertile nuclei with a large absorption cross-section (σ_a). By absorbing neutrons, these materials significantly reduce the neutron population during the reactor’s operational cycle. As the inventory of burnable absorbers decreases through irradiation, their effect on reactivity diminishes.

Burnable absorbers are particularly important for controlling reactivity in long-term fuel cycles [29–34]. They are often employed to reduce peak reactor power levels. Ideally, a burnable absorber at a rate comparable to the fuel consumption rate, thereby maintaining a relatively stable reactivity balance over time. In the operating fuel cycle, if a burnable absorber burns at a high rate, the positive feedback oscillations can exceed the limits of the fission reactor, while if the burnable absorber burns at a low rate, the remaining burnable absorber will result in negative feedback oscillations. Fuel rods containing gadolinium are applied to control the reaction rate of boiling water reactors, while boron solutions are used to control the reaction rate in the pressurized water reactors.

Since neutron absorption cross-section in burnable poisons is a function of energy, burnable absorbers are related to temperature variations. The properties of six different burnable absorber isotopes are briefly presented below. I) Boron (^{10}B): Its neutron absorption cross-section reduces exponentially with neutron energy. II) Gadolinium (^{155}Gd and ^{157}Gd): These isotopes of gadolinium are burnable absorbers with resonance energies higher than 1eV. Depending on the spectrum of the reactor, these two isotopes will have an increase in reaction rate as a function of temperature. Some gadolinium isotopes are stable, and some of them are strong neutron absorbers. ^{157}Gd has a very high thermal absorption cross-section. III) Europium (^{167}Er): This isotope has a large thermal resonance at $1eV$, which leads to increased absorption and, thus, a negative reaction rate in terms of temperature. Note that in fast reactors, B and Gd are two common burnable absorbers. One of the main challenges of isotopes is their separation, which is expensive. IV) Hafnium (Hf): Although hafnium-based materials are not very common, they are good burnable absorber candidates due to their ability to absorb neutrons with more than thermal energy. If a neutron is absorbed by hafnium, another isotope of hafnium is created, which is a neutron absorber. If a layer of hafnium dioxide is created on the surface of the Hf metal, it will show good corrosion resistance against hot water. V) Cadmium: Cd-based burnable absorbers exhibit favorable neutronic behavior in extended fuel cycles. Cd is one of the components of control rods containing Ag-In-Cd in fission reactors. Cadmium-based burnable absorbers are made as cadmium wires or cadmium oxide pellets [35-38]. However, the use of Cd-based burnable absorbers in fission reactors poses significant challenges due to the high cost of production and the need for safe handling and storage, given cadmium's health hazards. VI) Samarium: Natural samarium contains six stable isotopes, of which ^{149}Sm accounts for about 14%. This isotope is a strong neutron absorber with a large cross-section, making it particularly effective in reactivity control. In this paper, we will focus on the above burnable absorbers with their properties summarized in Table 1, where $\sigma_{a,th}$ and $\sigma_{a,fast}$ are the thermal and fast cross-sections at neutron energies of $0.025\ eV$ and $200\ keV$, respectively [39].

TABLE 1. Properties of selected burnable absorbers [39].

Burnable absorber	Symbol	$T_{1/2}$	Abundance, %	$\sigma_{a,th}(b)$	$\sigma_{a,fast}(b)$
Boron	^{10}B	stable	19.9	3844	1.47
Cadmium	^{113}Cd	$8.0 \times 10^{15} y$	12.2	19969	0.28
Samarium	^{149}Sm	stable	13.8	40150	0.70
Europium	^{151}Eu	$5.0 \times 10^{18} y$	47.8	9185	0.30
Hafnium	^{177}Hf	stable	18.5	375	0.55
Gadolinium	^{157}Gd	stable	15.7	252912	0.33

It is worth noting that some isotopes have been omitted from Table 1 because they are either highly unstable or have low neutron absorption capabilities. Figure 1 shows the absorption cross-sections of the selected burnable absorbers as a function of neutron energy [40].

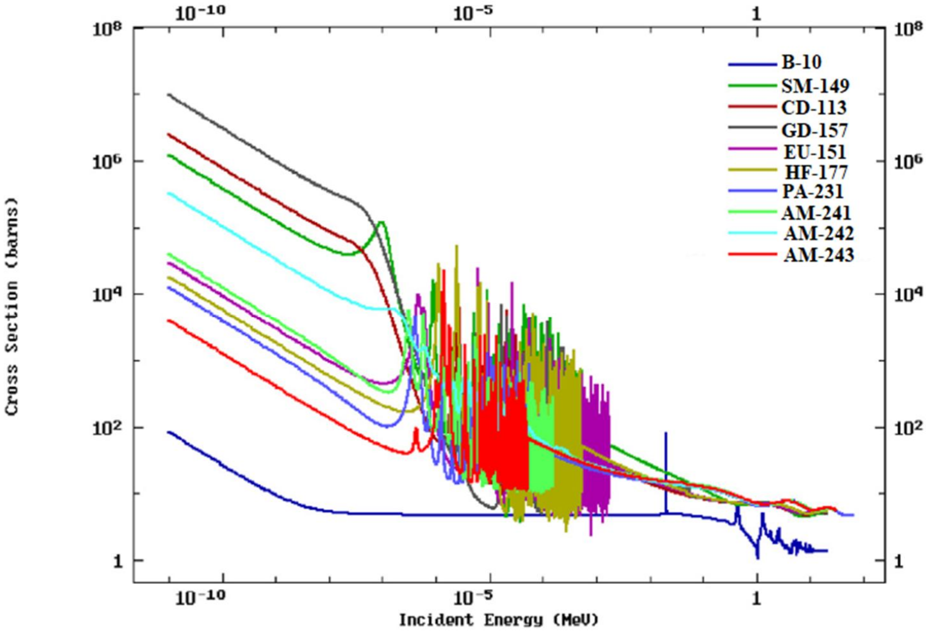

FIG. 1. Comparison of capture cross-sections [40].

5. Description of Variables

Before entering into the discussion about the absorbing and diffusive medium, it is better to get familiar with the following parameters. These parameters are general and can also be used to describe the characteristics of soliton burnup in absorbing and diffusive materials. In soliton systems, these parameters should be designed as optimal parameters.

a. Phase of Transient

1) Transient time duration (TTD): TTD is the time duration of the transient phase. For determining the TTD parameter, the following two criteria can be used: I) The time duration at which a TTD aims 95 percent of its stationary state amount. II) Time duration at which a TTD aims 99 percent of its stationary state amount. In these two cases, the transient phase value varies very fast in the initial states and very slowly as it approaches the stationary state.
2) Transient distance (TD): TD is equal to the distance the wave travels to reach its stationary state shape. Similar to TTD, TDs are known as TD 95 and 99 percent.

b. Phase of Stationary State

1) Wave speed: It is the same as the propagation speed of a burning wave, and this quantity can be interpreted as flux per nuclide density.
2) The width of the reaction rate region:

i) FWHM: The FWHM parameter equals the width of the reaction rate curve measured between half of its maximum value.

ii) 1% of FWHM: This parameter is defined as the width of the reaction rate curve measured between 1% of its maximum value.

It is worth noting that the mean free path of the burnable absorbers presented above depends on σ_a, which represents the absorption cross-section.

6. Solution of Partial Differential Soliton Wave Equations in a Diffusive Medium

In general, the neutron diffusion equation in the fission reactor is as follows:

$$D\frac{\partial^2\phi(x,t)}{\partial x^2}-\sigma N(x,t)\phi(x,t)=\frac{1}{v}\frac{\partial\phi(x,t)}{\partial t} \qquad (5)$$

where $\phi(x,t), N(x,t), \sigma, D$, and v are the flux of neutrons, the nuclide density of neutron burnable absorber, the cross-section of absorber‘ the diffusion coefficient, and the neutron speed, respectively. We assume that the scattering matter does not absorb any neutrons. The right-hand side of the above equation is omitted because the time-dependence of $\phi(x,t)$ changes slowly, whereas the v variations are high. Therefore, Eq. (5) can be written in the following form:

$$D\frac{\partial^2\phi(x,t)}{\partial x^2}-\sigma N(x,t)\phi(x,t)=0 \qquad (6)$$

The equation of burnup for a neutron burnable absorber is given by:

$$\frac{\partial N(x,t)}{\partial t} = -\sigma N(x,t)\phi(x,t) \tag{7}$$

The required conditions for solving these equations are: $J(0,t) = J_0$, $N(x,t) = N_0$ and $\phi(100,\mathrm{t}) = \phi_0$, where $J(x,t)$ is the current density, and $\phi(x,t)$ must be zero at the boundary. The reaction rate, $R(x,t)$, is determined by the following expression:

$$R(x,t) = \sigma N(x,t)\phi(\mathrm{x},\mathrm{t}) \tag{8}$$

We can solve Eqs. (6) and (7) using the asymptotic solution. Choosing appropriate boundary conditions, we obtain the asymptotic solutions, which are as follows:

$$N_{as}(x,t) = \frac{N_0}{\left(1+\exp\left(-\frac{x-vt}{l_0}\right)\right)^{3.5}} \tag{9}$$

$$\varphi_{as}(x,t) = \frac{v\sqrt{2}}{\sigma l_0}\left(\frac{N}{N_0} - 1 - \ln\left(\frac{N}{N_0}\right)\right)^{\frac{1}{2}} \tag{10}$$

and the asymptotic form of reaction rate density is given by:

$$R_{as}(x,t) = \frac{v\sqrt{2}}{l_0}N_{as}\left(\frac{N_{as}}{N_0} - 1 - \ln\left(\frac{N_{as}}{N_0}\right)\right)^{\frac{1}{2}} \tag{11}$$

Here, l_0, represents the initial diffusion length of neutrons in the medium. The diffusion length is obtained using the following equation:

$$l_0 = \sqrt{\frac{D}{N_0\sigma}} \tag{12}$$

For example, for boron as a neutron absorber, the diffusion length is L = 5 cm. In this study, we consider a graphite diffusive medium with six neutron absorbers: boron (^{10}B), cadmium (^{113}Cd), samarium (^{149}Sm), europium (^{151}Eu), hafnium (^{177}Hf), and gadolinium (^{157}Gd), each studied separately. In order to make a better comparison, we consider the diffusion length of the media under study to be 5 cm, similar to the diffusion length of graphite and boron neutron absorbers, and we will calculate the density of different neutron absorbers according to Table 2. It should be noted that in all environments, the net incoming neutron flow is 10^{14}cm^{-2} s^{-1}.

TABLE 2. Properties of six neutron absorbers in a graphite diffusive medium.

Element	^{10}B	^{113}Cd	^{149}Sm	^{151}Eu	^{177}Hf	^{157}Gd
Burnup wave speed (cm/day)	0.83	4.55	8.80	2.0	0.09	54
Diffusion length (cm)	5	5	5	5	5	5
Initial absorber density (cm^{-3})	1.04×10^{19}	19×10^{17}	9.8×10^{17}	44×10^{17}	11×10^{19}	1.58×10^{17}

7. Geometry of the Neutron Diffusive and Absorbing Medium

It is assumed that the diffusive medium is graphite, and no neutrons are absorbed through this medium. In order to simplify the matter under discussion, the geometrical shape of our system is considered as a finite slab. In this study, the neutron flux is calculated using a one-dimensional diffusion equation along the xxx-direction, with a slab length of 100 cm. This length is chosen so that variations along the reactor core height can be neglected (see Fig. 2). It should be noted that the authors of this article have chosen the geometry presented in Ref. [41].

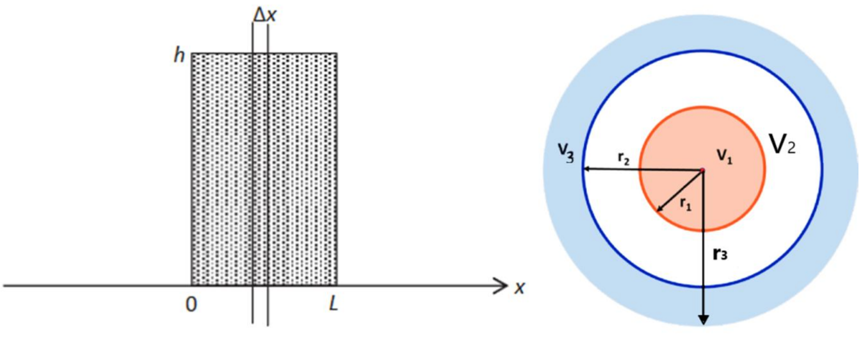

a) b)

FIG. 2. (a) The selected slab geometry for the reactor core, with height h and width L; (b) the regions of the nuclear fuel cell design.

The nuclear fuel cell geometry is cylindrical and is divided into three regions: fuel, cladding, and coolant, as shown in Fig.1(b). The reactor core design is constructed using several meshes Δx and boundary conditions. The selected parameters for this calculation are: natural absorber impurities in uranium = 4 ppm, natural absorber impurities in graphite = 1.3 ppm, density of graphite in the fueled zone = 1.73 g/cc, and UO_2 density = 10.4 $g/cm^{3.}$

It should be noted that the *GEANT4*-11.2.2. code was used in this work, and the graphs were drawn with the help of MAPLE.20 programming. Also, we used the parameters and specifications of nuclear fuel cell design from Table 1 of Ref. [41]. In Monte Carlo simulation methods, neutrons are tracked individually from emission to their final interaction or removal by any process, including leakage. This method is able to treat complex geometries with high resolution and fidelity. With the need for accurate modeling in the physics and dynamics of reactors and the great innovation in computer technology, the Monte Carlo method is becoming a more powerful tool and attracting increasing attention. That is why we used this method in this article. In general, calculations for thick samples rely on empirical expressions and numerical methods such as Monte Carlo computer simulation codes.

In Fig. 3, we plotted the two- and three-dimensional variations of the reaction rate density in solitary wave form for six selected neutron-absorbing media, as a function of space and time. Figure 3(a) shows boron (^{10}B) plotted at an interval of 10 days and covers a period of 100 days. Figure 3(b) presents cadmium (^{113}Cd) at 1-day intervals over 10 days, while Figs. 3(c) and 3(d) illustrate samarium (^{149}Sm) and europium (^{151}Eu), respectively, both plotted at 1-day intervals over a 10-day period. Hafnium (^{177}Hf) is depicted in Fig. 3(e) at 10-day intervals over 100 days, and gadolinium (^{157}Gd) is shown in Fig. 3(f), plotted at 0.1-day intervals over a 1-day period. According to the applied boundary conditions governing the proposed geometry, the peak reaction rate (R) for all neutron absorbers is $\sim 6.5 \times 10^{12} cm^{-2}s^{-1}$. Our numerical calculations indicate that Hafnium has the longest transition time among the examined materials. This means that, for a constant transition length, Hafnium requires more time to reach a steady state. Its efficiency as a neutron absorber is determined not only by its thermal neutron absorption cross-section but also by its exceptional ability to absorb higher-energy neutrons during their deceleration.

From the comparison of the graphs in Fig. 3, it is evident that all the curves physically follow the transient and stationary-state phases described in Section 5. The figures show the gradual development of the asymptotic (steady-state) burnup wave through the transient phase. During this phase, the shapes of the neutron flux and nuclide density evolve until they attain their steady-state forms. (Note: To better illustrate the role of neutron absorbers, both 2D and 3D diagrams are provided.)

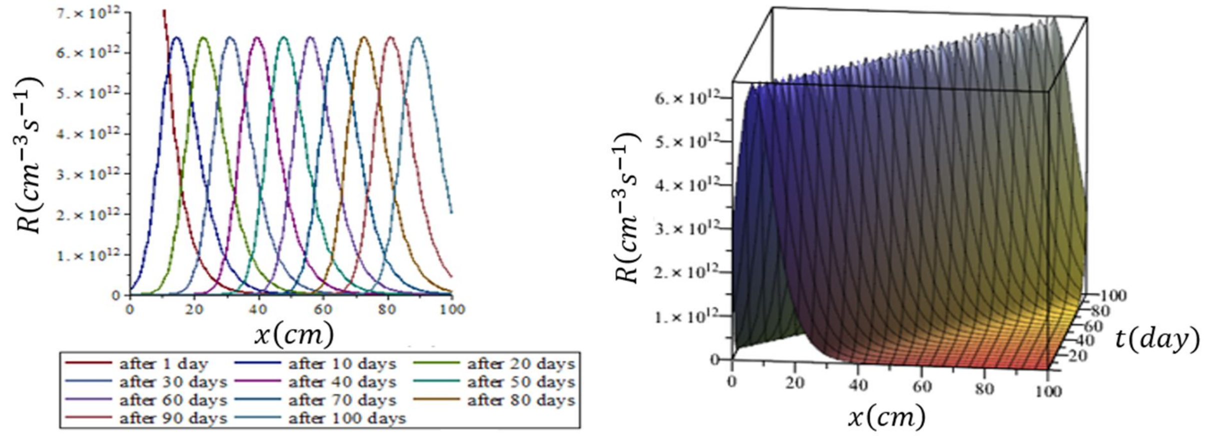

(a) Boron (^{10}B)

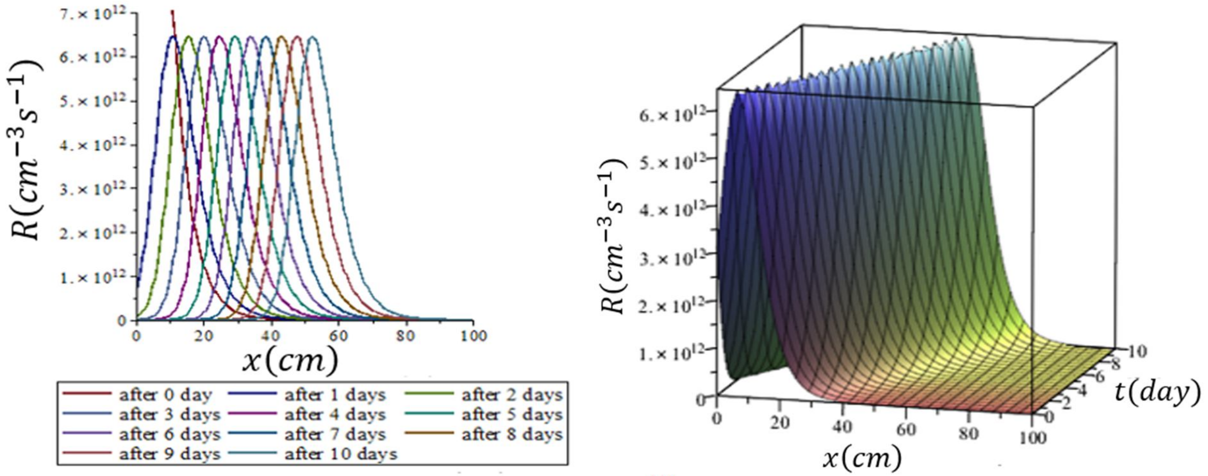

(b) Cadmium (^{113}Cd)

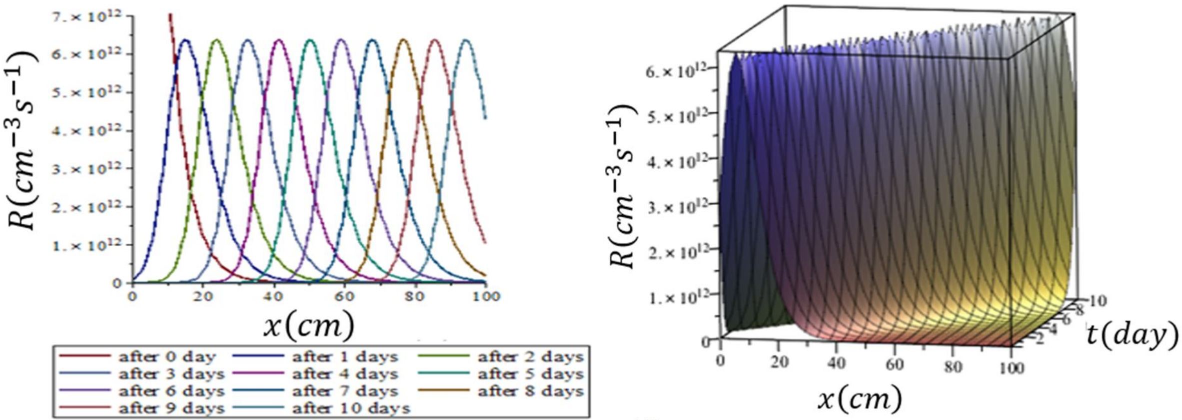

(c) Samarium (^{149}Sm)

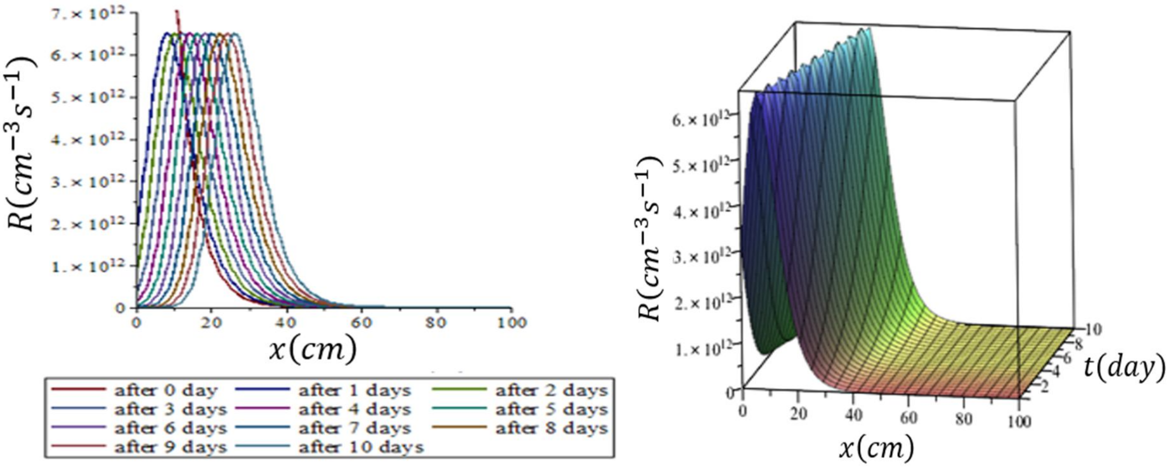

(d) Europium(^{151}Eu)

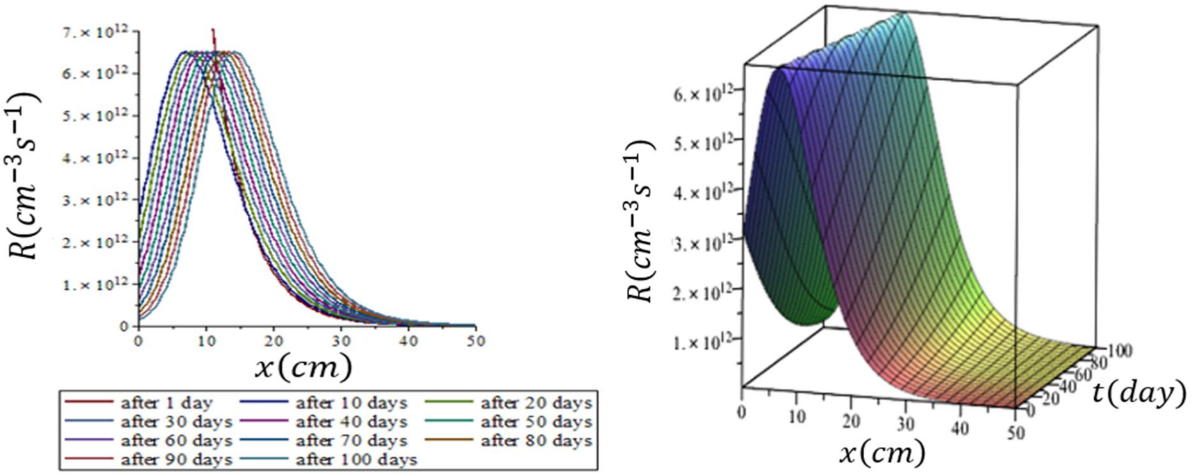

(e) Hafnium(^{177}Hf)

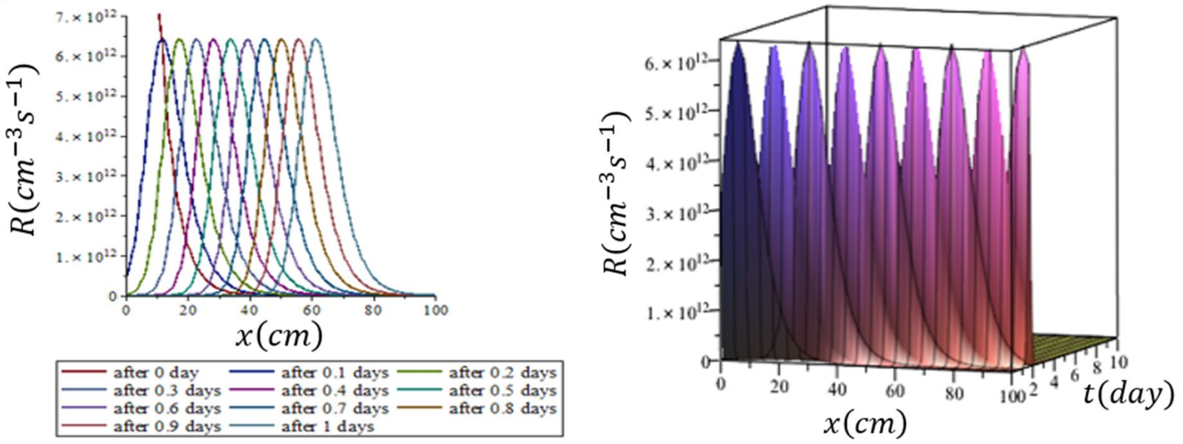

(f) Gadolinium (^{157}Gd)

FIG. 3. Two and three-dimensional variations of the reaction rate for different neutron-absorbing media in terms of x and t.

Our numerical results show that, as neutrons gradually penetrate the medium, the primary nuclides of the absorbing material begin to be consumed, leading to a decrease in the density of the neutron-absorbing nuclides. This action intensifies over time and continues until the end. The transition time depends on the σ_a. As σ_a decreases, the transition time increases. Our numerical calculations show that hafnium has the longest transition time among the materials examined in this research. It means that with the constant length of the transition among these materials, hafnium spends more time reaching a steady state. From the plotted diagrams in Fig. 2, we find that the reaction rate distribution quickly approaches the asymptotic form given in Eq. (11). The transition time for the cadmium, samarium, europium, and gadolinium neutron absorbers is less than that of boron and hafnium. For this reason, we have considered a period of ten days to draw the diagrams for boron and hafnium. From these figures, we calculated the special properties of the solitary burnup wave for selected absorbers in a graphite diffusive medium, and we listed them in Table 3.

TABLE 3. Properties of the solitary burnup wave for the selected absorbers in a graphite diffusive medium.

Element	^{10}B	^{113}Cd	^{149}Sm	^{151}Eu	^{177}Hf	^{157}Gd
Initial absorber density (atoms/cm^3)	1.04×10^{19}	19×10^{17}	9.8×10^{17}	44×10^{17}	11×10^{19}	1.58×10^{17}
Speed simulation (cm/day)	0.83	4.6	8.8	2	0.08	55
Speed analytical	0.83	4.6	8.8	2	0.09	54

Element	^{10}B	^{113}Cd	^{149}Sm	^{151}Eu	^{177}Hf	^{157}Gd
(cm/day)						
Transient time duration (days)	20.7	3.4	1.75	7.49	184.5	0.3
Characteristics time, τ (days)	6	1.11	0.56	2.52	61.4	0.1
Transient time duration / Characteristics time	3.4	3.1	3.1	3	3	3
FWHM (cm)	14	14	14.1	14	13.9	14
FWHM/ Diffusion length	2.8	2.8	2.82	2.8	2.78	2.8

8. Conclusions

In this work, solitary burnup waves in a graphite diffusion medium containing six pure neutron absorbers, namely boron (^{10}B), cadmium (^{113}Cd), samarium (^{149}Sm), europium (^{151}Eu), hafnium (^{177}Hf), and gadolinium (^{157}Gd), were examined separately. The results of our studies show that the speed of the burnup solitary wave in the desired medium is a function of transient time, transient length until it finally reaches its asymptotic form, and the width of the propagation zone (FWHM) of soliton waves in the environment under investigation. For the first time, this article examines the conditions of soliton wave development and its related parameters in reactor design. The results of our calculations about the characteristics of the burnup solitary wave in the graphite diffusion environment and the different mentioned neutron absorbers are classified into two groups:

Group 1. a: The estimated burnup wave solitary speed is independent of the cross-section of the absorber (σ_a), b: when σ_a increases, the transient length increases, c: transient time decreases with the increase of σ_a, and d: the burnup solitary wave FWHM grows with the mean free path of neutron absorption.

Group 2. a: The estimated burnup solitary wave speed is independent of σ_a and D (diffusion coefficient), b: when the D increases, the TD increases; we also found that TD per D does not change, c: TTD grows with increasing D, TTD per characteristic time does not change, and d: the burnup solitary wave FWHM grows with D. Our numerical calculations reveal that hafnium exhibits the longest transition time among the studied materials. With a constant transition length, hafnium requires more time to reach steady state due to its ability to absorb not only thermal neutrons but also higher-energy neutrons during their deceleration. Boron, particularly the ^{10}B isotope, is also effective due to its high thermal absorption cross-section and natural abundance (about 20%), allowing unenriched compounds to be used efficiently as absorbers.

Recent studies have highlighted important criteria for selecting neutron absorbers [22, 23]. Elements such as boron, gadolinium, and samarium, when combined with polymers, offer advantages in neutron absorption and reduction of external radiation dose, as evaluated by Castley *et al.* [22]. For materials dominated by absorption, increasing the cross-section reduces transmission, while scattering and diffraction can create features such as the Bragg slope. Neutron-absorbing polymer composites provide good mechanical and thermal properties, enabling fabrication of complex shapes for diaphragms, baffles, and collimators.

Based on these findings, further research is recommended to study solitary waveforms of reaction rates in other diffusive media using neutron-absorbing polymer composites and alternative reactor core geometries.

References

[1] Russell, J.S., Edin. Dublin Philos. Mag. J. Sci., 39 (240) (1895) 422.

[2] Arora, G., Richa, R., and Emadifar, H., Heliyon, 8 (2022) e12122.

[3] Zabusky N.J. and Kruskal M.D., Phys. Rev., 15 (6) (1965) 240.

[4] Herman, R., Am. Sci., 80 (4) (1992) 350.

[5] Gardner, C.S., Greene, J.M., Kruskal, M.D., and Miura, R.M., Phys. Rev., 19 (19) (1967) 1095.

[6] Wadati, M., Pramana, 57 (2001) 5841.

[7] Sandstede, B., In: “Handbook of Dynamical Systems”, (Elsevier, 2002) 983.

[8] Curry, J.M., Math. Rev., 43 (2002).

[9] Kaman, A., Curr. Sci., 115 (8) (2018) 00113891.

[10] Bæcklund, A. and Weston, D., Royal Institute of Technology, (2010).

[11] Hereman, W., arXiv preprint arXiv: 1308 (2013) 5383.

[12] Hirota, R., The direct method in soliton theory, (Cambridge University Press, 2004).

[13] Manukure, S., Zhou, Y., and Ma, W.X., Comput. Math. Appl., 75 (7) (2018) 2414.

[14] Turitsyn, S. and Mikhailov, A., Applications of solitons. Scattering (Elsevier, 1741, 2002)

[15] Prosimian, K. and Kuriakose, V.C., Elastic Light Scattering by Dielectric Microspheres for C-Band Applications (Springer Science & Business Media, 613, 2003).

[16] Kuwayama H. and Ishida, S., Sci. Rep., 3 (1) (2013) 1.

[17] Zabusky, N.J. and Porter, M.A., Scholarpedia, 5 (8) (2010) 2068.

[18] Manukure, S. and Zhou, Y., Int. J. Mod. Phys. B, 33 (07) (2019) 1950038.

[19] Ma, W.X., Qin, Z., and Lu, X., Nonlinear Dyn., 84 (2) (2016) 923.

[20] Chen, S.T. and Maw. X., Front. Math. China, 13 (2018).

[21] Adrian, R.R, Adam, E., Olle, E., and Robert, M.D., Nucl. Instrum. Methods Phys. Res. A, 984 (2020) 164613.

[22] Castley, D., Goodwin, C., and Liu, J., Radiat. Phys. Chem., 165 (2019) 108435.

[23] Stone, M.B., Crow, L., Fanelli, V.R., and Niedziela, J.L., Nucl. Instrum. Methods Phys. Res. A, 946 (2019) 162708.

[24] Zabusky, N.J. and Kruskal, M.D., Phys. Rev., 15 (6) (1965) 240.

[25] Zhenghua Huang, J.Y., Qin Zhou, Y.Z., Li, J., Sun, Y.H., Alshehri, M., and Biswas, A., Results Phys., 30 (2021) 104831.

[26] Sun, Y.H., Rev. E, 93 (2016) 052222.

[27] Gelash, A., Phys. Rev. E, 97 (2018) 022208.

[28] Kachulin, D., Dyachenko, A., and Dremov, S., Fluids, 5 (2020) 65

[29] Pavlov, V.I., Sidorenko, V.D., and Pozdnyakov, N.E., At. Energy, 73 (6) (1992) 977.

[30] Bachman, W.H., Harris, R.P., and Matzie, R.A., Trans. Am. Nucl. Soc., 47 (1984) 68.

[31] Frank, F.J. and Scherpereel, L.R., Trans. Am. Nucl. Soc., 40 (1982) 191.

[32] Doshi, P.K., Orr, W.L., and Rombouts, D., Trans. Am. Nucl. Soc., 40 (1982) 188.

[33] Sofer, G.A., Trans. Am. Nucl. Soc., 40 (1982) 183.

[34] Skogen, F.B., Stout, R.B., and Sofer, G.A., Trans. Am. Nucl. Soc., 39 (1981) 401.

[35] Kalcheva, S. and Branden, G.V.D, Korean Nucl. Soc., Jeju, Korea, (2017).

[36] Franck, N., Kalcheva, S., and Koonen, E., Proc. 13th Int. Topical Meeting on Research Reactor Fuel Management, Vienna, Austria, (2009).

[37] Cameron, I.R., Nuclear Fission Reactors. Plenum press (New York; 1982).

[38] Chubb, W., Cadmium Oxide Glazed Nuclear Fuel Pellet and Glazing Composition, In: U. States (Ed.) CBS Corp, (United States, 1986).

[39] Obara, T., Onoe, T., Tran. Am., Nucl. Soc. 107(2012)1023.

[40] Umme, M.N., Sahadath, M.H., Towhid, H.M., and Farshid, R., Nucl. Eng. Technol., 54 (2022) 3516e3525.

[41] Shafii, M.A., Zakiya, I., Fitriyani, D., Tongkukut, S.H.J., and Abdullah, A.G., J. Phys.: Conf. Ser., 1869 (2021) 012202.

Volume 18, Number 3, 2025. pp. 411-422

Jordan Journal of Physics

ARTICLE

Synergistic Antibacterial Properties of Zinc Oxide Nanoparticles Embedded in Chitosan and PVA Composite

Saif M. Alghazaly, Khalid H. Hatif Al-Atiya and **Hikmat A. J. Banimuslem**

Department of Physics, College of Science, University of Babylon, Babel, Iraq.

Doi: **https://doi.org/10.47011/18.3.13**

Received on: 22/07/2024; *Accepted on: 09/10/2024*

Abstract: In this study, zinc oxide nanostructures were synthesized via the sol-gel technique and characterized utilizing XRD, FE–SEM, FT–IR, and UV–vis. The solution casting approach was used to insert zinc oxide nanoparticles (ZnO NPs) into a series of chitosan and polyvinyl alcohol (Cs/PVA) mix films. X-ray diffraction (XRD) analysis demonstrated that increasing the ZnO nanostructures wt% leads to structural changes in the Cs/PVA blend. UV–vis analysis showed that with increased zinc oxide nanoparticles, the optical bandgap of Cs/PVA decreased from 5.45 to 4.5 eV. The antimicrobial tests revealed that the nanocomposite films demonstrated significantly improved antimicrobial effectiveness compared to the pure Cs/PVA film. This improvement directly corresponds to the increasing concentration of ZnO nanoparticles within the matrix. This nanocomposite can be used as a filter against *Brevibacterium epidermidis,* a bacterium responsible for unpleasant odor during sweating and when wearing shoes for long periods.

Keywords: Cs/PVA, Zinc oxide nanoparticles, Sol-gel, Optical bandgap, *Brevibacterium epidermidis*.

Introduction

Zinc oxide (ZnO) is an inorganic compound found naturally in the earth's crust, though most commercially used zinc oxide is synthetically produced [1]. It has the chemical formula ZnOand often appears as a white powder that is essentially insoluble in water. ZnO is one of the most studied materials and is employed in many electronic, healthcare, and environmental applications, confirming its significance to modern life. Because of this, ZnO is crucial in many industries and allows for fresh answers to modern challenges. Its characteristics encompass a high electrochemical coupling coefficient, exceptional photostability, wide radiation absorption, and remarkable chemical stability [2]. ZnO powder is widely applied across industries, including in paints, catalysts, and various technological, medical, and industrial applications, where particle size plays a crucial role. Therefore, many synthetic methods have been developed for the substance, such as sol-gel, precipitation, green leaf extract, microwave, wet chemical, and hydrothermal methods, which have succeeded in nanoparticle formation [3]. Among all the nanoparticle synthesis methods, sol-gel has attracted a lot of attention as an efficient, easy-to-process, and low-cost technique [4]. The sol-gel (SG) process typically unfolds in four stages: dissolution, hydrolysis, polymerization, and conversion to isolated ZnO solid powder [5]. Given the natural antimicrobial activity of chitosan, a biopolymer, it can be helpful in synthesizing antibacterial hydrogels. Most of the chitosan-based hydrogels have proven to exhibit good antibacterial effects on several microbial forms, such as bacteria, yeast, mold, and algae [6]. Chitosan (Cs) is an intriguing natural biopolymer with multiple

Corresponding Author: Saif M. Alghazaly **Email**: sci.saif.mohamed@uobabylon.edu.iq

desirable characteristics, namely, biocompatibility, biodegradability, non-toxicity, odorlessness, and the solubility of the chemical modifications. This is important because of the challenges associated with the disposal of synthetic polymers that result in environmental pollution [7]. Chitosan can be modified by blending with other materials, altering its chemical properties, or incorporating it with other polymers and inorganic particles. Through physical blending and cross-linking, the functionality of chitosan-based materials can be enhanced, thereby extending their applications. Additionally, chemical treatments can further improve the solubility and mechanical properties of chitosan [8, 9]. A blend of chitosan and polyvinyl alcohol (PVA) is particularly attractive due to its favorable mechanical, physical, and chemical characteristics. A number of features explain why PVA is selected: good mechanical properties, biodegradability, ease of preparation, high film-forming ability, and excellent chemical resistance [10]. Incorporation of such materials has attracted growing interest for antibacterial and antifungal applications. Wearing closed shoes, sweating, and having sensitive feet are some of the causes of foot odor. Closed shoes create a confined and humid environment that restricts air circulation, retains moisture, and promotes bacterial growth, which in turn leads to unpleasant odors [11]. Hyperhidrosis, characterized by excessive sweating, creates an optimal habitat for the proliferation of bacteria and fungi, contributing to odor in dark, warm, and moist areas of the body [12]. Two newly identified species of the genus *Brevibacterium* have been found in dairy and skin samples. The strains obtained from cheese and milk, specifically identified as *Brevibacterium casei*, are the culprits behind the distinctive aroma of cheese. *Brevibacterium epidermidis,* commonly found on human skin, is responsible for body odor. The skin debris shed by humans serves as a food source for the *Brevibacterium* bacteria. Because most people wear shoes and socks when walking, they provide an ideal environment for these microbes, as they thrive in warm, damp environments. *Brevibacterium* converts the amino acid methionine into the volatile molecule methanethiol (CH_3SH), which has a strong and disagreeable odor [13, 14]. This research aims to manufacture zinc oxide nanoparticles and study their structural properties, as well as the effect of incorporating them into Cs/PVA blend films. The resulting nanocomposites hold potential for use in deodorant formulations and as protective shoe linings, serving as promising candidates against *Brevibacterium epidermidis*, the bacterium responsible for unpleasant odors associated with sweating and prolonged shoe use.

Experimental Part

Materials

Chitosan $(C_6H_{11}NO_4)n$, medium molecular weight (300-1000 cps, average M.W.=1250000) was obtained from Glentham Life Sciences Ltd, United Kingdom. Polyvinyl alcohol (PVA) $(C_2H_4O)n$ was obtained from Central Drug House (P) Ltd., India [M.W. = 85000 to 124000]. Zinc acetate (ZA) $(CH_3COO)_2Zn$ $2H_2O$, [M.W. = 219.49] and acetic acid (CH3COOH) 99.5% [M.W. = 60.05] were obtained from Thomas Baker, India. Sodium hydroxide (NaOH) [M.W. = 40] was supplied by SDFCL, India. All chemicals and reagents used in this study were of analytical grade and were employed without further purification.

Preparation of ZnO Nanoparticles (ZnO NPs)

ZnO nanoparticles were synthesized using zinc acetate as the precursor, ethanol as the solvent, and sodium hydroxide as the catalyst, following a sol-gel-based procedure [15,16]. Specifically, 5.402 g of zinc acetate was dissolved in 200 mL of ethanol and stirred vigorously at room temperature with a magnetic stirrer. The solution was sonicated for 15 minutes until it became clear. Subsequently, the pH was adjusted to 8 by the dropwise addition of 40 mL of 1 M NaOH. The reaction mixture was stirred for 3 hours to ensure completion, then left undisturbed for 24 hours to allow for precipitation. The resulting product was dried at 70 °C in an electric oven, followed by calcination at 400 °C for 3 hours to remove residual impurities and obtain highly crystalline ZnO nanoparticles.

Nanocomposites (ZnO/CS-PVA) Sample Preparation

Nanocomposite films were prepared using the solution casting method. First, 5 g of chitosan was dissolved in 480 mL of a 2% (v/v) aqueous acetic acid solution and stirred vigorously at 50 °C for 2 h until a clear solution was obtained. Next, 5 grams of PVA were dissolved in 200 mL of deionized water and stirred vigorously with a magnetic stirrer at 50 °C for 1 hour until a homogeneous solution was achieved. The slow addition of the PVA and CS solutions ensures proper mixing. Prolonged stirring helps in the dispersion of any large particles or lumps, yielding a more homogeneous product. Upon mixing, the polymer chains of PVA and CS were able to interact through hydrogen bonding between hydroxyl OH^{-} and amino (NH^{2-}) groups, stabilizing the blended solution and promoting the formation of a coherent material. It should also be noted that some experimentation may require the sample to be stirred for different durations depending on the volume of the solutions used, as well as the concentrations of PVA and CS used in the experiment. The first model of the pure membrane containing no nanoparticles was cast into a 10 cm diameter plastic dish. A series of ZnO/CS-PVA membranes with different nanohybrid content was prepared by adding appropriate amounts of ZnO nanoparticles to the CS/PVA solution. The nanohybrid content levels mentioned were 2.5, 5, 7.5, 10, 12.5, and 15 wt/wt percent. The accurate quantity of ZnO nanoparticles was dispersed in 10 mL of distilled water. The ZnO nanoparticle suspension was then agitated to make sure that the nanoparticles were well dispersed. The suspension was then put in an ultrasound machine for 15 minutes in order to increase the nanoparticles' dispersion and to eliminate the agglomeration. The well-dispersed ZnO nanoparticle suspension was later added to the CS-PVA solution that was prepared earlier. Stirring was carried out for 20 minutes to guarantee the homogenization of the Cs-PVA/ ZnO nanoparticles throughout the solution, including the distribution of ZnO nanoparticles in the Cs-PVA matrix. The ZnO/CS-PVA solution samples were then cast into plastic dishes or molds. The cast samples were transferred to an oven at a temperature of 45 °C to dry the films for three days.

Characterization Methods

Structural investigations of the synthesized ZnO nanoparticles and ZnO/CS-PVA hybrid films were conducted using XRD (600 Miniflex, Rigaku, Japan) with a Bruker D8 advanced powder XRD, utilizing a CuKα radiation source (λ = 1.5417 Å, I = 0.05 A, V = 40 keV). The scan rate was set at 3° per minute, covering a 2θ range from 40° to 70°. The Fourier transform approach was employed to analyze infrared spectra of very intricate combinations using an FTIR analysis instrument, IR Affinity-1, made in Kyoto, Japan. The surface morphology of ZnO nanoparticles and nanocomposites was analyzed using a field-emission scanning electron microscope (FE-SEM) (Ltd., Tokyo, Japan) equipped with an X-Act EDS detector from Oxford Instruments, Abingdon, United Kingdom. Optical characterization was conducted at room temperature using a SHIMADZU UV-1800 spectrophotometer, covering the ultraviolet and visible light (UV-vis) wavelength range from 200 to 800 nm.

Brevibacterium Epidermidis Bacteria Activity Assay

Brevibacterium epidermidis is an obligate aerobe, mesophilic, Gram-positive bacterium commonly isolated from human skin and classified under the genus *Brevibacterium* [17]. It is rod-shaped and includes species of both biotechnological and clinical relevance. Although *Brevibacterium epidermidis* is not typically associated with pathogenesis, it has been implicated in infections such as bacteremia in immunocompromised patients with central venous catheters [18]. It is an irregular Gram-positive rod resembling corynebacteria and is also found in dairy products, where it contributes to aroma and coloration [18].

Understanding its characteristics, antimicrobial susceptibility, and clinical implications is important for evaluating potential therapeutic and preventive strategies. The magnitude of the inhibition zone is directly proportional to the antibacterial activity of the tested material, reflecting its inhibitory effect on bacterial growth [19].

The antibacterial activity of the nanocomposites was evaluated using the agar disk diffusion method, a simple and cost-effective technique widely applied for antimicrobial testing. Sterile Mueller-Hinton agar (20 mL) was poured into 10 cm diameter Petri dishes. After the media solidified, 0.1 mL of bacterial suspension was evenly spread on the surface. Following a 5-minute absorption period, 6 mm diameter disks of each nanocomposite (NC) sample were placed in the center of the plates. The pure polymer mixture served as the control. The dishes were incubated at 37 °C for 24 hours [20, 21]. The inhibition zones were measured in millimeters, and each test was performed in triplicate for all prepared nanomembrane models.

Results and Discussion

Fourier-transform Infrared Spectroscopy (FT-IR)

Figure 1 presents the FT-IR spectrum used to analyze and identify the functional groups of ZnO nanoparticles produced via the sol-gel method. As reported previously in the literature [22], the FT-IR spectrum revealed a broad absorption band at 408 cm⁻¹, attributed to the Zn-O stretching vibration. To verify these findings, previous literature was consulted, confirming that all peaks appeared around 400 cm⁻¹. Additionally, peaks were identified at 2939 and 2854 cm⁻¹, attributed to the CH_3 group's symmetric and asymmetric stretching frequencies [23]. A peak at 1651 cm^{-1} is characteristic of the hydroxyl group (O-H). However, the peaks at 1047 1/cm may be ascribed to the stretching modes of carbon-oxygen bonds and indicate lattice vibration of the absorption peaks. These findings are similarly reported elsewhere [24]. Moreover, stretching of the hydroxyl group can be observed at the absorption peak at 3464 1/cm. The peaks at 1473 and 1327 1/cm indicate the presence of $Zn(CH_3COO)_2{\cdot}2H_2O$ associated with CH_3 bending modes, as observed in previous studies [23].

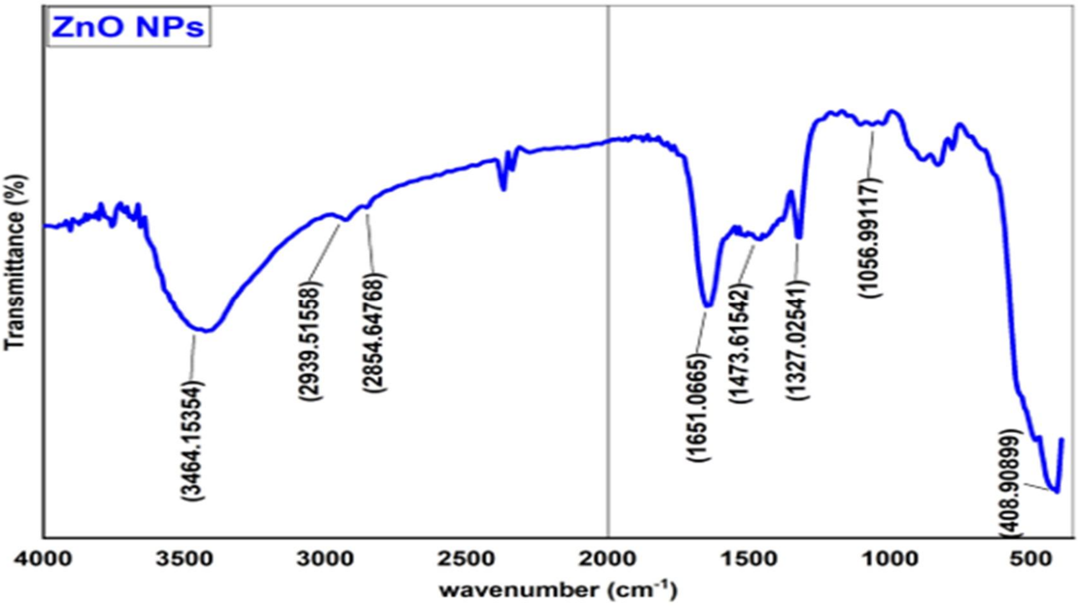

FIG. 1. FT-IR spectra of ZnO nanoparticles from 400–4000 1/cm.

An Investigation Using X-ray Diffraction

X-ray diffraction (XRD) is a non-destructive technique for studying the crystal structures of materials. Figure 2(a) displays the XRD pattern of the ZnO nanoparticles prepared by the sol-gel method, indicating the presence of the wurtzite phase. The peaks observed in the XRD pattern are consistent with the hexagonal structure of the wurtzite phase, as described in the reference code. The peaks at 2θ = 31.792°, 34.452°, 36.272°, 47.555°, 56.664°, 62.875°, 66.434°, 67.992°, 69.113°, 72.526°, and 77.093° are several sharp diffraction peaks. These peaks correspond to (1 0 0), (0 0 2), (1 0 1), (1 0 2), (1 1 0), (1 0 3), (2 0 0), (1 1 2), (2 0 1), (0 0 4), and (2 0 2) according to card number 01-079-0206 [25, 26]. Scherer's formula [27] was used to determine the crystallite size:

$$D = 0.89\lambda / (\beta\cos\theta) \,, \quad (1)$$

where λ is the wavelength of the X-ray (0.1541 nm), βi is the FWHM (full width at half maximum) in radians, θ is the diffraction angle, and D is the particle diameter.

Based on this calculation, the average crystallite size is 15.8 nm, and the dislocation density is 0.004 nm^{-2}. The dislocation density (δ), which shows the nanoparticles' flaws, was determined using the following formula:

$$\delta = \frac{1}{D^2} \quad (2)$$

The dislocation density of ZnO nanoparticles is inversely proportional to their grain size or crystalline size. The figure clearly demonstrates that no impurities or unreacted phase peaks were present in the ZnO samples produced using the sol-gel technique. At the calcination temperature of 400 °C, the precursors were completely disintegrated, resulting in pure ZnO.

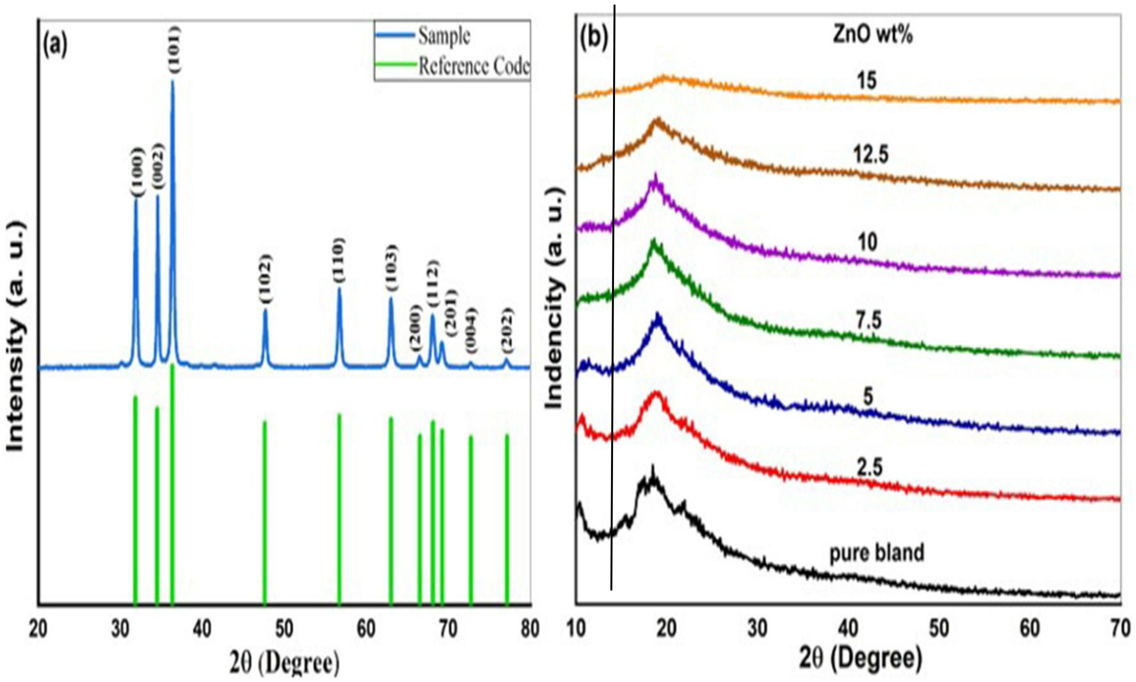

FIG. 2. XRD spectra of (a) zinc oxide nanoparticles; (b) pure Cs/PVA blend and ZnO NPs doped Cs/PVA composite.

Figure 2(b) displays the X-ray diffraction (XRD) spectrum of both the Cs/PVA polymer blend and the Cs/PVA/zinc oxide nanocomposites. The X-ray diffraction (XRD) investigation of the Cs/PVA polymer blend reveals two clearly identifiable diffraction peaks at 2θ = 10.30° and 18.23°. The prominent peak observed at 2θ = 18.58° indicates a semicrystalline structure of the pure Cs/PVA polymer blend. This is a result of the hydrogen bonding interactions that occur between the PVA and chitosan chains, both inside and between the molecules. In contrast, the XRD patterns of the Cs/PVA/zinc oxide nanocomposites display peak broadening and decreased intensity as the ZnO nanoparticle concentration increases. This indicates that the polymer blend of PVA/Cs has a larger amorphous phase when compared to pure PVA.

The decrease in intensity and concomitant increase in breadths of the XRD peaks recorded for the nanocomposite films are evidence of an increased degree of amorphization of the polymer blend owing to its interface interactions with the incorporated ZnO NPs. In the nanocomposites with higher ZnO concentrations, the broad peak present in the pure blend completely disappeared. Additionally, the absence of sharp diffraction peaks at any zinc oxide nanoparticle content suggests that the filler is effectively dispersed and fully integrated into the polymer matrix. The nanoparticles probably cause this by being embedded in the matrix's interplane gap [27, 28].

FE-SEM Analysis

Figure 3 presents FE-SEM analysis of pure ZnO's surface morphology, clearly showing ZnO nanorods with varying diameters. Zinc oxide nanostructures' antibacterial effectiveness is heavily dependent on their morphological impacts. Zinc oxide nanostructures can take many different shapes depending on the synthesis circumstances. These include rods, wires, tubes, spheres, needles, discs, rings, spirals, polyhedrons, flowers, plates, stars, and boxes. Different synthesis methods result in shapes with distinct physicochemical qualities. Moreover, rod-like nanostructures stand out as superior among their nano peers [29]. These one-dimensional nanorods, nanowires, and nanotubes offer a streamlined path for carriers, ensuring efficient transport. They reduce grain boundaries, surface imperfections, disorderliness, and short interface lengths, providing a smooth path for both electrons and holes. Thus, besides being functional, this design is quite symbolic, but let us leave symbolic concerns for another piece and return to the analysis of nanowires. Their ability to transport electricity with minimal loss results from natural selection for conductivity optimized at the nanoscale [30]. This research has revealed that the synthesized zinc oxide possesses a rod-like morphology attributed to zinc acetate as a precursor [30]. Furthermore, the nanorod's shape is greatly influenced by the concentration of the precursor [31].

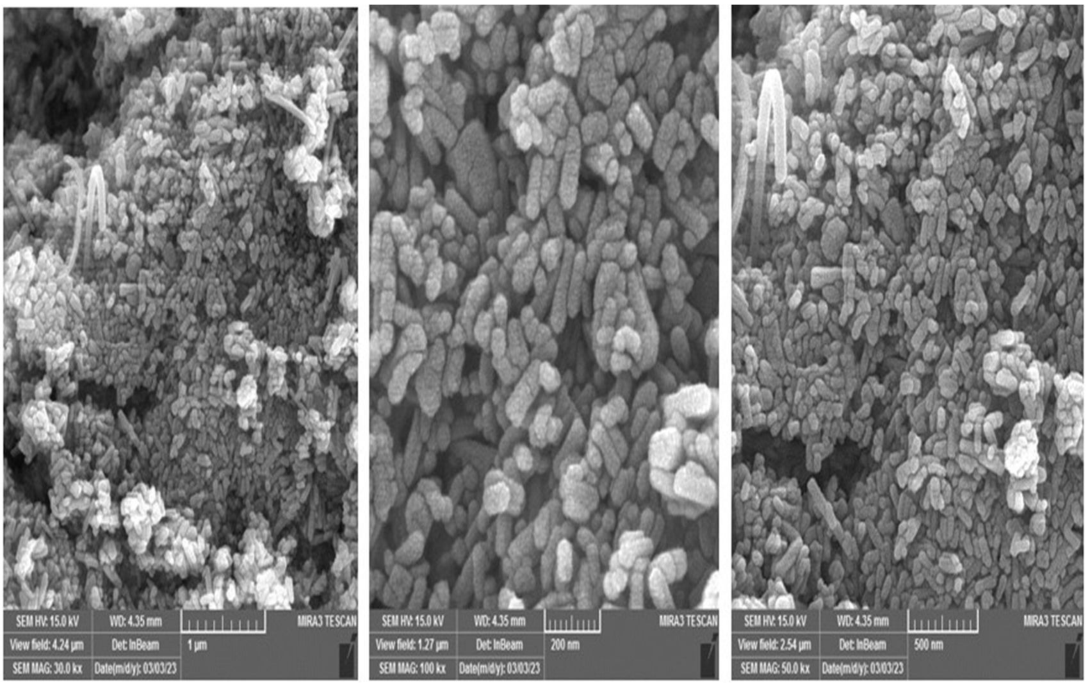

FIG. 3. FE-SEM images for zinc oxide nanoparticles.

UV-Vis Spectroscopy

UV-Vis spectroscopy, a critical technique for verifying the production of Cs/PVA/ZnO nanocomposites and determining, for example, the direct band gap energy, was used to investigate the optical absorption properties of the materials in more detail. Figures 4 and 5 show the UV-Vis spectrum of the ZnO nanostructures and the blend spectra. Figure 5(A) reveals interesting spectra: pure PVA/Cs showed a prominent absorption peak at 292 nm with a subtle shoulder at 204 nm. These features stem from its semi-crystalline structure, the PVA/Cs mixture, and the presence of C=O bonds within its structure, indicating π - π * and n - π * transitions, respectively [32–34]. Upon introduction of ZnO nanoparticles, these absorption bands significantly shifted to 212 and 240 nm. Notably, the absorption peak characteristic of zinc oxide appeared prominently at 315 nm in high-performance Cs/PVA/ZnO nanocomposites [35]. This indicates a compelling interaction between zinc oxide nanoparticles and the Cs/PVA matrix, possibly facilitated by hydrogen bonding through OH groups. Furthermore, we observed a significant redshift in the absorption edge of the material toward longer wavelengths (lower energy) with increasing concentration of zinc oxide nanoparticles within the Cs/PVA/ZnO NCs (see Fig. 5, inset B, for more clarity). This phenomenon underscores the dynamic interaction between nanomaterials and their host matrix, revealing promising approaches to customized optical and functional properties in nanocomposite materials [36].

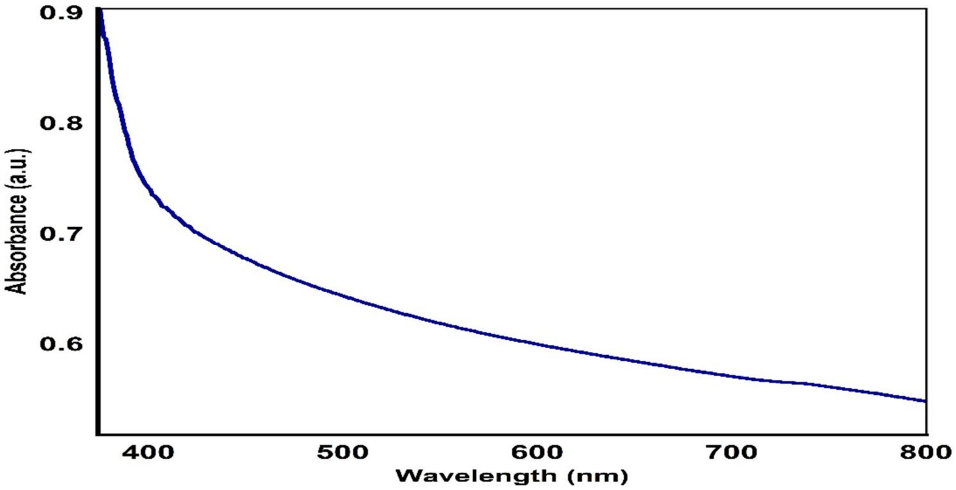

FIG. 4. UV–Vis pattern for ZnO nanoparticles.

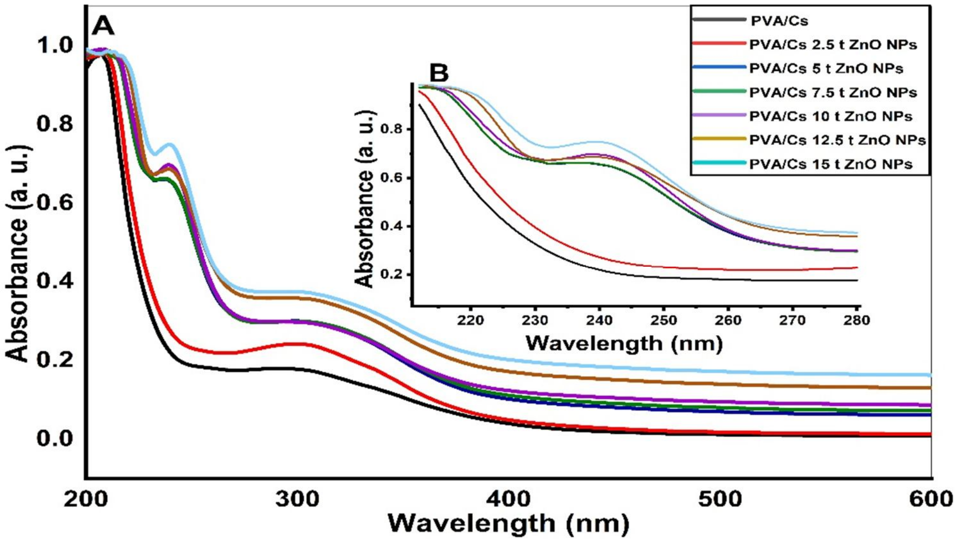

FIG. 5. UV–Vis pattern for Cs/PVA and Cs/PVA–ZnO NCs.

The optical bandgap energy (E_g) of the materials was estimated using Tauc's equation [37]:

$$(\alpha h\nu)^{1/n} = B\,(h\nu - E_g) \qquad (3)$$

where hν is the energy of the incident photon and α is the absorption coefficient, which can be obtained by using the Beer–Lambert relation [38]:

$$I = I_o e^{-\propto t} \qquad (4)$$

By taking the log of both sides of Eq. (4), we get:

$$\alpha(\nu) = 2.303(A/t) \qquad (5)$$

where A represents the absorbance, t is the thickness of the sample, n is a numerical guide to the type of transition, B is a constant, and E_g is the optical energy gap. The value of n can be 1/2, 2, 3/2, and 3, matching up with direct and indirect, allowed or forbidden transitions. Figure 6 represents plotting $(\alpha h\nu)^2$ against hν for both the pristine blend and its ZnO NP-doped counterpart. By using Eq. (3), the energy gap is the intercept of the tangent line drawn along the sharp drop of the Tauc plot. These visuals reveal a noteworthy trend: a steady decrease in the optical energy band gap as the concentration of ZnO NPs ramps up. This shift likely arises from the intricate dance between the pure blend and the zinc oxide nanoparticles. It's not just about the mixing; those ZnO NPs seem to be crafting some intriguing defects in the Cs/PVA films. These defects set the stage for localized environments that hint at increased disorder across the samples [39]. These results are consistent with the XRD data. The values obtained for the allowed direct electron transitions are listed in Table 1.

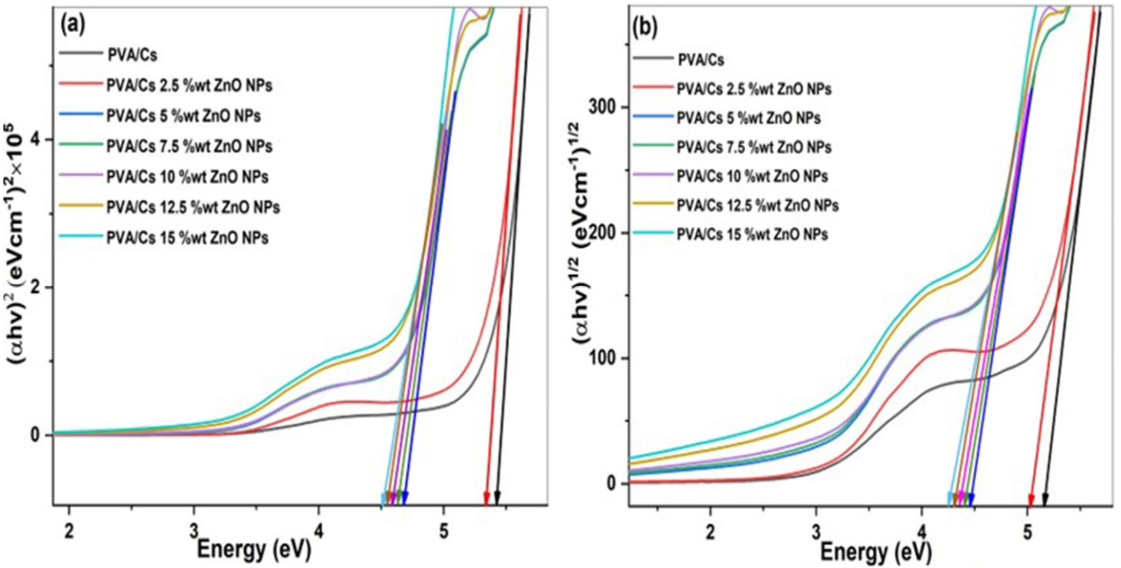

FIG. 6. Plots of for Cs/PVA and Cs/PVA–ZnO nanocomposites: (a) $(\alpha h\nu)^2$ and (b) $(\alpha h\nu)^{1/2}$ versus hν.

TABLE 1. The values of the optical energy gap (direct and indirect) for the prepared films.

ZnO/Cs-PVA (wt. %)	E_g^d(eV)	E_g^{in}(eV)
PVA/Cs	5.45	5.16
2.5	4.70	5.02
5	4.67	4.40
7.5	4.65	4.36
10	4.64	4.32
12.5	4.61	4.26
15	4.50	4.25

Antibacterial Activity Study

The widely employed agar well diffusion strategy serves as a standard method for evaluating the antimicrobial activity. Nanoparticles stand out as a compelling option for antibiotics due to their ability to exert a wide-ranging antibacterial impact, even at minimal doses. Their effectiveness spans across diverse bacterial strains, making them a promising solution in the fight against infections [40]. The mixture of PVA-Cs polymer and nanocomposites with different ratios (2.5, 5, 7.5, 10, 12.5, and 15 wt% ZnO NPs) was used to study the antibacterial activity against *Brevibacterium epidermidis*, an obligate aerobe, mesophilic, and Gram-positive bacterium isolated from human skin [17]. As shown in Figs. 7 and 9, the agar disk diffusion method was used to measure antibacterial sensitivity by determining the diameter of inhibition zones in millimeters (Table 2). The findings revealed that while the polymer alone exhibited minimal antimicrobial effect against *Brevibacterium epidermidis*, the nanocomposite samples displayed notable antibacterial activity. Incorporation of zinc oxide nanoparticles distinctly boosted this activity, showing a clear upward trend with increasing nanoparticle concentration, peaking at 15 wt. % ZnO NPs. As the amount of zinc oxide in the nanocomposites rose, so did the diameter of inhibition zones, culminating in maximum effectiveness at the highest nanoparticle concentration tested. These results vividly demonstrate how the presence of ZnO nanoparticles enhances antimicrobial performance, underscoring their potential in combating bacterial threats.

Zinc oxide nanoparticles exert their broad-spectrum antibacterial activity through several mechanisms, including ROS such as OH^-, H_2O_2, and O^{2-}, as well as disruption of the bacterial membrane [41]. The ROS damage bacterial cellular components—proteins, DNA, and lipids—due to their high reactivity and redox potential [42]. As illustrated in Fig. 8, ZnO nanoparticles interact with bacterial cells: negatively charged hydroxyl radicals and peroxides act on the bacterial surface, while H_2O_2 molecules penetrate the cell wall, causing bacterial cell damage, structural disruption, and ultimately, cell death [43]. Then, it can be suggested that ZnO nanoparticles covalently attached to bacteria may not have any antibacterial effect, even if the bacteria are killed or survive. However, inactivation caused by their presence in growth media continues to release peroxides, enhancing bactericidal efficacy over time. Moreover, zinc ions (Zn^{2+}) released from ZnO nanoparticles enhance the antimicrobial ability of these nanoparticles due to the effect of these ions on microorganism cell membranes and intracellular components, including mitochondrial membranes and physiological processes such as active transport and acid metabolism. This ultimately leads to swelling of the bacterial cells, which in turn leads to rupture of the cell membrane and thus rupture of the bacterial cells and leakage of DNA, proteins, and lipids. Therefore, the combined effect of ROS and Zn^{2+} confirms that ZnO nanoparticles are indeed an effective mechanism for bacterial inactivation [44].

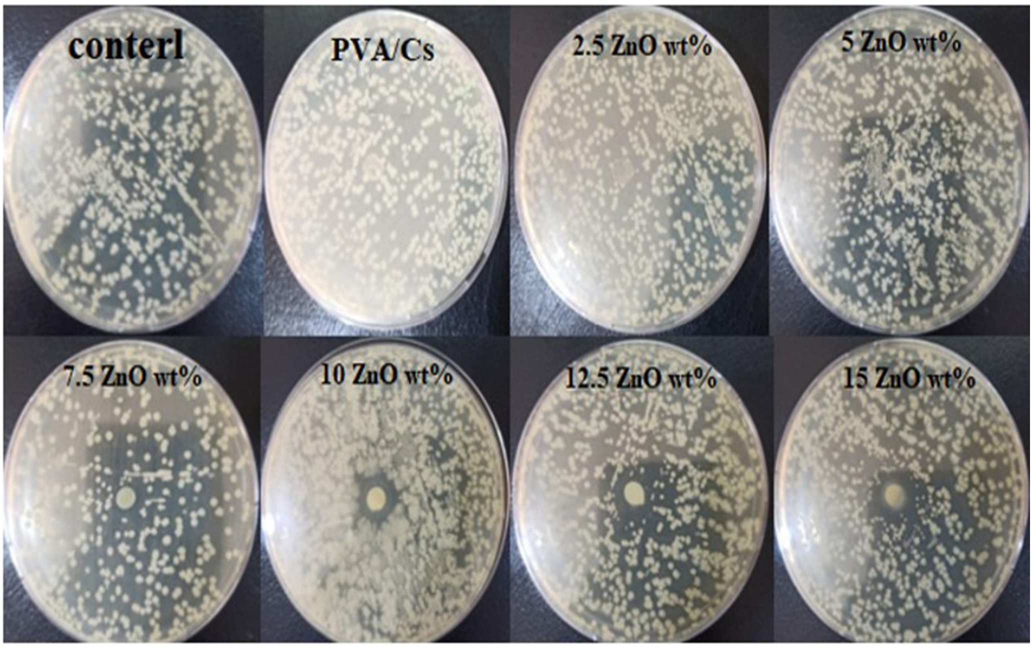

FIG. 7. Images for inhibition zones of Cs/PVA and Cs/PVA/ZnO NPs against *Brevibacterium epidermidis* bacteria.

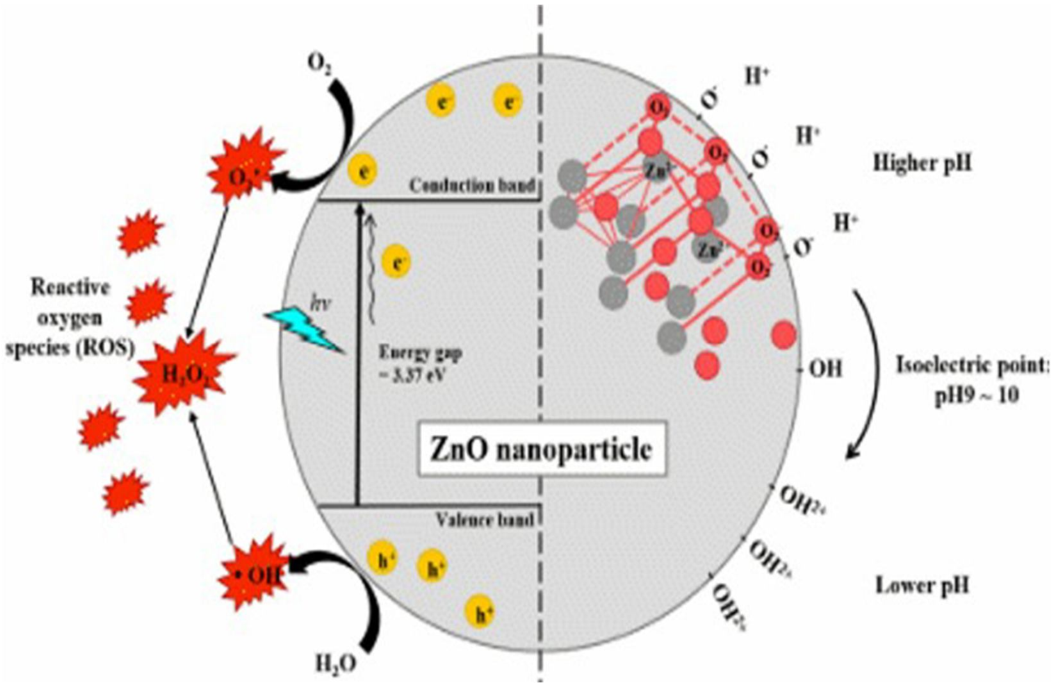

FIG. 8. Qualities of ZnO NPs influenced by their structure [45].

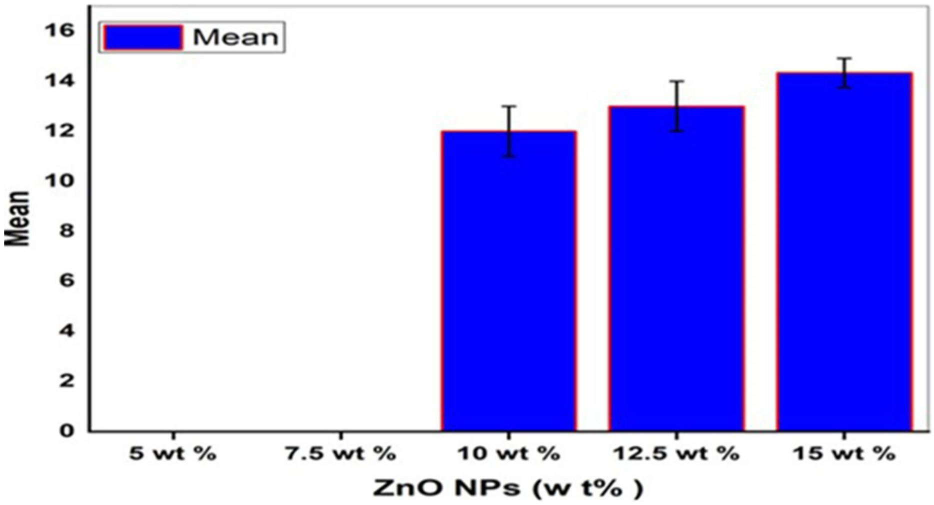

FIG. 9. The antibacterial activity of Cs/PVA and Cs/PVA/ZnO NPs against *Brevibacterium epidermidis* bacteria.

TABLE 2. Inhibition zones and mean of NCs against bacterial strains.

Sample	Inhibition zones (mm)			Mean ± S. D.
PVA-Cs	0	0	0	0
PVA/Cs 2.5 wt.% ZnO NPs	0	0	0	0
PVA/Cs 5 wt.% ZnO NPs	0	0	0	0 a
PVA/Cs 7.5 wt.% ZnO NPs	0	0	0	0 a
PVA/Cs 10 wt % ZnO NPs	13	11	12	12.000±1.000 b
PVA/Cs 12.5 wt. % ZnO NPs	14	12	13	13.000±1.000 b
PVA/Cs 15 wt. % ZnO NPs	15	14	14	14.333±0.5773 c

There is no significant difference ($p>0.05$) because the vital coefficients have similar letters.

Conclusions

In this research, zinc oxide nanoparticles prepared by the sol–gel method were incorporated into chitosan (Cs) and polyvinyl alcohol (PVA) blend films to fabricate nanocomposites by the casting method. As evident from the infrared spectrum obtained from the Cs/PVA blend with incorporated ZnO NPs, characteristic absorption bands in the range of 2000–1250 cm^{-1} are found to change. These changes indicate the interaction of zinc ions with the polymer matrix, which can be in the form of coordination or hydrogen bonding. Such reactions are important because they can change the physical and/or chemical properties of the compound, improving the suitability of the product for various uses. XRD analysis further revealed structural modifications of the Cs/PVA matrix with increasing ZnO content, indicated by reduced peak intensities and shifts in diffraction angles, evidencing strong nanoparticle–polymer interactions. These structural changes indicate the presence of ZnO nanoparticles in the polymer network and may also lead to new composite properties. Furthermore, UV and visible analyses revealed a reduction in the optical band energy (both direct and indirect) of the Cs/PVA blend when ZnO nanoparticles were added. This decrease indicates significant changes in the electronic state of the material. The enhancement of the interfacial contacts between ZnO nanoparticles (NPs) and the polymer matrix can be credited for this improvement. These interactions can create new electronic states and hybridization effects, further enhancing optoelectronic performance. The dispersion of ZnO nanoparticles also increased the antimicrobial activity of the nanocomposite samples. Therefore, this can be attributed to the bactericidal properties of zinc oxide, which act through mechanisms such as ROS formation, Zn^{2+} ion release, and microbial cell wall destruction. Moreover, due to the high surface area of ZnO nanoparticles combined with the matrix (Cs/PVA), the antimicrobial activity is enhanced. All these factors lead to improved efficiency of antimicrobial property, and hence the nanocomposite is suitable for use in biomedical applications, food packaging, and coatings.

References

[1] Sabir, S., Arshad, M., and Chaudhari, S.K., World J., 2014 (2014) 1.

[2] Zhou, X.-Q., Hayat, Z., Zhang, D.-D., Li, M.-Y., Hu, S., Wu, Q., Cao, Y.-F., and Yuan, Y., Processes, 11 (2023) 1193.

[3] Moezzi, A., McDonagh, A.M., and Cortie, M.B., Chem. Eng. J., 185–186 (2012) 1.

[4] Auda, A.A., Banimuslem, H.A.J., and Kadem, B.Y., J. Nanostruct., 2023 (2023) 2251.

[5] Ismail, A.M., Menazea, A.A., Kabary, H.A., El-Sherbiny, A.E., and Samy, A., J. Mol. Struct., 1196 (2019) 332.

[6] Iber, B.T., Kasan, N.A., Torsabo, D., and Omuwa, J.W., J. Renew. Mater. 10 (2022) 1097.

[7] Lam, W.S., Lam, W.H., and Lee, P.F., Mater. (Basel), 16 (2023) 2857.

[8] Maliki, S., Sharma, G., Kumar, A., Moral-Zamorano, M., Moradi, O., Baselga, J., Stadler, F.J., and García-Peñas, A., Polym. (Basel), 14 (2022) 1475.

[9] Ruiz, G.A.M. and Corrales, H.F.Z., "Chitosan, Chitosan Derivatives and their Biomedical Applications", In: "Biol. Act. Appl. Mar. Polysaccharides", (InTech, 2017).

[10] Kouchak M., Ameri, A., Naseri, B., and Boldaji, S.K., Iran. J. Basic Med. Sci., 17 (2014) 14.

[11] Connolly, M. and De Berker, D., Am. J. Clin. Dermatol., 4 (2003) 681.

[12] Kanlayavattanakul, M. and Lourith, N., Int. J. Cosmet. Sci., 33 (2011) 298.

[13] Collins, M.D., Farrow, J.A.E., Goodfellow, M., and Minnikin, D.E., Syst. Appl. Microbiol., 4 (1983) 388.

[14] Sharquie, K.E., Noaimi, A.A., and Hameed, S.D., J. Cosmet. Dermatol. Sci. Appl., 03 (2013) 203.

[15] Haque, M.J., Bellah, M.M., Hassan, M.R., and Rahman, S., Nano Express, 1 (2020) 010007.

[16] Mahamuni, P.P., Patil, P.M., Dhanavade, M.J., Badiger, M.V., Shadija, P.G., Lokhande, A.C., and Bohara, R.A., Biophys. Rep., 17 (2019) 71.

[17] Forquin, M.-P. and Weimer, B.C., "Brevibacterium", In: "Encycl. Food Microbiol.", (Elsevier, 2014) pp. 324–330.

[18] Benson, C.E. and Tatem, L., "Successful Treatment of Brevibacterium Bacteremia Solely With Antimicrobial Therapy", (Cureus, 2021).

[19] Díez-Pascual, A.M. and Luceño-Sánchez, J.A., Polym. (Basel), 13 (2021) 2105.

[20] Revathi, T. and Thambidurai, S., Adv. Powder Technol., 29 (2018) 1445.

[21] Abdeen, Z.I., El Farargy, A.F., and Negm, N.A., J. Mol. Liq., 250 (2018) 335.

[22] Yang, K., Lin, D. and Xing, B., Langmuir, 25 (2009) 3571.

[23] Lavand, A.B. and Malghe, Y.S., J. King Saud Univ. Sci., 30 (2018) 65.

[24] Fardood, S.T., Ramazani, A., and Joo, S.W., J. Appl. Chem. Res., 11 (2017) 8.

[25] Karpuraranjith, M. and Thambidurai, S., Int. J. Biol. Macromol., 104 (2017) 1753.

[26] Malini, M., Thirumavalavan, M., Yang, W.-Y., Lee, J.-F., and Annadurai, G., Int. J. Biol. Macromol., 80 (2015) 121.

[27] Chen, R., So, M.H., Che, C.-M., and Sun, H., J. Mater. Chem., 15 (2005) 4540.

[28] Hebbar, V., Bhajantri, R.F., and Naik, J., J. Mater. Sci. Mater. Electron., 28 (2017) 5827.

[29] Yang, H., Liu, C., Yang, D., Zhang, H., and Xi, Z., J. Appl. Toxicol., 29 (2009) 69.

[30] Bahadur, H., Srivastava, A., Sharma, R., and Chandra, S., Nanoscale Res. Lett., 2 (2007) 469.

[31] Pourrahimi, A.M., Liu, D., Pallon, L.K.H., Andersson, R.L., Martínez Abad, A., Lagarón, J.-M., Hedenqvist, M.S., Ström, V., Gedde, U.W., and Olsson, R.T., RSC Adv., 4 (2014) 35568.

[32] Clémenson, S., David, L., and Espuche, E., J. Polym. Sci. Part A Polym. Chem., 45 (2007) 2657.

[33] Hemalatha, K.S., Rukmani, K., Suriyamurthy, N., and Nagabhushana, B.M., Mater. Res. Bull., 51 (2014) 438.

[34] Ambrosio, R., Carrillo, A., Mota, M., de la Torre, K., Torrealba, R., Moreno, M., Vazquez, H., Flores, J., and Vivaldo, I., Polym. (Basel), 10 (2018) 1370.

[35] Urbach, F., Phys. Rev., 92 (1953) 1324.

[36] Abdelfattah, E.M., Elzanaty, H., Elsharkawy, W.B., Azzam, M.A., Elqahtani, Z.M., Alotibi, S., Alyami, M., and Fahmy, T., Polym. (Basel), 15 (2023).

[37] Morsi, M.A., El-Khodary, S.A., and Rajeh, A., Phys. B Condens. Matter., 539 (2018) 88.

[38] Abdelrazek, E.M., Elashmawi, I.S., El-khodary, A., and Yassin, A., Curr. Appl. Phys., 10 (2010) 607.

[39] Kandulna R. and Choudhary, R.B., Polym. Bull., 75 (2018) 3089.

[40] Herman, A. and Herman, A.P., J. Nanosci. Nanotechnol., 14 (2014) 946.

[41] Perelshtein, I., Ruderman, E., Perkas, N., Tzanov, T., Beddow, J., Joyce, E., Mason, T.J., Blanes, M., Mollá, K., Patlolla, A., Frenkel, A.I., and Gedanken, A., J. Mater. Chem. B, 1 (2013) 1968.

[42] Xie, Y., He, Y., Irwin, P.L., Jin, T., and Shi, X., Appl. Environ. Microbiol., 77 (2011) 2325.

[43] Zhang, L., Jiang, Y., Ding, Y., Povey, M., and York, D., J. Nanopart. Res., 9 (2007) 479.

[44] Sirelkhatim, A., Mahmud, S., Seeni, A., Kaus, N.H.M., Ann, L.C., Bakhori, S.K.M., Hasan, H., and Mohamad, D., Nano-Micro Lett., 7 (2015) 219.

[45] Sharma, P., Jang, N.Y., Lee, J.W., Park, B.C., Kim, Y.K., and Cho, N.H., Pharmaceutics, 11 (2019) 6.

الجداول: تعطى الجداول أرقاما متسلسلة يشار إليها في النص. ويجب طباعة كل جدول على صفحة منفصلة مع عنوان فوق الجدول. أما الحواشي التفسيرية، التي يشار إليها بحرف فوقي، فتكتب أسفل الجدول.

الرسوم التوضيحية: يتم ترقيم الأشكال والرسومات والرسومات البيانية (المخططات) والصور، بصورة متسلسلة كما وردت في النص.

تقبل الرسوم التوضيحية المستخرجة من الحاسوب والصور الرقمية ذات النوعية الجيدة بالأبيض والأسود، على ان تكون أصيلة وليست نسخة عنها، وكل منها على ورقة منفصلة ومعرفة برقمها بالمقابل. ويجب تزويد المجلة بالرسومات بحجمها الأصلي بحيث لا تحتاج إلى معالجة لاحقة، وألا تقل الحروف عن الحجم 8 من نوع Times New Roman، وألا تقل سماكة الخطوط عن 0.5 وبكثافة متجانسة. ويجب إزالة جميع الألوان من الرسومات ما عدا تلك التي ستنشر ملونة. وفي حالة إرسال الرسومات بصورة رقمية، يجب أن تتوافق مع متطلبات الحد الأدنى من التمايز (1200 dpi Resolution) لرسومات الأبيض والأسود الخطية، و 600 dpi للرسومات باللون الرمادي، و300 dpi للرسومات الملونة. ويجب تخزين جميع ملفات الرسومات على شكل (jpg)، وأن ترسل الرسوم التوضيحية بالحجم الفعلي الذي سيظهر في المجلة. وسواء أرسل المخطوط بالبريد أو عن طريق الشبكة (Online)، يجب أرسال نسخة ورقية أصلية ذات نوعية جيدة للرسومات التوضيحية.

مواد إضافية: تشجع المجلة الباحثين على إرفاق جميع المواد الإضافية التي يمكن أن تسهل عملية التحكيم. وتشمل المواد الإضافية أي اشتقاقات رياضية مفصلة لا تظهر في المخطوط.

المخطوط المنقح (المعدَل) والأقراص المدمجة: بعد قبول البحث للنشر وإجراء جميع التعديلات المطلوبة، فعلى الباحثين تقديم نسخة أصلية ونسخة أخرى مطابقة للأصلية مطبوعة بأسطر مزدوجة، وكذلك تقديم نسخة إلكترونية تحتوي على المخطوط كاملا مكتوبا على Microsoft Word for Windows 2000 أو ما هو استجد منه. ويجب إرفاق الأشكال الأصلية مع المخطوط النهائي المعدل حتى لو تم تقديم الأشكال إلكترونيا. وتخزن جميع ملفات الرسومات على شكل (jpg)، وتقدم جميع الرسومات التوضيحية بالحجم الحقيقي الذي ستظهر به في المجلة. ويجب إرفاق قائمة ببرامج الحاسوب التي استعملت في كتابة النص، وأسماء الملفات على قرص مدمج، حيث يعلَم القرص بالاسم الأخير للباحث، وبالرقم المرجعي للمخطوط للمراسلة، وعنوان المقالة، والتاريخ. ويحفظ في مغلف واقٍ.

حقوق الطبع

يُشكِّل تقديم مخطوط البحث للمجلة اعترافاً صريحاً من الباحثين بأنّ مخطوط البحث لم يُنْشَر ولم يُقَدَّم للنشر لدى أي جهَة أخرى كانت وبأي صيغة ورقية أو إلكترونية أو غيرها. ويُشترط على الباحثين ملء أنموذج يَنُصُ على نقْل حقوق الطبع لتُصبح ملكاً لجامعة اليرموك قبل الموافقة على نشر المخطوط. ويقوم رئيس التحرير بتزويد الباحثين بإنموذج نقل حقوق الطبع مع النسخة المُرْسَلَة للتنقيح. كما ويُمنع إعادة إنتاج أيِّ جزء من الأعمال المنشورة في المجلّة من دون إذن خَطِّيٍّ مُسْبَق من رئيس التحرير.

إخلاء المسؤولية

إن ما ورد في هذه المجلة يعبر عن آراء المؤلفين، ولا يعكس بالضرورة آراء هيئة التحرير أو الجامعة أو سياسة اللجنة العليا للبحث العلمي أو وزارة التعليم العالي والبحث العلمي. ولا يتحمل ناشر المجلة أي تبعات مادية أو معنوية أو مسؤوليات عن استعمال المعلومات المنشورة في المجلة أو سوء استعمالها.

الفهرسة: المجلة مفهرسة في:

Emerging Sources Citation Index (ESCI) Journal Impact Factor 2022 0.7	Scopus
ULRICHSWEB GLOBAL SERIALS DIRECTORY	

معلومات عامة

المجلة الأردنية للفيزياء هي مجلة بحوث علميّة عالمية متخصصة مُحكمة تصدر بدعم من صندوق دعم البحث العلمي والابتكار، وزارة التعليم العالي والبحث العلمي، عمان، الأردن. وتقوم بنشر المجلة عمادة البحث العلمي والدراسات العليا في جامعة اليرموك، إربد، الأردن. وتنشر البحوث العلمية الأصيلة، إضافة إلى المراسلات القصيرة Short Communications، والملاحظات الفنية Technical Notes، والمقالات الخاصّة Feature Articles، ومقالات المراجعة Review Articles، في مجالات الفيزياء النظرية والتجريبية، باللغتين العربية والإنجليزية.

تقديم مخطوط البحث

تقدم المخطوطات إلكترونيًا عن طريق موقع المجلة: https://jjp.yu.edu.jo

ويجري تحكيمُ البحوثِ الأصيلة والمراسلات القصيرة والملاحظات الفنية من جانب مُحكِّمين اثنين في الأقل من ذوي الاختصاص والخبرة. وتُشَجِّع المجلة الباحثين على اقتراح أسماء المحكمين. أما نشر المقالات الخاصّة في المجالات الفيزيائية النَشِطَة، فيتم بدعوة من هيئة التحرير، ويُشار إليها كذلك عند النشر. ويُطْلَب من كاتب المقال الخاص تقديم تقرير واضح يتّسم بالدقة والإيجاز عن مجال البحث تمهيداً للمقال. وتنشر المجلةُ أيضاً مقالات المراجعة في الحقول الفيزيائية النشطة سريعة التغيُر، وتُشَجَع كاتبي مقالات المراجعة أو مُستَكتبيها على إرسال مقترحٍ من صفحتين إلى رئيس التحرير. ويُرْفَق مع البحث المكتوب باللغة العربية ملخص (Abstract) وكلمات دالة (Keywords) باللغة الإنجليزية.

ترتيب مخطوط البحث

يجب أن تتم طباعة مخطوط البحث ببنط 12 نوعه Times New Roman، وبسطر مزدوج، على وجه واحد من ورق A4 (21.6 × 27.9 سم) مع حواشي 3.71 سم ، باستخدام معالج كلمات ميكروسوفت وورد 2000 أو ما استَجَد منه. ويجري تنظيم أجزاء المخطوط وفق الترتيب التالي: صفحة العنوان، الملخص، رموز التصنيف (PACS)، المقدّمة، طرق البحث، النتائج، المناقشة، الخلاصة، الشكر والعرفان، المراجع، الجداول، قائمة بدليل الأشكال والصور والإيضاحات، ثَمَّ الأشكال والصور والإيضاحات. وتُكْتَب العناوين الرئيسة بخطٍ **غامق**، بينما تُكْتَب العناوين الفرعية بخطٍ *مائل*.

صفحة العنوان: وتشمل عنوان المقالة، أسماء الباحثين الكاملة وعناوين العمل كاملة. ويكتب الباحث المسؤول عن المراسلات اسمه مشارا إليه بنجمة، والبريد الإلكتروني الخاص به. ويجب أن يكون عنوان المقالة موجزا وواضحا ومعبرا عن فحوى (محتوى) المخطوط، وذلك لأهمية هذا العنوان لأغراض استرجاع المعلومات.

الملخص: المطلوب كتابة فقرة واحدة لا تزيد على مائتي كلمة، موضحة هدف البحث، والمنهج المتبع فيه والنتائج وأهم ما توصل إليه الباحثون.

الكلمات الدالة: يجب أن يلي الملخص قائمة من 4-6 كلمات دالة تعبر عن المحتوى الدقيق للمخطوط لأغراض الفهرسة.

PACS: يجب إرفاق الرموز التصنيفية، وهي متوافرة في الموقع http://www.aip.org/pacs/pacs06/pacs06-toc.html.

المقدمة: يجب أن توضّح الهدف من الدراسة وعلاقتها بالأعمال السابقة في المجال، لا أن تكون مراجعة مكثفة لما نشر (لا تزيد المقدمة عن صفحة ونصف الصفحة مطبوعة).

طرائق البحث (التجريبية / النظرية): يجب أن تكون هذه الطرائق موضحة بتفصيل كاف لإتاحة إعادة إجرائها بكفاءة، ولكن باختصار مناسب، حتى لا تكون تكرارا للطرائق المنشورة سابقا.

النتائج: يستحسن عرض النتائج على صورة جداول وأشكال حيثما أمكن، مع شرح قليل في النص ومن دون مناقشة تفصيلية.

المناقشة: يجب أن تكون موجزة وتركز على تفسير النتائج.

الاستنتاج: يجب أن يكون وصفا موجزا لأهم ما توصلت إليه الدراسة ولا يزيد عن صفحة مطبوعة واحدة.

الشكر والعرفان: الشكر والإشارة إلى مصدر المنح والدعم المالي يكتبان في فقرة واحدة تسبق المراجع مباشرة.

المراجع: يجب طباعة المراجع بأسطر مزدوجة ومرقمة حسب تسلسلها في النص. وتكتب المراجع في النص بين قوسين مربعين. ويتم اعتماد اختصارات الدوريات حسب نظام Wordlist of Scientific Reviewers.

Subscription Form

Jordan Journal of
PHYSICS

An International Peer-Reviewed Research Journal issued by the Support of the Scientific Research and Innovation Support Fund

Published by the Deanship of Research & Graduate Studies, Yarmouk University, Irbid, Jordan

Name: .... الأسم:
Specialty:.. التخصص:
Address: .... العنوان:
P.O. Box:.. صندوق البريد:
City & Postal Code: .... المدينة/الرمز البريدي:
Country: .... الدولة:
Phone: .... رقم الهاتف:
Fax No:... رقم الفاكس:
E-mail:... البريد الإلكتروني:
No. of Subscription: .... عدد الإشتراكات:
Method of Payment:... طريقة الدفع:
Amount Enclosed:... المبلغ المرفق:
Signature: .... التوقيع:

Cheques should be paid to Deanship of Research and Graduate Studies - Yarmouk University.

I would like to subscribe to the Journal
For

☐ One Year
☐ Two Years
☐ Three Years

One Year Subscription Rates

	Inside Jordan	Outside Jordan
Individuals	JD 8	€ 40
Students	JD 4	€ 20
Institutions	JD 12	€ 60

Correspondence

Subscriptions and Sales:

Prof. Muhammad S. Bawa'aneh
Deanship of Research and Graduate Studies
Yarmouk University
Irbid – Jordan
Telephone: 00 962 2 711111 Ext. 2074
Fax No.: 00 962 2 7211121

المملكة الأردنية الهاشمية

جامعة اليرموك

المجلة الأردنية
للفيزياء

مجلة بحوث علمية عالمية متخصصة محكّمة

تصدر بدعم من صندوق دعم البحث العلمي والابتكار

المجلد (18)، العدد (3)، آب 2025م / ربيع الأول 1447هـ

المجلة الأردنية

للفيزياء

مجلة بحوث علمية عالمية محكّمة

المجلد (18)، العدد (3)، آب 2025م / ربيع الأول 1447هـ

المجلة الأردنية للفيزياء: مجلة علمية عالمية متخصصة محكّمة تصدر بدعم من صندوق دعم البحث العلمي والإبتكار، عمان، الأردن، وتصدر عن عمادة البحث العلمي والدراسات العليا، جامعة اليرموك، إربد، الأردن.

ترسل البحوث إلى العنوان التالي:

الأستاذ الدكتور محمد سالم بواعنة
رئيس تحرير المجلة الأردنية للفيزياء
عمادة البحث العلمي والدراسات العليا، جامعة اليرموك
إربد ، الأردن
هاتف 00 962 2 7211111 **فرعي** 2074
E-mail: *jjp@yu.edu.jo* **Website**: *http:// jjp.yu.edu.jo*